UNIVERSITÄT OSNABRÜCK

Fachbereich Biologie / Chemie

Institut für Chemie neuer Materialien

Dissertation

Zur Erlangung des Grades eines Doktors der Naturwissenschaften

(Dr. rer. nat.)

Electrochemical AFM and STM Studies of Redox Active Oligomers, Polymers and Drugs at Graphitic Materials

vorgelegt von

Shamaila Sadaf

Osnabrück 2017

This doctoral thesis was carried out at the Institut für Chemie neuer Materialien, Fachbereiche Biologe / Chemie, Universität Osnabrück, Germany, under the supervision of Prof. Dr. Lorenz Walder. The studies were performed in the period from Jan. 2011 to 2017, interrupted by the birth of my Son on 27 September 2013.

Hauptberichterstatter: Prof. Dr. Lorenz Walder, Universität Osnabrück

Zweitberichtestatter: Prof. Dr. Markus Haase, Universität Osnabrück

Weitere Mitglieder: Prof. Dr Helmut Rosemeyer, Universität Osnabrück

Dr. Kasten Kömpe, Universität Osnabrück

To My Father and Mother

Acknowledgement

I thank Almighty Allah for blessing me with this opportunity to help me to go through this journey.

This dissertation could not have been completed without the great support that I have received from so many people over the years. I wish to offer my most heartfelt thanks to the following people.

First and foremost I would like to record to my thesis advisor Professor Dr. Lorenz Walder for his supervision, advice, and guidance right from the beginning of this research work as well as giving me extraordinary experiences throughout this endeavor. I am extremely thankful to him for investing his valuable time in fruitful discussions regarding my experimental results and assistance with writing research papers as well as this dissertation. Above all he provided me unflinching encouragement and support in various ways, especially his patience and cooperation which kept me motivated to complete my thesis before and after having a baby. This study would not have been possible without his kind support. I am indebted to him more than I could ever express.

Besides my advisor, I gratefully acknowledge the other members of the review committee Prof. Dr. Markus Haase, Prof. Dr. Helmut Rosemeyer, and Dr. Kasten Kömpe. I thank them for their availability and consent to evaluate my thesis.

I appreciate the whole faculty and colleagues of Institute für Chemie Neuer Materialien for offering friendly and comfortable environment to work in.

My deepest gratitude to my research group members in the University of Osnabrück for their support and productive discussions. I have learned a lot working with them all; Dr. Veronica-Alina Constantin, Dr. Liang Cheng Cao, Dr. Seyyed Mohsen Beladi Mousavi , Dr. Marius Ciobanu, Patrick Harpel, Sascha lax, Jonas Klein, and, Arsalan Mahmood.

Many thanks go in particular to Dr. Veronica-Alina Constantin and Dr. Seyyed Mohsen Beladi Mousavi for the synthesis of several compounds which I used for my research project.

I am greatly indebted to Mrs. Simona Webersinn and Mrs. Christine Schulz-Kölbel for the friendly working environment in the lab and their continued support regarding the laboratory and administrative works.

I would like to acknowledge Ms. Lily Schneider for facilitating Raman and XPS measurements in Department of Physics.

I am pleased to thank Dr. Helmut Schäfer for collaboration and thoughtful scientific discussion. My sincere thanks go to Ms. Wajiha Akram for English proofreading of my thesis.

I would like to express my thanks to our institute and department secretaries, Claudia Drieschner and Monika Dubiel for their kind help in administrative work.

I would also like to appreciate the support extended by my colleagues and friends in difficult times in Germany.

I am thankful to Prof. Dr. Inam-ul-Haque from University of Engineering and Technology Lahore-Pakistan for motivating me to pursue PhD abroad.

Deepest thanks are due to DAAD for their financial contribution during early couple of years of my PhD.

I also wish to thank my friends Dr. Kiran Waseem, Wajiha Ali, Sabeen Amin Farhan, Farah Atif and Hira Ajmal for their constant support and help during my stay in Germany and helping me not to feel homesick.

Last but not least I would like to acknowledge my family. My very special gratitude to my loving parents who have raised me and especially my father Muhammad Amin Bhatti, who always encouraged and supported me to achieve academic heights and my mother Aziz-un-Nisa for her constant and countless prayers which made my journey blessed, smooth and easy. I am deeply indebted to my siblings and whole family for providing me with consistent support and incessant encouragement and prayers throughout my years of study, research and writing this thesis. This accomplishment is simply impossible without them.

Words cannot express how grateful I am to my beloved husband Ehsan-ur-Rehman for his unflagging love, believing in me and being there for practical support in all those things of life beyond doing a PhD, and finally, my adored son Hasan, for being a good baby and cheering me up all the time which sustained me all the way through.

Thank you very much, everyone!

Osnabrück, October 13, 2017.

Shamaila

Table of Contents

Thesis Abstract

Carbon nanotubes (CNTs) and graphene (G) are the two (semi-)conducting allotropes of carbon offering a very high surface to bulk ratio. When combined with electrochemistry and using the principles of molecular self-assembling, many new applications of CNTs and graphene have become feasible, e.g. in the field of molecular electronics, as energy storage materials and for drug delivery.

In this work scanning probe microscopy techniques (STM, AFM and EC-AFM) are used to understand the structure of self-assembled organic and electroactive molecules, oligomers and polymers on the surface of CNTs and graphene, and to rationalize their function as supramolecular system in the macroscopic world. It was found that there is a strong tendency for self-assembling in solution of aromatic electrophores with HOMO/LUMO levels close to the semiconducting CNT frontier orbitals. The tunneling currents through the aromatic guest molecules on CNT are much higher than for the same molecule on highly oriented pyrolytic graphite (HOPG).

In the 1st chapter of this thesis the different microscopic techniques used with special emphasis on the electrochemical atomic force microscopy (EC-AFM), a relatively new combination technique which plays an important role in this work, are presented.

It is followed by the structural analysis of stiff, semi-flexible and flexible oligo-viologen on CNTs. Using a large set of molecules with well defined small structural differences allowed to study how the superstructure (guests@CNT) is determined by the tiny changes in the guest structure. Mostly helical super structures of guests around the CNT host were observed. The guest's rod length, its side chain length and its flexibility translate unambiguously into the

corresponding STM images. A non-linear, star shaped oligo-viologen cannot wrap CNT without overlapping star branches, as expected from model considerations. In collaboration with a Korean research group we were able to build an n-doped FET using a reduced rigid oligo-viologen@CNT.

Along with the oligomer the formation of stiff poly-viologens@CNT and poy-imides@CNT are studied. As compared to the oligomers@CNT, the polymers@CNT have less conformational freedom when wrapping a CNT. Thus, exclusively double to multi stranded helical wrapping was observed. An interesting new phenomenon was discovered with stiff poly-viologen or poly-naphthaline tetracarboxylic acid diimide with purely sp2 configured atoms, i.e. an outer, large diameter helical structure of "the guest" polymer and a CNT "host" sitting inside the spiral. The spiral diameter was simulated using PM7 calculations. The CNT can be moved within the large spiral by voltage pulse application.

Subsequently, the conformation of flexible poly-viologens and poly-TEMPO on host materials such as CNTs and vapor grown carbon fibers (VGCF) was studies. Again, helical wrapping is observed, but the diameter adapts here to the CNT diameter. Monomer subunit resolution was achieved in case of polyTEMPO. The practical importance in energy storage is discussed in the corresponding original paper.

The next chapter of thesis focuses on AFM imaging of a new battery material, i.e. poly-ferrocene on graphene oxide (PVF@GO) and on reduced graphene oxide (PVF@rGO), as well as poly-viologen as PV@GO and PV@rGO. A highlight is definitely the visualization of the so-called ion-breathing, i.e. the reversible counter ion movement from solution into the battery material composite upon electrochemical reduction/oxidation. To the best of my knowledge, this

phenomenon is for the first time visualized here by a combination of electrochemistry and AFM. STM analysis of electrically conductive rGO allows for subunit resolution of polyviologen@rGO sitting in partially 2D crystalline structure on rGO.

In the last chapter, my publication on the drug delivery system doxorubicin at carbon nanotubes is described. Dox@CNT is already used as drug delivery system in animal tests, but little is known on the structure of the drug on the carrier, and a reductive release trigger has so far not been identified. Rich structural variations of the drug on the CNT (helical strands of monomers and dimers) were found. It is possible to get the drug loading efficiency from STM image analysis. Reductive release of Dox@CNT was also unknown so far. Electron injection into Dox@CNT from an electrode or from the biological reducing agent glutathione (GSH) leads to irreversible release of Dox. Experimental results are in excellent agreement with semi-empirical simulations.

Chapter 1

Introduction

Carbon nanotubes especially single wall carbon nanotubes have been phrased as "materials of 21st century" due to their mechanical, electrical and thermal properties that these molecules (ranging in size from macro to nano molecule) possess. They have potentially important application for classical materials such as molecular electronics.[1]

Research based on Carbon nanotubes is multi- and interdisciplinary as chemists are investigating carbon nanotubes as host for molecules[2], oligomers and polymers; engineers are developing next generation copmposite[3] and molecular electronic devices[1] while biologist perceive nanotubes as a potential host for drug delivery and other therapeutic purposes.

The physico-chemical nature of carbon nanotubes, which essentially can be viewed as fully conjugated polyaromatic macromolecules with a hollow, inert interior and reactive exterior and ends make it attractive for the application in all fields.

Whereas elementary research of carbon nanotubes focuses on the intrinsic properties of individual or isolated carbon nanotubes, these applications mainly depend on the interaction of CNTs with their surrounding environment. These interactions can be marked in many non-covalent forces present between CNTs and molecules, ions or polymers present in the surrounding environment.

This reactive exterior has big room for interaction with other molecules via covalent or non covalent interaction.

Noncovalent interactions of CNTs with other molecules (which can be small molecules, oligomers as well as polymers)[4,5] ends up as supramolecular assembly which can be due to π-π, electrostatic as well as Van der Waals interactions.

Supramolecular chemistry is all about the noncovalent interaction between the molecules; it shows how they self-assemble together identify each other and perform unique functions at molecular level. This self-assembly is nature architecture that happens when two things come together, they arrange in a best possible way without damaging each other properties. Supramolecular chemistry gives a bottom up approach to nanotechnology from its applications from material sciences to the biological sciences.

In this regards carbon nanotubes and graphene oxide play a major rule as a host for many molecules ranging metals, redox active organic molecules as well as many drugs.

There are few techniques which give direct visualization of this supramolecular self-assembly, most well known are scanning probe microcopies. Scanning probe microscopy covers many related techniques for imaging surfaces from a few hundred µm down to nanometers, allowing to image microscopic structures down to single atoms, the molecular level up to the atoms or groups of atoms. This scale extends as scan over a distance of 100µm in x and y direction and upto 4µm in z direction. So development of this technology has profound effect in many areas of science and engineering. SPM technology deals with a concept of scanning a very sharp tip (3-50 µM radius of curvature) across the sample surface. This tip is usually mounted on a flexible cantilever which allows the tip to follow the surface profile easily.

There are mainly three common SPM techniques used such as (i) Scanning Tunneling Microcopies (STM) (ii) Atomic Force Microscopy (AFM) and (iii) Nearfield scanning optical microscopy (NSOM).

Whereas STM measures weak electrical current called tunneling current between tip and sample while AFM measures the interaction force between tip and sample surface and NSOM scans a very small light source very close to the sample and detection of this light energy forms the image.

These techniques have the ability to operate on a scale from microns down to nanometers and can image clusters of individual atoms and molecules. STM relies on the electrical conductivity of the sample, so at least some features on the sample surface must be electrically conductive to some degree. AFM is used for studies of non-conductors and is the technique more commonly used for studies of macromolecules and biological specimens.

In this thesis**,** two techniques AFM and STM are mainly used to visualize the interaction of redoxactive molecules such as oligomers, polymers as well as drugs with carbon allotropes such as carbon nanotubes and graphene oxide, while AFM with the combination of electrochemistry was used to analyze the performance of half cell of organic battery.

1.1. Scanning tunneling microscopy on carbon nanotubes

In 1981 a new type of microscope unveiled. In contrast to traditional microscopes, the scanning tunneling microscope (STM) did not use lenses. Instead, a sharp tip is moved in the vicinity of conductive surface for the electron wavefunctions of the atoms in the tip to overlap with the wavefunctions of the surface atoms[6]. When a bias voltage is applied, electrons started to 'tunnel'

through the gap, causing a current to flow from the foremost atom of the tip into the conducting surface.

Before this technique quantum tunneling had been studied theoretically, but was never established so elegantly.

Furthermore, the tunneling current depended exponentially on the distance (d, eq.1 between the tip and the conductive surface (Fig. 1), varying this distance by just an atomic diameter altered the current by a factor of a thousand. Therefore, by scanning the tip over a sample in two dimensions and keeping the tunneling current constant, it was possible to image surfaces on the atomic scale.[7]

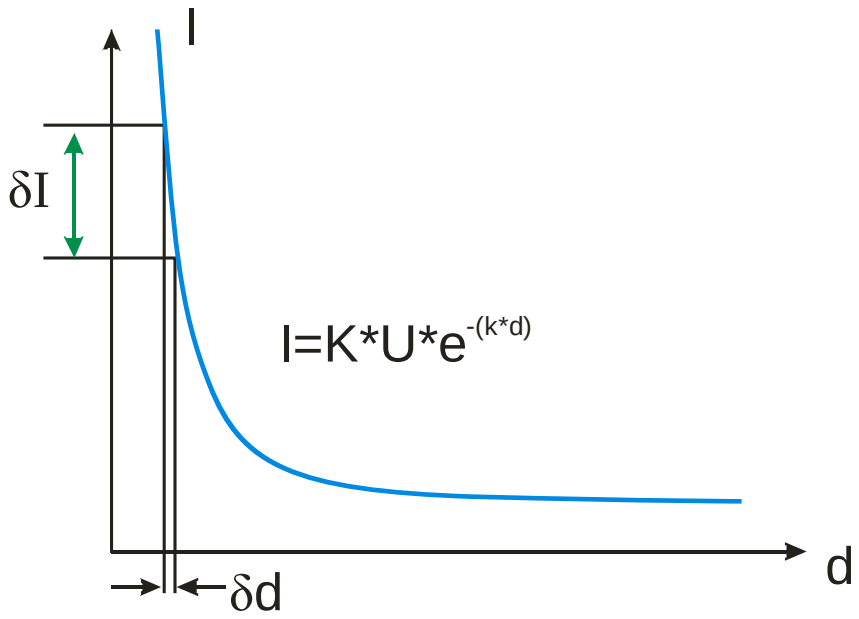

Figure 1: *Exponential decay of tunneling current with respect to distance*

$I = K*U*e^{-(k*d)}$ k and K are constants, U is the tunneling voltage bias

STM is a powerful tool capable of revealing detailed three-dimensional morphology at atomic scale for flat surfaces and self-assembled molecules. In the case of CNTs, however, there are considerable experimental difficulties associated with the heterogeneity of CNT samples and high mobility of the individual nanotubes over common STM supports. Nevertheless, STM turned to be suitable to characterize individual nanotubes, to explore the adsorption of biomolecules onto CNT sidewalls[8] and even to detect the phenomena of self-assembly for some complex organic molecules such as porphyrins.[9]

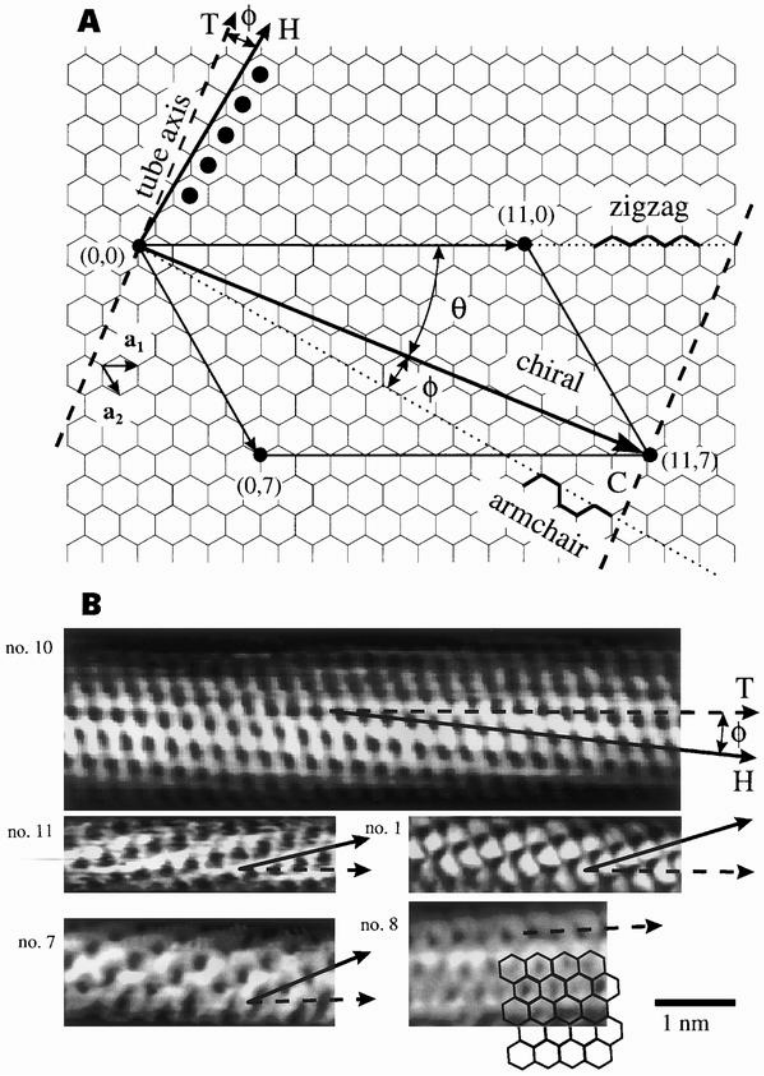

Figure 2: Relation between the hexagonal carbon lattice and the chirality of carbon nanotubes. ***A****, the construction of a carbon nanotube from a single graphene sheet. By rolling up the sheet along the wrapping vector* ***C****, that is, such that the origin (0,0) coincides with point C, a nanotube indicated by indices (11,7) is formed. Wrapping vectors along the dotted lines lead to tubes that are zigzag or armchair. All other wrapping angles lead to chiral tubes whose wrapping angle is specified relative to either the zigzag direction (θ) or to the armchair direction (ϕ = 30° - θ).* ***B****, Atomically resolved STM images of individual single-walled carbon nanotubes. The lattice on the surface of the cylinders allows a clear identification of the tube chirality. Topographic images were obtained by recording the tip height at constant tunnel current in a home-built STM operated at 4 K. The Pt/Ir tips were cut in ambient air by scissors. Typical bias parameters are those of image no. 10, that is, a tunnel current I = 60 pA, and a bias voltage* V_{bias} *= 500 mV.*[10]

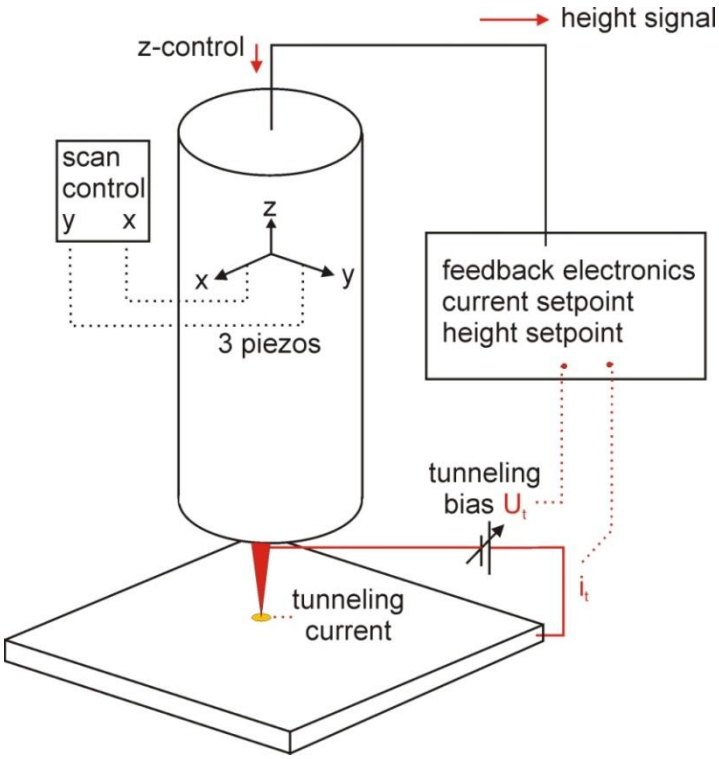

a) STM principle

Tunneling current (i_t) used to control z-piezo (height, constant current mode) or tunneling current measured at constant z (constant height mode). U_t adjusted for good dynamics and average height control ($25 < U_t < 300$ mV). Scan rate: 0.3 to 1 sec per line, usually 256 lines scanned; it in the range: 0.5 to 1.5 nA

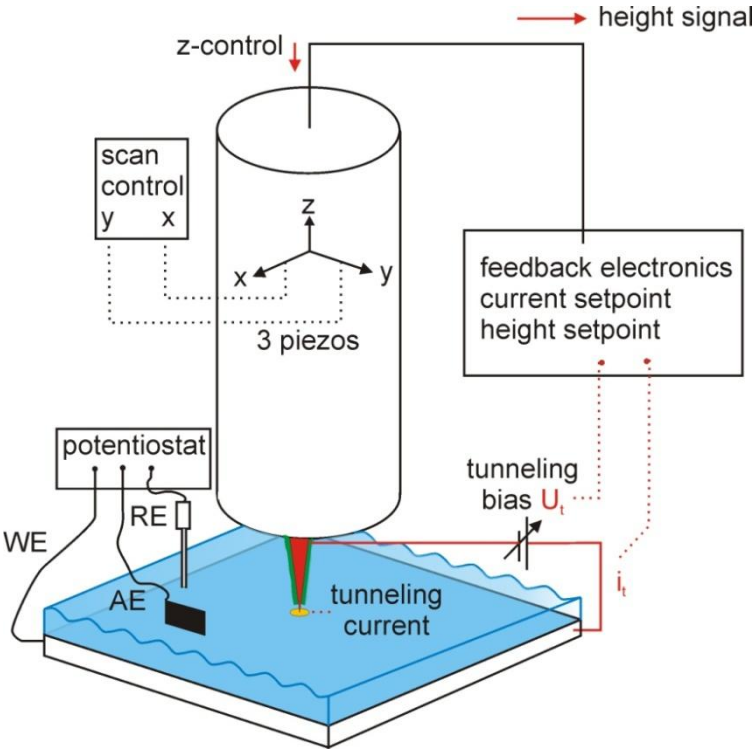

b) Electrochemical STM (EC-STM) principle;

As a) but tip is isolated (green layer), solvent/electrolyte, counter electrode, reference electrode added, working electrode is substrate, potentiostatic conditions; parallel electrochemical oxidation/reduction and STM imaging.

STM plays an essential role in understanding the atomic arrangement and electronic structure of carbon nanotubes [10,11]. Since this technique enables direct and simultaneous monitoring of chirality and local density of states, it has been widely applied to SWNTs[10,11] The first remarkable STM investigation on pristine single wall carbon nanotubes showed a complete atomically resolved structural and electronic characterization (Fig. 2) the authors were able to measure the diameter (D), the chirality, and the chiral indices.[10]

Later, STM images with molecular resolution of different polymeric and monomeric compounds which self-assemble on CNT have been reported, e.g. DNA on 6,5-CNT[8], lipid derivatives[12], polymers[13,14](poly thiophenes)[15-17], metal adsorption[18], physisorption of linear-chain alkane and fatty acid molecules on the outer surface of single-wall carbon nanotubes[19] and drugs.[20]

1.2. Atomic force microscopy at graphene

As described earlier atomic-scale STM images are ultimately the result of a convolution of the surface topography and the electronic structure of both tip and surface. While in AFM, atomic resolution is based on detecting the forces ascribed to the onset of the short-range bonding interaction between the foremost atom of a sharp tip at the end of a cantilever and the atoms at the surface.[21-23] These interatomic forces are of the order of pico to nanonewtons, and they start being appreciable at a separation distance between the closest tip and surface atoms typically shorter than 5 Å. These short-range interatomic forces are detected, and very precisely quantified, by operating the AFM in dynamic mode. In this operation scheme, the cantilever is oscillated at resonance while keeping the oscillation amplitude constant, and the forces acting on the AFM tip are detected as changes in the cantilever resonant frequency. In contrast to the STM, where the tunnelling current does not combine with other observables, the tip–surface

interatomic forces responsible for atomic contrast in AFM cumulate with additional tip–surface interactions spanning over a longer distance range.[24]

Since 1986, the AFM has proved its suitability in various applications. First designed as an instrument to image the surfaces of non-conductive materials with high lateral and vertical resolution, the technique has been adapted to work in various environments (for example, in liquids, at low temperatures, in high magnetic fields and so on), and also for chemical and biological applications when the tip is suitably modified.

The development of surface-structure-sensitive techniques in last few years has led to in situ electrochemical atomic force microscopy (EC-AFM), which has made possible the performance of detailed studies of the surface chemistry, morphology, 3D structure, electrochemical response, and performance of battery electrodes[25-29]. Important aspects revealed by EC-AFM studies on Li-ion battery electrodes are especially useful in explaining surface modifications in relation to the other surface-sensitive techniques.

EC-AFM is a powerful in situ tool to study both surface morphology and chemistry of the Li-ion battery electrodes during the cycling of an electrochemical cell. However, the sample used for EC-AFM to study the morphology change and aging phenomenon in some researches was extracted from commercially available battery.[28,30] These samples resulted in different potential distributions and uncertain electrode surface since the sample generally contains active materials, organic binders, and conductive additives.

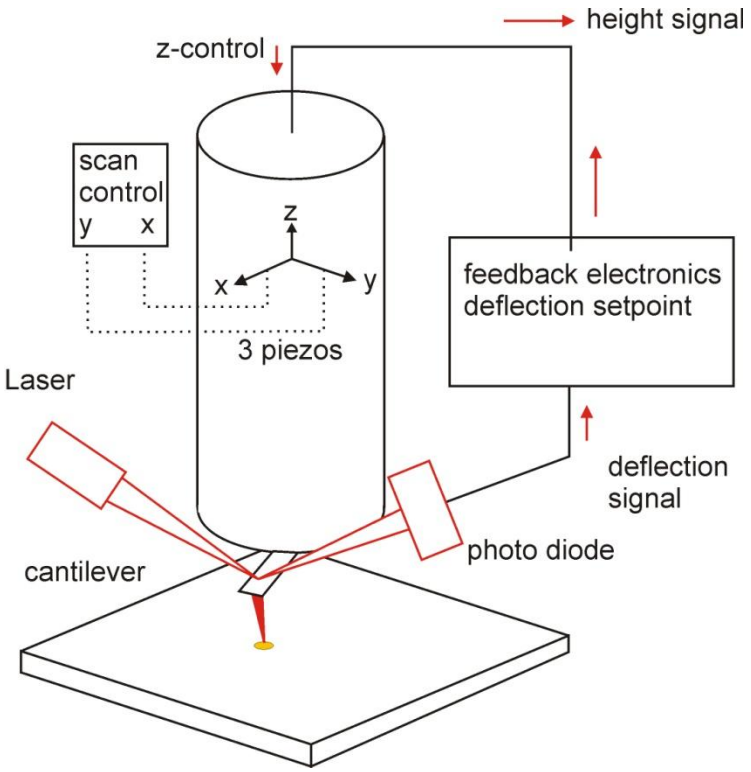

c) AFM principle;

Deflection of reflected laser signal used as feedback for z-piezo height control and as topology signal, either in contact or non-contact mode.

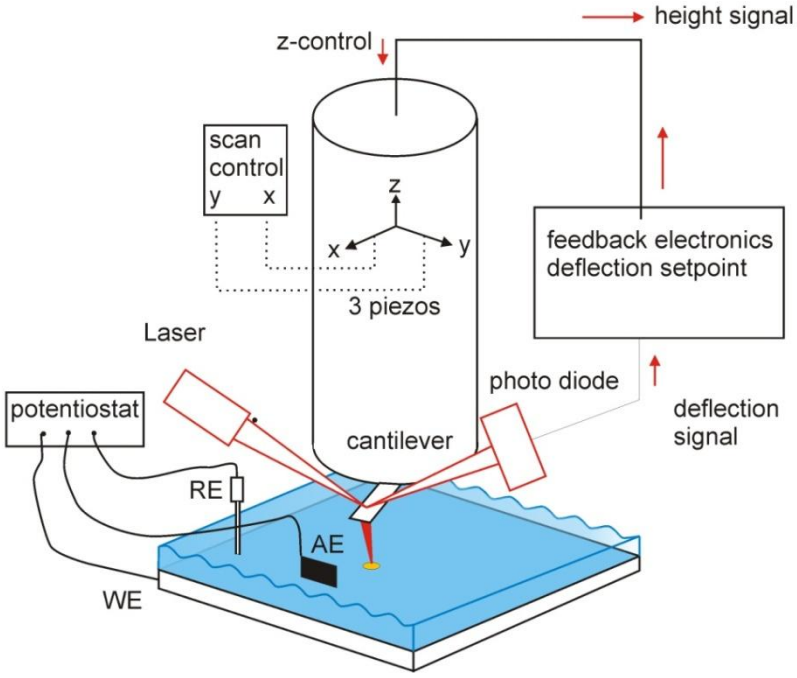

d) Eectrochemical AFM (EC-AFM) principle;

As a) solvent/electrolyte, counter electrode, reference electrode added, working electrode is substrate, potentiostatic conditions; parallel electrochemical oxidation/reduction and AFM imaging.

Graphene is an allotrope of carbon that takes the form of a two-dimensional single layer hexagonal lattice of tightly bonded carbon atoms in a sp2 hybridised arrangement.[31] Graphene has a single atom thickness of around 3.45 Å and has extraordinary electrical and mechanical properties. It is a zero-overlap semi-metal (with both holes and electrons as charge carriers) with very high electrical conductivity, meaning that it has great potential in the electronics/semiconductor industry. Graphene is also extremely light (0.77 mg/m^2) and elastic giving it enormous potential in the development of new materials.

Graphene, a single layer of graphite, is currently the subject of a massive research interest and an equally immense number of publications due to its novel physical properties and vast potential in technological applications.

For numerous industrial applications (i.e., electrochemistry, electronic, environmental and chemical sensors, heterogeneous catalysis, supercapacitors, nanoparticle self-assembly, corrosion, lubricants, etc.) it is essential to know and control the state of the graphene surface.

References

[1] P. Avouris, Accounts Chem Res 2002, 35, 1026.

[2] M. Monthioux, Carbon 2002, 40, 1809.

[3] E. T. Thostenson, Z. F. Ren, T. W. Chou, Compos Sci Technol 2001, 61, 1899.

[4] E. Zaminpayma, K. Mirabbaszadeh, Comp Mater Sci 2012, 58, 7; M. J. Yang, V. Koutsos, M. Zaiser, J Phys Chem B 2005, 109, 10009.

[5] C. Gerber, H. P. Lang, Nat Nanotechnol 2006, 1, 3.

[6] G. Binnig, H. Rohrer, C. Gerber, E. Weibel, Appl Phys Lett 1982, 40, 178.

[7] D. A. Yarotski, S. V. Kilina, A. A. Talin, S. Tretiak, O. V. Prezhdo, A. V. Balatsky, A. J. Taylor, Nano Lett 2009, 9, 12.

[8] M. Bassiouk, V. A. Basiuk, E. V. Basiuk, E. Alvarez-Zauco, M. Martinez-Herrera, A. Rojas-Aguilar, I. Puente-Lee, Appl Surf Sci 2013, 275, 168.

[9] J. W. G. Wildoer, L. C. Venema, A. G. Rinzler, R. E. Smalley, C. Dekker, Nature 1998, 391, 59.

[10] T. W. Odom, J.-L. Huang, P. Kim, C. M. Lieber, Nature 1998, 391, 62.

[11] C. Richard, F. Balavoine, P. Schultz, T. W. Ebbesen, C. Mioskowski, Science 2003, 300, 775.

[12] a) R. Czerw, Z. X. Guo, P. M. Ajayan, Y. P. Sun, D. L. Carroll, Nano Lett 2001, 1, 423; b) L. C. Cao, S. Sadaf, S. M. Beladi-Mousavi, L. Walder, Eur Polym J 2013, 49, 1923.

[13] a) M. Giulianini, E. R. Waclawik, J. M. Bell, M. De Crescenzi, P. Castrucci, M. Scarselli, N. Motta, Appl Phys Lett 2009, 95; b) M. Giulianini, E. R. Waclawik, J. M. Bell, M. Scarselli, P. Castrucci, M. De Crescenzi, N. Motta, Polymers-Basel 2011, 3, 1433; c) R. G. S. Goh, N. Motta, J. M. Bell, E. R. Waclawik, Appl Phys Lett 2006, 88.

[14] N. Shah, P. Basu, P. Prakash, S. Donck, E. Gravel, I. N. N. Namboothiri, E. Doris, Nanomaterials-Basel 2016, 6.

[15] H. Ago, R. Azumi, S. Ohshima, Y. J. Zhang, H. Kataura, M. Yumura, Chem Phys Lett 2004, 383, 469.

[16] A. Rodriguez-Galvan, O. Amelines-Sarria, M. Rivera, M. D. Carreon-Castro, V. A. Basiuk, Nano 2016, 11.

[17] R. Perez, M. C. Payne, I. Stich, K. Terakura, Phys Rev Lett 1997, 78, 678; A. I. Livshits, A. L. Shluger, A. L. Rohl, A. S. Foster, Phys Rev B 1999, 59, 2436; P. Dieska, I. Stich, R. Perez, Phys Rev Lett 2003, 91.

[18] O. Custance, R. Perez, S. Morita, Nat Nanotechnol 2009, 4, 803.

[19] a) Y. Yamaguchi, M. Shiota, Y. Nakayama, N. Hirai, S. Hara, J Power Sources 2001, 93, 104; b) Y. Yamaguchi, M. Shiota, Y. Nakayama, N. Hirai, S. Hara, J Power Sources 2000, 85, 22; b) R. Vidu, F. T. Quinlan, P. Stroeve, Ind Eng Chem Res 2002, 41, 6546; c) C. R. Becker, K. E. Strawhecker, Q. P. McAllister, C. A. Lundgren, Acs Nano 2013, 7, 9173.

[20] S. Ramdon, B. Bhushan, S. C. Nagpure, J Power Sources 2014, 249, 373.

[21] D. E. Demirocak, B. Bhushan, J Colloid Interf Sci 2014, 423, 151.

[22] A. K. Geim, Phys Scripta 2012, T146.

Part 1

Supramolecular Self-assembly of Redox Active Oligomers and Polymers@CNT

Chapter 2

STM Investigations on Self-assembled Viologen Oligomers at the Outer Surface of CNT - and Application

2.1. Introduction

The following STM studies are mainly structural investigations on the self-assembly of oligo-viologens on carbon nanotubes. The origin of the viologen oligomers is indicated in the sub-sections. They are flexible (benzylic), semi-flexible (mixed benzylic and phenylic) and rigid (purely phenylic) structures (see Scheme 1).

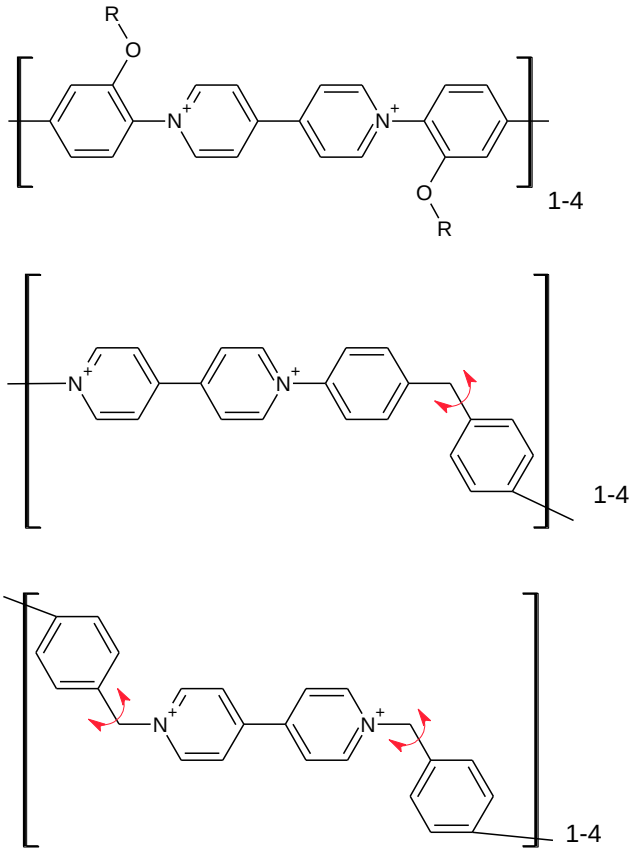

Scheme1: *Rigid, semiflexible and flexible oligomers, classification based on the amount of benzylic subunits.*

My studies involving carbon nanotubes (CNTs), including both single-walled (SWNTs) and multi-walled CNTs (MWNTs) in contact with electroactive mono- and oligomers are of fundamental and applied interest. Both aspects are addressed in chapter 2.

Fundamental and applied aspects result from the supramolecular interaction of elecroactive monomers with low lying LUMO (main concern in my thesis) or with high HOMO and the complicated frontier orbitals of CNTs. Mutual interaction of these orbitals can lead to supramolecular complex formation and allow the design of novel hybrid nanomaterials combining the unique electronic and redox properties of viologen and CNTs. The noncovalent functionalization of CNTs with viologens is based on π–π-interactions between the two components possessing highly delocalized π-electrons. The supremolecular complex formation - as compared to the covalent functionalization techniques - has inherent advantages as it does not disrupt the intrinsic electronic structure of the nanotubes, keeping them totally intact. It has been shown that the nanohybrids composed of CNTs and viologens, can be obtained, and that they undergo charge transfer easily.[32] Thus, CNTs noncovalently functionalized with simple viologen deserve definitely a more detailed characterization and it is of interest, if oligomeric viologens@CNT display similar structural and applied properties.

Viologens without CNT are well known electrochromic redox systems exhibiting two reversible well separated reduction waves and used as fast electron transfer mediators. They were used in mono-, oligo- and polymeric state as molecular building blocks in supramolecular chemistry. Little is known about their interaction with flat macroscopic surfaces but recently their self-assembly on modified Cu (100) surface was reported. The supramolecular interaction of viologen species with nanoscopic structures is of special interest raising fundamental questions, e.g. can the interaction of the LUMO of viologens with the orbitals of CNT lead to new behavior

of the complete nanoscopic system? or: can the color of the viologen radical be influenced by close interaction with CNT and allow for the construction of new electrochromic devices. The main question in context with my STM investigations, however, is: what is the structure of mono- or oligomeric viologens, which exhibits a conjugated sp2-system of variable stiffness on the curved cylindrical surface of a carbon nanotube. From recent molecular electronics investigation, more specifically from field effect transistor fabrications using sc-CNTs and monomeric viologen, we know that so-called ambiently stable n-doping of the CNT can be achieved. However, little is known about the arrangement of the viologens on the CNT FET. It is also unknown if oligomeric viologens of different flexibility @CNT display also or can even improve the FET behavior, and if they can be constructed by self-assembling at all. It is further not clear if the well described electrochemistry of viologens in solution will persist when the viologens are adsorbed on CNT.[33]

There are some aspects of CNTs that need to be taken into account with respect to the electrochemistry of such systems, i.e. the so-called wrapping angle of supramolecularly hold guest molecules, and the distance of a self-assembled layer of guest molecules on a CNT.

Wrapping angle, chirality, interactions within the host-guest complex

For this study I used chiral SWCNT with 6,5 chirality. As shown in Fig.1, the 6,5-sc-CNT displays several lines representing options for ideal phenyl overlap between the CNT phenyl groups and the guest molecules consisting of poly-phenyl (poly-4,4' bipyridinium) or condensed polyaromatic systems. Notably, the CNT's chirality depends on its theoretical construction from a graphene sheet (Fig. 1) and the 6,5-chirality I used is not a 100 % but only enriched. The natural angle is ca. 5^{o}, 27^{o} or multiples of this value (see Fig. 1). In Fig. 1 I also show the well

known source of these angles related to the formal construction of a tube from a sheet of graphene. The construction angle, e.g. in the 6,5-case, determines the diameter of the tube and its conductivity as semiconductor. Accordingly, other angles, typical for metallic behavior of the tube result in thicker tubes without appearance of a CNT helix. It is also known that chirality favors strongly donor-acceptor complex formation. [18,34]

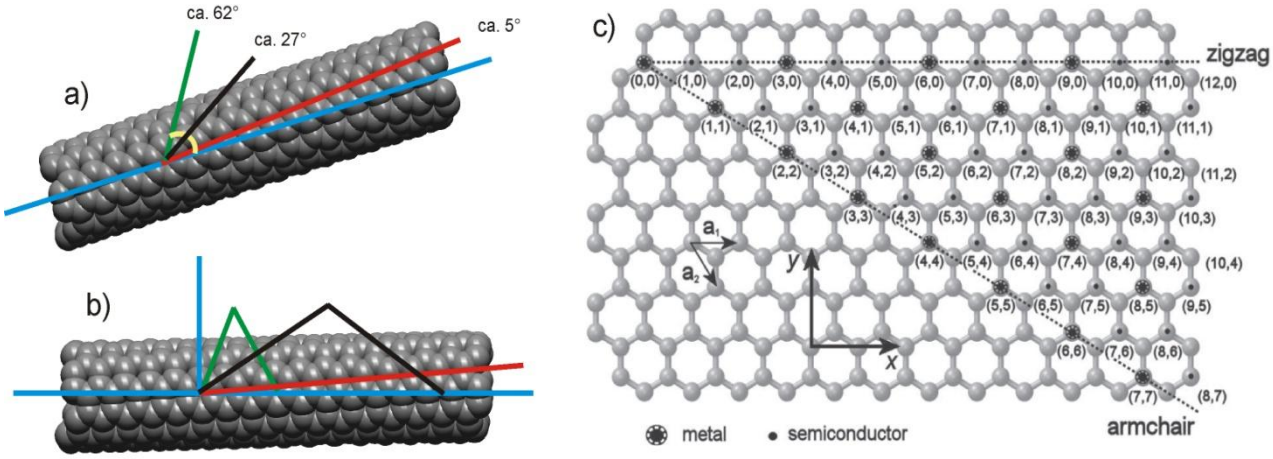

Figure 1*: a,b) 6,5 Chiral carbon nanotubes in space-filling presentation as constructed in nanotubes modeler with lines indicating repetitive patterns (red, black, green) and lines in blue representing the CNT main axes and its orthogonal; a) prominent angles with respect to the main axis of CNT connecting centers of the phenyl rings; b) including starting point and direction of backside helical chain according to c); c) Definition of the chiral index (n, m) of a carbon nanotubes on the grapheme lattice.*

Along with chirality and π–π interaction many other factors typical for non-covalent interaction between the guest molecules or with respect to the CNT-guest interaction such as Van der Waals interaction, hydrogen bonding and others can play a role. I expect, furthermore, for stiff molecules and oligomers another type of geometry, to stack coplanar and have their main axis in the aromatic system parallel to the CNT main axis because of minimal torsion energy build-up. Finally, reports on guests@CNT in which the aromatic part of the guest molecules adopts a

perpendicular orientation with respect to the carbonaceous surface have appeared, and this conformation was explained to the presence of the so-called CH···π interaction.[35] This weak attraction between a C−H bond and a π system is a quite unique type of non-covalent interaction in which the π electrons can be viewed as the proton acceptor and they play a significant role in aromatic π networks, but have not been shown for guests on CNTs. All over, a rich variety of interactions is expected reflecting the result for 2D-crystallization on a cylinder under restraint conditions. I will show that using the STM technique the problem could be highlighted.

In STM images of redox oligomers or polymers covered CNTs we expect to see the projection of the tubes with their guest molecules as shown in Fig. 2. In the geometrical analysis r1 and r2 must be taken into account in order to distinguish double and single helical wrapping.

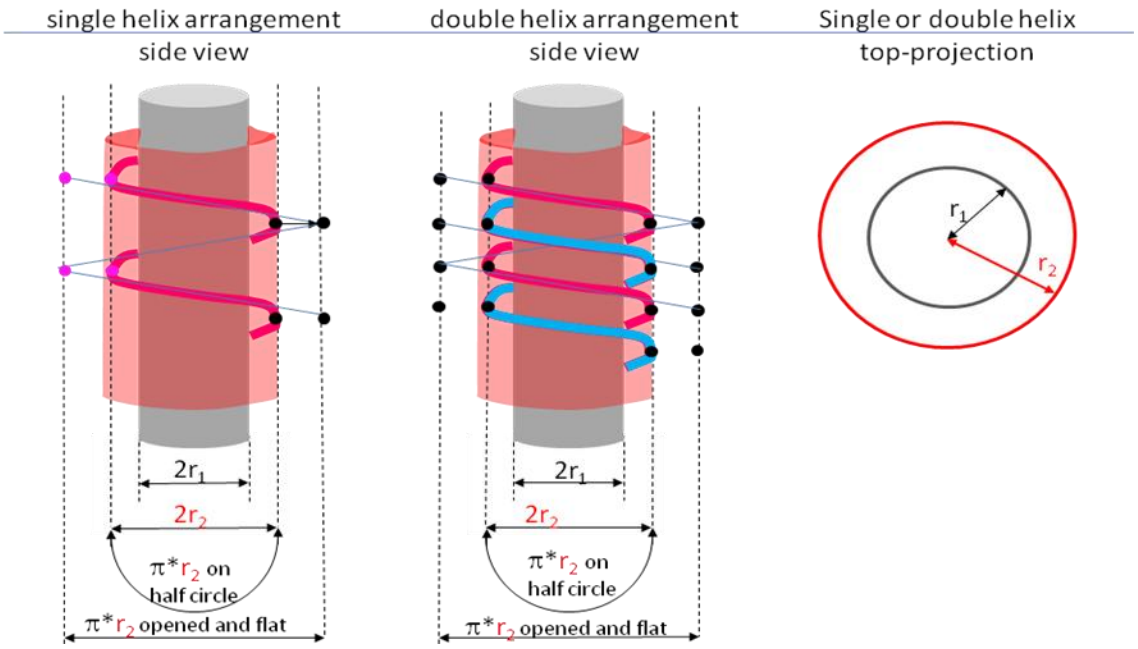

Figure 2: *Schematic representation of a single and double strand wrapping along the axis of a nanotube (left) with r_1: CNT diameter; r_2: wrapping guest cylindrical diameter; cross section (right, adapted from;* [36] *r2-r1 represents the distance between guest and CNT (ca. 0.38 to 0.6 nm); the outermost black and pink dots and the outermost dotted lines represent the half width of the hypothetical cut cylinders – they are of importance for the analysis of mono-, double, triple stranded situations in experimental STM pictures.*

2.2. Results and Discussion

2.2.1. STM Morphology of Different Viologen Oligomers Self-assembled on 6,5-CNTs

Depending on the flexibility of the poly-viologen rod structures it is expected that the higher the flexibility the larger the tendency of self-assembling on a curved path on the CNT cylinder. Obviously, a curved path means adsorption of the oligo with its main axis at 90^{o} or close to 90^{o} with respect to the nanotube main axis. Notably, such a study has not been reported. Here I have had access to a large amount of similar oligos with different flexibility.

STM topographic results are therefore discussed and analyzed on the bases classification of redox oligomers having sp2, sp3, and mixed hybridized carbon content. First the rigid all-sp2 oligomers presented in Scheme 2 and 3 are discussed.

2.2.1.1. Rigid rod viologen oligomers

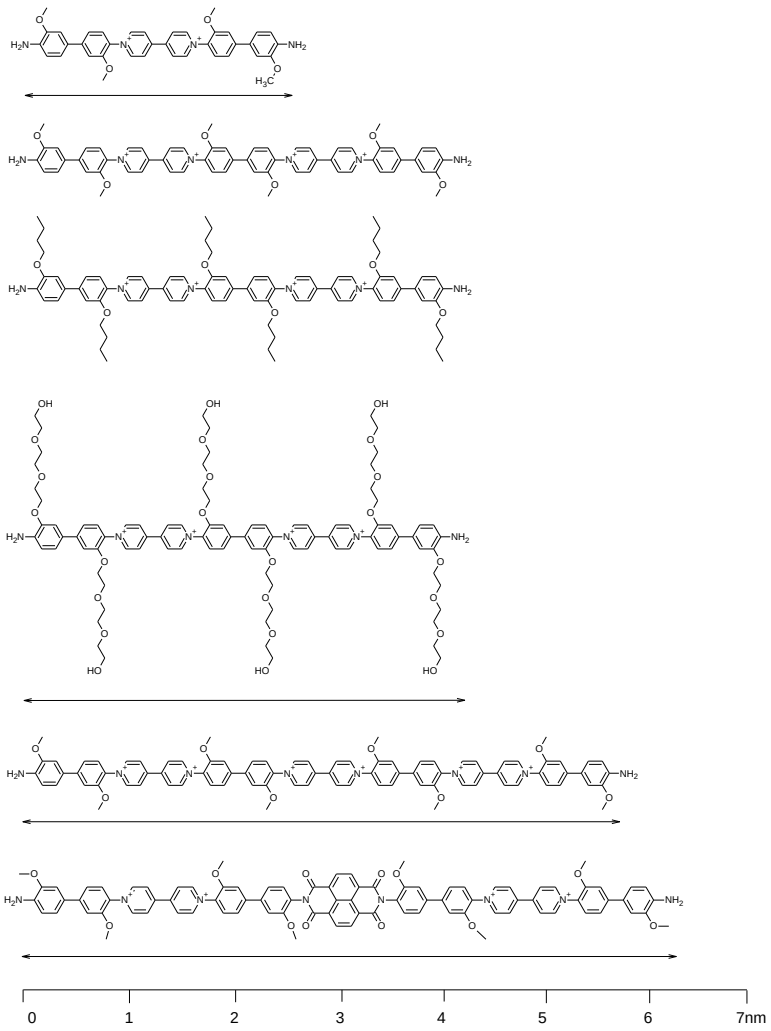

Scheme 2: *Overview of the rigid rod oligomers with abbreviations and molecule number*

Rod length and side chain length

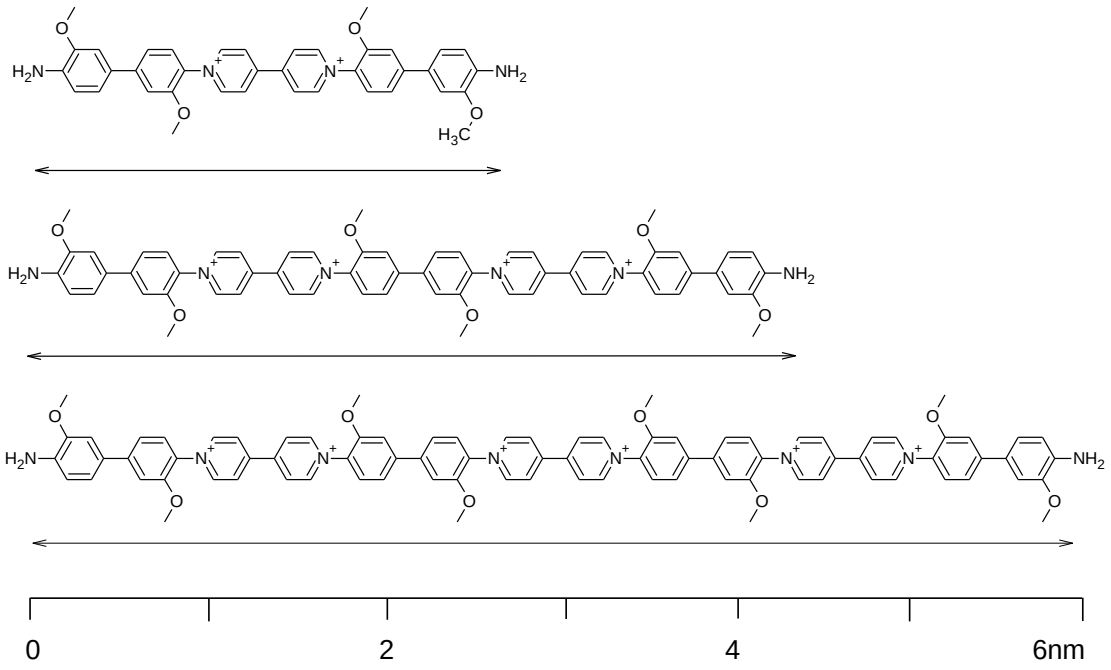

Scheme 3: *Rigid rod oligomer with different backbone length*

The molecule **1** to **3** presented (Scheme 2) consist of 1,4-connected aromats (phenyl and pyridinium moieties). Their backbones are considered relatively rigid towards any deviation from linearity because of the exclusive presence of sp2 carbons and nitrogens in their main chain. Taking advantage of the high resolution obtainable for aromatic systems on CNTs compounds **1**-**3** should allow to observe the length of the oligomers which varies from 2.4 to 6.1 nm, and their tendency to self-assemble parallel or inclined to the CNT main axis. As shown in Fig. 3a-c, compound **1** is at right angle to the CNT main axis, and according to my interpretation, it forms length-offset dimers (3d) of ca. 2.5 nm long species (*cfm* theoretical length of 2.4 nm, Fig. 3a). The driving force for such lateral dimmer formation is probably a donor-acceptor interaction of phenyl and pyridinium subunits. The phenomenon will be

discussed in more detail later. A similar laterally offset self-assembly perpendicular to the CNT axis is observed for compound **2** (Fig. 3h-j). The experimental oligomer length is 4.1 nm similar to the model length showing 4.4 nm. The longer compound **3** (model length: 6.1 nm) can sit inclined at 50° degree on the CNT and extend its ends onto the HOPG surface (overall experimental length: ca. 6 nm, (Fig. 3k-n).

As shown in Fig. 4, the long rigid rod can wrap a bundle of CNTs helically in a conformation of the individual molecules parallel to the main axis of the CNT. The length of the oligomer can be determined experimentally as 6 nm (model: 6.1 nm).

One explanation for the observed pitch is the lateral donor (D) –acceptor (A) interaction of the bipyridinium and the bis-anisidine moieties (cfm. Fig.4d). Notably, in case of the rigid viologens **1**-**3** only the longest shows (in a few cases) such parallel conformation of CNT- and molecule main axis.

As shown in Fig. 3e), compound **3** can adopt also a "zigzag" and a "boxed" conformation with the molecules sitting parallel to each other at right angle to the CNT main axis (Fig. 5c). The boxed conformation shows the highest resolution of sub-molecular units in the whole set of molecules and STM measurements used and performed in this study. In Fig. 5d, I show that such geometry is probably related to (partially) reduced viologen subunits in **3**. Generation of two sp3 centers at N allows the molecule to be in more tight contact with the tube even in a conformation perpendicular to the CNT axis. Three shiny subunits of ca. 3 nm are observed for the **3**-boxed CNT in Fig. 5c. According to the model these subunits can be interpreted as a viologen flanked by two bis-anisidines (Fig. 5a).

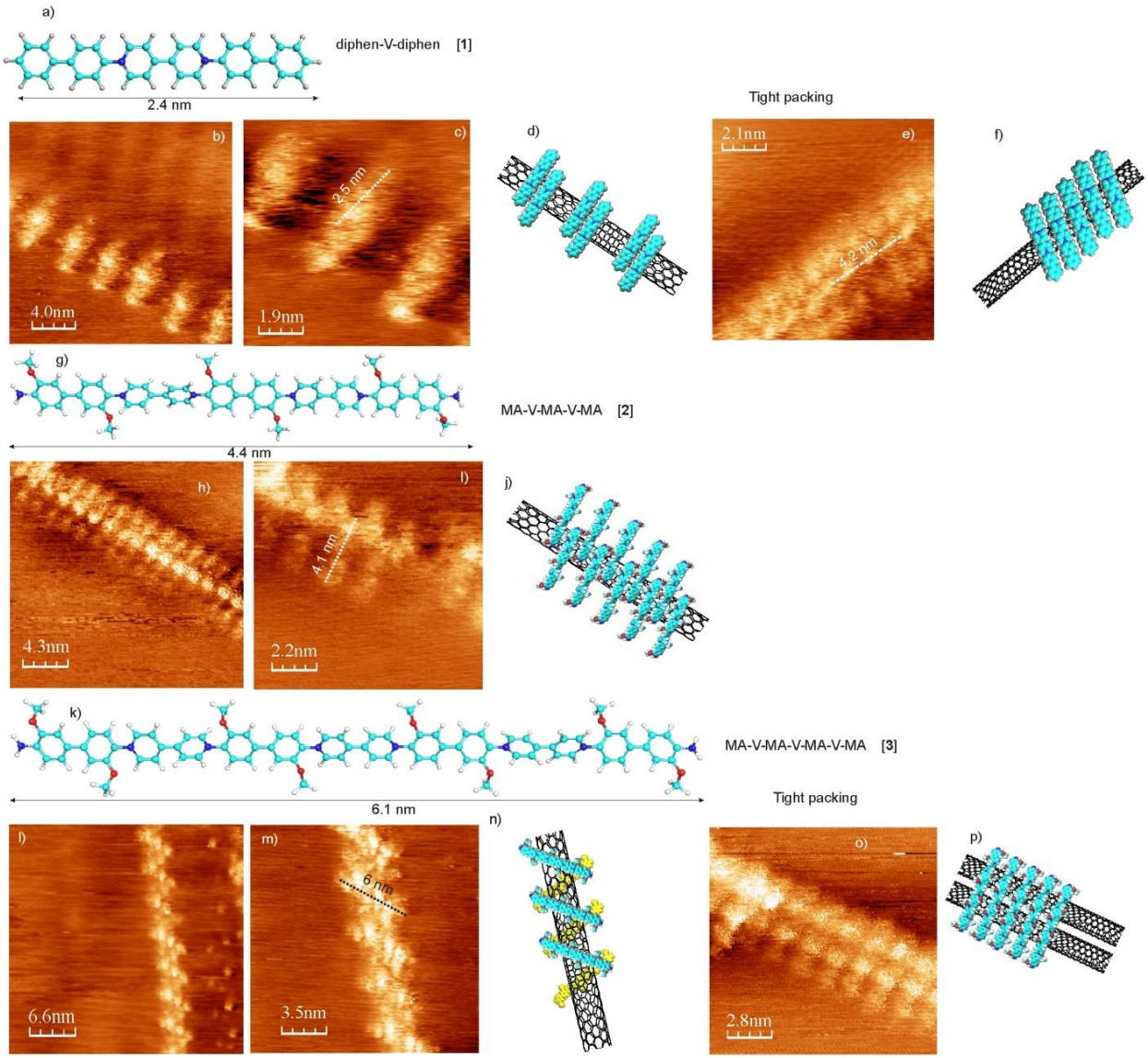

Figure 3: *STM images of self-assembled rigid rod oligomers **1**, **2**, and **3** with different back bone length in vertical or inclined conformation with respect to the CNT axis (boxed case excluded);* ***(a-f)*** *a) modeled structure of **1** (length: 2.4 nm; b) r.a_diluted_**1**@CNT ; c) zoomed-in b) showing 2.5 nm lenth (white dotted line); d) proposed structure of r.a._d_**1**@CNT;(or another interpretation could be that compound is sitting on a bundle of three) e) r.a._t.p._**1**@CNT (r.a. = right angle, t.p.=tightly packed, d=diluted) f) is the proposed structure of e).*

(g-j) *g) chemical structure of **2** (MA-V-MA-V-MA) with a modeled length of 4.4 nm; h) **2**@CNT shows increased tunneling current where the underlying CNT is close; i) zoom-in of h) indicating an alternate arrangement of the molecules with the length of 4.1 nm (dotted line); j) proposed arrangement of **2**@CNT in i).*

(k-p) *k) chemical structure of **3** (MA-V-MAV-MA-V-MA) with modeled length of 6.1 nm; l) STM topographic image of **3** self-assembled on CNT exhibiting an inclined conformation (angle 50^o) with respect to the CNT main axis; m) zoom-in of l) showing **3** as fully extended single molecule (6 nm (highlighted by black line), i.e. close to the modeled value), showing subunit resolution of consecutive bicyclic systems in the molecule (5-7 subunits resolved); n) proposed arrangement of 3@CNT in l-m); o) alternate arrangement of **3** wrapping two tubes with conformation at right angle to the main CNT axis; p) proposed structure of **3**@CNT in o).*

As already indicated, the wrapping angle of **1**-**3** on CNT depends on the length of the oligomer. The smaller molecules prefer to adopt a perpendicular conformation to the main axis of the CNT while the longer oligos tend to be inclined with respect to the main axis of CNT or to self-assemble even parallel to the CNT main axis (see below). The inclination angle may reflect the position of benzene rings in the CNT given by the chirality of the CNT. All-over it is probably an energy optimization process involving criteria such as (i) rigidity of the oligomer towards bending, (ii) the length of the oligomer, (iii) the oxidation state of the viologen subunits (reduction adds sp3 centers into the oligomer chain), (iv) contact area, i.e. distance between CNT and oligomer, as well as (v) torsional energy build-up in the oligomer deviation from linearity. As seen in Fig.3 (a-j) molecules with one or two bipy subunits prefer to stay at right angle to CNT obviously allowing orbital overlap of CNT and oligomer. In case of the longer rigid oligomers the deviation from linearity would be large and energetically unfavorable. Long oligomers prefer therefore to wrap at 0 degree angle or inclined (90 > angle > 0 degree). The inclined angle may represent the angle of benzene rings present in the chiral 6,5-CNT, but I could not confirm this hypothesis clearly in the course of my work.

In Table 1, I represent the measured vs. the theoretical length of compounds **1** to **3**, measured in their different conformation. The observed lengths are in good agreement with the calculated lengths (MM+, by Arguslab[37] (slope = 1.03, ideally: 1.0).

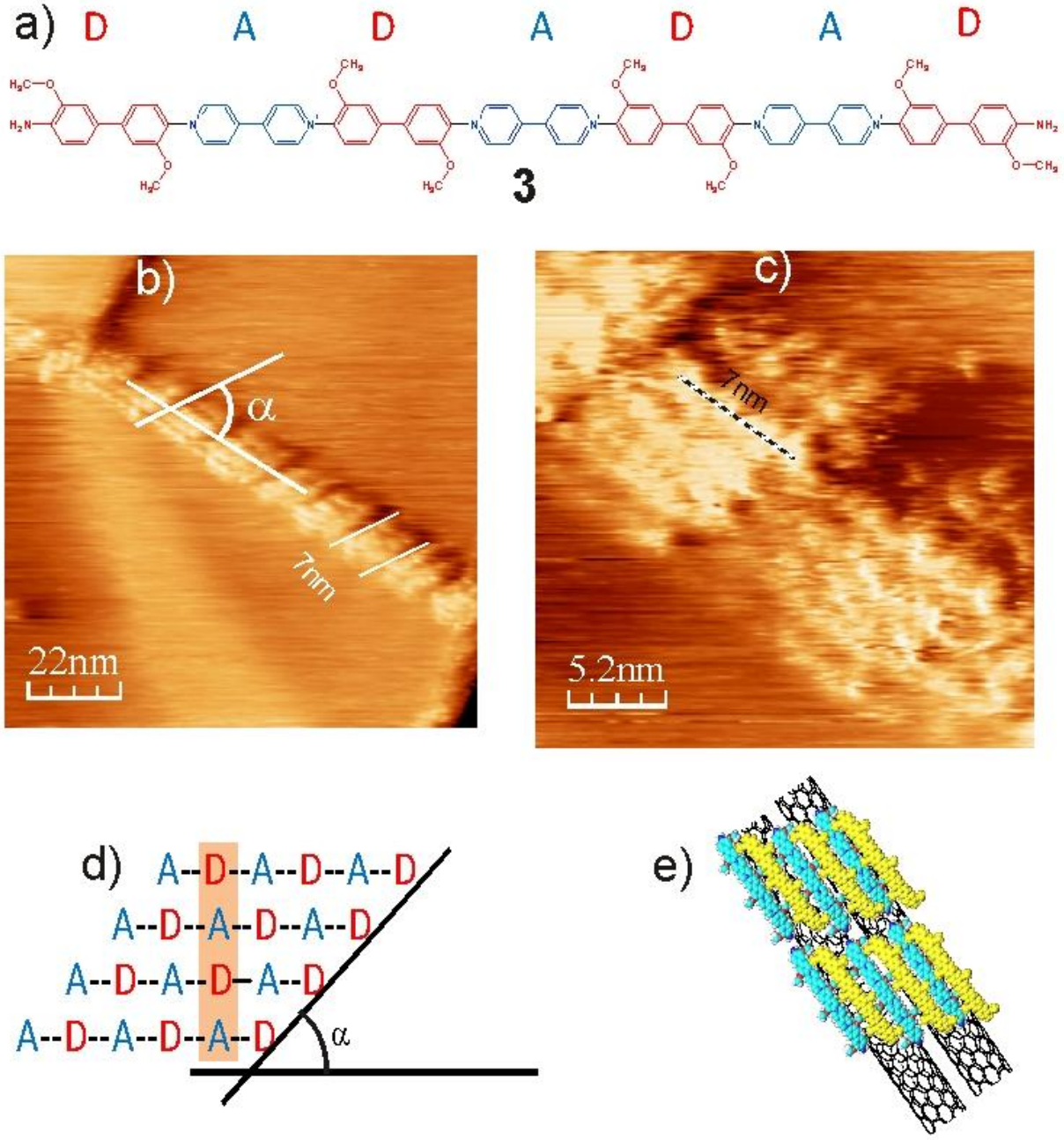

Figure 4: *Rigid rod **3** in parallel – offset conformation on CNT – Indication for donor-acceptor interactions. a) model of **3** with electron donor (bis-anidisin, red) and electron acceptor (bipyridinium, blue) subunits; d) principle of optimization of lateral charge transfer interaction between bisanisidin and bipyridinium subunits in parallel arranged **3**@CNT; b) STM structure of the parallel conformation of **3**@CNT exhibiting an angle a of ca. 60 degree and a lateral spacing between molecules of ca. 1.2 to 1.5 nm; c) zoom-in of b).*

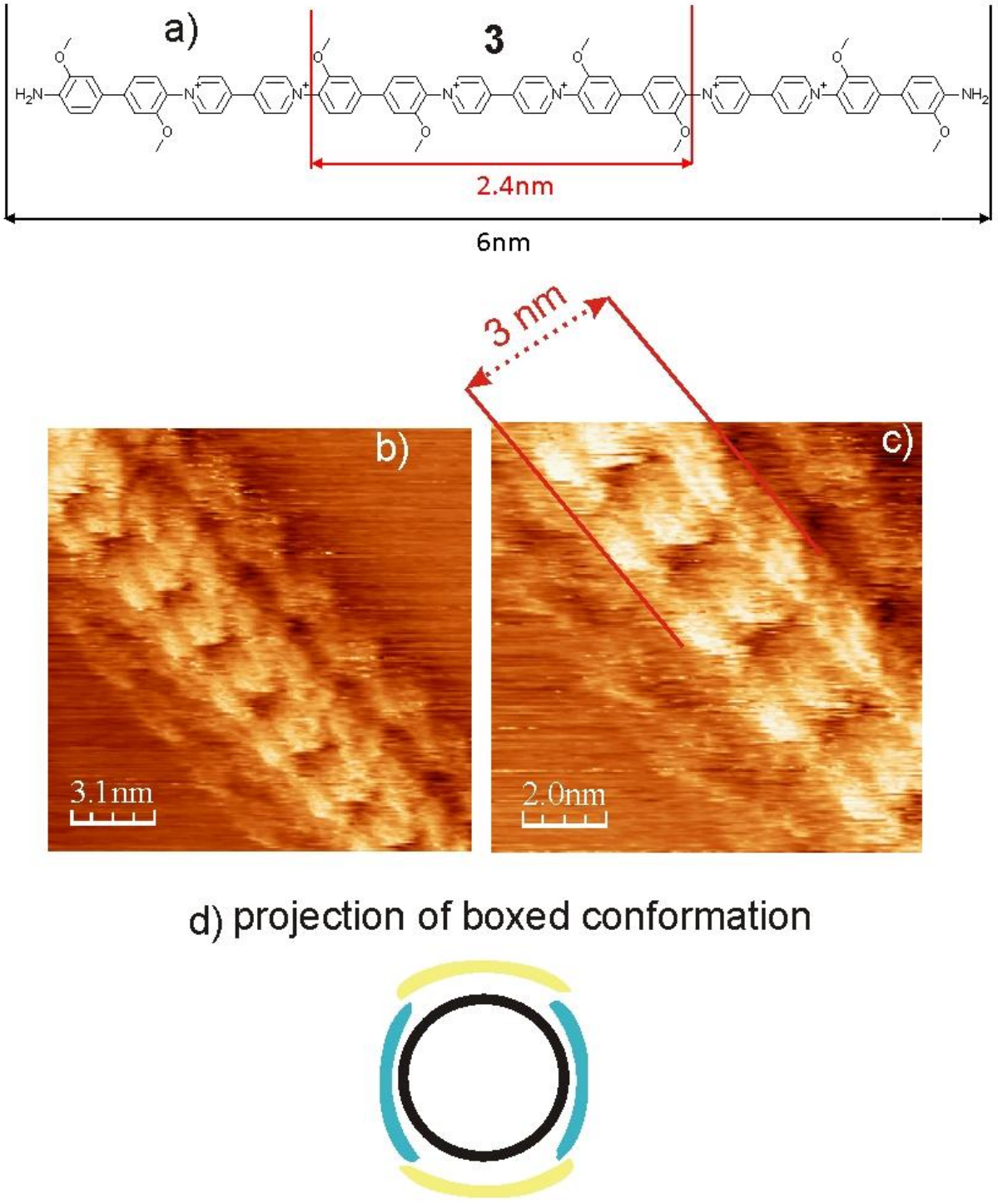

Figure 5: *High-resolution STM of boxed-shape **3** on a CNT (for the definition of boxed-shape see d). a) total and subunit lengths of **3**; b) STM topology of **3**@CNT in box shape conformation; c) zoom-in of b) showing the three subunits interpreted as viologen/bis-anisidine/viologen; d) model for the boxed-shape conformation.*

Table1: Rgid rod oligomers backbone length analysis

Compound no.	no of viologen subunits	length of the molecule theoretical (MM+)	length of the molecule observed (experimental)
1	1	2.4	2.5 (Fig 2c)
2	2	4.4	4.1 (Fig 2i) 4.5 (Fig 6c)
3	3	6.1	6.0 (Fig 2m) 7nm (Fig 3c)
3	3	3 (partial structure)	3.0 (Fig 4c)

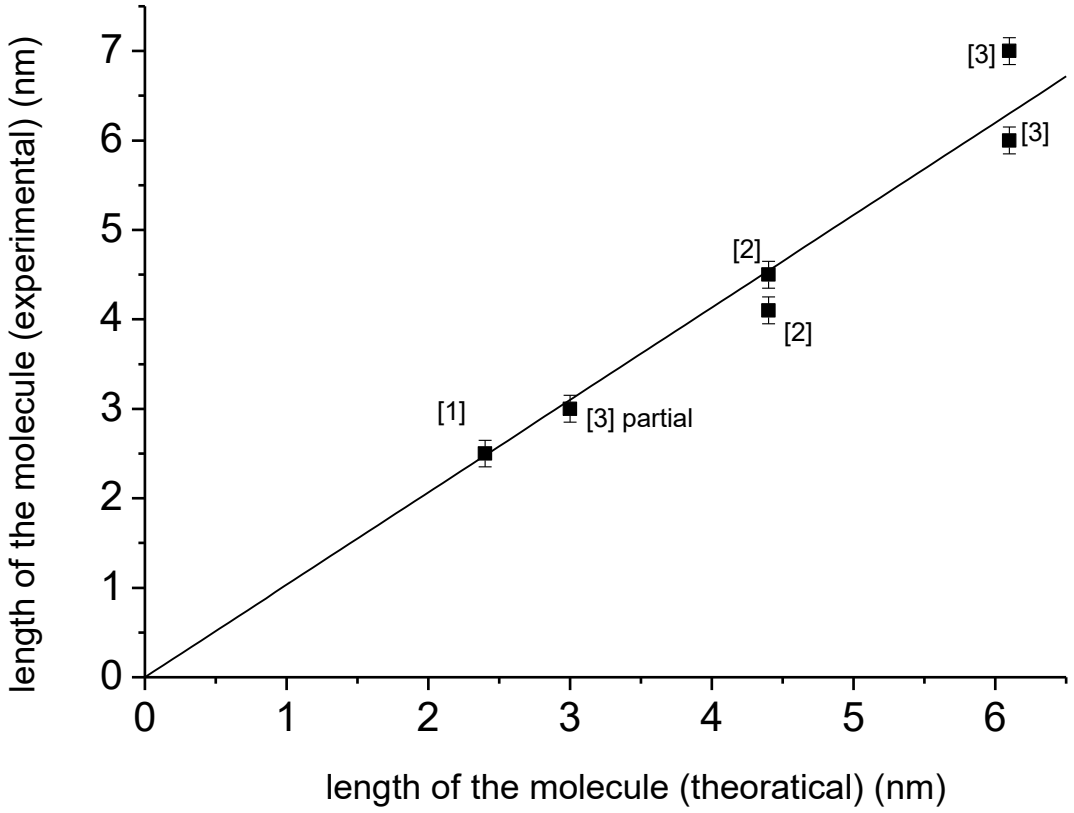

Figure 6: *Experimental vs. modeled molecule lengths (values from Table 1). Slope is 1.03, intercept was set to 0.*

In Fig. 6, I show a plot of measured *vs.* modeled molecular lengths. The good correlation is supporting the correct interpretation.

After backbone length determination the analysis was extended to the investigation of the length of side chains keeping backbone constant. For this purpose the "dimeric molecules" **2**, **2a** and **3b** were chosen. They have side chains ranging from 2 to 10 C-C or C-O bond length and a constant backbone length of 4.4 nm as shown in Scheme 2.

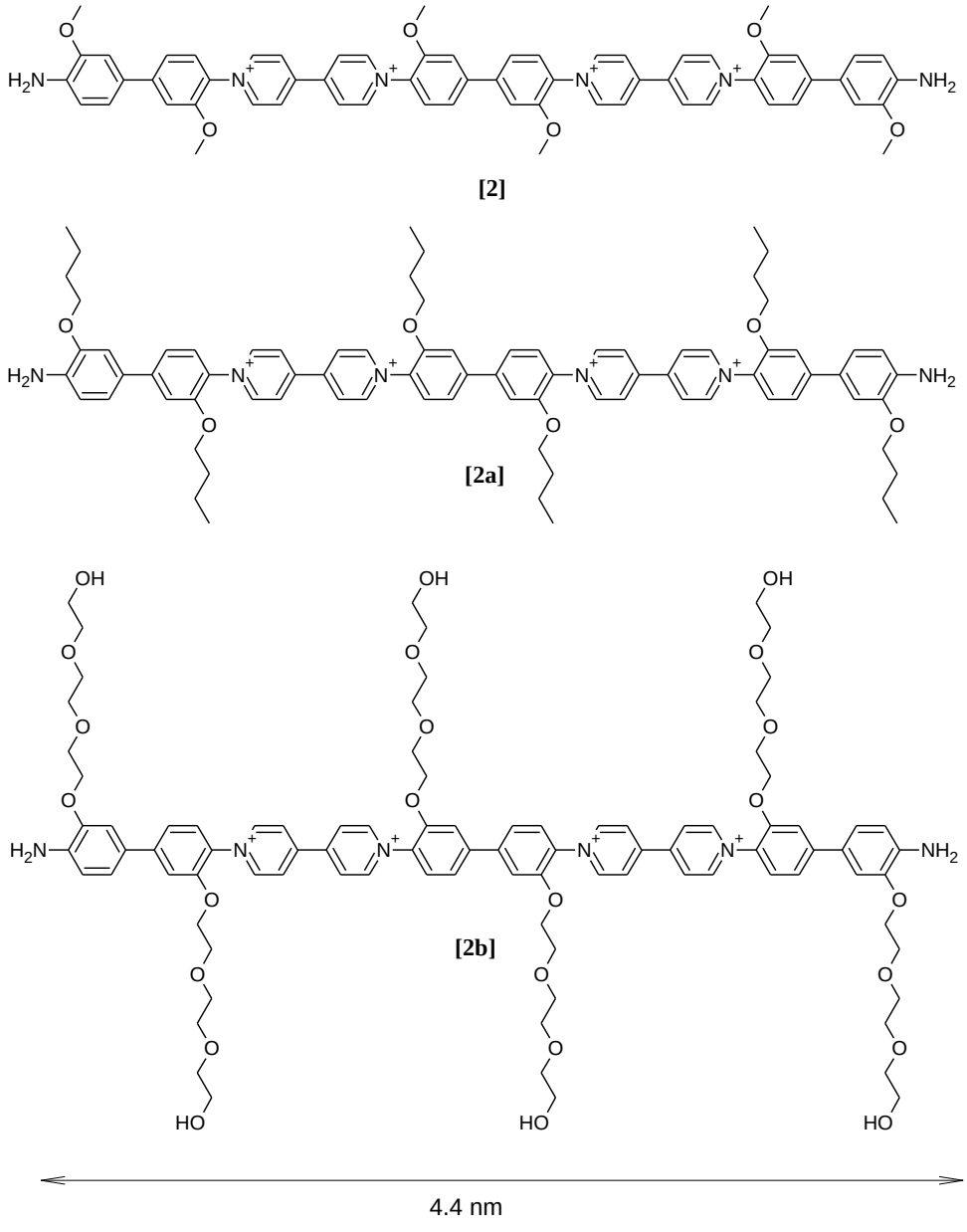

Scheme 4: *Rigid rod oligomers with different side chain length but fixed backbone length*

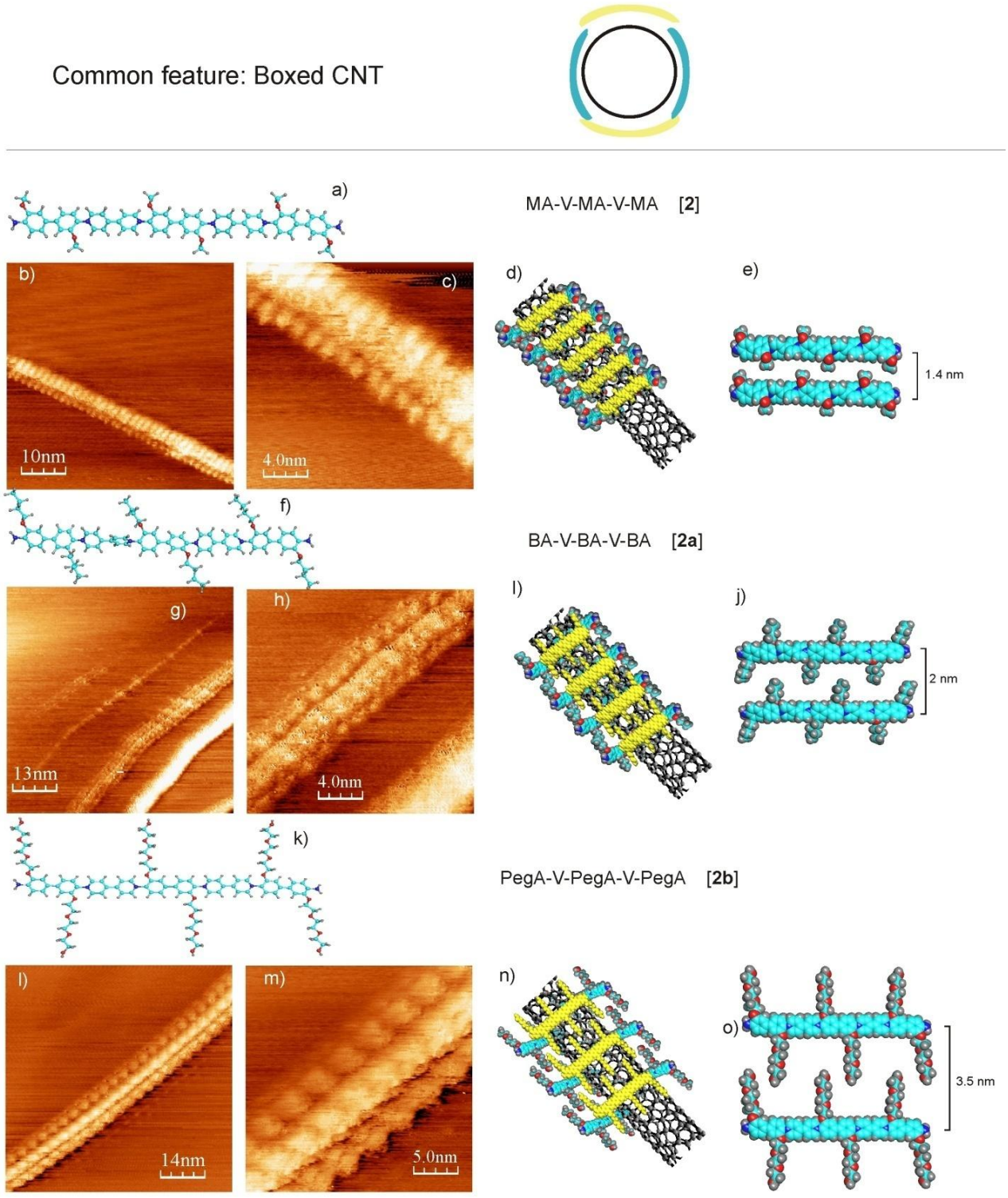

Figure 7: *Lateral distance influenced by side chain length in compounds* ***2*** *(methoxylated),* ***2a*** *(butoxylated) and* ***2b*** *(pegylated) with identical main chain length @CNT.* ***a-e)*** ***2*** *(MA-V-MA-V-MA); a) modeled structure (length 4.4 nm); b) STM images of* ***2****@CNT c)- zoom-in of b) with laterally assembled* ***2*** *full-length visible structure (exp. measured length: 4.5 nm); d) proposed*

coverage model in a boxed manner at right angle to the main axis of CNT; e) experimental lateral repetition distance (including thickness of backbone and "free space" between molecules: 2nm;

(f-j) 2a *(BA-V-BA-V-BA), corresponding series of images and models; the modeled molecule length is 4.4 nm, the experimental length is slightly smaller (4.2 nm) and the lateral repetition distance is larger 2 nm as expected for the butoxy as compared to the methoxy side chain;*

(l-o) 2b *(pegA-V-pegA-V-pegA), corresponding series of images and models; the modeled molecule length is the same (4.4 nm), the experimental length is again 4.2 nm as for* ***2a*** *but the lateral repetition distance is larger (3.5 nm) as expected for the peg substituent as compared to the butoxy side chain.*

The lateral distance was determined from 10 rods in line (divided by 10) yielding the average thickness of a rod including the intermolecular distance containing the side chains of two neighboring rods. The distance values are reported in Table 2. A plot of the distance values vs. the number of carbons + oxygen in the side chain is shown in Fig. 8. The points are approximately on a line. The following information can be extracted:

When extrapolated to x = 0 we can read out the thickness of the benzene ring of the bipy and anisidine including the spacing to the next neighbor rod. The value of ca. 0.8 nm points to a relatively tight packing. The slope can reflect many parameters.

Table 2: Rgid rod dimer side chain length analysis

Compound No.	**No of (C+O) atoms in side chain**	**Repetition distance (nm)**
2	2 (methoxy)	1.5
2a	5 (butoxy)	2.0
2b	10 (peg)	3.5

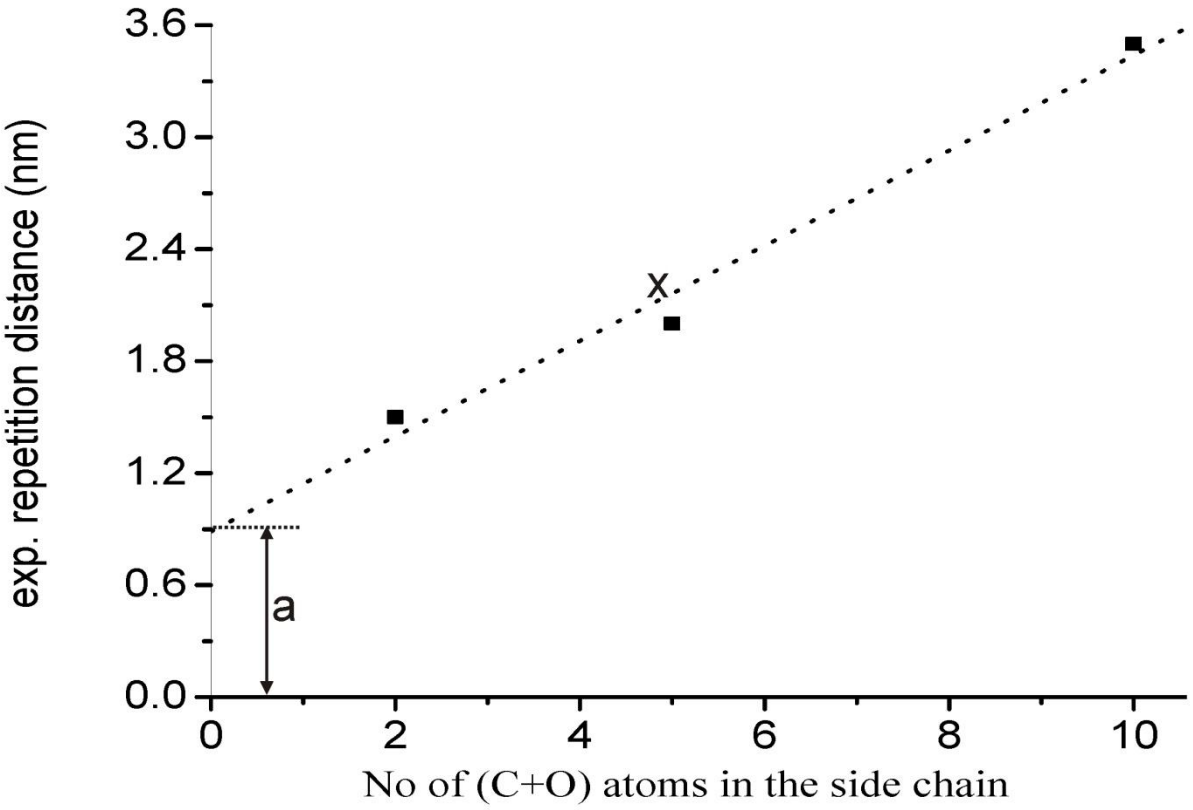

Figure 8: *No of (C+O) in sidechain vs. exp. repetition length (Table 2); y-intercept a is the hypothetical repetition distance for a oligo phenylic viologen without side chain, e.g.* ***1*** *(Fig.2e) with an exp. repletion distance of 1.05nm); the slope of the plot (0.25 nm per heteroatom) reflects obviously many parameters. x)*[15] *value for a poly thiophene 1.98±0.14 nm) from literature.*

Wrapping of CNT bundles

With thick single wall CNTs I observed **3** self-assembling in a box shaped way on a bundle of CNTs. The tubes were mixture of metallic and semiconducting tubes. In this case, DMF was used as solvent to disperse the CNTs was which owing to its dimethyl amine content has some reducing effect on viologen. That is why I observed a greenish coloration of the solution upon addition of viologen (partial formation of the pyridine radical). Remember, reduction induces

sp2 to sp3 transformation at N. Bending around CNT is, therefore, facilitated upon partial reduction. This is also observed in the MM+ model Fig. 9, i.e. bending and shortening by 1 nm.

Fig. 9 (c-h) shows the corn shaped structured of **3** on a bundle of CNTs sitting on top of graphite terraces of the HOPG substrate (Fig. 9c). The zoom-in adequately reveals the molecular subunit structure (d-h). The zoomed-in images indicate that at least three CNTs are underneath the self-assembled **3** and that **3** is arranged in a boxed manner.

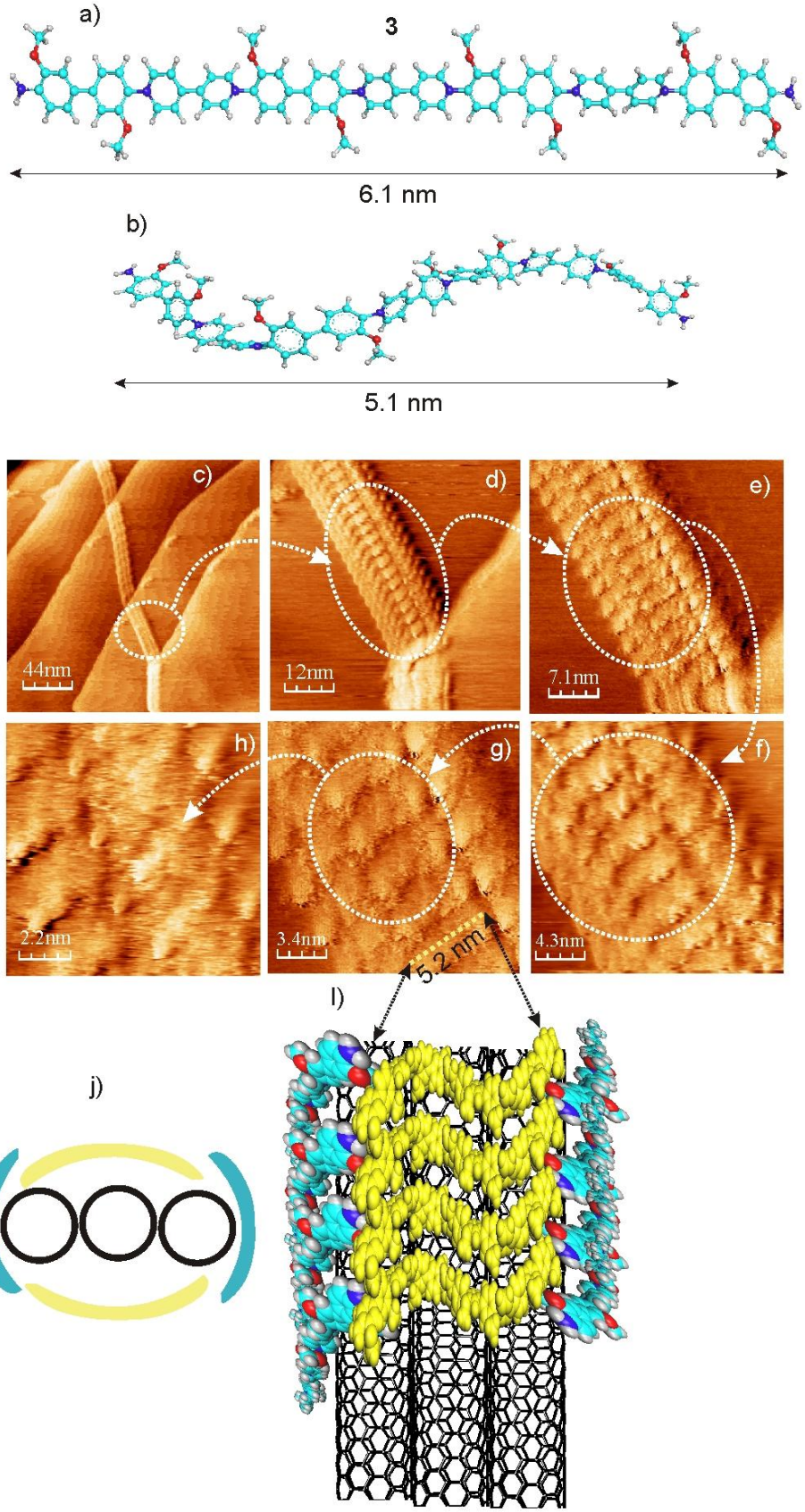

Figure 9: *Self-assembly of the rigid rod viologen trimer **3** on a bundle of CNTs or a multiwall metallic CNT (mixture of metallic and thick semi-conducting nanotubes used); a-b) modeled structure and projected lengths of **3** in stretched and twisted conformation (6.1 and 5.1 nm, respectively); c-h) **3**-decorated CNT (or bundle of CNT(s), ca. 7nm thick, crossing 4 graphene terraces of the HOPG support from overview (c) ca 200 nm side length) to phenilic/pyridinium subunit resolution (h) ca. 10 nm side length); i,j) proposed conformation of **3** on the CNT bundle in top view (i)) and in cross-section (j)).*

Diimid anisidine viologen

Compound **4** is another example of a rigid oligomer additionally containing the naphthalene tetracarboxylic acid diimide subunit. The arrangement of the **4** on CNT (Fig.10) exhibits a similar structure as the anisidin viologen **3** in a boxed manner. I interpret the large shiny spots at the center of repetitive hexagons as the large naphthalene subunit, at least this interpretation is in accordance with the corresponding molecular distance.

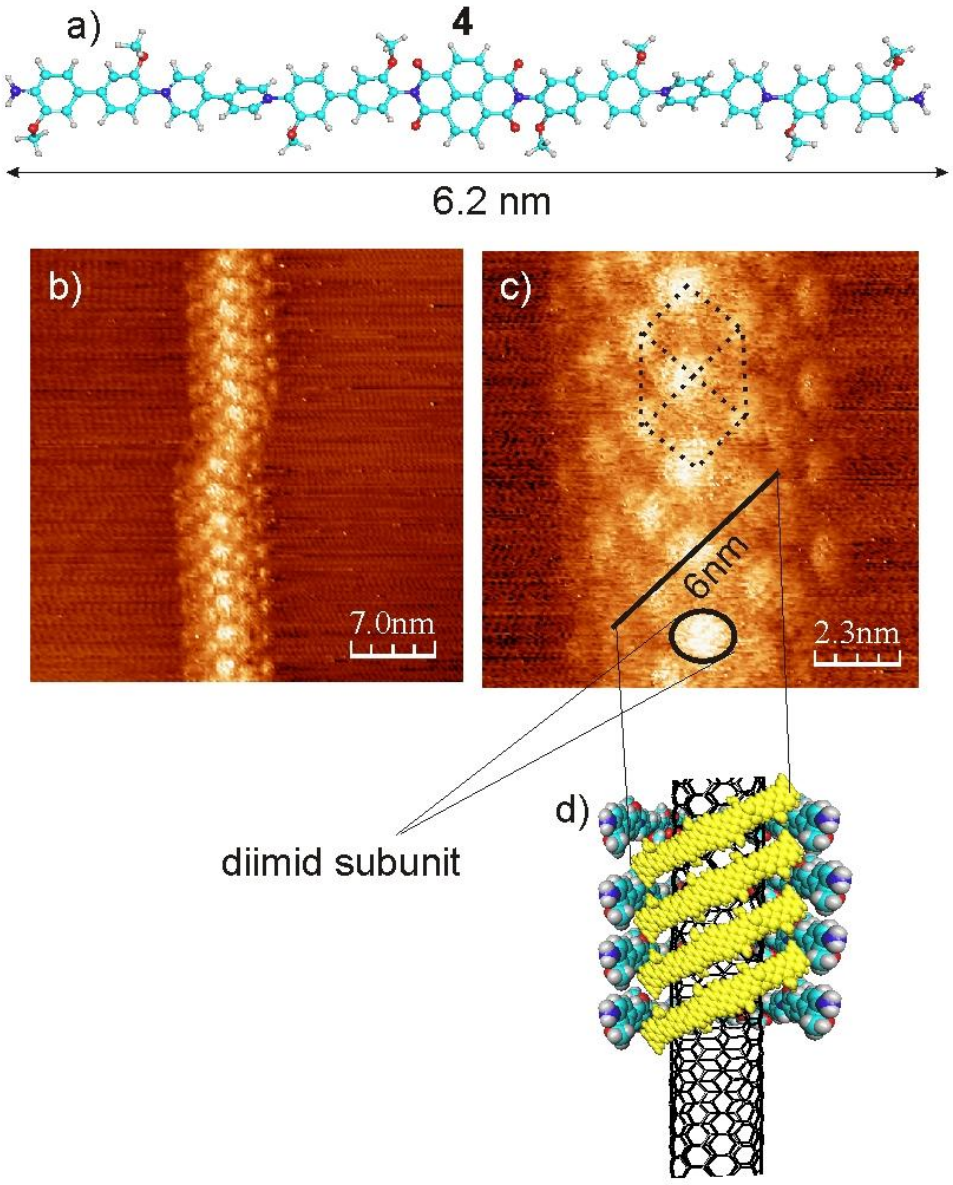

Figure 10: *Self-assembled rigid rod bis-viologen diimid (MA-V-MA-diimid-MA-V-MA,* ***4****) at CNT; a) structure of* ***4*** *with modeled length 6.2 nm; b) STM of* ***4****@CNT and c) zoomed-in b) with indication of the 2d-hexagonal structure of light dots (stretched along the CNT main axis), the bar of 6nm indicates the length of the molecule, the diimid annotation for a possible diimid subunit position (because it is different (more shiny) than the others; d) proposed boxed conformation with yellow molecules on top and the others sidewise.*

2.2.1.2. Semi flexible viologens

In this subsection the semi-flexible rods **5** and **6** and their interactions with CNTs are discussed. As compared to the rigid rods they contain additional benzylic linkages which allow them to adopt non-linear conformations (Scheme 5)

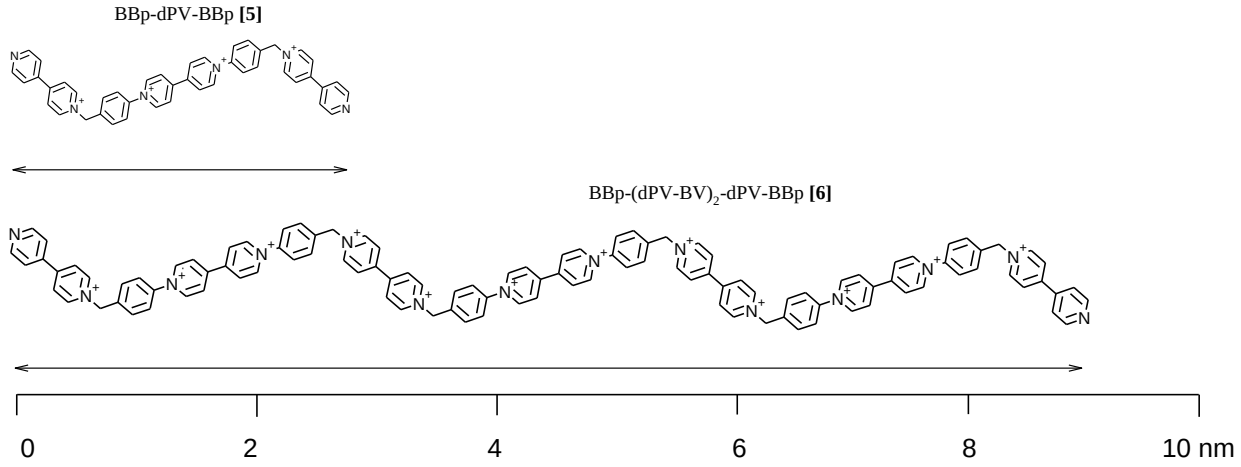

Scheme 5: *Structure of the semi flexible oligomers **5** and **6**.*

Interestingly – and *a priori* not really as expected - the small semi-flexible molecules **5** and **6** have a higher tendency to self-assemble parallel to the main axis of CNT as compared to the rigid rods discussed previously. In Fig 11, this arrangement parallel to the main axis of CNT or at an angle of 5-10° can be observed. As indicated in Fig. 1a 5-10° can be the result of the 6,5-CNT chirality inducing the same angle in the guest assembly. The offset observed in **5**@CNT could be due to the knee at the point of the benzylic carbons in the molecule. It has been observed in Fig. 11 that the experimentally observed size of individual molecules is in

agreement with the calculated length of the MM+ optimized molecule in its double transoid conformation.

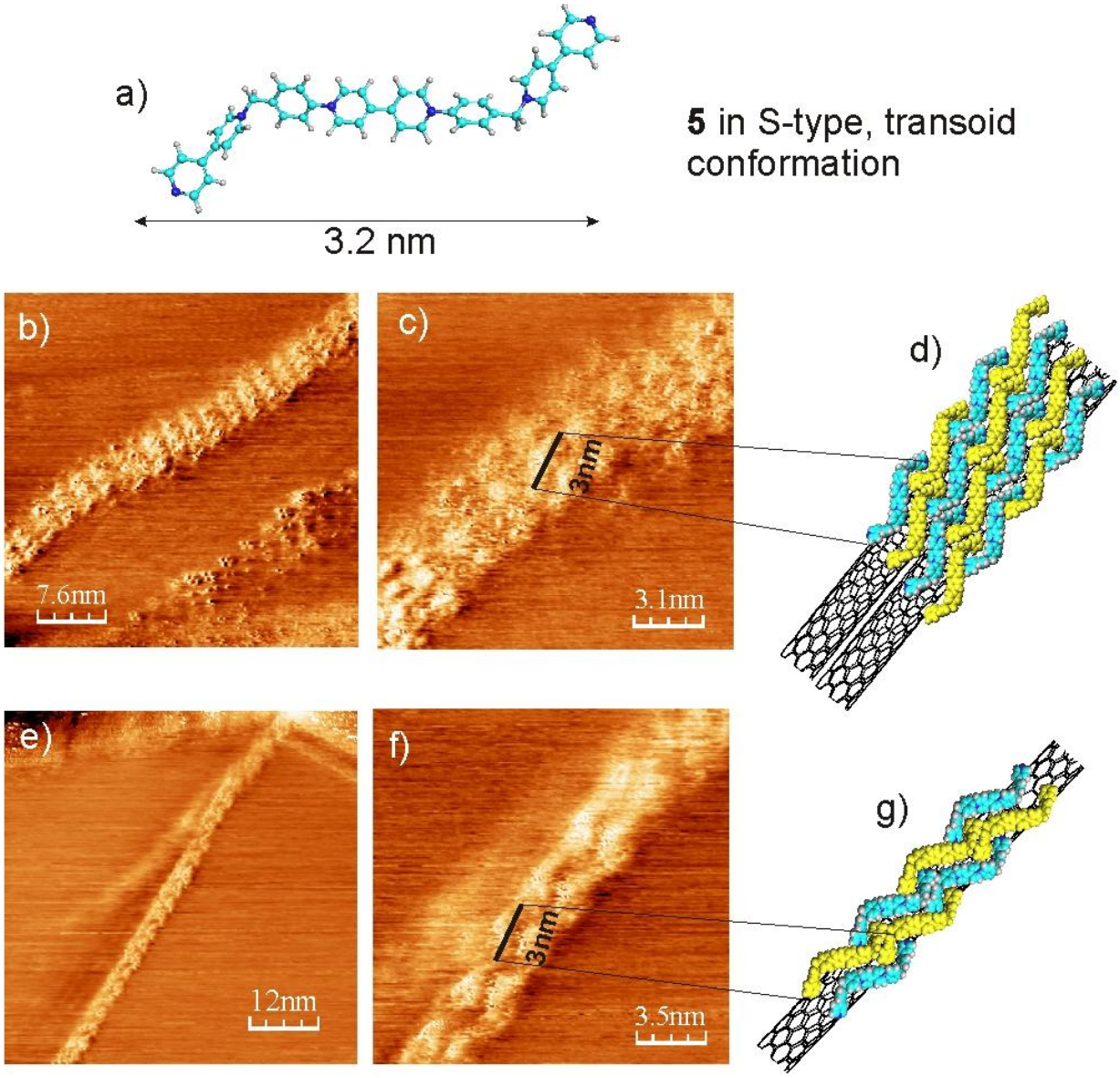

Figure 11: *Semi-flexible viologen oligomer **5**@CNT; a) chemical structure of **5** in S-type transoid conformation with two benzylic bond angles and modeled projected length of 3.2 nm; (b-c) **5** oligomers on a bundle of two CNTs c) zoom-in of b) showing molecular resolution of single molecules with approx. length of 3 nm almost parallel or slightly inclined to the main axis of CNT with S-type conformation; d) proposed arrangement of an array of **5**@CNT with 3 nm*

exp. projected length. (e-g) showing similar arrangement as in (b-d) but on a single underlying tube.

On the other hand, the longer semiflexible molecules tend to wrap the CNT in a diluted ring shaped fashion (as shown in Fig. 12) with an inclined angle that can also be referred or attributed to the chirality of the CNT (Fig 1).

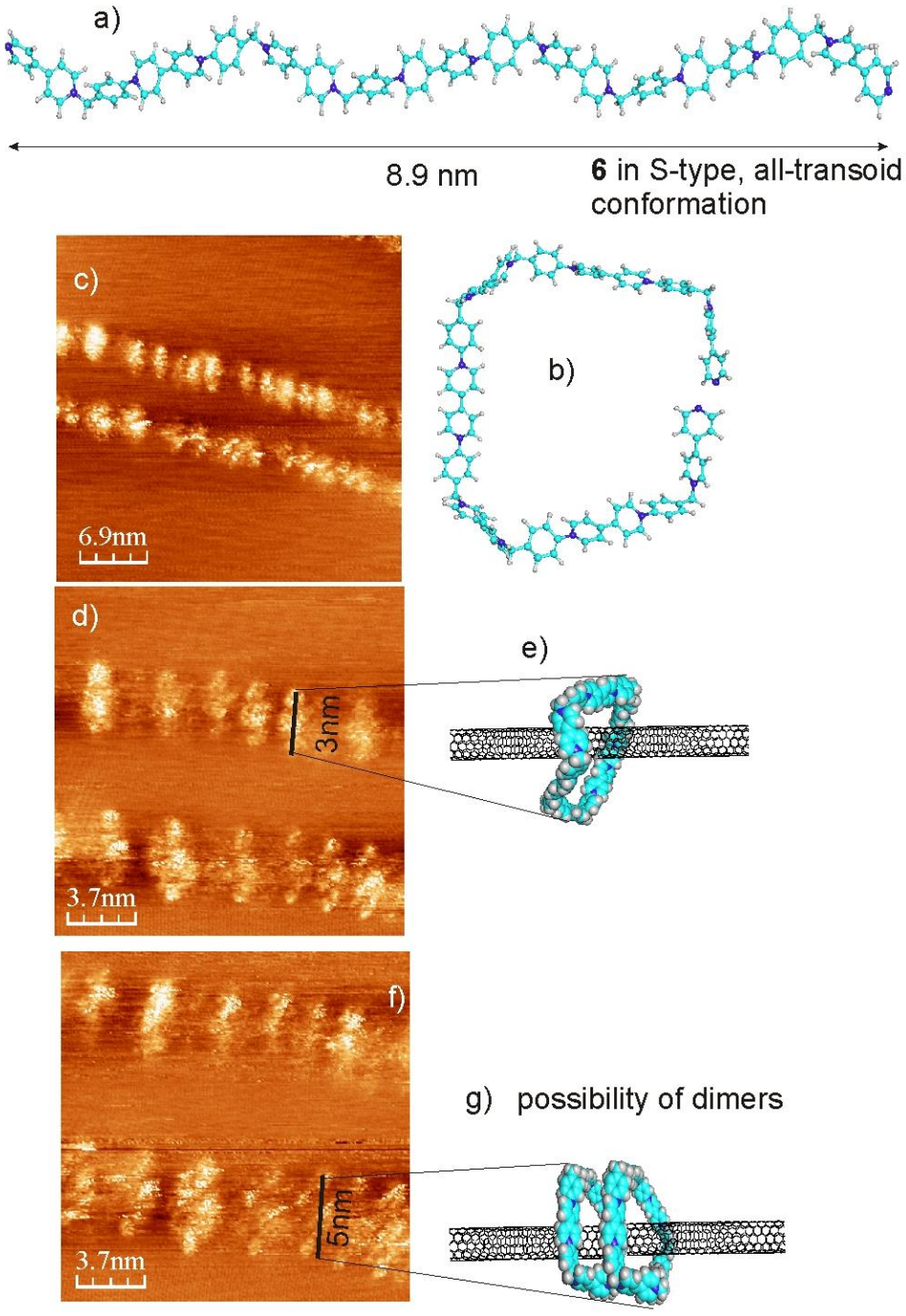

Figure 12: *Self-assembly semi-flexible viologen oligomer **6**@CNT; a,b) chemical structure of all-transoid and all cisoid **6** with modeled projected length 8.9 nm and ca. 3 nm, respectively; (c,d, f) **6** at two separated CNTs; d and f) zoom-in of image c with d showing single molecule resolution and modeled interpretation (e) squared ring conformational (3nm side length as in b)). f) sidewise dimeric squared-ring conformation with the corresponding model in g).*

2.2.1.3. Flexible viologens

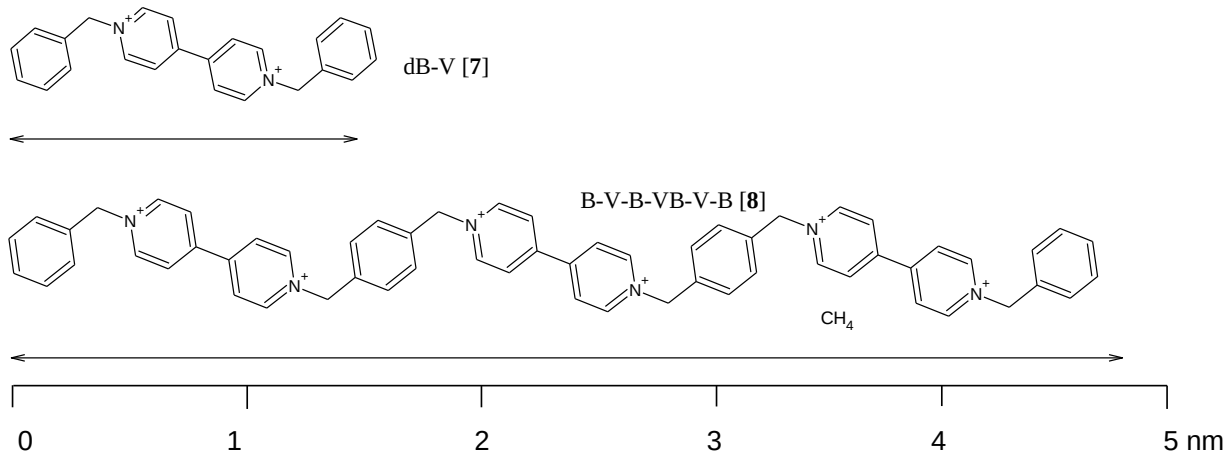

Scheme 6: *Flexible oligomers with abbreviations and molecule numbers*

As representatives of the flexible viologen guest molecules, I have chosen dibenzyl viologen (**7**) and the xylene-bridged viologen compound **8**. The dibenzyl viologen wraps the 6,5-CNT (Fig. 13, a-e), obviously as a double helix with cisoidal conformation of the dibenzyl viologen as shown in the interpretation. The transoidal conformation is nicely imaged by STM (see zoom-in Fig. 13d). The tri-viologen **8** shows diluted ring structures with strongly inclined ring plane rather than a helical wrapping (Fig. 13f-m).

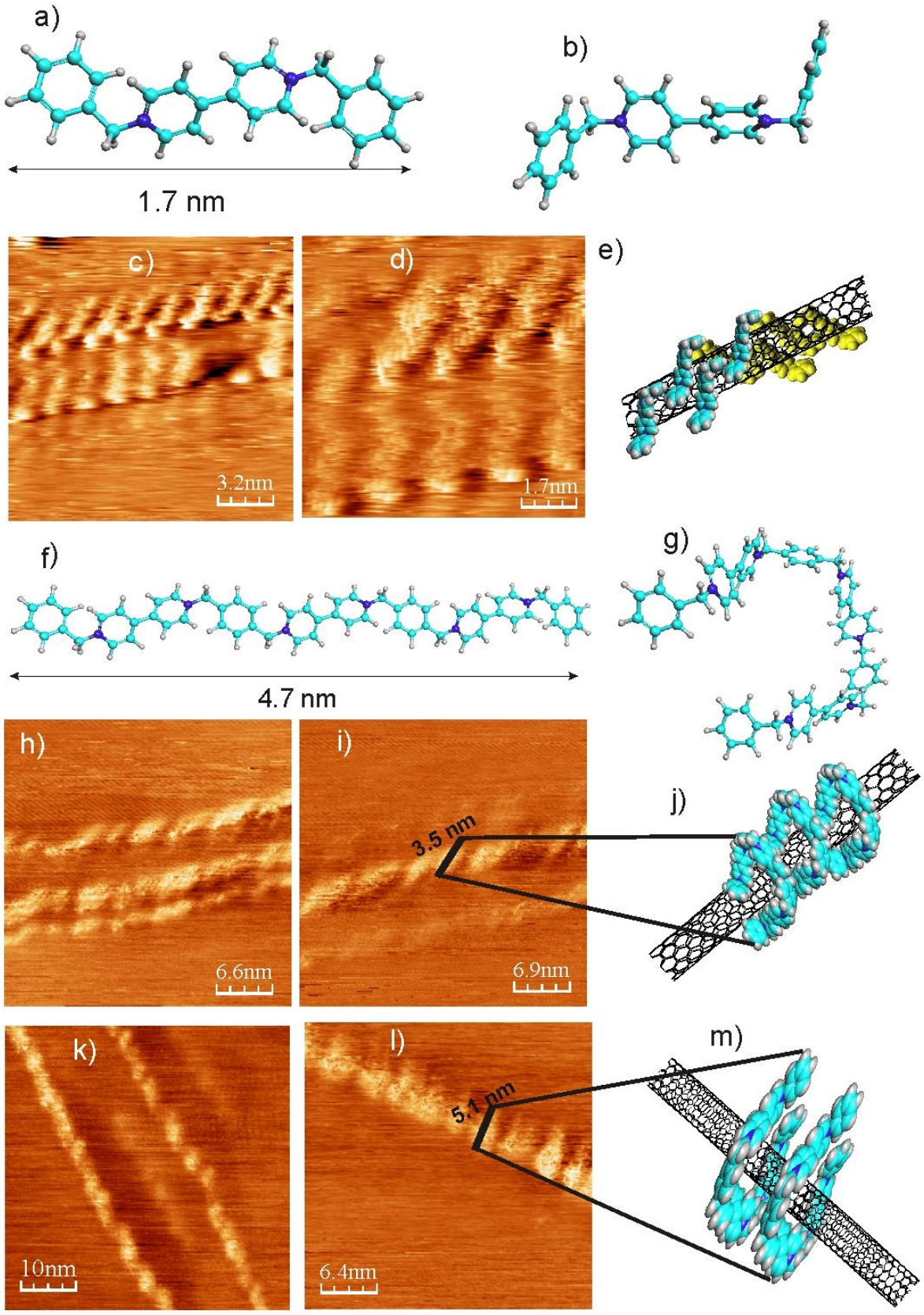
a)
1.7 nm
b)
c)
3.2nm
d)
1.7nm
e)
f)
4.7 nm
g)
h)
6.6nm
i)
3.5 nm
6.9nm
j)
k)
10nm
l)
5.1 nm
6.4nm
m)

Figure 13: *STM images of flexible viologen oligomer **7** and **8** at CNT ;**(a-e)** a) structure of **7** with modeled length 1.7 nm; b) is the side view of the optimized molecule **7**; c and d) shows respective oligomer at two different CNTs; e) is the proposed structures in respective images.*

(f-j) *f) chemical structure of **8** with modeled length (4.7 nm) after geometrical optimization; g) **8** in semi circle conformation; h and i) shows respective oligomer at three separate CNTs; i) is the zoom-in of one of the CNTs show molecules wrapped in semi circle form with a diameter of 3.5 nm; j) is the proposed structure of respective images;*

(k-m) *k and l) shows arrangement of **8** at two separate CNTs; l) is the zoom-in of one of the CNTs showing molecules wrapped in a dimeric semi circle fashion with a diameter of 5.1 nm; m) proposed structure of respective images.*

In Fig. 14 the influence of the oxidation state of **8** on the structure of **8**@CNT was studied. Beside benzylic sp3, we expect now tetrahedral viologen Ns. As compared to Fig. 13, the CNT-**8** interaction seems to be increased as there are no "diluted" regions on the CNT observed. The tetrahedral edges are more pronounced as expected. Wrapping seems to be double or triple helical with sidewise interacting **8** on CNT.

It was observed that applying a voltage pulse on a bundle of **8**-covered CNT leads to separation of the bundle with the CNTs individually covered by **8** (Fig. 15).

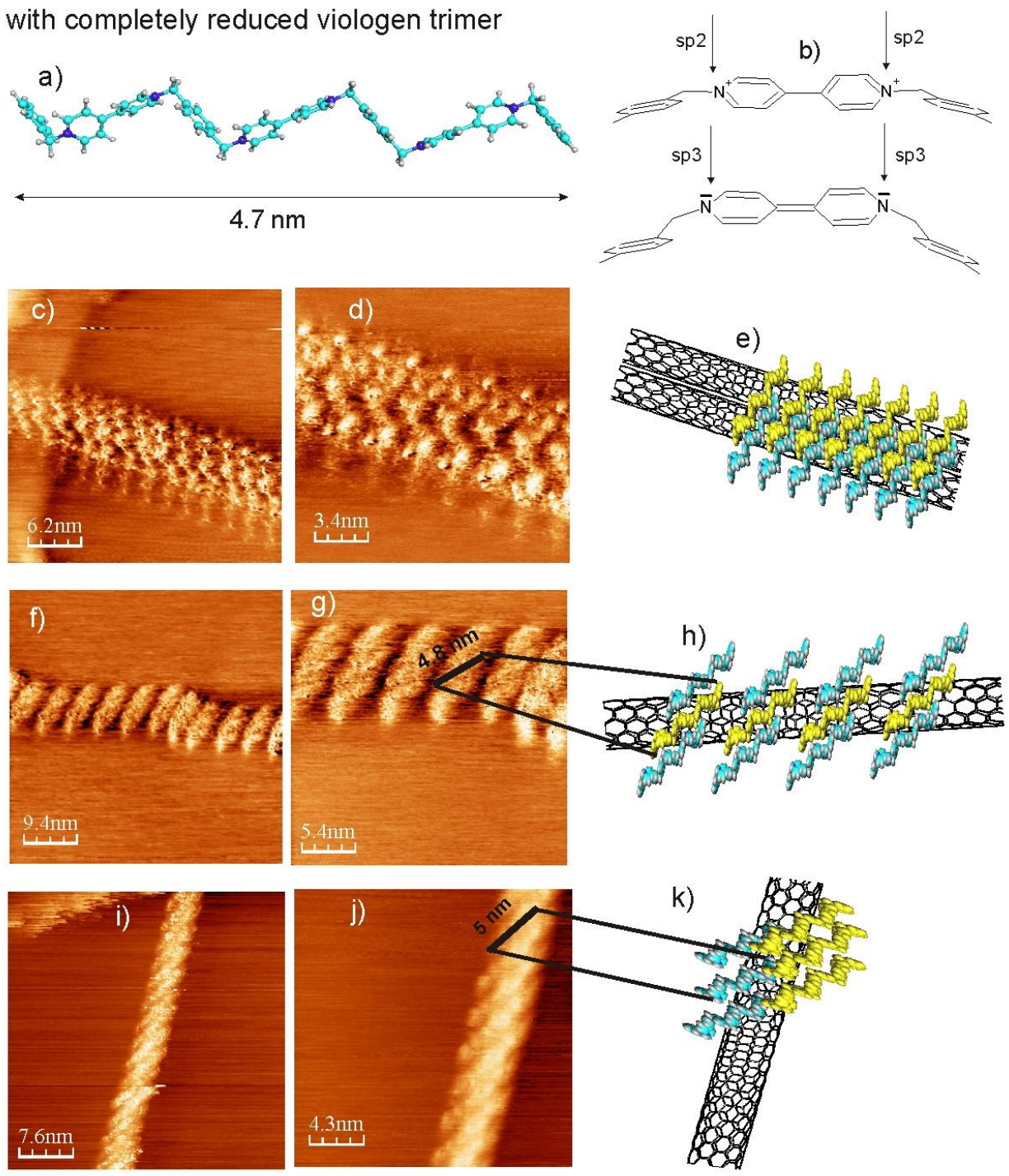

Figure 14: *STM images of reduced flexible* ***8****@CNT; a) modeled all-transoid structure of* ***8****; build up of additional deviation from linearity upon reduction of* N^{+}*(sp2) to N(sp3); c) endwise intertangled* ***8*** *with double- or triple helical wrapping; d) zoom-in of d); e) corresponding model for c,d) (without considering the helical wrapping); f) sidewise intertangled conformation with g) zoom-in of f); h) corresponding model (without considering the helical wrapping); I,j) endwise intertangled* ***8****@CNT as in c (but multistranded helical wrapping) but on a single tube.*

Splitting of CNTs by application of Voltage Pulse

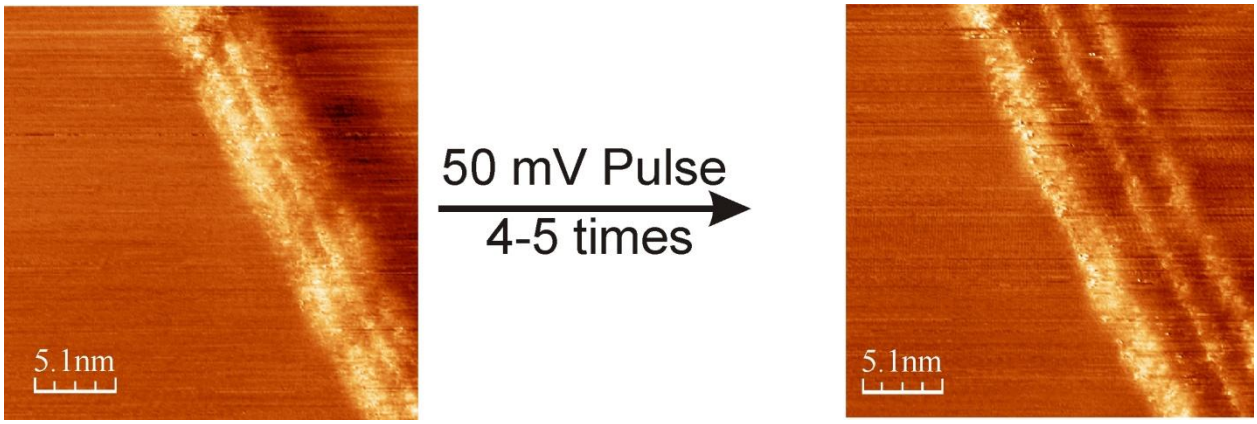

Figure 15: *Influence of 4-5, 50 mV pulses on reduced **8**@CNT (bundle). It split the bundle of **8**@CNT into three CNTs.*

2.2.1.4. Semiflexible star type viologen

So far I have presented only linear viologen oligomers. They showed different self-assembly geometries with all of them allowing to cover the CNT surface as a hole-free molecular monolayer.

This situation is totally different for the star shaped viologen oligomer **9** shown in Fig. **16**b). There exists no simple conformation of **9** allowing for a "hole-free", monomolecular adsorption on CNT. The STM image (Fig. 16a) shows an interesting pattern with a ca. 1.7 nm repetition distances over a length of 16.9 nm along the CNT main axis, i.e. stars compressed in a way so as to completely cover the CNT. One tends, therefore, to interpret the repetitive lobes at the upper periphery as 11 star legs and the same interpretation may be applied to the lobes at the lower periphery. However, each star has 3 legs. Careful inspection of the lower periphery in Fig. 16a)

shows an oscillating height which may be due to one leg underneath the observed leg. In Fig. 16b,c) the conformation of the green molecule indicates a more condensed structure.

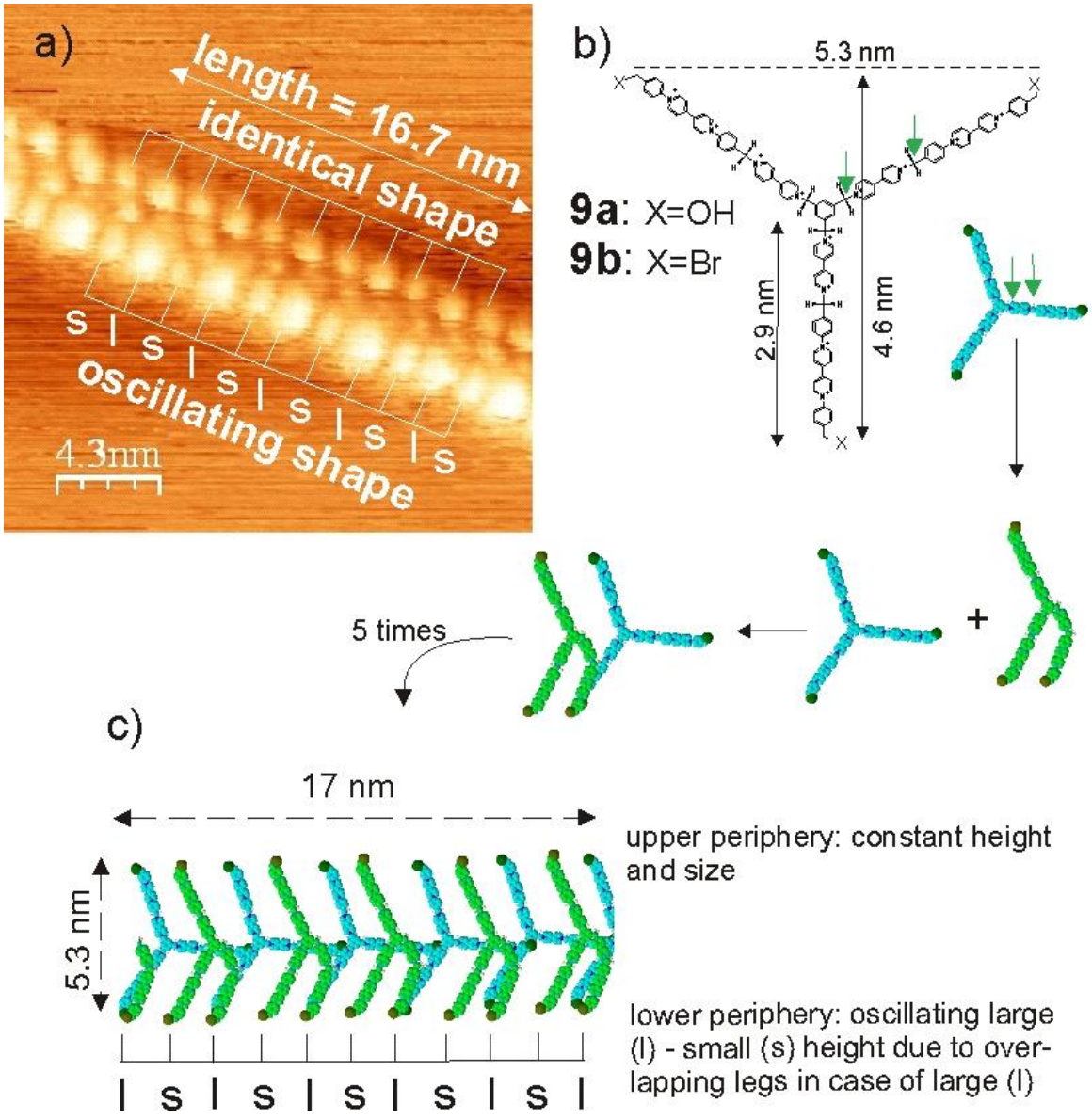

Figure 16: *STM image of the 3-legged star viologen* ***9a*** *on a 6,5 CNT. a) STM image of* ***9a****@CNT showing molecular subunit resolution; 11 subunits of identical shape in the upper periphery and 11 subunit with oscillating large (l) and small (s) shape in the lower periphery over 16.7 nm observed; b) structure of* ***9a*** *with green arrows indicating conformational flexibility leading to the green structure, and self-assembling of green and a blue structures to a band structure in c) with every second height consisting of two star superimposed legs.*

If the green conformation self-assemblies with the blue structure one can construct a band of **9a** with each second leg in the lower periphery sitting on another leg thus showing a double height as observed in the STM picture.

Fig. 17 shows another conformation for **9b**@CNT. In this case each lower protuberance represents two legs on top of each other.

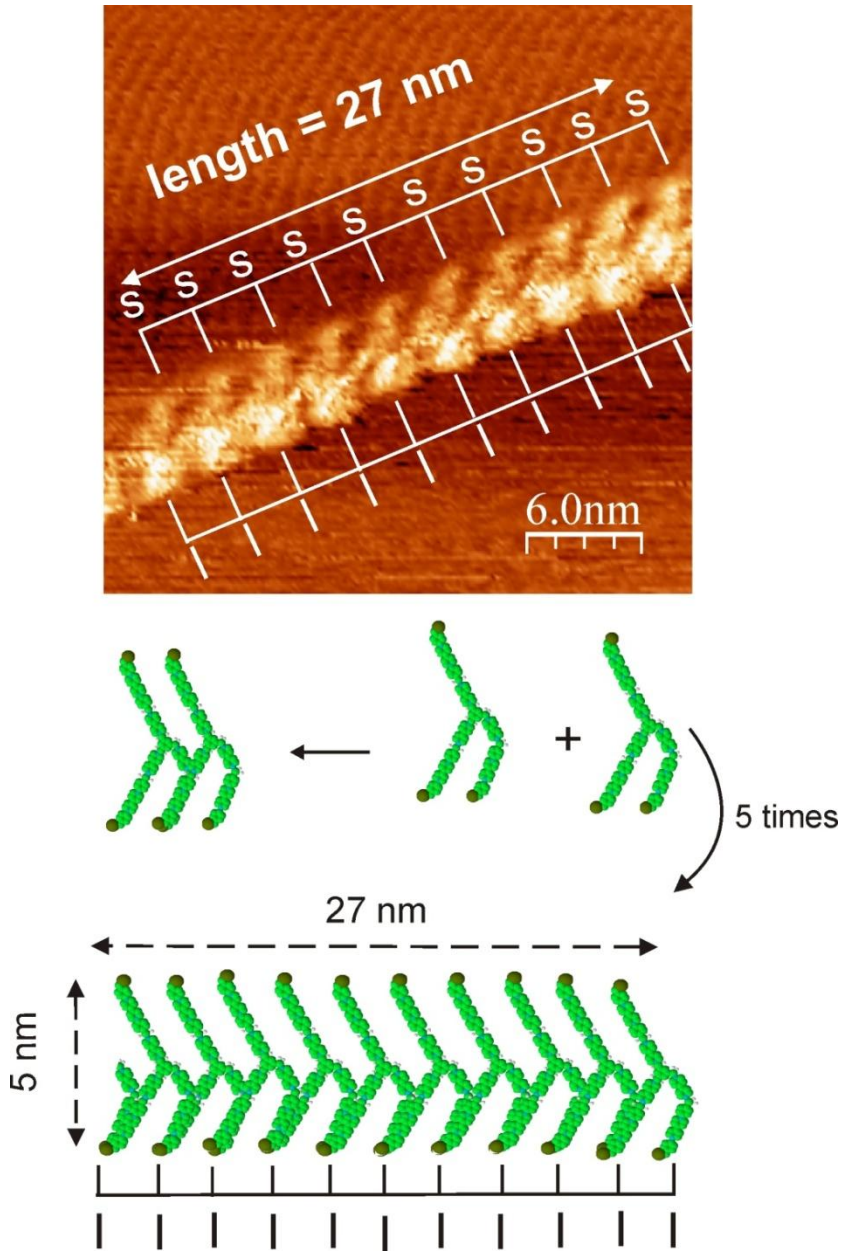

Figure 17: *STM image of the 3-legged star viologen* ***9b*** *on a 6,5-CNT*

2.3. Conclusions

1. Stiff, semi-flexible and flexible aromatic and electroactive oligomers self-assemble all on sc- or metallic CNTs, preferably as a single-, double or multi-stranded helix. The cylinder radius of the helix is 2 to 4 nm larger than the CNT radius. This difference corresponds to the π–π stacking value for an aromat on a CNT.
2. The tunneling current for such guest aromats on CNTs is strongly amplified as compared to the current observed for the same molecule on HOPG. The amplification allows to image molecular subunits of the size of a phenyl- or pyridine moiety by STM under ambient conditions.
3. In most cases, I have clear evidence for a helical arrangement but other types of self-assembled structures were also observed, e.g. the so called "boxed structure" with the oligomers at a 90^{o} angle to the main axis of the CNT with the rigid rod **3**. However, the same **3** can also self-assemble helically, parallel to the main axis, with a length offset typical for a donor acceptor interaction. Different types of arrangements appearing on the same HOPG sample indicate very small energy differences for the different arrangements.
4. An electrical voltage pulse can push apart parallel CNTs, which are individually semiflexible **8** wrapped, a phenomenon that is also observed in case of polymer entrapped CNTs (see next chapter).
5. Rigid - as compared to flexible rods - show less deviation from linearity in STM analysis – however, partial reduction of the viologen subunit leads to sp2→sp3 transformation at N, allowing the rigid rods to easily deviate from linearity, e.g. in the boxed shape conformation (Fig. 5).

6. The highest density of sp3 centers is present in the flexible rods and leads to STM images as shown in Fig. 14 exhibiting mainly sp3 knees.

2.4. Experimental

Single walled carbon nanotubes (CNTs) with an unknown but considerable metallic content (m-CNTs) were purchased from *IoLiTec Technologies GmbH* (Germany, **CNT** >90%, **SWNT** >50%, OD <2 nm, L <20 μm), semiconducting CNTs (sc-CNT chirality: (6,5), d: 0.7 to 0.9 nm) were from *Sigma Aldrich.*

Syntheses

1,2 and **3** were prepared and characterized by Dr. Alina Constantin.[38]

*Synthesis of **4**:*

4 was synthesized and characterized by Sascha Lax (Master thesis 2014) under Dr. Mohsen Beladi-Mousavi's and my guidance as follows:

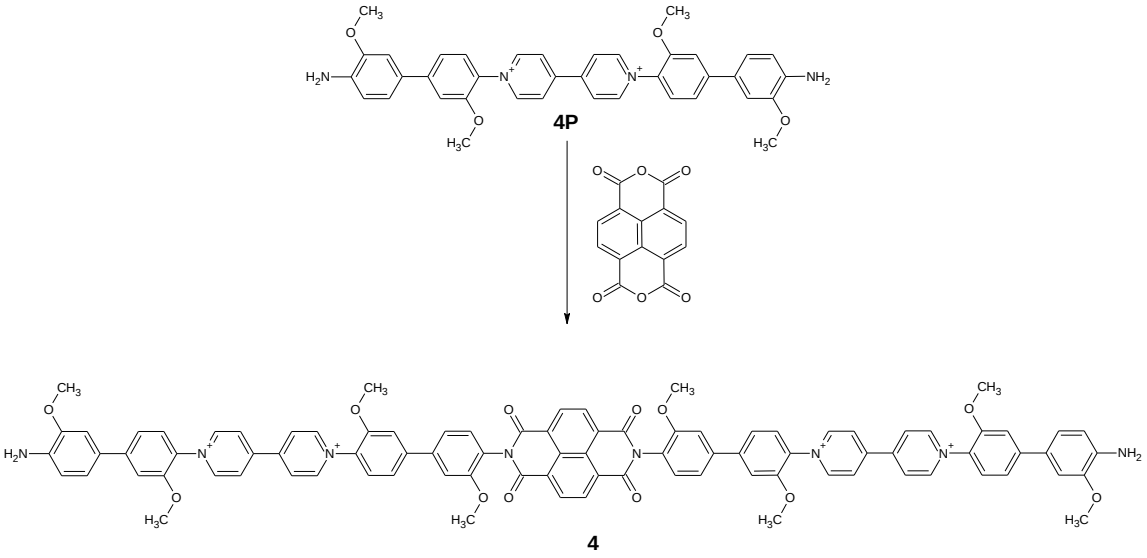

4P was synthesized as described.[38] 248 mg (0.27 mmol) **4P** was dissolved in 10 ml DMA at 50°C under Ar atmosphere. 24 mg (0.09 mmol) naphthalene tetracarboxylic acid dianhydride (NTCDA) was added in small portions over 10 min. The mixture was heated to 135 °C for 20 h under Ar. After cooling to RT, 50 ml diethyl ether was added. The precipitated product was isolated by filtration, washed with diethyl ether and dried. It was then dissolved in MeCN and the product was separated from the starting materials by column chromatography (Sephadex LH-20). The first fraction yielded after drying the compound **4***4 PF_6 (26 mg, 0.013 mmol, 14 %).

^{1}HNMR (CD_3CN, 250 MHz) δ: 9.16 (m, 8H); 8.83 (m, 4H); 8.66 (m,8H); 7.83-7.27 (m, 20H); 6.85 (m, 4H) 4.07 (m, 12H); 3.98 (m, 12H)

*Synthesis of **5** and **6**:*

5 and **6** were synthesized as follows:

5:

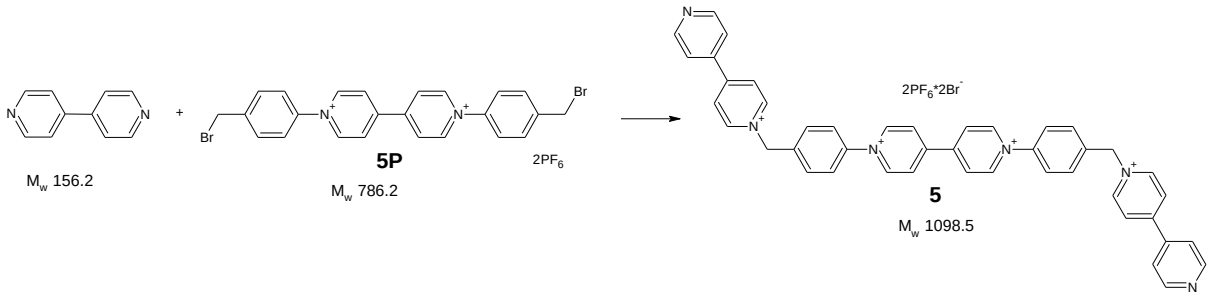

596 mg (3.816 mmol) 4,4'-bipyridin was dissolved in 7.5 ml MeCN at 70°C. 500 mg (0.636 mmol) **5P** (synthesized as described[38]) was dissolved in 5 ml MeCN and this solution was added slowly (10 drops / 30 min) to the bipyridin solution. Another addition of 500 mg bipy followed. After 48 h the solid precipitate was collected by filtration, washed with MeCN, and dried under

HV for 1 h to yield **5***2PF_6^-2Br^- (218 mg, 0.198 mmol, yield: 31 %) . From the mother liquor another portion of product was isolated upon addition of ether to give a total yield of 43 %.

Ion exchange **5***2PF_6^-2Br^- to **5***$(PF_6^-)_4$: The mixed counter ion **5** was dissolved in a minimum amount of MeOH/H_2O and treated with aqueous 3M NH_4PF_6 solution. The beige colored **5***$(PF_6^-)_4$ precipitated, was washed with water and dried.

Analysis:

Electrochemical purity check: The CVs of the first and second precipitation were identical. The two waves in the range of 0 to -0.6V were assigned to the di-phenyl bipyridinium subunit, the wave at ca. -0.9V to the peripheral mono-alkylated bipy systems, as confirmed by the current ratio 1:2, respectively.

^{1}H-NMR (CD_3CN, 250 MHz) δ: 9.21 (d, 4H(8)); 8.93 (dd, 8H((9)); 8.70 (d, 4H(2)); 8.43 (d, 4H(3)); 7.95 (m, 4H(1),8H(6,7)); 5.98 (s, 4H(5)).

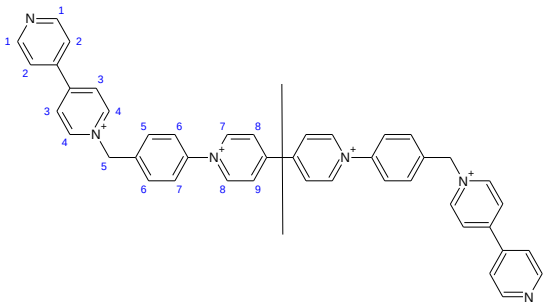

5, proton resonance assignment

6:

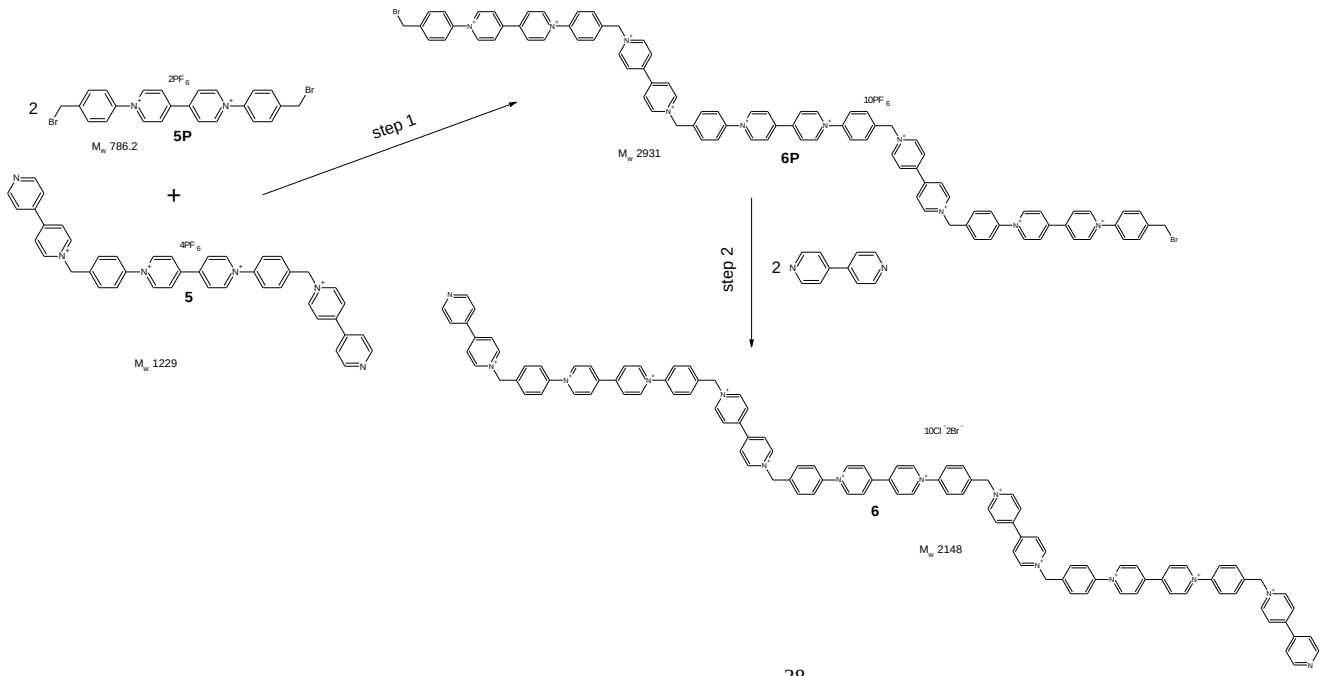

Step 1: 766 mg (0.976 mmol) **5P** (synthesized as described[38]) was dissolved in 5 ml MeCN at 60°C. 200 mg (0.163 mmol) **5** was dissolved in 4 ml MeCN and this solution was added slowly drop wise to the **5P** solution held at 60^{o} over the period of 4 h. The reaction was held at 60^{o} for 4 d. The precipitate (ca. 90 mg) was separated from the mother liquor, which was diluted with 40 ml MeCN. To this solution 1 M TBACl was dropped until precipitation stopped. The Cl- salt was isolated by filtration and washed with MeCN. The residue was dissolved in MeOH and precipitated by addition of diethyl ether. This compound was isolated and dissolved again in H_2O. Addition of 5 ml aqueous NH_4PF_6 solution led to the precipitation of **6P** as a PF_6 salt (643 mg (with a high content **5P** present)). 90 mg of the crude 6P were purified on a sephadex column, yielding 60 mg of pure **6P***10 PF_6^-. Used in step 2 without further analysis.

Step 2: 32 mg (0.011 mmol) **6P** and 85 mg (0.544 mmol) bipyridine was dissolved in 5 ml MeCN and reacted at 60 ^{o}C for 4 d. The solvent was evaporated and the residue was treated several times with 4 ml CH_2Cl_2 under sonification to extract the starting materials. The solid

was finally dried under HV to yield 11.4 mg (31 %) which was further analyzed and used for the STM experiments.

Cyclic Voltammetry of **6**@CNT@GC shows that it holds better at the electrode surface when it is in 1 to1 ratio of viologen and CNT as compared to 2 to 1 ratio of viologen and CNT.

*Synthesis of **7**:*

Commercially available compound **7** was synthesized by a known procedure as follows:

7: 4,4'-Bipyridine (1.2 g, 7.68 mmol) and benzyl bromide (2.96 ml, 25 mmol) were dissolved in MeCN and refluxed for 20 hours. The yellow precipitates were collected and washed with acetonitrile and dichloromethane and dried under high vacuum (85% yields).

^{1}H-NMR (250 MHz, D_2O): δ 9.14 (d, 4H), 8.52 (d, 4H), 7.53 (s, 10H), 5.93 (s, 4H). Elemental analysis ($C_{24}H_{22}Br_2N_2$): Calcd.: C, 57.85; H, 4.45; N, 5.62, found: C, 57.77; H, 4.42; N, 5.72.

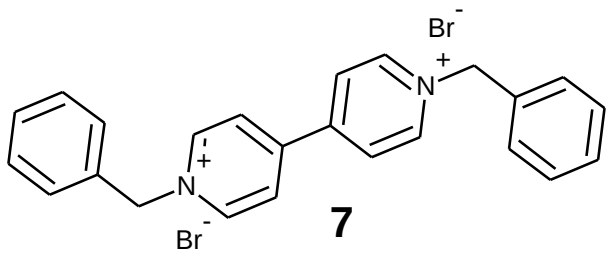

7

*Synthesis of **8**:*

8 was synthesized by Dr. Mohsen Beladi-Mousavi as follows:

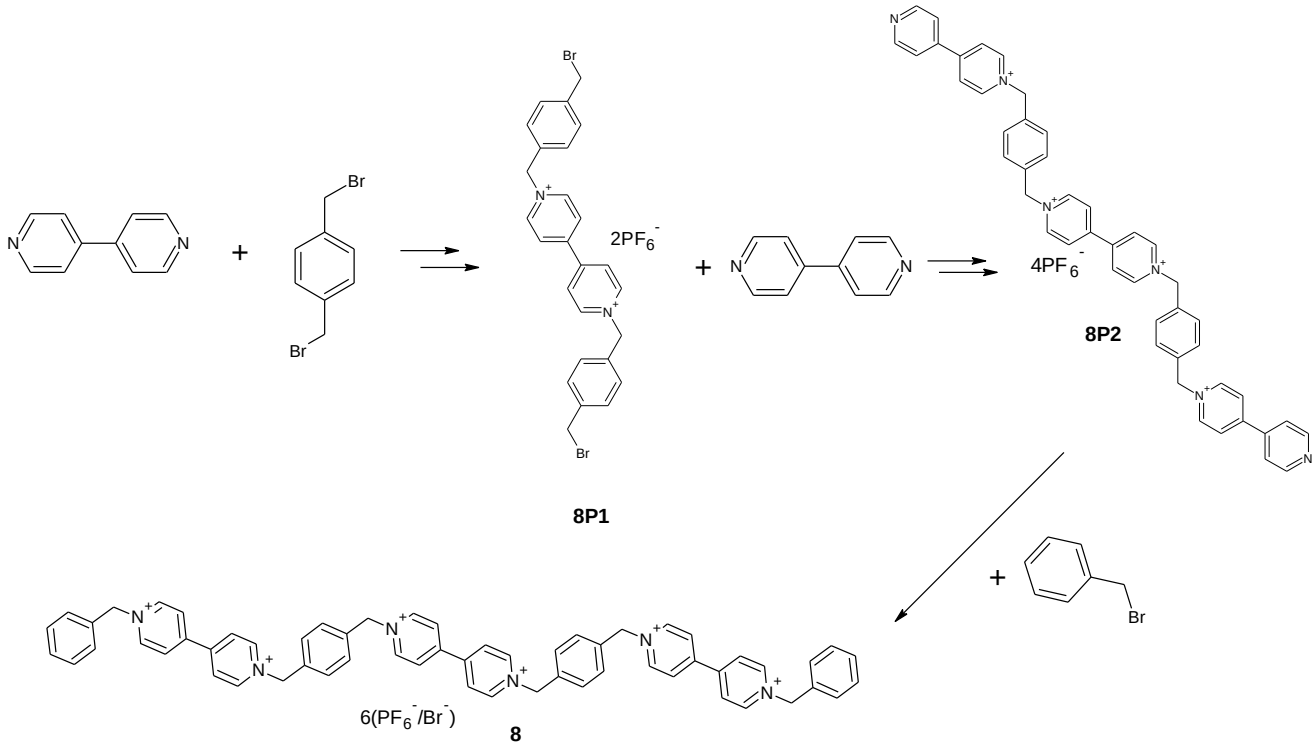

8P1: 4,4'-Bipyridine (1.56 g, 10 mmol) and α,α′-Dibromo-p-xylene (0.396 g, 1.5 mmol) was dissolved in MeCN and refluxed. After 5 hours green precipitates formed and were collected, washed with dichloromethane and diethyl ether and dried under high vacuum. As the procedure is described for **5**, the counter anions were changed to PF^-_6 and **8P1** was dried under high vacuum (91% yields).

^{1}H-NMR (250 MHz, DMSO): δ 9.48 (d, 4H), 8.71 (d, 4H), 7.55 (d, 8H), 5.9 (s, 4H), 4.7 (s, 4H).

8P2: 8P1 (3.09 g, 3.8 mmol) was dissolved in MeCN and added drop wise to an MeCN solution of 4,4'-bipyridine (5.93 g, 38 mmol). The mixture was refluxed for 52 hours and the yellow

precipitate was collected and dried under high vacuum. The counter anions were exchanged for PF_6^- and **8P2** was dried under high

8: 8P2 (0.676 g, 0.6 mmol) and benzyl bromide (0.385 ml, 3.24 mmol) was dissolved in MeCN and refluxed for 30 hours. The light yellow precipitates were collected and washed with dichloromethane and diethyl ether and dried under high vacuum (67.8% yields).

^{1}H-NMR (250 MHz, D_2O): δ 9.14 (d, 12H), 8.53 (d, 12H), 7.61-7.52 (d, 18H), 5.94 (d, 12H). Elemental analysis ($C_{60}H_{54}Br_3F_{18}N_6P_3$): Calc.: C, 46.99; H, 3.55; N, 5.48, found: C, 46.79; H, 3.55; N, 5.48.

Preparation of viologen compound@CNT

General procedure: The viologen compound (2mg) was dissolved in 2 ml DMF or water depending upon its solubility, 1 mg of 6,5-CNT was added. The solution was sonicated in an ice cold bath for 30 min in order to disperse the CNTs. Ca. 2 µl of the solution was spread on the freshly cleaved graphite substrate. The solvent was evaporated at r.t. overnight.

Prior to self assembly several parameters have been evaluated with respect to structures observed in the self-assembling on 6,5-CNTs, e.g. concentration, CNT/modifier weight ratio, solvent and reduction of the electroactive viologen compounds prior to self-assembly.

The influence of solvents on the self-assembly was studied in case of rigid rod **3**. The compound dissolved in DMF as PF_6^- salt and the CNTs were also dispersible. The solution turned slightly greenish indicating partial reduction of **3** under these conditions. In dichloromethane the two compounds were also well dispersible. In water I used the Cl^- salt and observed dispersibility but the CNT dispersed only in the presence of **3**. The STM images were

generally better resolved using the chloride modifier and the CNT dispersed in water, thus this solvent system was generally used for most cases. In case of **3,** STM images from dispersions in DMF (Fig.3 and Fig. 9) and water (Fig.4 and Fig.5) can be compared. There is no general difference in the self-assembled structure observed, except that the formation of CNT bundles happens more often from the DMF solution. Most importantly, partial reduction was only observed in DMF, probably due to the presence of some dimethyl amine.

In case of water and dichloromethane the images are resolvable up to subunit level. While when zinc pallets were added in the dispersion in water and sonicated for some time the green color in the solution was observed indicating viologens are totally or partially reduced and in imaging it gave same results as in case of DMF.

Other sequence used for FET measurements was tried to reproduce by STM imaging but the resolution was not as high as in case of colloidal solution measurements.

Reduction

Reduction of **3**

With activated zinc:

4 Zinc pallets were taken and put into 5 ml of conc. HCl for 30 sec followed by removal from HCl and subsequently put into water for some sec in order to remove acid the dried quickly with filter paper and put into the dispersion of **3** with CNTs and stirred under Argon atmosphere and STM sample was prepared.

With a reducing agent:

Method 1: 5 mg of **3** was dissolved in 20 ml water then added 20 ml toluene and 32 mg $NABH_4$ and let it stay overnight. Water phase was separated. While all the compound was moved to toluene phase and settled down, toluene phase was ultrasonicated to dissolve it and added SWCNT and prepared STM sample.

Method 2: 11.2 mg of **3** was dissolved in 10 ml water and added 23 mg of $NaBH_4$ and stirred for 10 min. Upon addition of $NaBH_4$ precipitate appeared. Filtered the precipitate and washed with water extensively to remove $NaBH_4$ and dried. Then checked the solubility of reduced viologen in different solvents such as, DMF (completely soluble), Toluene (slightly soluble), CH_2Cl_2 (completely soluble) and DMSO (completely soluble).

Reduction of **7** and **8**@CNT

Took 6 mg of viologen dissolved in 2 ml water, added 2 ml toluene and 20 mg of $NaBH_4$, let it stir overnight. Initially, the color of water phase turned dark blue indicating reduction of viologen. With the passage of time blue color from water phase started disappearing and the toluene phase started turning yellow indicating presence of neutral viologen which is usually yellow in color. In case of 8, first the anion was exchanged from PF_6^- to Br^-.

XPS and Raman analysis

Took 2 mg of 6,5-CNT and 2 mg of different oligomers dispersed in DMF and ultrasonicated in ice bath and put on stirring for 48 h followed by filtering with polyimide membrane and washing several times with DMF and acetone first and at the end with diethyl ether. Removed from membrane, dried and given for XPS and Raman studies.

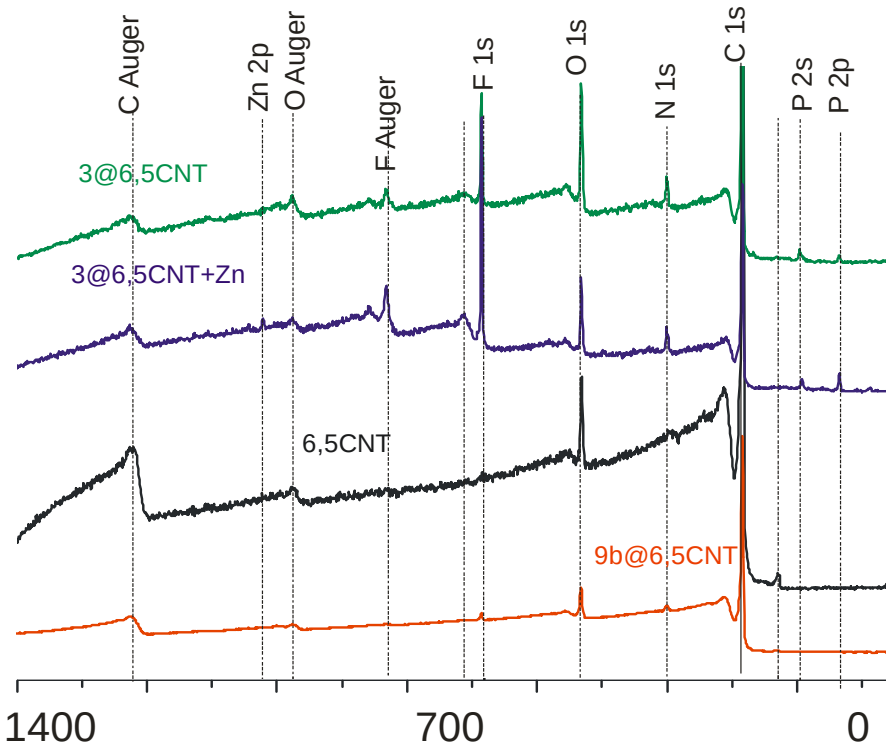

Figure 18: *XPS of 6,5-CNT,* ***3****@CNT+Zn as* PF_6 *salt and* ***3****@CNT as* PF_6 *salt and* ***9b*** *as* Br^- *salt*

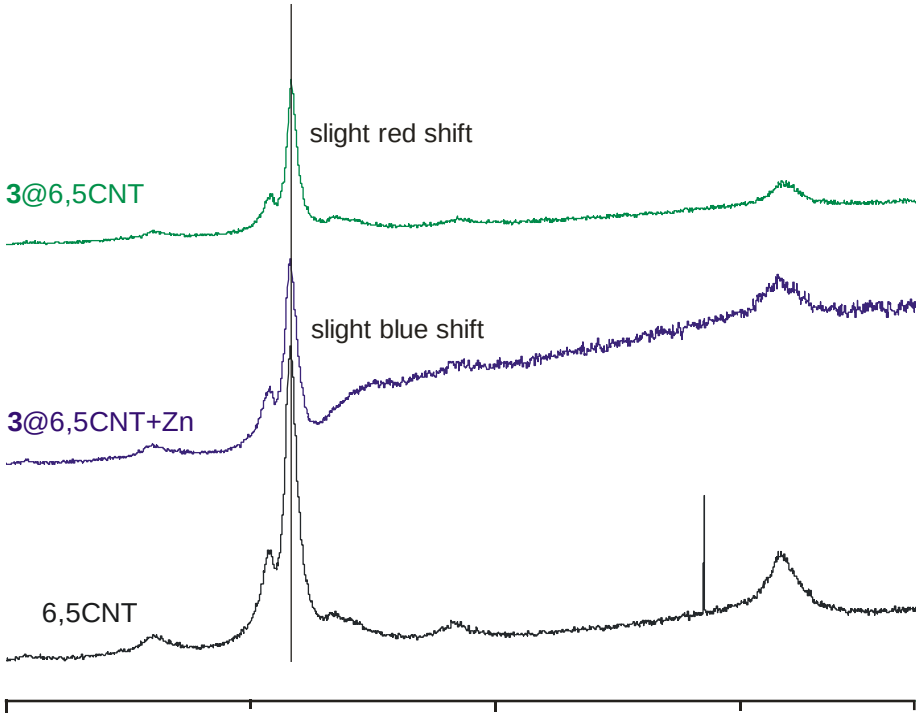

Figure 19: *Raman spectroscopy of 6,5-CNT, **3**@CNT+Zn and **3**@CNT*

It is clear from Raman that compound **3** is able to switch the CNT character between red and blue shifts on the bases of oxidized or reduced states (while in case of Zn only partially reduced). So charge transfer is switchable and the CNT doping can be adjusted.

6,5 CNT + Oxidized **3** ⟶ p-Type doping

6,5 CNT + Reduced **3** ⟶ n-Type doping

Instrumentation

STM imaging

An EasyScan *Nanosurf II* (Switzerland) instrument was used. The STM tips were cut from Pt/Ir wire (0.25 mm, *Schaefer Technologie GmbH,* Langen, Germany), the substrate was a HOPG 5*5 mm piece from *Schaefer Technology GmbH*. All measurements were done at room temperature under ambient conditions using typically 0.050 V bias voltage and 1.000 nA tunneling current.

XPS measurements

XPS measurements were performed using a PHI 5600ci multitechnique spectrometer equipped with a monochromatic Al Kα source with 0.3 eV full width at half-maximum. The overall resolution of the spectrometer is 1.5% of the pass energy of the analyser, 0.45 eV in the present case. The measurements were recorded with the sample at room temperature.

Raman measurements

Raman experiments were performed with a Raman microspectrometer (LabRam, Horiba-Jobin-Yvon). Radiation from the 632.8 nm line of a He-Ne laser was focused by a 50x microscope objective (Olympus, model LM Plan Fl) with a power of ~ 3-4 mW at the sample.

2.5. Device Application as FET

FET behavior of pristine CNT and **7**@CNT – ambient stable n-doping

The so called Schottky barrier, i.e. an electrical contact between a semi-conducting material and a metal is used as the basis for current/voltage rectifying devices from slow AC up to the GHz region.

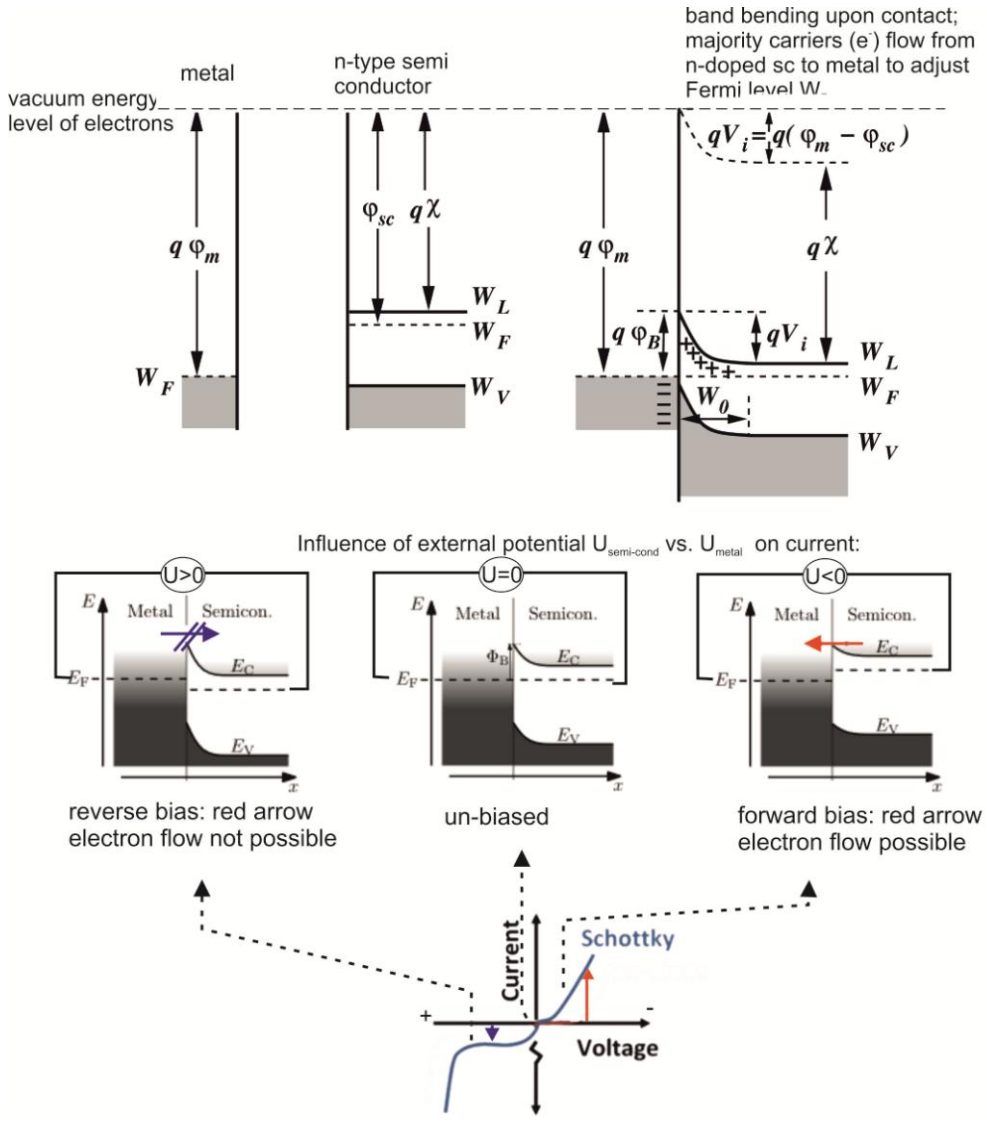

Figure 20: *Band structure and band bending upon contact between a n-type semiconductor and a metal. The Fermi levels (WF) in both materials adjust to the same energy by charge dislocation from the n-doped semiconductor to the metal. The resulting interface acts as a diode, i.e. large red current if forward biased and blue small current if reverse biased (pictures adapted from Wikipedia).*

Semi-conducting CNTs can be doped with electron donors or with hole donors leading to n-type and p-type CNTs, respectively. A pristine 6,5-sc-CNT exhibits p-type doping naturally. Such diodes are usually studied in a so called "field effect transistor (FET)" arrangement with either top or bottom gate. We used for our preliminary studies a bottom gated FET transistor with the principle shown in Fig. 21.

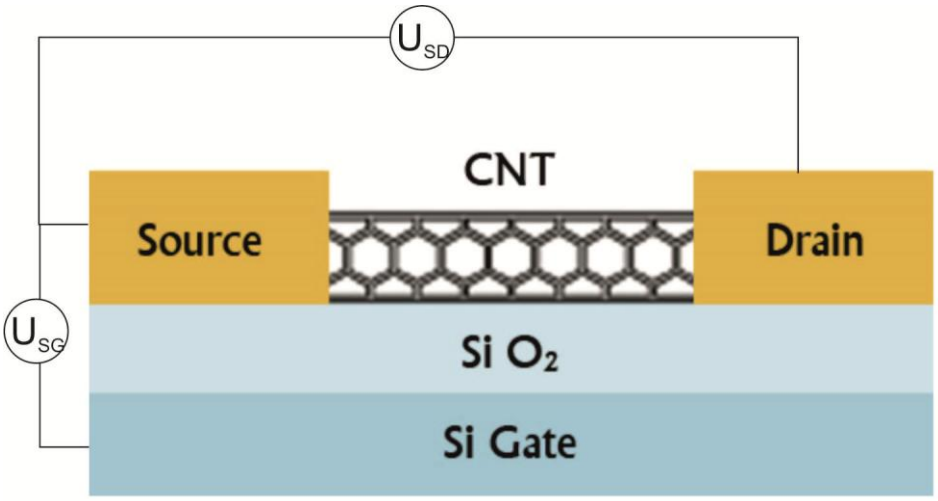

Figure 21: *Principal setup for FET measurements of the Schottky m-CNT interface using a bottom gated FET transistor (adapted from Keithley Newsletter)*[39] *U_{GS}: Source Gate voltage (+/- 20 V), U_{SD}: Source drain voltage.*

Originally, alkali metals were used for doping but the resulting n-doped CNT diodes were not stable in air. More recently, Lee et al. have demonstrated that semiconducting benzyl viologen wrapping CNT (**7**@CNT, prepared by the interaction of $2e^-$-reduced **7** with chiral CNTs) exhibit stable n-dopping of the CNT.[40] Accordingly, I expected that reduced **3** should be interacting with 6,5-CNT should lead to n-doping. The experiments were carried out in Siegmar Roth's

group in Korea. He used arrangements similar to that in Fig. 21 except that it was done on a random network of modified CNTs but not on a single CNT.

Experimental

Preparation of the single walled carbon nanotube field effect transistors (SWNT-FETs)

Single walled carbon nanotubes (SWNTs) were purchased in the form of a dispersion of enriched semiconducting tubes, IsoNanotubes-S (99 %) from NanoIntegris, USA. A highly p-doped Si covered with SiO_2 layer (300 nm) was used as a substrate. The Pt/Pd source and drain electrodes were sputtered on the substrate using the Hitachi ion sputter E-1045. The length of the active channel (30 μm) was determined by the gap between the electrodes. In order to enhance the adhesion of SWNTs to the SiO_2 surface the substrate was immersed in a 1 wt % solution of 3-aminopropyltriethoxysilane (APTES) for 30 min. Then 3 μL of the semiconducting SWCNT dispersion was dropped onto the device and dried at room temperature. Following rinsing with de-ionized water was used to remove surfactant. Fig. 1 demonstrates a nanotube network spread over the surface of conductive channel and electrode. Transfer characteristics were measured using HP 4155C (Agilent) at room temperature under ambient conditions. The gate voltage was swept from +20 to -20 V and the source-drain voltage (V_{SD}) was changed from 0 to 5 V to demonstrate the dependence of the source-drain current on the gate voltage. Doping experiment was performed by immersing the device into the $CHCl_3$ solution of reduced oligoviologen followed by drying in air.

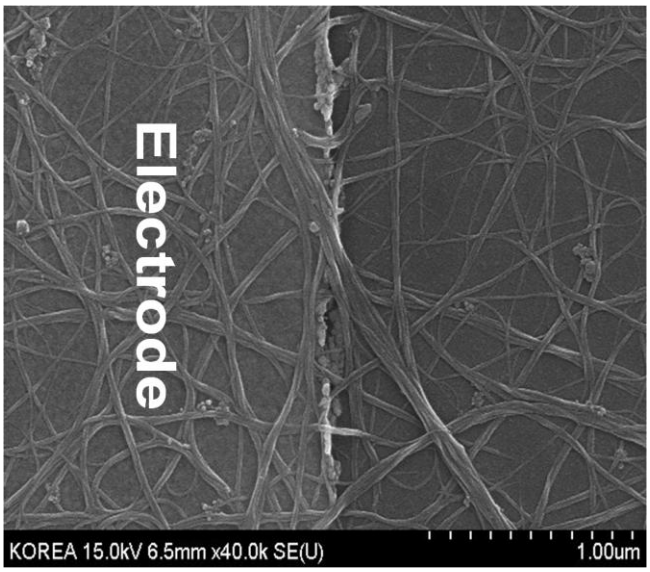

Figure 22: *Scanning Electron Microscopy image of the SWCNT network forming a channel of the field effect transistor.*

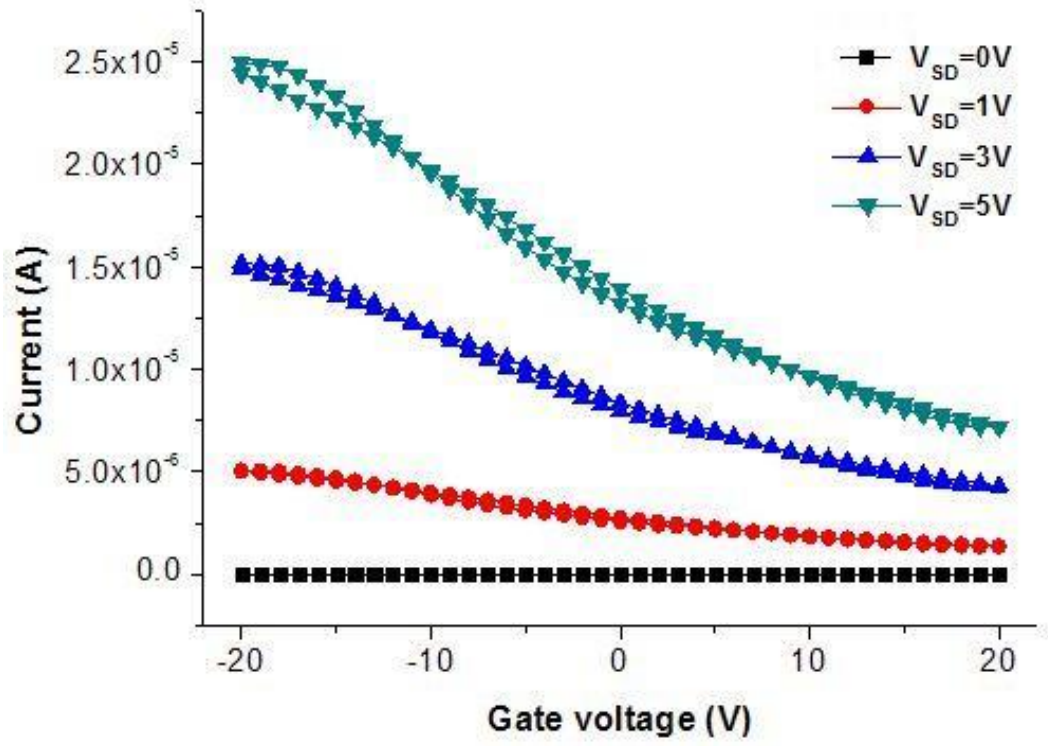

Figure 23: *I-V Characteristics of the pristine SWNT network used as a channel in the FET.*

A typical gate response of the SWNT network showing a p-type behavior (high current at negative gate bias and low current at positive gate bias) is presented in Fig. 23.

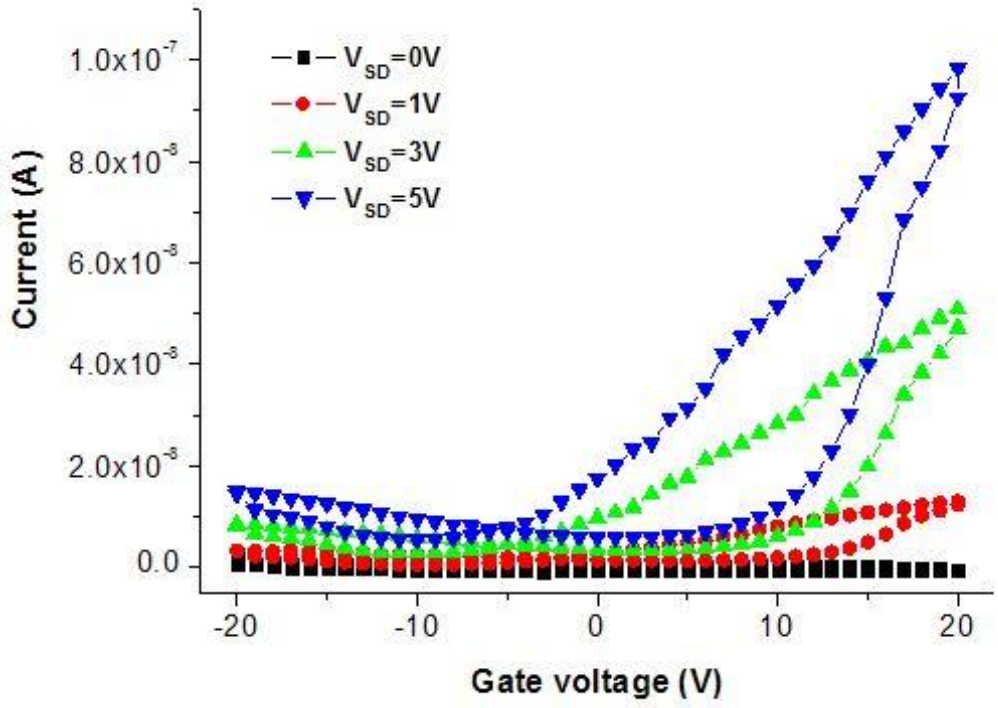

Figure 24: *Characteristics of the SWNT-FET treated with reduced oligoviologene **3**.*

Generally, the effect of the SWNT doping by oligoviologen samples was not confirmed when solutions of positively charged oligoviologene in the form of salts were used. However, a clear n-type doping was found for the neutral oligoviologen **3** obtained after reduction process. The interaction of oligoviologen 3 with the SWNT network dramatically changed the transfer characteristics of the pristine SWNT network, as shown in Fig. 24. One can clearly see that the majority of charge carrier in SWNT channel of the field effect transistor was converted from holes to electrons (high current at positive gate bias and low current at negative gate bias). We

interpret the observed changes in the SWNT-FET behavior by the formation of charge transfer complexes between oligoviologen **3** and nanotubes which lead to a charge redistribution resulting in electron donation to the sp2-bonded system and the n-type doping.

Reduction of oligoviologen **3**

1 mg of the solid oligoviologen **3** was dissolved in 1 ml water resulting in a light yellow solution. An equal volume of $CHCl_3$ was added to form a separated organic phase. After adding 100 µl of $NaBH_4$ solution (c=0.1 mol/L) the mixture was shaken to perform the reduction. The colorless organic layer turned to light yellow, when the reaction finished and the phases separated indicating that the reduced form of oligoviologen **3** was transferred to the $CHCl_3$ phase.

References

[1] A. Kongkanand, P. V. Kamat, J Phys Chem C 2007, 111, 9012.
[2] C. L. Bird, A. T. Kuhn, Chem Soc Rev 1981, 10, 49.
[3] N. Shah, P. Basu, P. Prakash, S. Donck, E. Gravel, I. N. N. Namboothiri, E. Doris, Nanomaterials-Basel 2016, 6; Y. S. Chen, R. N. Gunasinghe, X. Q. Wang, Y. Pang, Rsc Adv 2013, 3, 25097.
[4] D. Umadevi, S. Panigrahi, G. N. Sastry, Accounts Chem Res 2014, 47, 2574.
[5] J. N. Coleman, M. S. Ferreira, Appl Phys Lett 2004, 84, 798.
[6] M. A. Thompson, Abstr Pap Am Chem S 2004, 228, U360.
[7] M. Giulianini, E. R. Waclawik, J. M. Bell, M. De Crescenzi, P. Castrucci, M. Scarselli, N. Motta, Appl Phys Lett 2009, 95.
[8] V.-A. Constantin, Vol. PhD, Universität Osnabrück, 2012.
[9] *Characterization of CNT FETs*, http://www.ggcomm.com/client/Keithley/Newsletters/TestPatterns-Mar11/TP_Mar11_US.html#FO1.
[10] S. M. Kim, J. H. Jang, K. K. Kim, H. K. Park, J. J. Bae, W. J. Yu, I. H. Lee, G. Kim, D. D. Loc, U. J. Kim, E. H. Lee, H. J. Shin, J. Y. Choi, Y. H. Lee, J Am Chem Soc 2009, 131, 5010.

Chapter 3

Self-assembly of Electroactive Polymers on CNT

3.1. Introduction

Beside mono- and oligomers many conjugated or non-conjugated polymers@CNT or @graphene have attracted attention for their potential application in organic electronic devices such as batteries, field effect transistors, optical devices, and chemical sensors.[14,41-43]

The limited solubility of single walled carbon nanotubes driven by van der Waals interaction limits their utilization in device applications. Polymers wrapping of CNT has so far mainly used to de-bundle CNT especially in aqueous solutions. Device application is a more recent reason to study the wrapping of CNT. Conjugated polymer-SWNT such as polythiophene@CNT can manifest dramatically enhanced conductivities and charge mobility.[44-46]

Water-soluble amphiphilic polyelectrolytes consisting of a linear conjugated backbone have been claimed to lead to amphiphilic structural motifs promoting the dispersion of SWNTs at high mass percent in the aqueous phase[47] as well as substantial $\pi-\pi$ interactions provided by the conjugated system of these polymers as observed with AFM.

Adsorption of aromatic polymers on carbon nanotubes surfaces has been the object of several theoretical studies. The resultant organization has been reported mainly as aligned along the nanotube axis.[48] Extended self-organized arrangements such as single and multi helical structures have been proposed[36,49] and observed for poly(p-phenyleneethynylene) with

AFM[47] but the self-assembly of charged polymer has not been studied and evidenced by a microscopic techniques.

The structural self-organization of polythiophenes on nanotube surface has been observed with STM.[16] The strong π–π bonds interaction is believed to bring the alignment of the polymer backbone along the CNT axis or along directions with large coiling angles.

In this chapter it is shown that redox polymers form a helical superstructure upon associating with CNTs, despite their intrinsic linear, conformationally restricted nature, and that the superstructure has substantial aqueous phase solubility. In order to understand short-range interactions between polymer and nanotubes and to provide key information for the comprehension of the basic mechanisms affecting their bulk properties, accurate STM analyses have been performed.

To probe the structure of polymer@CNTs microscopy experiments were carried out. It was found that the polymer wrapped CNTs show up as much thicker cylinders as compared to bare CNTs as it is also indicated in literature for poly(*p*-phenyleneethynylene)[47], see also Fig. 2, in Chapter 2.

3.2. Results and Discussion

The polymers studied in this study are presented in Table1 including structure, abbreviation and geometrical analysis. They exhibit stiff (**1-6**), or flexible (**Chapter 4**) band structures (see Table 1) due to the presence of sp2 and sp3 centers (exclusively sp2 centers, low degree of sp3 centers and a high degree of sp3 centers, respectively). All polymers consist generally of more than 10 subunits (as judged from ^{1}H-NMR, and more than 100 subunits as judged from STM analysis.

Table1: Overview of the polymers and their structural analysis

Polymer No.	Abbreviation	Chemical structure	Fig. No.	Pitch x[a] (nm)	Helix diameter y[b](nm)	No. of Helices	Angle[c]	Chirality
Viologen Polymers								
1	$[MA\text{-}V]_n$	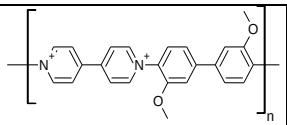	Chiral CNT					
			2a,b	16	8	Double	45°	-
			2d,e	7	6	triple	45°	+
			2g,h	7.5	7.5	3-4 helix	48°	
			2j,k	10.5	11-12 (bundle)	6-7 helix	-	
			2m,n	4.5	3.5	Double	45°	
			Metallic CNT					
			2p,q	6.5	3.5	Double	45°	+
			2s,t	14	16 (bundle)	4-5 helix	-	
2	$[P\text{-}V]_n$	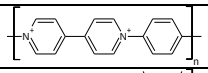	5a,b	1.8	5	single	73°	
3	$[tetraM\text{-}P\text{-}V]_n$	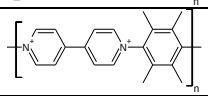	6a,b	4.0	8	Single	78°	
Diimid Polymers								
4	$[MA\text{ -diimid}]_n$	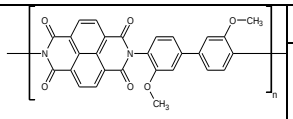	7a,b	3	3.5	Single	55°	
			7c,d	5	4	Double	48°	-
5	$[P\text{-diimid}]_n$	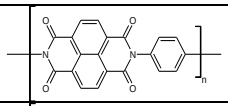	9a-c	2.7	6	Single	70°	
6	$[tetraM\text{-}P\text{-diimid}]_n$	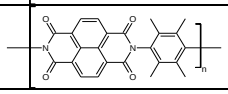	10a-c	8	4	3-4 helix	48°	
Flexible Viologen Polymers (chapter 4)								
		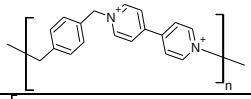		2-3	2.5	Single		
		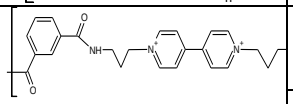		4-6	5	Single (loose wrapping)		
				3.5	12	Single (tight wrapping of a bundle)		

a= x in Fig. 2 b= y in Fig. 2 (polymer+CNT) measured at right angle to the main axis of CNT c=wrapping angel with respect to main axis of CNT, n > 100 as no break observed

All polymers exhibit helical wrapping. Judgment of the length by STM image analysis is based on the observation of the start and end of a strand. In case of (**5-6**) such a situation is observed.

In contrast to the small rods we found exclusively for the rigid polymers helical structures with helix diameters to be much bigger than the wrapped CNT (see Fig. 2). It is related to the stiffness of the polymer backbone and its resistance towards further bending below a certain spiral diameter.

3.2.1. Rigid viologen polymers

Rigid polymer **1** was found to be the best dispersing agent for CNT in aqueous media among the series of polymers presented in Table 1. Dispersions are stable over months for sc-CNT or m-CNT as shown in Fig. 1.

Figure 1: *Rigid polymer **1** dispersion with (right) 6,5 SWCNT and (left) m-CNT*

As observed in Fig. 2, polymer **1** tends to wrap the sc-CNTs again in helical fashion. The type of helical wrapping is either two helices (Fig. 2a-b) or more (Fig. 2d-e): triple helix, (Fig. 2g-h):3-4 helices, (Fig. 2j-k) 6-7 helices). Most impressive is the fact that generally the helix diameter (6-

12 nm) is much larger than the CNT diameter (theoretically: 0.9 nm) inside the helix – except in (Fig. 2m-n) and (Fig. 2p-q) (see Table 1). Notably, large helix diameter shows up with "free space" (Fig. 2a-c) if one CNT is inside or offers space for more than one CNT guest (Fig. 2j-l). Notably, CNTs are observed preferentially for polymer **1** with its rigid backbone as compared to the rods discussed in Chapter 2. There is no fundamental change when changing from semiconducting (Fig. 2a-o) to metallic CNTs (Fig. 2p-u).

In Fig. 3 more inside into the helical spiral system of double stranded helical **1** with a single sc-CNT guest is shown (I change the host and guest notion here for obvious reasons). First, it is clearly observed that the CNT is contacting only a band (a segment of the helix parallel to the CNT). Second, the interaction energy is low, and a 50 mV pulse from the STM tip is able to displace the CNT relative to the helix over a distance in the range of the helix diameter.

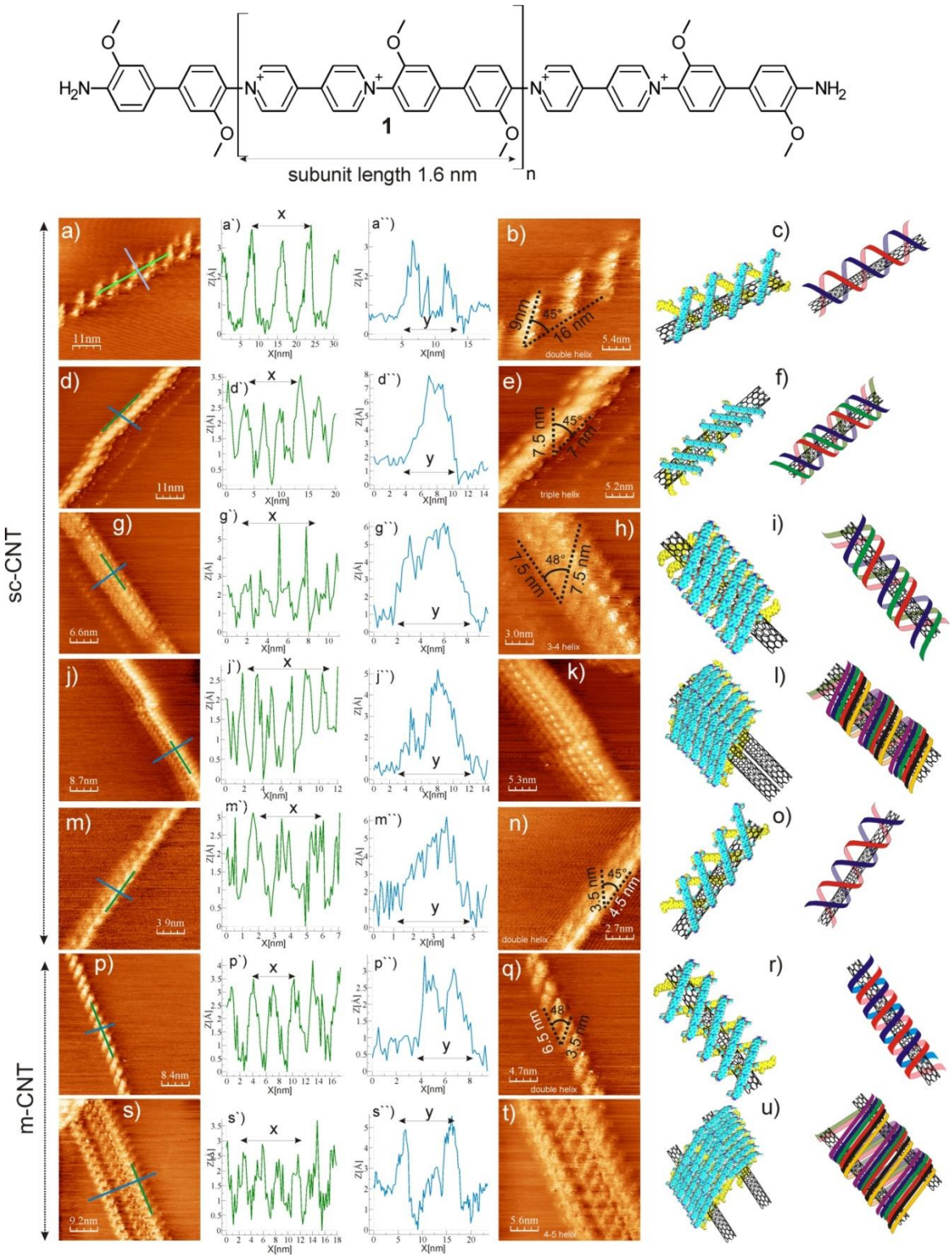

***Figure 2*: Diversity in self-assembled structure of 1@CNT** *(with modeled subunit length 1.6nm)*

(a-o) self-assembly of 1@ sc-CNTs;

(a-c) *a) STM of **1**@CNT wrapped in dilute double helical conformation with the helix diameter much larger than CNT diameter; a`) profile along CNT axis with x pitch of a single helix; a``) profile perpendicular to the main CNT axis (thickness of helix), values of x and y given in Table 1 ; b) zoom-in showing 1 turn consist of 9 nm length ca. 6 sub units per turn, wrapping angle 45° attributed to the stiffness in the backbone; c) model;*

(d-f) *d) similar conformation as in (a-c) but triple helix and smaller pitch; d`) pitch analysis; d``) right angle thickness, values of x and y given in Table 1; e) zoom-in of d) pitch of 7 nm and turn length 7.5 nm corresponding to 4.7 subunits, wrapping angel is 45°; f) model;*

(g-i) *g) polymer wrapping 3-4 helices; g`) pitch analysis; g``) right angle thickness, values of x and y given in Table 1; h) zoom-in with pitch 7.5 nm and turn length 7.5 nm, wrapping angle is 48°; i) model;*

(j-l) *multi stranded wrapping of a CNT bundle; l) proposed conformation;*

(m-o) *similar to (a-c) **1** forming double helix thinner and showing tube sitting on one side; m`) pitch analysis; m``) right angle thickness, values of x and y given in Table 1; n) zoom-in showing 4.5 nm pitch and turn length 3.5 nm corresponding to ca. 2 subunits per turn, wrapping angle is 45°; o) model;*

(p-u) self-assembly of 1@m-CNTs;

(p-r) *p) thin double stranded with pronounced offset as compared to sc-CNTs; p`) pitch analysis; p``) right angle thickness, values of x and y given in Table 1; q) zoom-in pitch of 6.5 nm and turn length 3.5 nm, wrapping angel is 48°; r) model;*

(s-u) *multi-stranded polymer wrapping of a bundle of two tubes ca. 4-5 nm apart; s`) pitch analysis; s``) right angle thickness, values of x and y are given in Table 1; t) zoom in showing the central apart of the two tubes with woven structures; u) model;*

*It is observed that **1** always wrap CNT with 45-48° angles whether it is double or multi-stranded wrapping.*

The rigidity of polymer **1** towards a helical deformation can be judged from the heat of formation (ΔH_f) of hypothetical ring-shaped poly-**1** with different numbers of MA-V subunits in the ring, i.e. with different ring diameters, such as shown in Fig. 4 for the case of **1** with two subunits. In Fig. 5 ΔH_f per subunit for the closed rings are presented as a function of the theoretical diameter and as a function of the MA-V subunit number. The PM7 calculations were performed for the cases with viologen as dication and with the fully reduced uncharged case.

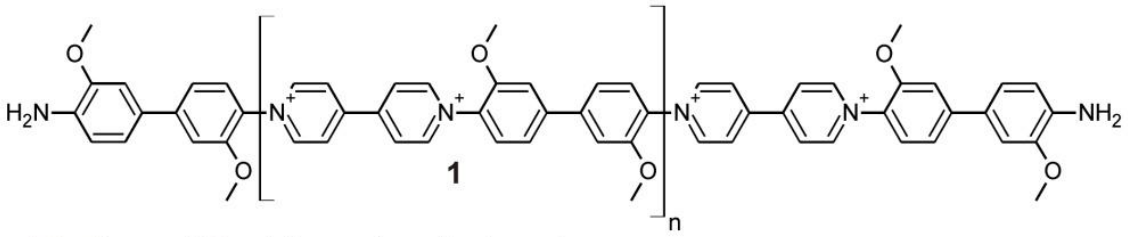

Before 50mV potential pulse

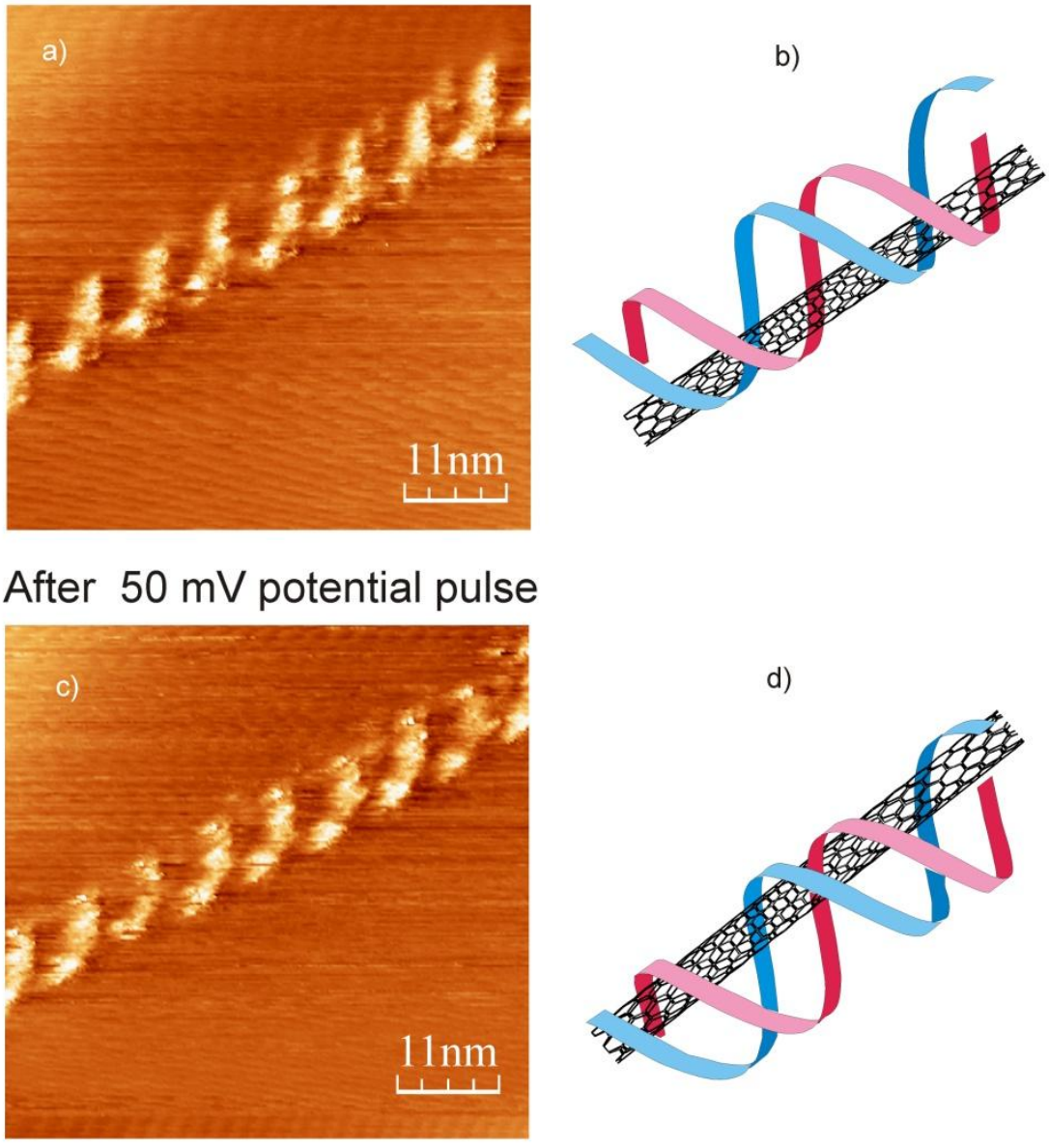

Figure 3: *Impact of a potential pulse on the CNT loosely wrapped by polymer **1**; a) STM image showing CNT lying on the lower side of the helix; b) model; c) upon application of 50mV pulse CNT moves to the upper side of helix; d) model.*

In case of fully oxidized viologens, ΔH_f/subunit decreases from 2 to 7 subunits in an asymptotic curve reaching a constant value at ca. 6-7 subunits. While in case of fully reduced viologens, a constant value for ΔH_f/subunit is already attained at subunit number 4-5.

The difference in energy build-up for small rings in the above two cases is related to the presence of only sp2 hybridized nitrogens and carbons in the completely oxidized MA-V, whereas in case of the ring structures with 2 electron reduced viologens, all nitrogens are sp3. The sp3 centers facilitate a ring structure and therefore smaller rings and less torsional energy are possible.

Table 2: Polymer 1 Geometry optimization using semi empirical methods

No of MA-V Subunits	H_f With (n*2) Oxidized Vio KCAL/MOL	H_f/sub	Diameter r1, r2	H_f Reduced vio KCAL/MOL	H_f/sub	Diameter r1, r2
2	50.31494	25.158	1.4, 0.61	120.84617	60.423	1.3, 0.77
3	-44.57183	-14.857	1.7, 1.4	161.24011	53.747	1.6, 1.5
4	-86.27313	-21.568	2.2, 2.1	205.93175	51.483	2.1, 2.2
5	-87.73647	-17.547	2.9, 2.4	254.71381	50.9428	2.9, 2.5
6	-153.59007	-25.598	3.3, 3.3	301.00973	50.168	3.2, 3.2
7	-173.23065	-24.747	3.9, 3.7	345.19662	49.314	3.8, 3.8

The frontier orbitals of the PM7-modeled structures of **1** (with four subunits) on 6,5-CNT are presented in Fig. 6. Notably the calculation was executed on the whole systems including all 386 carbons (+ peripheral H) of the CNT and 197 atoms of the **1**-model. Two calculations with total =+1 and +9 were made. These charges will distribute on the separated but partially interacting MO levels of 1 and the CNT. As observed for the more reduced case (total charge = +1), all calculated LUMOs (LUMO, LUMO+1, LUMO+2) are located on CNT and all HOMOs (HOMO, HOMO+1, HOMO+2) are located on **1**.

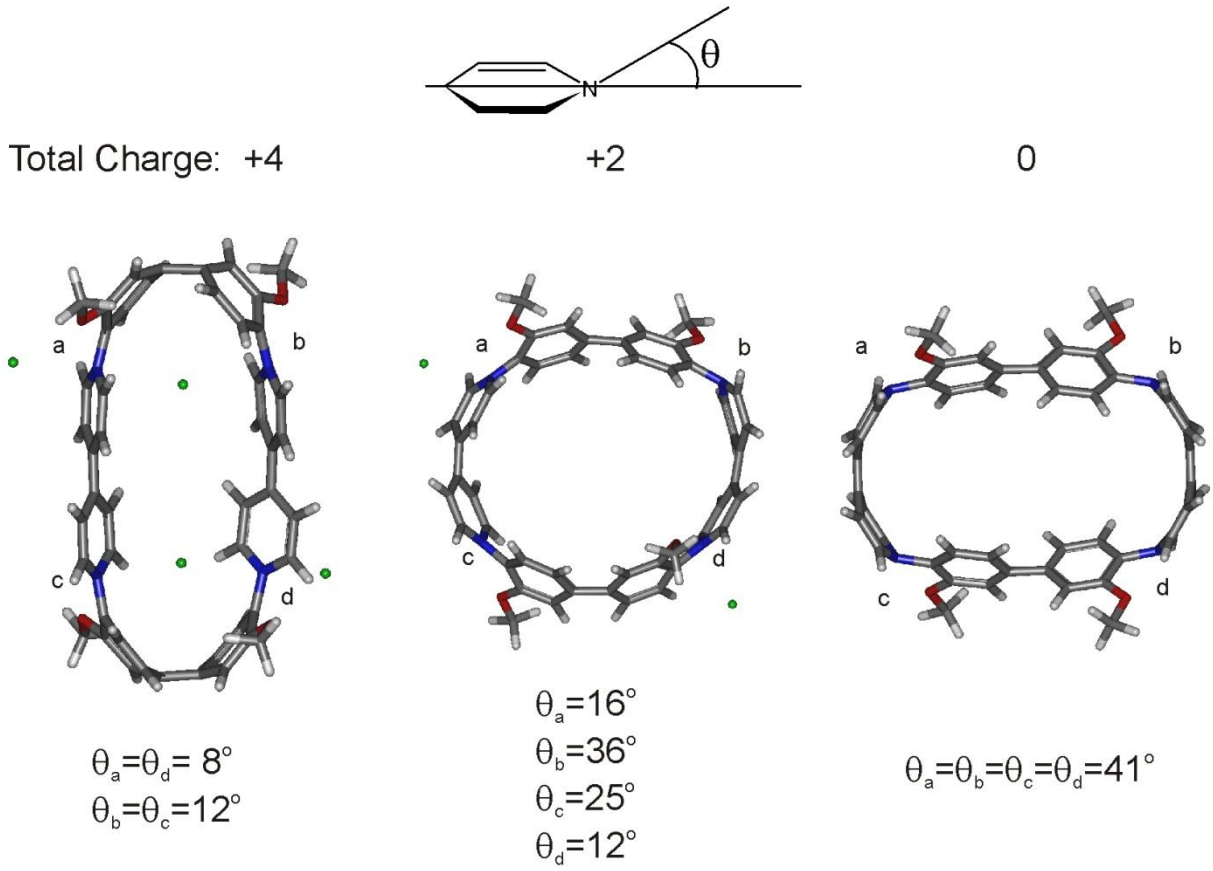

Figure 4: *PM7-modeled ring geometries for hypothetical rings of* ***1*** *with 2 subunits with total charge on the rings of +4, +2, and 0 (in calculations with positively charged subunits, the positive charge was compensated by chloride ions); indicated are torsional angles at the centers a-d; the completely reduced compound shows 41° torsion mainly at the nitrogens.*

On the other hand, upon withdrawal of 8 electrons (total charge: +9) all HOMOs are located on CNT, and two of the three calculated LUMOs are located on **1**. We conclude from this that the HOMO-LUMO role depends strongly on the total charge and that some of the frontier orbitals are interdigitated.

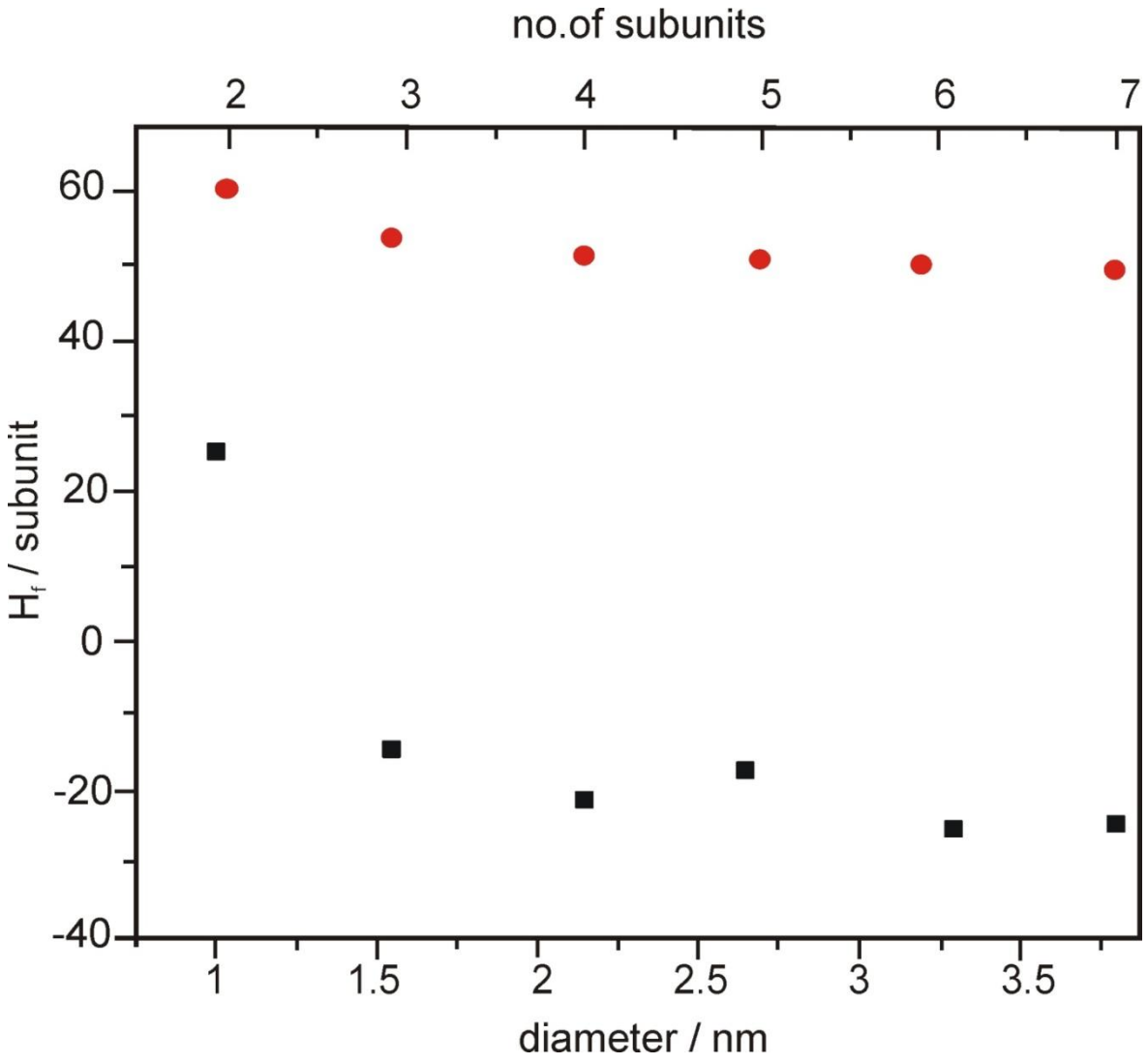

Figure 5: *Plot of calculated ΔH_f/subunit vs. no of subunits and vs. averaged diameter of* ***1*** *from PM7 modelling; circles reduced subunits, squares dicationic subunits.*

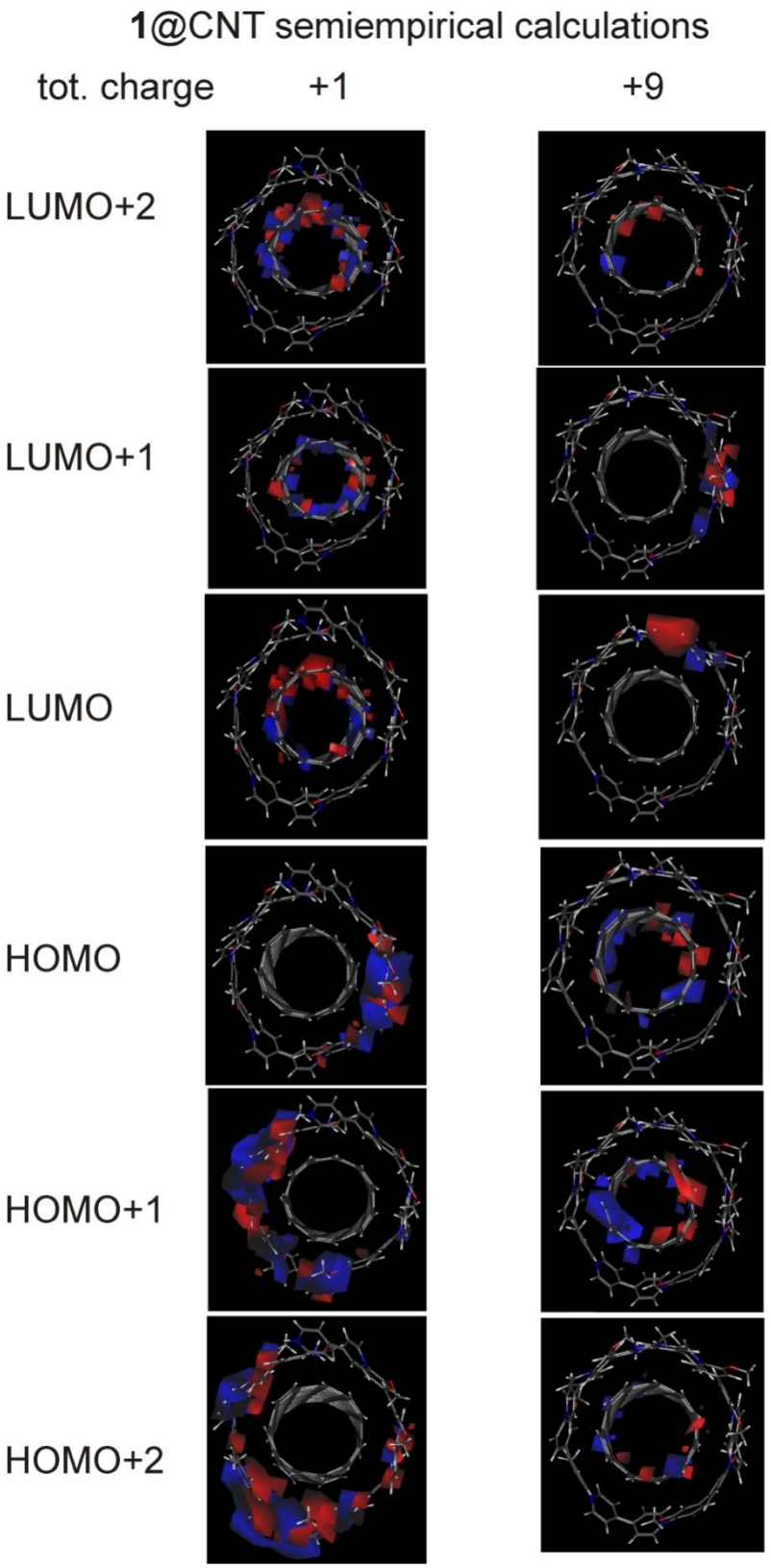

Figure 6: *Semi-empirical PM7 calculations of **1** at CNT with H at open valences (C+H = 386) and **1** (4subunits, 197 atoms) at total charge +1 (left) and +9 (right). Frontier HOMO and LUMO are presented.*

Such presentations have been used to judge the MO localization in the frontier orbitals range -10 to +10. It nicely represents that in reduced state (+1 total charge) LUMO localized on CNT while HOMO localized on polymer and in case of oxidized states (+9 total charge) LUMO localized on polymer with one exception of LUMO+2 while HOMO localized at CNT.

The polymers **2** and **3** are closely related except that in **3** the phenyl groups are per-methylated. The influence of these methyl groups shows up clearly when comparing the inter-strand distance (empty place between consective strands) of **2**@CNT (0.8 nm) with the inter-strand distance in **3**@CNT (1.5 nm). This difference can be compared with the inter-strand-distances of viologen rods with different side chains discussed in Chapter 2. In case of the non-methylated polymer **2**, the single subunits are well separated and shiny allowing to count the subunit in the exposed half of a helical turn (see Fig. 7).

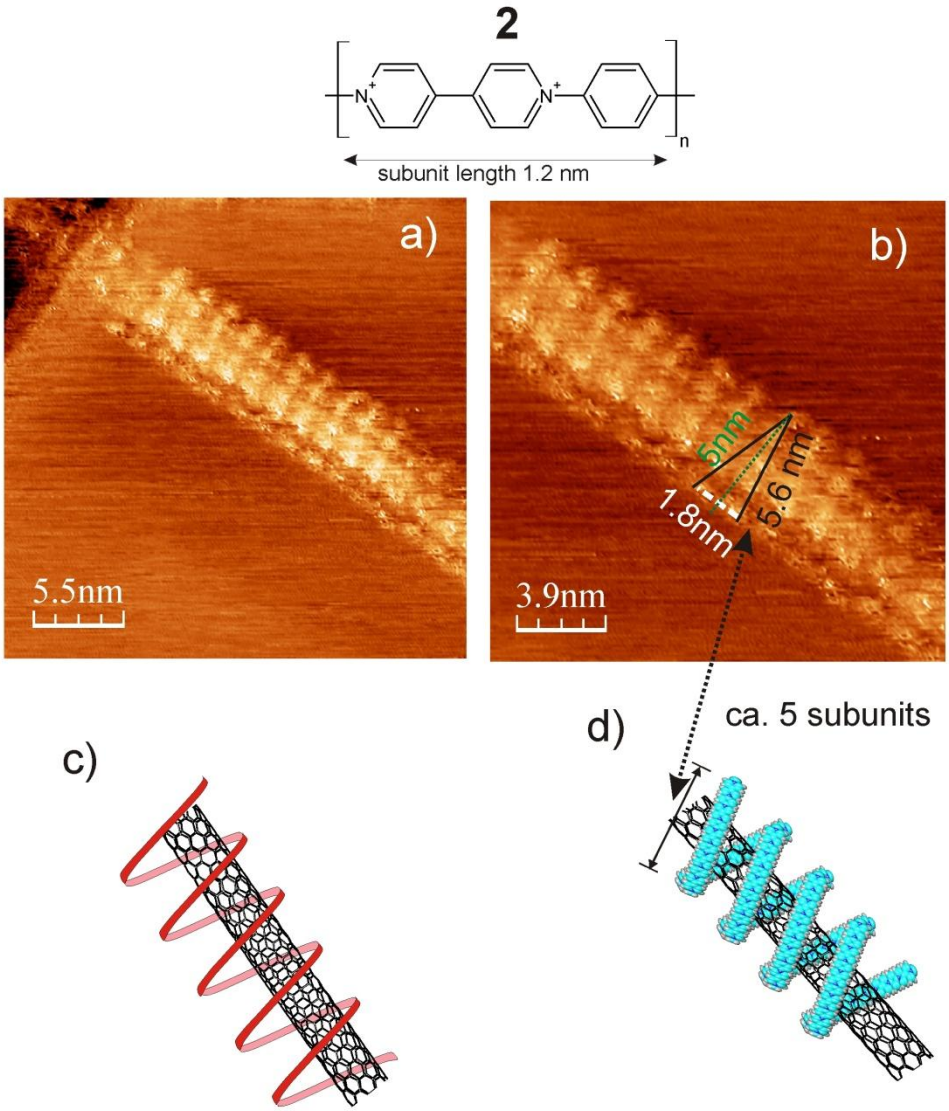

Figure 7: *a) Self-assembled* ***2*** *arranged in sigle helix conformation at chiral CNT; b) zoom-in showing 5 nm thick polymer wrapped CNT with 1.8 nm pitch per strand observed length is 5.6 nm corresponding to ca. 5 subunits on the frontside of helix. Inter strand distance is ca. 0.8 nm; wrapping angle is ca. 73°; c and d) model (see table 1).*

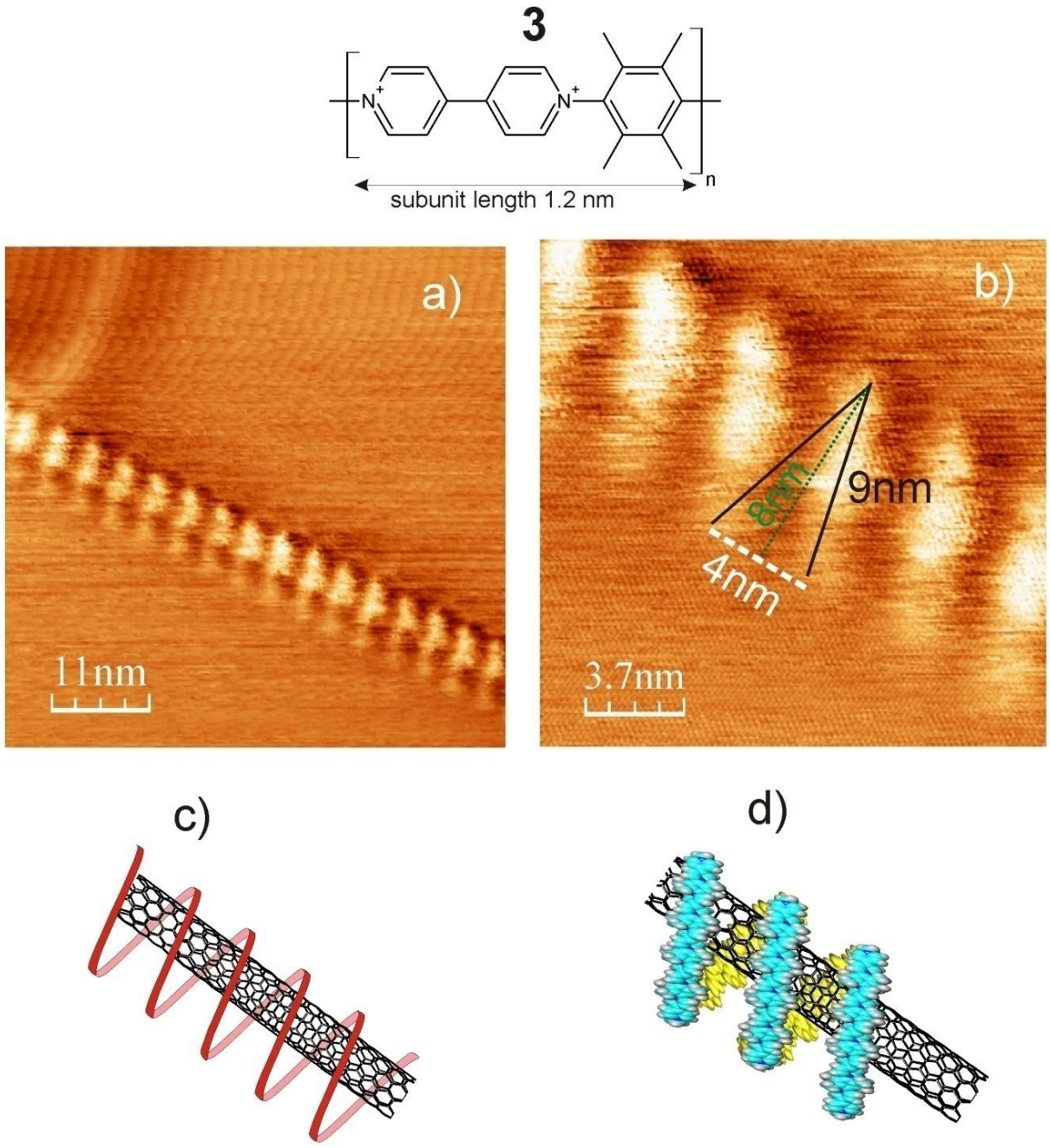

Figure 8: *a) Self-assembled **3** arranged in a single helix at chiral CNT; b) zoom-in showing 8 nm thick polymer wrapped CNT with 4 nm pitch per strand and 9 nm corresponding to 7.5 subunits on front side of helix, inter-strand distance is 1.5nm, wrapping angle is ca. 78°; c and d) models and generalized overview of wrapping style (see table 1).*

3.2.2. Rigid Diimid Polymers

As compared to viologen, the polymer dispersion of chiral CNT was not as homogenous with the diimid. **4** tend to wrap bundles of CNT more frequently than with the viologen polymers observed.

The diimid polymers **4**, **5** and **6** have no viologen subunits. The electroactive moiety is the naphthyl tetracarboxylic acid diimid, and the linking diamin is anisidin (**4**), p-diamino benzene (**5**) or tetramethyl-diamino bezene (**6**). They are, therefore, not positively charged as all compounds discussed so far. It was, however, possible to dissolve them in DMF or NMP and in both solvents the 6,5-CNT can also be dispersed. As shown in this chapter, the non-charged diimid polymers wrap around chiral CNTs as previously observed for the stiff viologen polymers.

Again, we observe that the helical diameter is generally much larger than the CNT diameter leading to "free CNT" in a helical cylinder of **4** (Fig. 9 a-d), Fig. 10)), and **5** (Fig. 12). For **4**@CNT, a similar voltage induced displacement reaction could be provoked (Fig. 10) as already observed for **1**@CNT (Fig. 3).

Another common property for polymers **4**-**6** all dissolved in DMF or NMP is that they tend to wrap bundles of CNTs preferentially. This could be related to the fact that CNTs were dispersed in DMF or NMP and this solvent may not disrupt all CNT bundles prior to the interaction with the polymer.

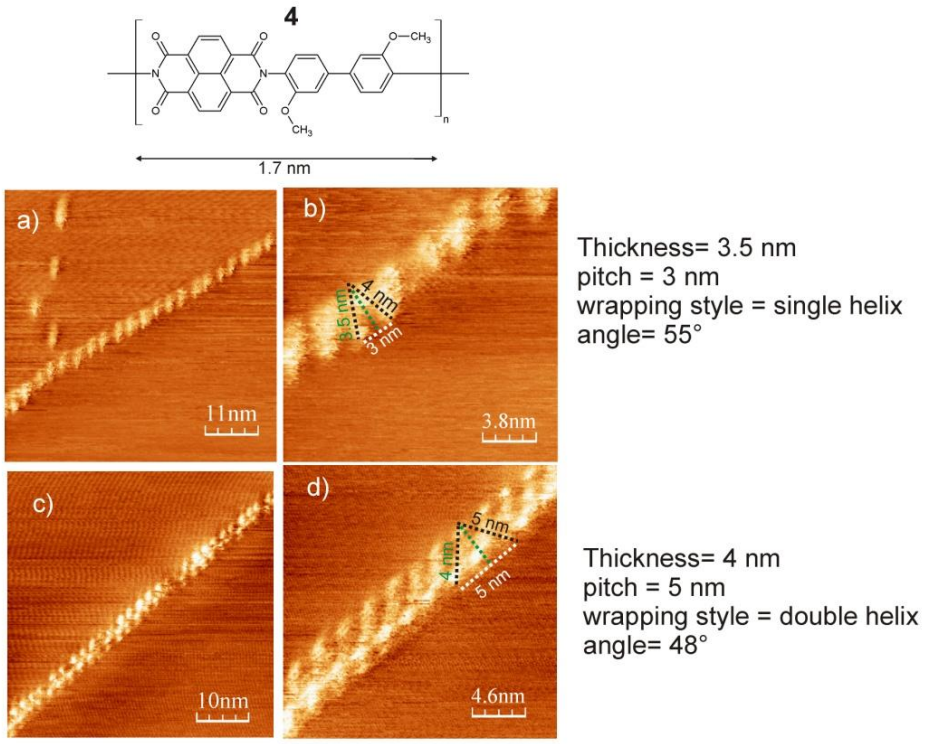

Figure 9: *Self-assembly of **4** at CNT a) wrapping in single helix conformation b) is zoom in showing 3.5 nm thick wrapping with 3 nm pitch per strand and 4 nm corresponding to 2.3 subunits on front side of helix.*

*c) shows **4** wrapping CNT in double helix form d) is zoom-in showing 4 nm thick self-assembly and 5 nm pitch per strand and 5 nm corresponding to 3 subunits on front side of helix.*

e) shows wrapping of a bundle with many breaks in polymer may be due to different sizes of polymer chains wrapped around as can be seen in (I),(II) and (III) length of the polymer can be measured experimentally and as a result subunits can be calculated.

f) is another example of a big bundle with breaks but complicated to analyze; g) is zoom in of f.

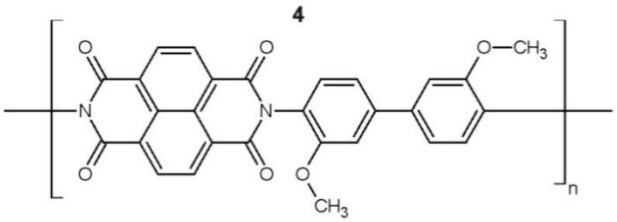

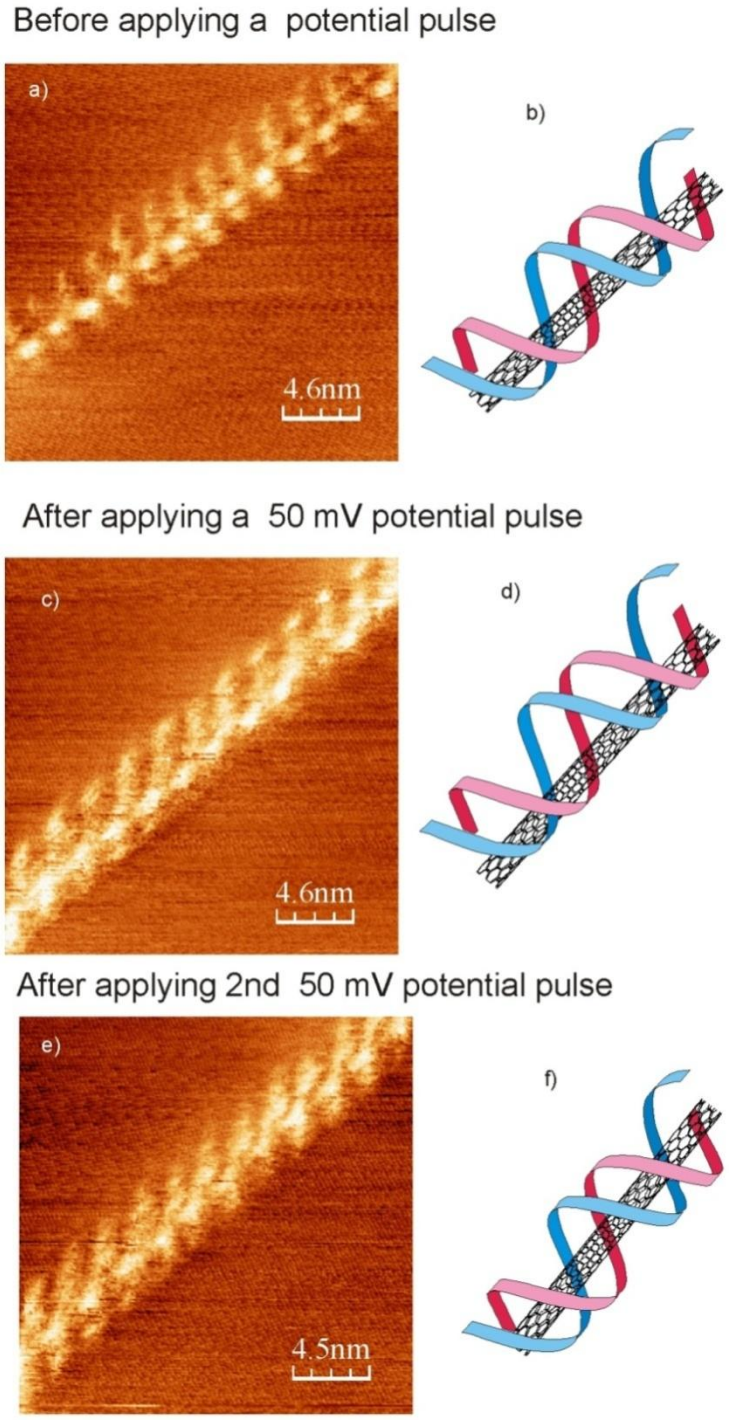

Figure 10: *Impact of potential induced pulse on the CNT loosely wrapped with polymer* ***4****; a) STM image showing CNT lying in the center of the helix which is highlighted in b.*

c) After application of stm tip induced pulse of 50mV the CNT moved to the lower side of helix as shown in proposed model d.

e) After application of 2nd stm tip induced pulse of 50mV the CNT moved back to the center of helix as shown in proposed model f.

The energy per subunit vs. the numbers of subunits necessary to enforce a ring type conformation in **4** is presented in Fig. 11. As already discussed for **1** in ring shape (Fig. 4), an asymptotic behavior is observed for **4.** A constant energy value is achieved for ca. 8 subunits (4-5 subunits for **1** in the oxidized situation, i.e. without sp3 content). It is also interesting to compare the energy difference between 2 subunits and the asymptotic limit which is, in case of **4,** ca. 30KCal/mol, and in case of **1** ca. 50KCal/mol. These values of **1** are almost double to that of **4** so it is clear there is a big influence of electrostatic interactions.

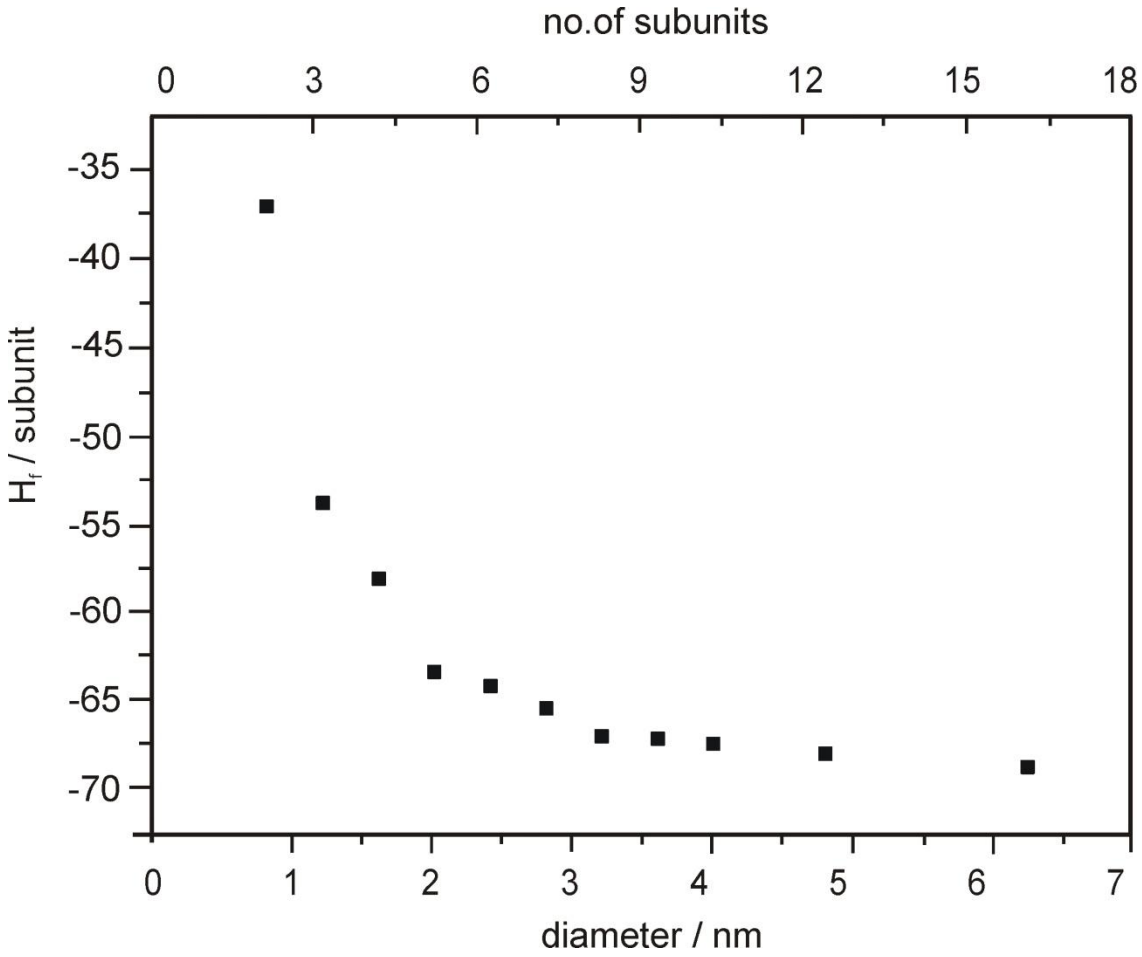

Figure 11: *Plot of calculated ΔH_f / subunit vs. no of subunits and vs. averaged diameter of* ***4*** *from PM7 modeling.*

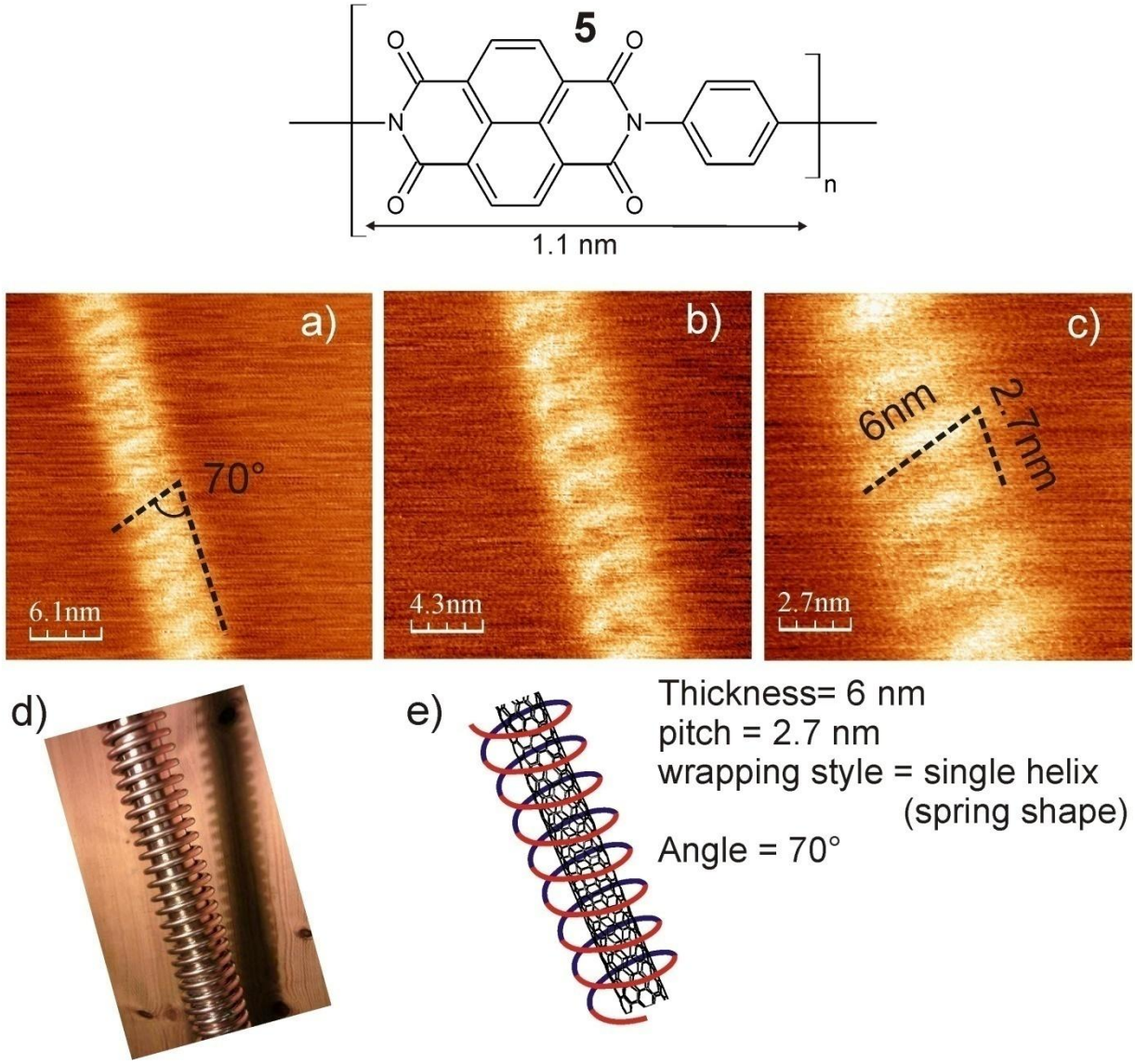

Figure 12: *a) Self-assembly of* ***5*** *arranged in single helical (spring) form at Chiral CNT; b and c) zoom-in showing 6 nm thick polymer wrapped CNT with 2.7 nm pitch, inter-strand distance is 2.2 nm; d and e) are generalized overview of wrapping style.*

An interesting STM structural property is observed exclusively for **6**@CNT (Fig. 13, b), e)). Isolated shiny spots in a regular pattern are observed. I explain these spots as increased tunneling current on NTCDA-imid subunits. The local isolation of large tunneling current spots

(only observed in **6** but not in **4** and **5**) could be related to an orthogonal conformation of the bulky tetra methyl-1,4-diamino benzene subunit, which is exclusively present in **6**. (Fig. 13, modeling of the subunit structure).

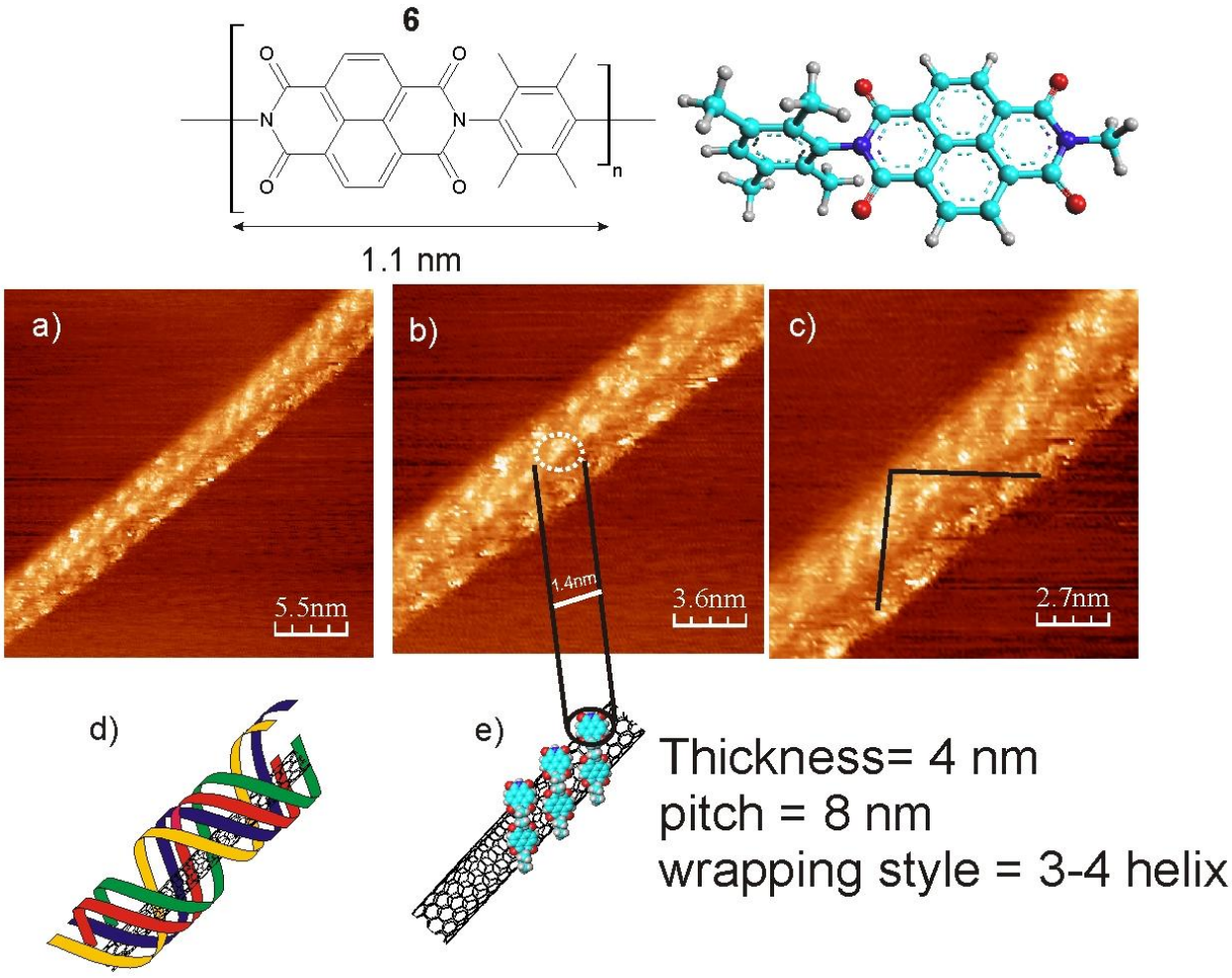

Figure 13: *top: Chemical structure and modeled methylated subunit conformation, a) Self-assembly of **6** arranged in 3-4 helixes at Chiral CNT; b) zoom-in showing 4 nm thick polymer wrapped CNT with 8 nm pitch for per strand. Inter strand distance is ca. 2.1 nm; c) wrapping angle is ca. 48°; d and e) are proposed model and generalized overview of wrapping style.*

In case of **5** and **6** the inter stranded distance is defined by diimid subunit rather than tetramethyl. So, in case of Fig. 10 and 11, it is observed that inter-stranded distance remains approximately the same.

3.3. Conclusion

1. Rigid linear and electro active polymers **1-6** wrap sc and m-CNT without exception in a helical manner.
2. The rigidity of polymers leads to helix diameters much larger than CNT diameter. Thus, the polymer helices offer place for more than one CNT guests. I have observed single and multiple polymer chains wrapping single CNT. A single CNT in a large polymer helix can be displaced by application of a potential step.
3. The wrapping angel is in the range of 45 to 80°. This steep arrangement was not observed for the wrapping angle in case of oligomer rods (chapter 2). A reasonable explanation is again the stiffness of polymer **1-6**, as a steep angle minimizes the torsional stress in the backbone of the polymer. The smallest wrapping angles were observed for the anisidine polymers **1** and **4** showing mainly multiple stranded helices.
4. A simple PM7 calculation for **1** and **4** shows torsional energy in ring shape polymers starting at 4 and 7 subunits respectively. That means rings with less subunits show energy buildup because of increasing deviation from sp2 geometry. Repulsive electrostatic interactions in case of the oxidized **1** show up by increased energy difference build up for small diameters as compared to the fully reduced **1**.

3.4. Experimental

Single walled carbon semiconducting CNTs (sc-CNT chirality: (6,5), d: 0.7 to 0.9 nm) were from Sigma Aldrich.

All the chemicals and solvents were from Sigma–Aldrich and used as received without further purification.

Syntheses

1 was synthesized as described.[41]

*Synthesis of **2** and **3**:*

2 and **3** were prepared and characterized by Dr. M. Beladi-Mousavi as follows:

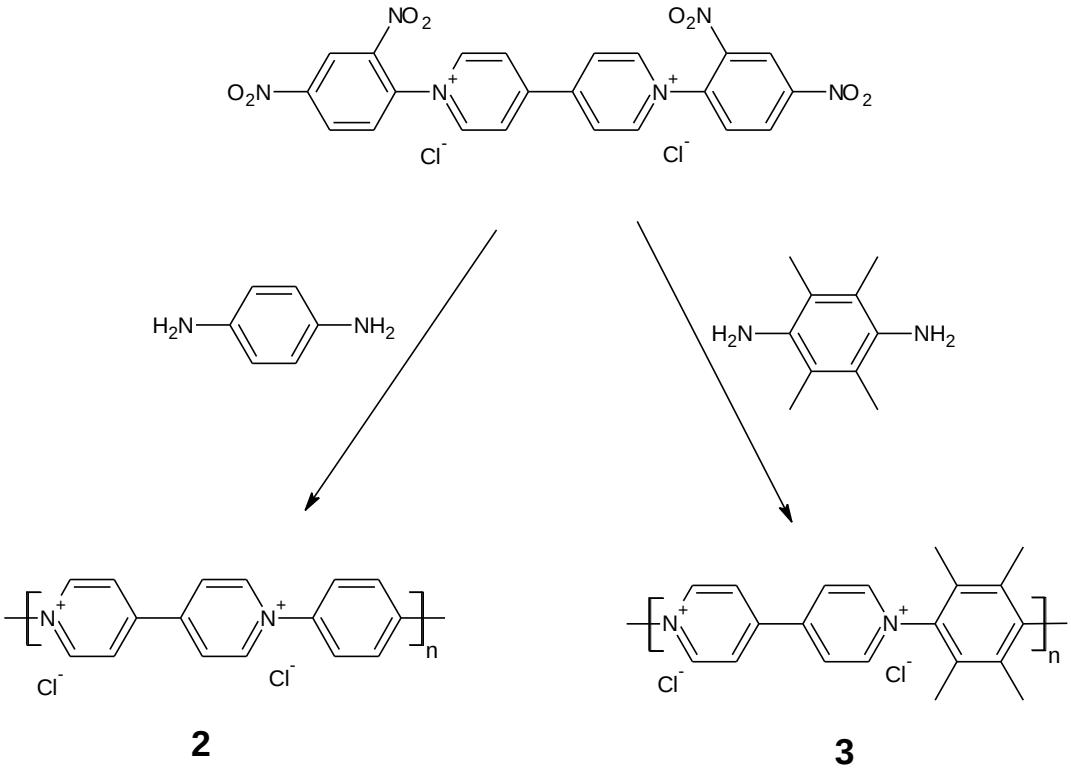

2 **3**

1 mmol (0.56 g) of bis-[1,1'-(2,4-dinitrophenyl-4,4'-bipyridinium dichloride)] and 1,4–phenylenediamine (1 mmol, 0.108 g) for the synthesis of **2** or 2,3,5,6-Tetramethyl- 1,4–phenylenediamine (1 mmol, 0.167 g) for **3** were dissolved in a mixture of methanol/water (8/2) and refluxed for 3 weeks. Then, solvents were evaporated and the solid residue was mixed with acetone and refluxed for 12 hours. The precipitate was collected and washed with acetone, and dried under high vacuum to yield 99% and 93% **2** and **3**, respectively. In order to evaluate the molecular weight, 100 mg of the polymers were separated in a column (Sephadex LH20) using methanol as the mobile phase, and the fractions were evaluated by ^{1}H-NMR.

^{1}H NMR of 2. (250 MHz; MeOD)) broad peaks at δ: 9.28 (4H); 8.91 (4H); 8.22 (4H);

^{1}H NMR of 3. (250 MHz; MeOD)) unstructured peak at δ: 8.0-9.8 (8H); 2.5 (12H+ end groups from short polymers);

*Synthesis of **4**:*

4 was synthesized and characterized by Sascha Lax (Master thesis 2014) under Dr. M. Beladi-Mousavi's and my guidance as follows:

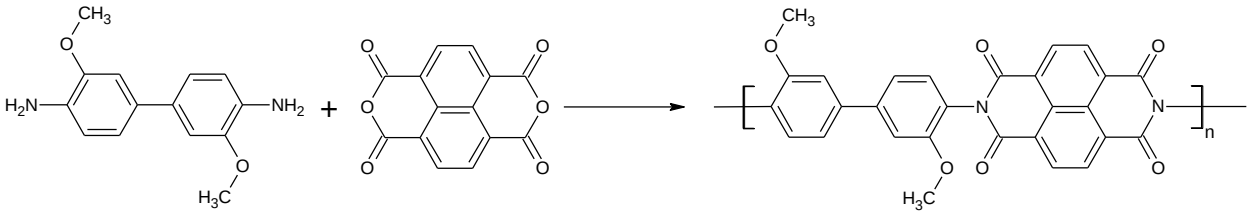

4

488 mg (2 mmol) *o*-anisidine was dissolved in 50 ml DMA under sonification, and 538 mg (2.01 mmol) was dissolved in 20 ml DMA at 40 °C. The two solutions were combined and heated at 140 °C for 3d. After cooling to r.t. the red precipitate was isolated by filtration and

washed with 20 ml water. To the mother liquor, 40 ml diethyl ether was added resulting in a reddish-brown precipitate.

^{1}H-NMR (250 MHz, DMSO): δ 8.818-8.620 (s, 4H); 7.561 (m, 6H); 3.905 (s, 6H)

IR: 1715 (C=O, ν_{as}), 1672 (C=O, ν_{s}), 1348 (C-N,ν), 767 (C=O, δ), 1579.74 (naphthalene)

*Synthesis of **5** and **6**:*

5 and **6** were synthesized and characterized by Patrick Harpel (Master thesis 2014) under M. Beladi-Mousavi's and my guidance as follows:

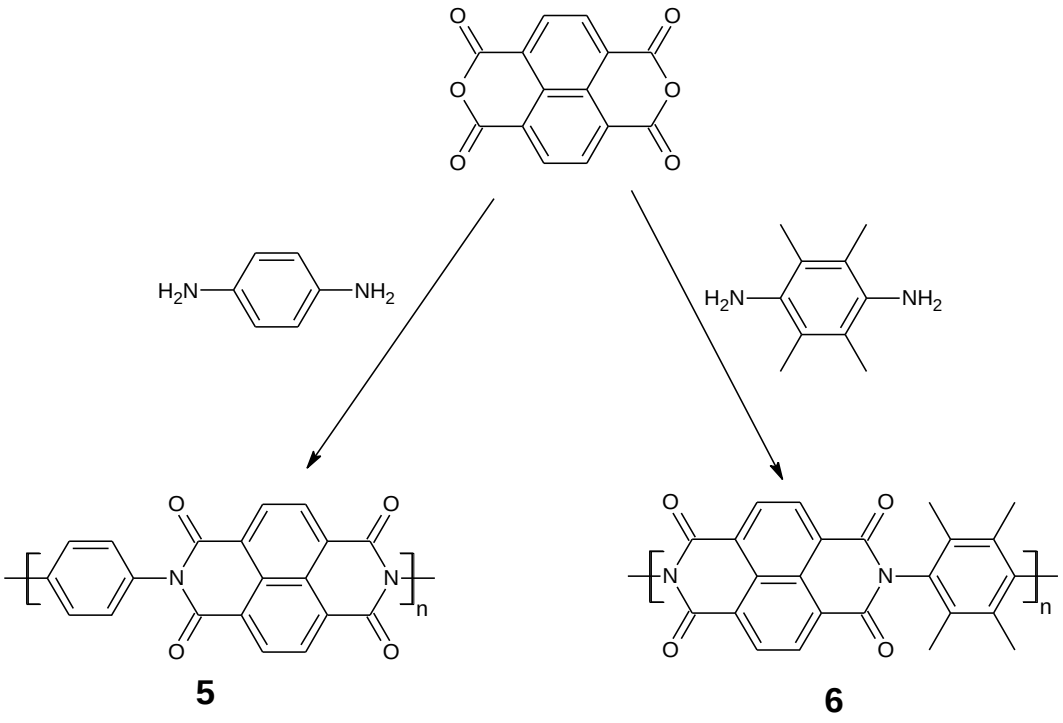

5 **6**

0.608 mmol (0.163 g) of bisNTCDA was dissolved in 36 ml DMA and heated at 100 °C for 30 min until it was completely dissolved then cooled to r.t. and 1,4– Phenylenediamine (0.608 mmol, 0.0657 g) for the synthesis of **5** or 2,3,5,6-Tetramethyl- 1,4– Phenylenediamine (0.608

mmol, 0.1 g) for **6** were dissolved in 13 ml of DMA and then added to NTCDA solution and heated at 100 °C for 5 days. Then temperature was raised to 140 °C for one hour (to eliminate water). Then cooled to r.t., 400 ml of diethyl ether was added to precipitate the product. Then washed with diethyl ether and water. Brown solid was dried under HV at 50 °C for one day. A portion of product was heated to 180 °C for 12 hr to get rid of H_2O to yield 33% and 31.87% of **5** and **6**, respectively.

IR: 1709.31 (C=O, ν_{as}), 1670.19 (C=O, ν_s), 1329.68 (C-N, ν), 764.96 (C=O, δ), 1580.20 (naphthalene)

7 and **8** was synthesized as described. [14]

Preparation of polymer@CNT

Polymer (2 mg) was dissolved in 2 ml of solvent (Table 3) and 1 mg of 6,5-CNT was added. The resulting suspension was sonicated for 30 min in ice cold water. A homogenous dispersion of polymer@CNT with excess polymer in solution resulted.

Scanning tunneling microscopy (STM) was performed with an EasyScan II from *NanoSurf* at r.t. The measurements were made mostly at a bias of 0.050 V and 1 nA tunneling current. The STM tips were prepared from a Pt/Ir (80/20) wire of 0.25 mm diameter from *PHYWE*. Highly oriented pyrolytic graphite (HOPG) from *Mikromesh* was used as a substrate.

2-5 µl of this dispersion was spread on the HOPG substrate and dried overnight. The amount applied results in a thin layer of single CNTs on HOPG. Then the measurements were made at different positions. STM images were analyzed by using the WSxM software.

Table3: Solvent used for preparation of colloidal solution of polymer and CNT

Polymer no	Compound mg	CNT mg	Dispersing Solvent
1	1.2	0.8	H_2O
2	2.9	1.5	H_2O
3	2	1	H_2O
4	2	0.9	DMF (Fig 8 1-d) NMP(Fig 8 e-g mostly bundles)
5	2	1	DMF
6	2	1	DMF

PM7 calculations

1@CNT was modeled in the gas phase using the semi-empirical method PM7 from the MOPAC package of Stewart using GABEDIT as graphical interface. Calculations were accelerated using the keyword MOZYME. In some calculation, the SETPI command was further used. All calculated total energies stem from the mozyme calculations.

References

[1] S. M. Beladi-Mousavi, S. Sadaf, A. M. Mahmood, L. Walder, Acs Nano 2017.

[2] L. C. Cao, S. Sadaf, S. M. Beladi-Mousavi, L. Walder, Eur Polym J 2013, 49, 1923.

[3] D. T. Chen, H. R. Fetterman, A. T. Chen, W. H. Steier, L. R. Dalton, W. S. Wang, Y. Q. Shi, Appl Phys Lett 1997, 70, 3335; D. T. McQuade, A. E. Pullen, T. M. Swager, Chem Rev 2000, 100, 2537.

[4] a) J. N. Coleman, S. Curran, A. B. Dalton, A. P. Davey, B. McCarthy, W. Blau, R. C. Barklie, Phys Rev B 1998, 58, R7492; b) S. H. Lee, D. Khim, Y. Xu, J. Kim, W. T. Park, D. Y. Kim, Y. Y. Noh, Sci Rep-Uk 2015, 5; c) J. N. Coleman, S. Curran, A. B. Dalton, A. P. Davey, B. Mc Carthy, W. Blau, R. C. Barklie, Synthetic Met 1999, 102, 1174.

[5] Y. K. Kang, O. S. Lee, P. Deria, S. H. Kim, T. H. Park, D. A. Bonnell, J. G. Saven, M. J. Therien, Nano Lett 2009, 9, 1414.

[6] S. Gotovac, H. Honda, Y. Hattori, K. Takahashi, H. Kanoh, K. Kaneko, Nano Lett 2007, 7, 583.

[7] a) M. J. O'Connell, P. Boul, L. M. Ericson, C. Huffman, Y. H. Wang, E. Haroz, C. Kuper, J. Tour, K. D. Ausman, R. E. Smalley, Chem Phys Lett 2001, 342, 265; b) J. N. Coleman, M. S. Ferreira, Appl Phys Lett 2004, 84, 798.

[8] M. Giulianini, E. R. Waclawik, J. M. Bell, M. Scarselli, P. Castrucci, M. De Crescenzi, N. Motta, Polymers-Basel 2011, 3, 1433.

Part 2

Work Published in Different Articles (Applications)

Chapter 4

PolyTEMPO and Polyviologen on Carbon Nanotubes - Syntheses, Structures and Organic Battery Applications

Liangcheng Cao, Shamaila Sadaf, Sayyed Mohsen Beladi Mousavi, Lorenz Walder[*] , European Polymer Journal, 49 (8) 1923-1934 (2013)

In this chapter I present SPM results from the above mentioned publication which I co-authored. The text here is restricted to my specific contribution, i.e. structural analysis of different redox polymers on CNT and VGCF, as well as some simple modeling studies. The compound numbering starts at 1.

Abstract

The abstract concerns both, the structural appearance of the polymers on the different graphitic materials and other aspects treated in the publication but performed by my coworkers, e.g. battery performance. Scanning tunneling microscopy of semiconducting carbon nanotubes (sc-CNTs) treated with four redox active linear polymers shows throughout complex formation by helical wrapping. The compounds used are **polyTEMPO I** (poly-acetylene backbone and TEMPO side chain, new compound), **polyTEMPO II** (polymethacrylate backbone and TEMPO side chain), **polyviologen I** (main chain polyamide of diaminopropyl viologen and isophthalic acid), **polyviologen II** (main chain bipyridine dibromoxylene polymer)). Monomer subunit

resolution was achieved in case of **polyTEMPO I** and **II**. Redox activity, such as in the TEMPO and viologen polymers is claimed crucial for electrostatically driven wrapping. Complex formation was modeled with the MM+ force field. No evidence of polymer complex formation was experimentally found with metallic CNTs and with vapor grown carbon fibers (VGCF), possibly because of "charge trapping" exclusively on the semiconducting nanotubes. Composite electrodes (cathods) were prepared according to **polyTEMPO I** or **II** / VGCF and or sc-CNTs / poly-vinylidene fluoride (PVDF) and studied vs. a lithium electrode. **polyTEMPO I** has a higher theoretical capacity than the standard **polyTEMPO II** (127 and 111 mAh/g, respectively), but other specifications of **polyTEMPO I**, such as stability during cycling and potential vs. Li are inferior. The ratio of CNTs and VGCF used in the composite electrode does not influence the battery performance.

4.1. Introduction

Helical wrapping of linear polymers on single-walled carbon nanotubes (CNTs) has been observed by microscopic techniques for poly(p-phenylene-ethynylene),[47,50] poly(3-hexyl-thiophene),[15,17,51,52] poly-2,2,6,6-tetramethyl-1-piperidinyl-*N-oxide (polyTEMPO)*[53] and for DNA,[54] or just claimed e.g. for polycarbazoles,[55] and for polyfluorene,[56] from indirect evidence. Notably, these polymers can all be oxidized. The reported reduction potentials (adapted from literature for the reference electrode Ag/AgCl) are ca. 1.7 V (poly(p-phenylene-ethynylene)),[57] 0.6/1.0 V (poly-3-hexyl-thiophene),[58] 0.8V polyTEMPO,[53] 0.8 to 1.2 V (DNA),[59,60] 0.9 V (poly-carbazoles),[61] and ca. 0.9 V (polyfluorene).[62] However, the redox activity of a linear polymer has not been generally considered in literature as a condition for wrapping CNTs, and there are

examples of non-electroactive CNT-wrapping polymers, e.g. polysugars.[63,64] On the other hand, there is evidence pointing to an electron transfer that accompanies supramolecular complex formation in case of small redox active molecules interacting with CNTs. It is also expected from my results presented earlier in chapter 2 and 3 of my thesis.Thus, Kongkanand et al. have shown that one-electron reduced viologen (ca. -0.4 V) can transfer an electron onto a CNT[32], and Kim et al. reported on "environmentally stable n-doping" of semiconducting CNTs (sc-CNTs) produced by reduced viologen.[40] The latter work is interesting because the authors claim a charge driven complex formation between viologen (cationic) and CNT (negative after electron transfer), albeit without structural proof. We have recently shown, that a polymerizable oligo-viologen wraps CNTs probably prior to polymerization, possibly again following the sequence: electron transfer – complexation.[65,66] Using two polyviologens and two polyTEMPO compounds we probe in the current work the hypothesis, that redox systems with a reduction potential in the +0.5 to +1.5 V range (polyTEMPO) may (in their oxidized state) accept an electron from a CNT, and that redox systems in the -0.5 V range (polyviologen, in its reduced state) may transfer electrons to a CNT. We further hypothize that electrostatic charge interaction after electron transfer between, e.g. CNT^{n-} and $viologen^{2+}$ can assist complex formation.

4.2. Results and Discussion

4.2.1. Carbon nanotube – redox polymer complex formation

Semiconducting carbon nanotubes (sc-CNTs) show n-doping after treatment with viologens,[40] and metallic CNTs may have a beneficial effect on the kinetics of radical batteries

as reported for VGCF and graphene, because they can act as nanometer sized currents collectors.[67,68] Naked sc-CNTs (ca. 1mg) do not well disperse in 2 ml of DMF or water even under sonication. Upon addition of 2 mg of any of the polymeric redox systems, the dispersibility increases, indicating strong interaction of the polymers with the sc-CNTs. Notably, a mass ratio polymer : CNT slightly above 1:1 would be expected if the polymers wrap tightly in a monomolecular layer around the CNTs, assuming a similar arial density for the polymer and the CNT surface. Upon prolonged standing the CNTs tend to agglomerate again. DMF with its free amine content leads to partial reduction of the viologens and this may help the electrostatically driven complex formation (eq. 1-3, for reduction potentials see Table 1) to proceed.

$$\text{DMF/amine} + \text{polyviologen}^{m+} \rightarrow \text{DMF/amine}^{x+} + \text{polyviologen}^{(m-x)+} \qquad \textbf{eq. 1}$$

$$\text{CNT} + \text{polyviologen}^{(m-x)+} \rightarrow \text{CNT}^{x-} + \text{polyviologen}^{m+} \qquad \textbf{eq. 2}$$

$$\text{CNT}^{x-} + \text{polyviologen}^{m+} \rightarrow [\text{CNT}^{x-} - \text{polyviologen}^{m+}] \qquad \textbf{eq. 3}$$

This interpretation is in line with recent reports of Kongkanand[32] and Kim[40].

Interestingly, no increased dispersibility was observed for metallic CNTs in presence of any of the redox polymers (for a comparison of sc-CNTs and metallic CNTs in presence of **polyviologen I** Fig. 8).

4.2.2. STM morphology and theoretical structure

The increased dispersibility and our recent results [69] lead us to look for microscopic evidence for complex formation between polymeric TEMPO or viologen with sc-CNTs, metallic CNTs and vapour grown carbon fibers (eq. 1 – eq. 3). We have chosen STM because its

ability to resolve organic compounds on carbon nanotubes down to the molecular level. Poly-redox – CNTs were prepared as described in the exp. part. Two µl of this solution was spread on the freshly cleaved HOPG substrate and the solvent was evaporated at r.t. overnight. STM images of the CNT-polymer complexes are shown in Fig. 1 and 2. It was possible to sort out HOPG artifacts[70], or polymers decorating graphite edges of the HOPG, as well as polymer strands on HOPG without CNT core (for STM images of CNTs without polymer treatment, Fig. 7).[71]

The typical appearance of edges of graphite planes can be observed in Fig. 2 a). STM images of the **polyTEMPO I** and **II** are shown in Fig. 1, those of **polyviologen I** and **II** in Fig. 2.

In all cases (except one conformation of **polyTEMPO I** (Fig. 2, a,b)) more or less tight, helical wrapping of the polymers around the CNTs is evident. The pitch of the helical wrapping is variable, e.g. for the same **polyviologen I** tight and loose wrapping is observed (see Fig. 2 b). This can be rationalized with the theoretical model presented in section 4.2.3. It predicts for the related **polyviologen II** that the amount of negative charge per carbon on the CNT influences the pitch distances. The larger the charge density on the CNT, the smaller is the theoretical pitch for **polyviologen II**. Polymer subunits on the CNT - and especially those centered in the CNT-central region - are higher in contrast than the same polymer chains on HOPG (not shown). **PolyTEMPO I** and **II** chains do not show any start or end, i.e. terminal groups, within the STM viewing field, indicating a high degree of polymerization with $n >> 100$, considering the fact that ca. 16 subunits are needed for a complete helical turn (model, Fig. 4). **Polyviologen 1** and **2** show shorter polymer chain fragments with $n > 50$, and $8 < n < 14$ respectively (Fig. 2a-c), f-h)). The latter value was also confirmed by ^{1}H-NMR. Polymer chain lengths observed on the

CNTs are generally larger than expected from the average chain length estimated from ^{1}H-NMR, possibly because longer chains are energetically favorable complexed.

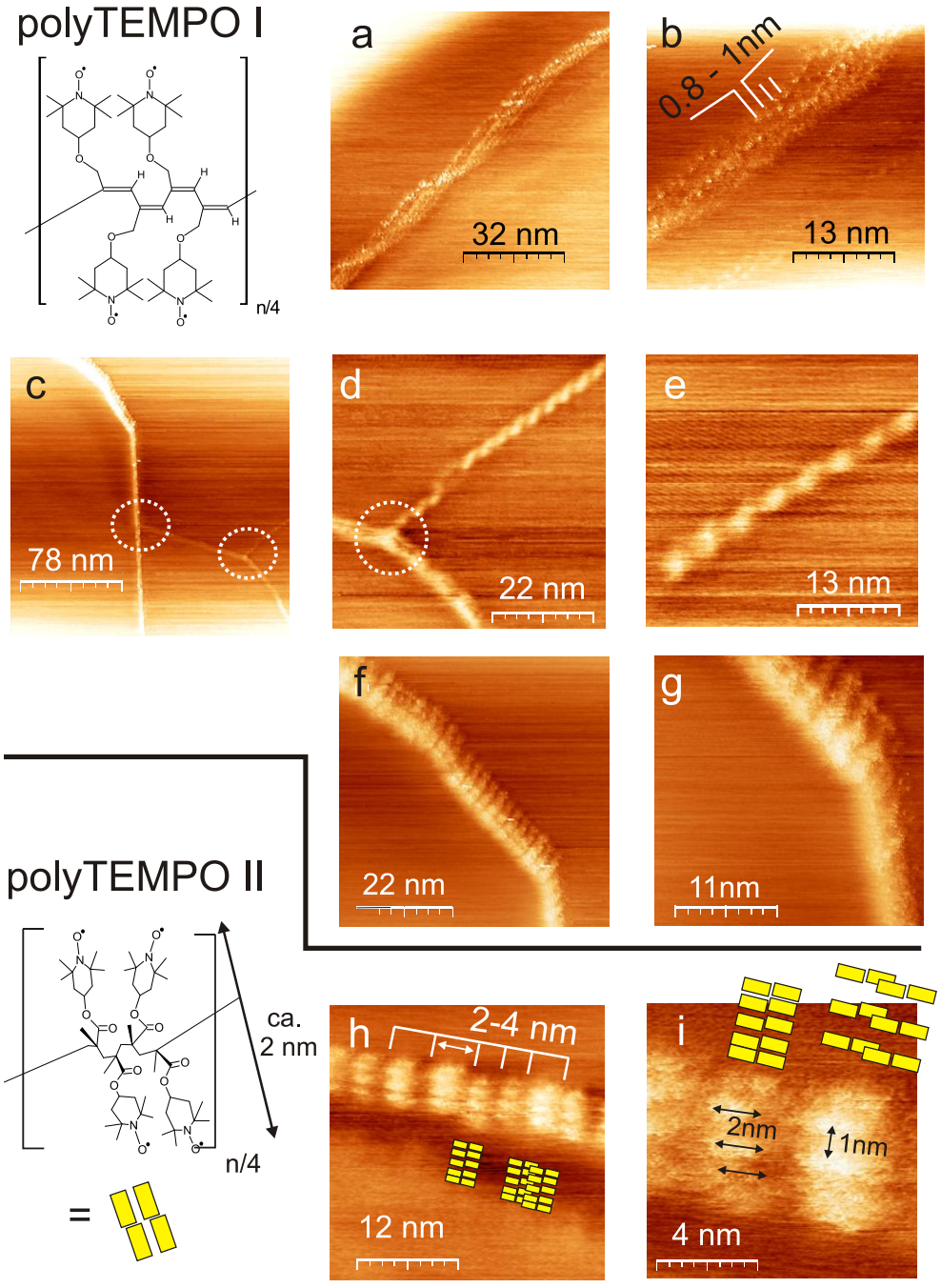

Figure 1: *STM measurements of* ***polyTEMPO I*** *(a-g) and* ***polyTEMPO II*** *(h-i) wrapped sc-SNTs at HOPG (Vtip = 50mV, I=1nA); left to right: zoom-in; a-b:* ***polyTEMPO I*** *wrapping CNTs with multiple chains and weak helical winding, with subunit distance (0.8-1 nm); (c-e)* ***polyTEMPO I*** *wrapping and interconnecting CNTs/CNT bundles (dotted circles); (f-g):* ***polyTEMPO I*** *tightly wrapping a bundle of 2-3 CNTs; (h-i):* ***polyTEMPO II*** *with helical wrapping showing subunit-pair resolution.; yellow: resolved polymer subunits.*

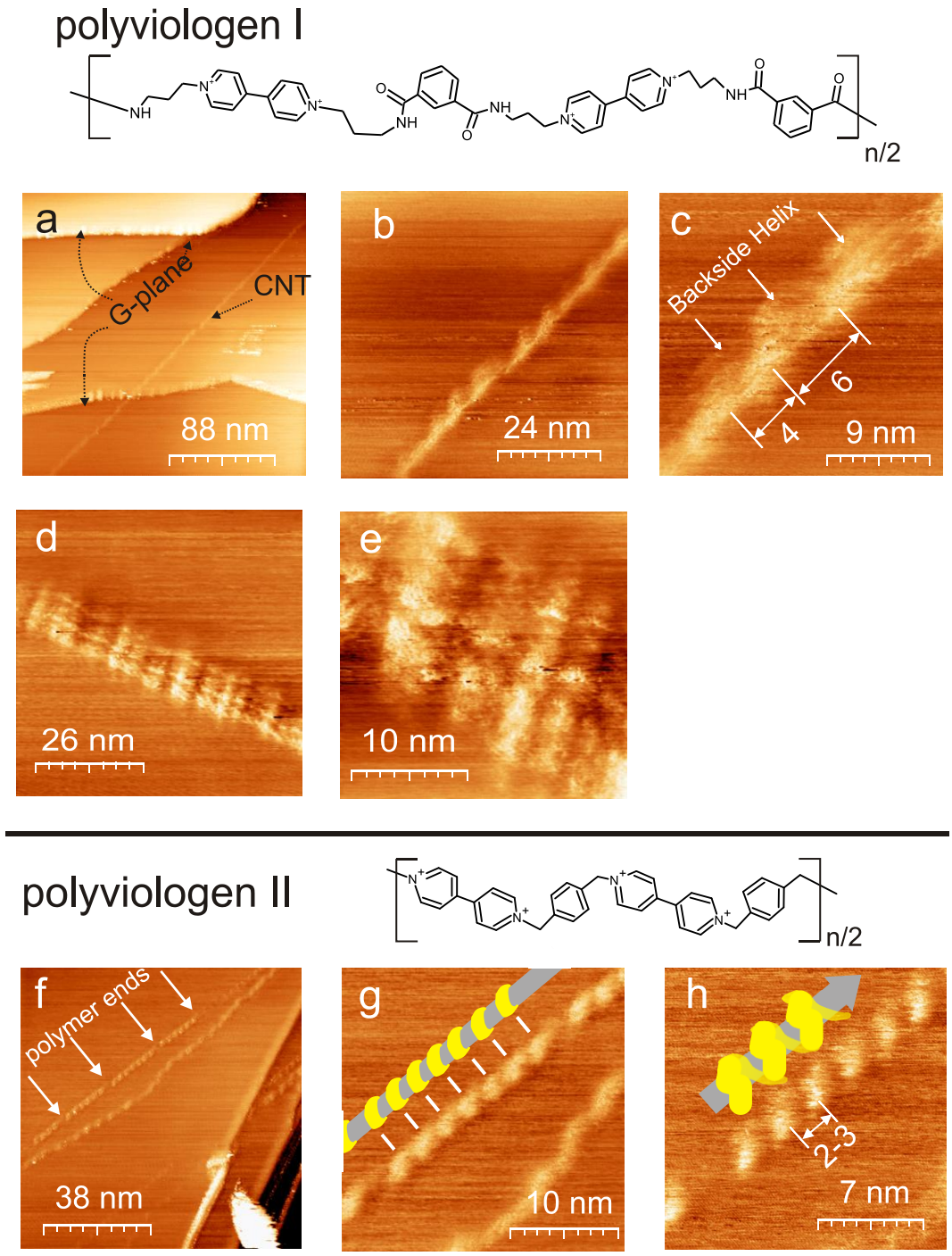

Figure 2: *STM measurements of* ***polyviologen I*** *(a-e) and* ***polyviologen II*** *(f-h) wrapped sc-CNTs at HOPG (Vtip = 50mV, I=1nA); left to right: zoom-in; a): appearance of graphite edges, (a-c)* ***polyviologen I*** *arranged in helical configuration around single CNTs with a variable pitch of 4-6nm;. (f-h):* ***polyviologen II*** *wrapped CNT with a 2-3 nm pitch; polymer length from polymer breaks recognizable.*

Polymer-related CNT-CNT-interconnections are mainly observed for the TEMPO polymers (Fig. 1 c, d)), a phenomenon that may be crucial for the current collection in redox polymer batteries. Two reasons may be invoked: The fact that the TEMPO polymers are longer than the polyviologens yielding a higher cross linking probability, and the fact that **PolyTEMPO I** can exist in a loosely bound configuration around a CNT (Fig. 1a,b) allowing free polymer segments to "look for" and bind neighboring CNTs. Another configuration is obvious: **polyTEMPO II** (Fig. 1, f,g)) and **polyviologen I** (Fig. 2 d,e) can wrap two or more CNTs helically. Typical monomer resolution can be found for **polyTEMPO II** (Fig. 1h, i). This polymethacrylate seems to arrange the TEMPO side chains in a syndiotactic manner yielding a 2 nm broad subunits consisting of 2 monomers (Fig. 1 h, i, yellow colored). The distance between the subunits is 0.7 nm according to the model (Fig. 4) and 1 nm is observed experimentally (Fig. 1 i). **PolyTEMPO I** with its more rigid polyacetylene backbone shows equidistant (0.8-1 nm) "high contrast spots" (Fig. 1 b) probably related to the N-oxide.[72] The "increased rigidity" of **polyTEMPO I** (poly-acetylene backbone) as compared to **polyTEMPO II** (polymethacrylate backbone) does not show up experimentally, i.e. no larger average pitch distance is found for **polyTEMPO I** (compare Fig. 1f) and h)). However, only **polyTEMPO I** "follows" in some images the CNT in parallel fashion. Comparative modeling of **polyTEMPO I** and **II** shows that upon decreasing the electric field of the CNT, the more rigid **polyTEMPO I** adapts parallel configuration earlier (Fig. 6). The polyviologens have their redox active group localized in and along the backbone and therefore the polymer strand is only ca. 0.7 nm thick. Both viologen polymers wrap nicely in a helical manner around the CNTs. Subunit resolution was not achieved. **Polyviologen II** shows much more strand terminations than the other 3 polymers (Fig.2 e). In contrast to the semi-conducting CNTs no wrapping was observed for the metallic

CNTs after exposition to the different polymers. The larger vapor grown carbon fibers (VGCF) are difficult to scan by STM.[73] We did observe some polymer deposition, e.g. of **polyTEMPO I** onto broken-up VGCF structures as shown in Fig. 3.

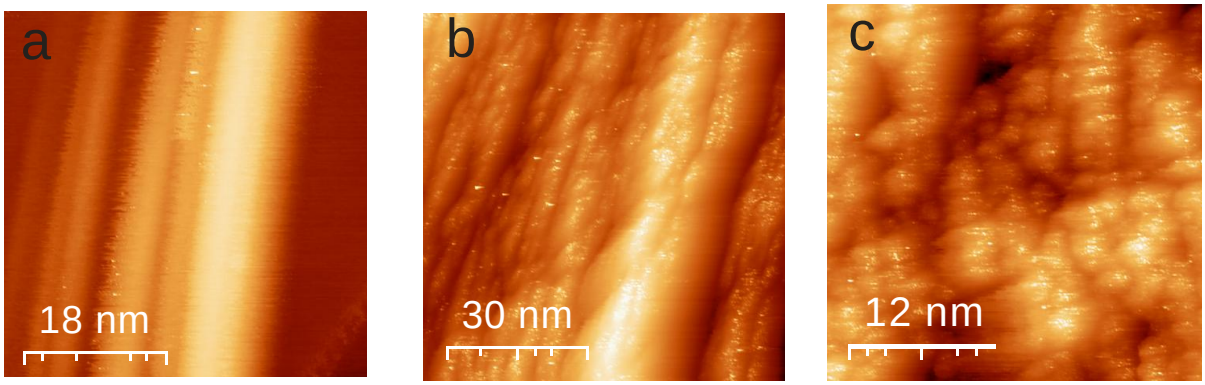

Figure 3: *STM images of vapor grown carbon fiber a) pristine, b) after contact with poly-TEMPO I, c) zoomed in portion of b.*

4.2.3. Force field modeling

The interaction between the four polymers and semiconducting carbon nanotubes (chirality 6,5) was modeled using the MM+ force field in HyperChem 8. The interaction was artificially driven by electrostatic interaction using one positive charge on each pyridinium and 0.02 to 0.2 negative charges per carbon on the 100 nm long CNT. The reasoning is that partially reduced viologens can transfer an electron onto a semiconducting CNT, allowing electrostatic interaction of thereafter (see eq. 1-3).[19] The -NO group can formally act as a reducing or oxidizing agent yielding a positively or negatively charged TEMPO, respectively. We modeled the situation with one negative charge on each nitrosyl oxygen and 0.02 to 0.2 positive charges per carbon on the CNT, i.e. a p-doped CNT.

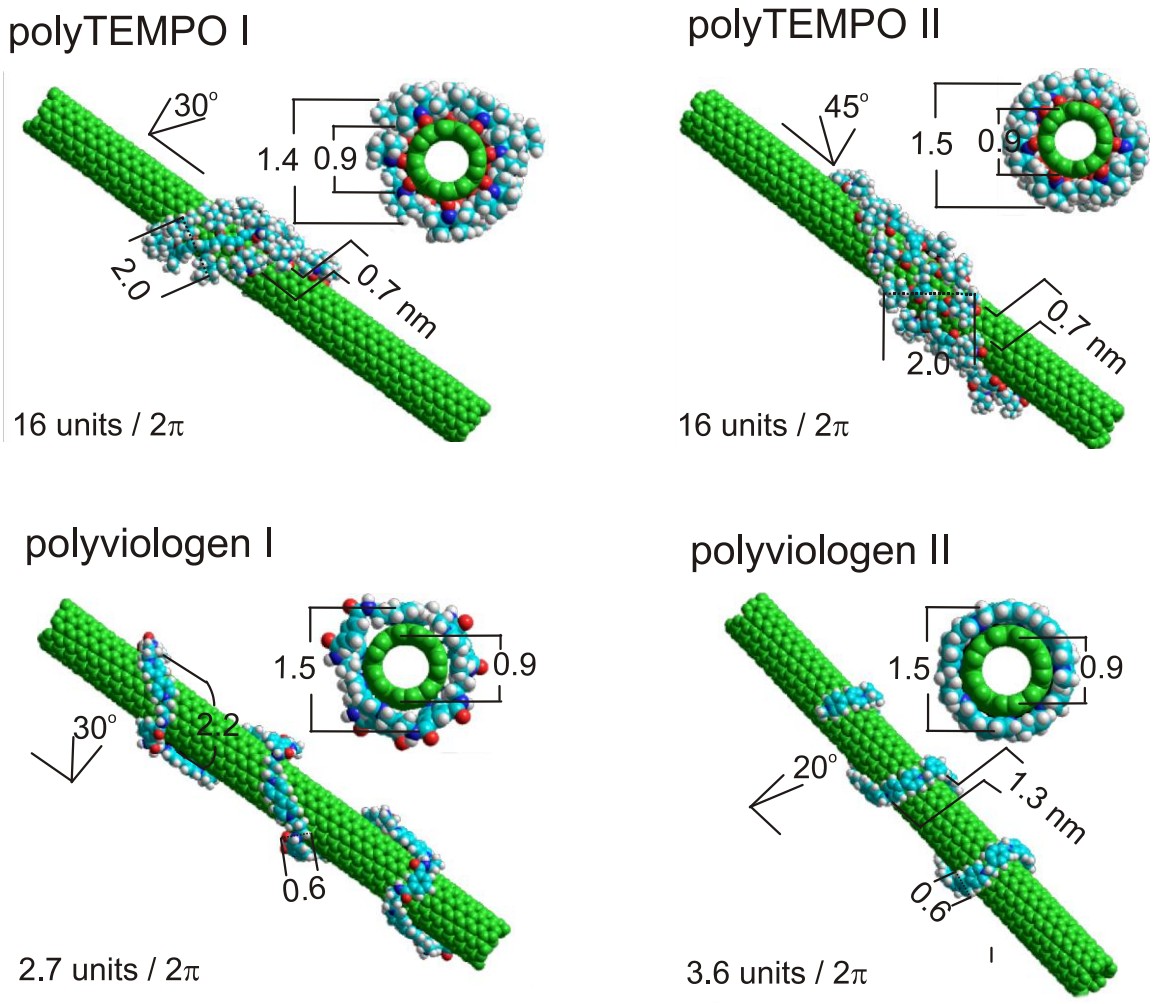

Figure 4: *MM+ Modeling of 16-mer* ***polyTEMPO I*** *(p-T I)),16-mer* ***polyTEMPO II*** *(p-T II), 8-mer* ***polyviologen I****, 8-mer* ***polyviologen II*** *on CNTs (1260 carbons). PolyTEMPOs: each -NO is -1 charged; polyviologens: each pyridinium N is +1 charged; all CNT carbons are + 0.2 or -0.2 charged, respectively. Indications without units are distances in nm.*

Under the given conditions (gas phase modeling) all polymers wrap around the CNTs if presented stretched orthogonally to the CNT at a centre-centre distance of 5 nm (Fig. 4). Oligomeric chains with 8 subunits were used as a model for the polyviologens, whereas 16 subunits were used for the polyTEMPO modeling. This takes into account the much longer backbone per subunit for the viologen as compared to the TEMPO compounds (21 C,C(N)

bonds in **polyviologen I**, 14 C,C(N) bonds in **polyviologen II**, and 2 C,C-carbon bonds in **poly TEMPO I** and **II**). The ratio 21:14:4 or ca. 5: 3.5:1 is qualitatively reflected by the number of full helical turns for the different polymers, i.e. 3:2.5:1.

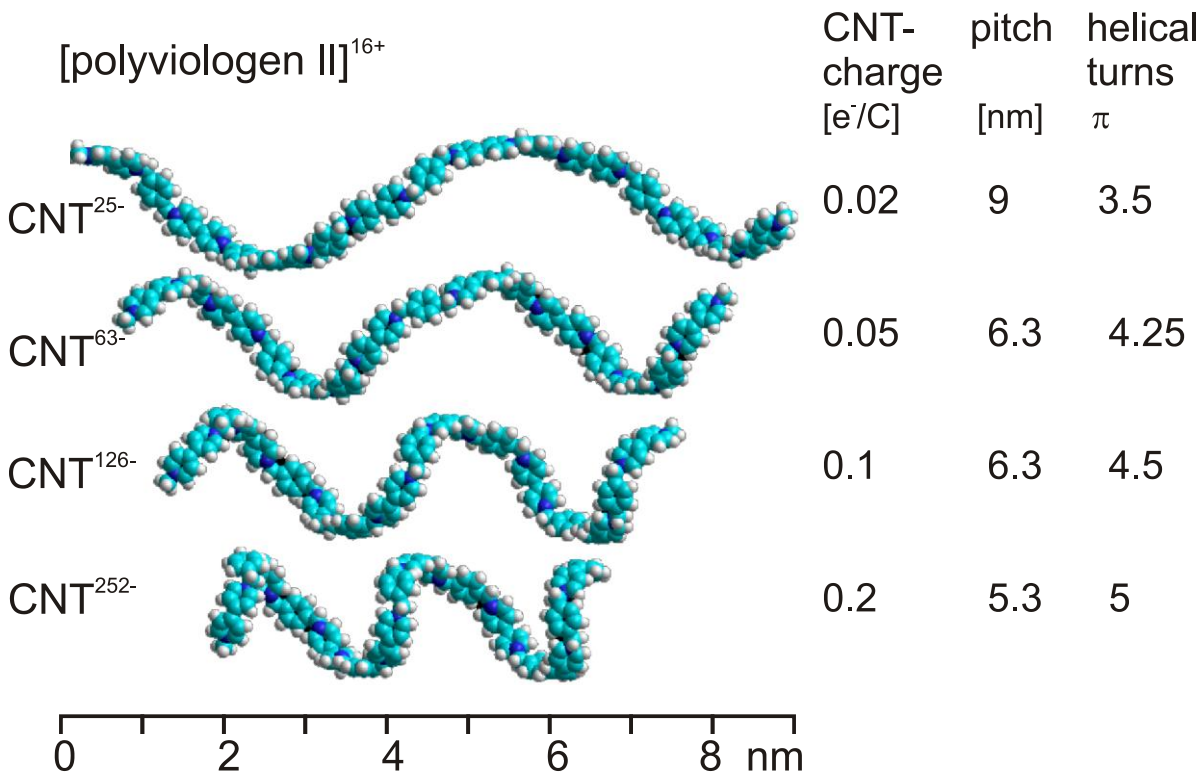

Figure 5: *MM+ optimized structures of* ***polyviologen II*** *on a CNT as a function of CNT charge; CNT structure omitted for clarity, wrapping angle given in multiples of* π *(*2π *= complete helical turn). The optimized structures at 0.1, 0.05, and 0.02* e^-/C *were found as local minima starting from the -0.2* e^-/C *situation*

The pitch of the helical turn is a function of the charge per carbon on the CNT. The smaller the charge per carbon, the larger is the observed pitch (Fig. 5). This is clearly related to the local charge compensation between polymer and CNT. If the CNT charge would be treated as mobile, i.e. as a mirror charge following the surface confined ionic charges, the observed

dependence would probably disappear. The more rigid backbone of **polyTEMPO I** as compared to **polyTEMPO II** is appearing in Fig. 6 as enhanced tendency to adapt a conformation parallel to the CNT for **polyTEMPO I**.

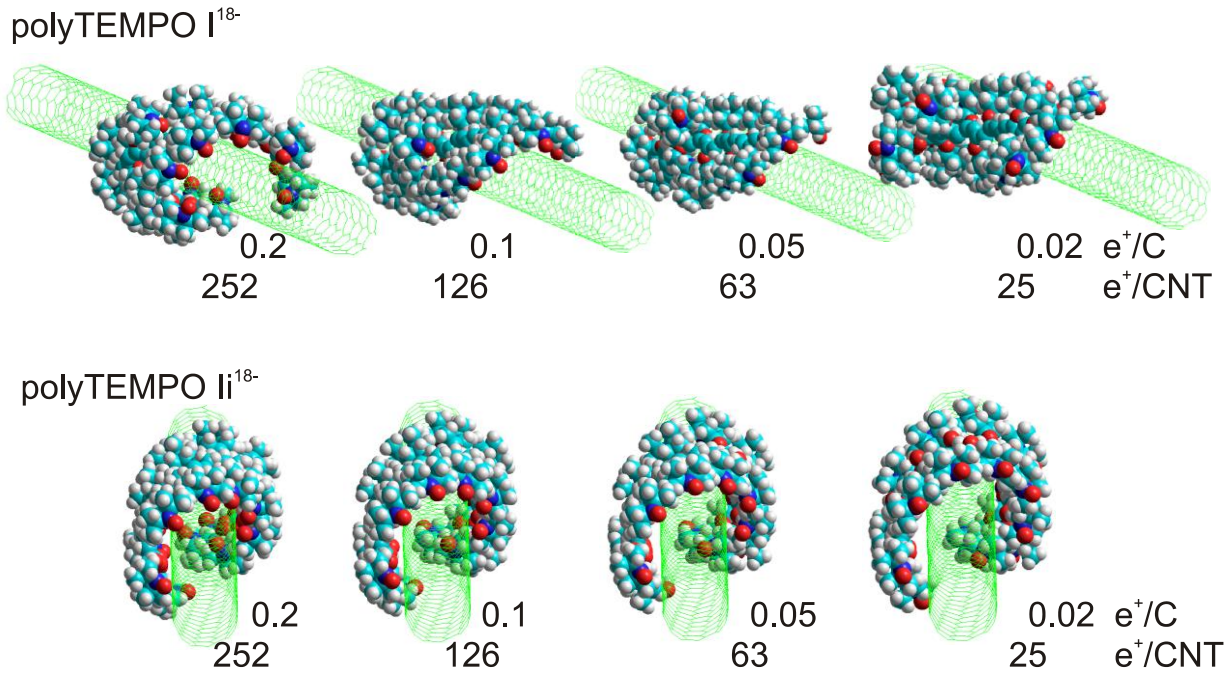

Figure 6: *MM+-optimized structures of* ***polyTEMPO I*** *and* ***II*** *as a function of CNT charge. Only the more rigid* ***polyTEMPO I*** *adapt a conformation parallel to the CNT axis upon reduction of the electrostatic field established by the CNT cylinder. The optimized structures at 0.1, 0.05, and 0.02 p^+/C were found as local minima starting from the 0.2 p^+/C situation.*

4.2.4. STM of pristine CNT and VGCF

Typical STM pictures of pristine CNT and VGCF on HOPG differ clearly from the polymer wrapped materials shown in the main text.

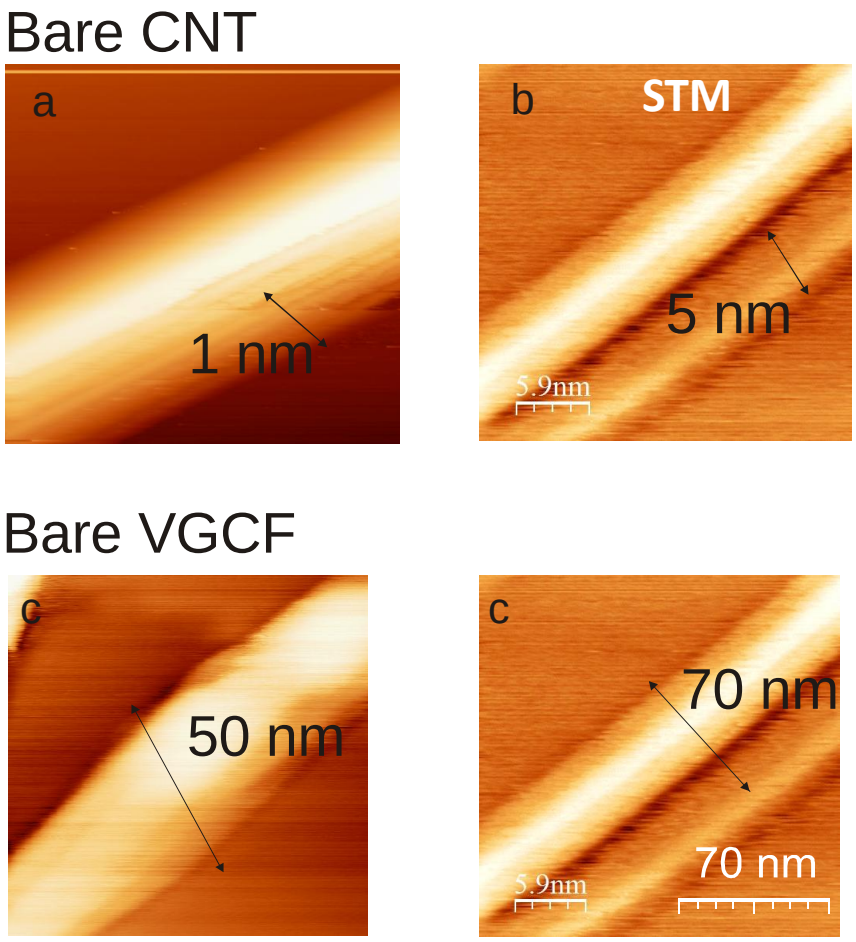

Figure 7: *Bare CNTs on HOPG (above) and bare VGCF (below), a) semi-conducting CNTs (sc-CNT Chirality: 6,5, d: 0.7 to 0.9 nm) from Sigma Aldrich, b) IoLiTec Technologies GmbH (Germany, CNT > 90%, SWNT >5 0%, OD < 2 nm, L < 20 µm) c) Vapor growing carbon fibers (VGCF) (average diameter: 150 nm from Showa Denko).*

4.3. Conclusion

Four electroactive linear polymers show all the same behavior when exposed to sc-CNTs: They wrap around the tubes in a helical manner. The model of interaction (eq. 1-3) assumes electron transfer followed by electrostatically driven complex formation. Electron transfer was clearly observed in case of **polyviologen I** from color changes. The electrostatically driven complex formation can principally be invoked for all redox active polymers, but the

HOMO and/or LUMO of the polymer has to match the band gap region of the CNT. No evidence for redox polymer wrapping was found for metallic CNTs, and VGCFs show only polymer deposition at non-intact positions. The semiconducting versus metallic character of the CNTs may be responsible: semiconducting CNTs may trap the charge, whereas metallic CNTs loose it by equilibration according to thermodynamics. The pitch distance of the helices is variable and could be related to the charge localized on the tube and an the polymer. This leads to a situation of structural optimization in a cylindrical electrical field. MM+ modeling is in line with this interpretation. Backbone stiffness tends to orientate the polymer along the CNT axis, anyhow, all the polymers described in this work wrap helically. There is just one indication presented in this work pointing to differences in backbone stiffness: polyTEMPO I with its polyacetylene type backbone shows (sometimes) a parallel arrangement with the CNT axis, whereas polyTEMPO II always wraps. The redox-polymers on the CNTs show surprising high contrast (higher than the same polymers on HOPG) pointing to a "current amplification" by the underlying CNT, a property worthwhile to be discussed on a more theoretical basis. This increased sensitivity allows the observation of the monomer subunits in the polymer chain even with simple instrumentation and under ambient conditions.

4.4. Experimental

General

All the chemicals and solvents are commercially available either from *Sigma-Aldrich* or *Alfa Aesar* and used as received without any treatment. Solvents for the electrochemistry and spectroscopy were of 99.9% purity. The 1M $LiPF_6$ in ethylencarborate/dimethylcarborate (1:1). electrolyte/solvent system used in the Swagelok cell was from *Merck*. Single walled carbon nanotubes (CNTs) with an unknown but considerable metallic content (m-CNTs) were purchased from *IoLiTec Technologies GmbH* (Germany, **CNT** >90%, **SWNT** >50%, OD <2 nm, L <20 μm), semiconducting CNTs (sc-CNT chirality: 6,5, d: 0.7 to 0.9 nm) were from *Sigma Aldrich*. Vapor growing carbon fibers (VGCF) (average diameter of 150 nm, length: 8 μm, conductivity: 10^{-4} Ω·cm), were kindly provided by *Showa Denko*. Carbon paper *SIGRACET®TF6* with a thickness of 6 mm and a electrical resistivity < 10 Ω·mm, was a gift from *SGL group.*

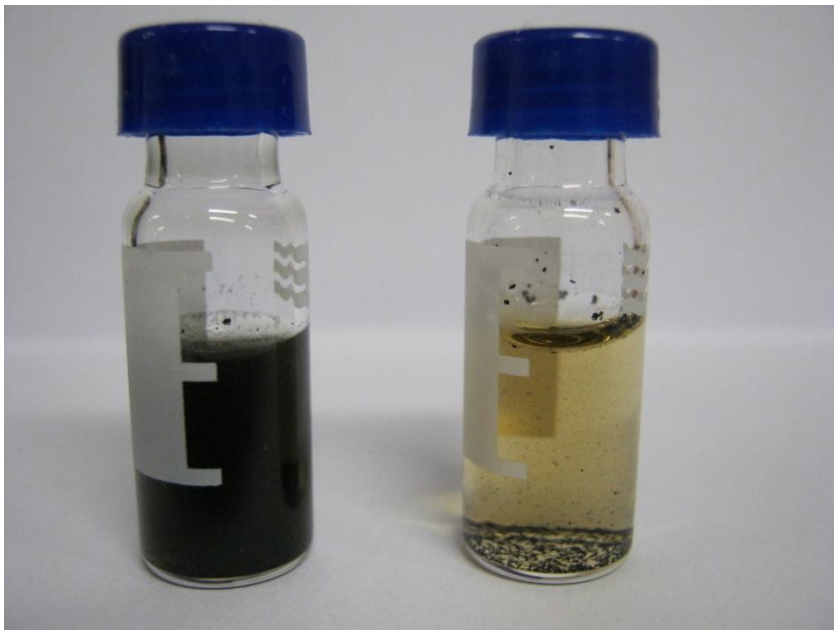

Figure 8: *Poly-viologen I in presence of sc-CNTs (left) and metallic CNTs (righ) after 30 minutes ultrsonification.*

Analytical methods

STM imaging

It was performed on an EasyScan *Nanosurf* (Switzerland) instrument at room temperature using typically 0.050 V bias voltages and 1.000 nA tunneling current. The STM tips were cut from Pt/Ir wire (0.25 mm, *Schaefer Technologie GmbH,* Langen, Germany), the substrate was a HOPG 5*5 mm piece from *Schaefer Technology GmbH*. STM sample preparation: The electroactive polymer (2mg) was dissolved in 2 ml DMF (polyTEMPO) or water (polyviologen) and 1 mg of sc-CNT was added. The solution was sonicated for 30 min in order to disperse the CNTs. Ca. 2 µl of the solution was spread on the freshly cleaved graphite substrate. The solvent was evaporated at r.t. overnight.

AFM measurements

This measurement were recorded in wave mode on a *Quesant Instrument Corp*. model Q250 (serial no.: 826011), using NSC16 type tips.

Modeling

MM+ using electrostatic interaction without cutoff. The 6,5 CNT (length: 100 nm) was constructed with Nanotube Modeler @JCrystalSoft, 2005 and imported in HyperChem™, Hypercube, Inc. Florida. The octameric TEMPO I, II and the octameric viologen I and II were constructed in chemscetch and imported in Hyperchem. Each pyridinium N was charged with one positive charge, each -NO was charged with one negative charge, each nanotube carbon was charged with 0.02 to 0.2 negative or positive charges, respectively.

References

[1] Y. K. Kang, O. S. Lee, P. Deria, S. H. Kim, T. H. Park, D. A. Bonnell, J. G. Saven, M. J. Therien, Nano Letters 2009, 9, 1414; N. A. Rice, K. Soper, N. Z. Zhou, E. Merschrod, Y. M. Zhao, Chemical Communications 2006, 4937.

[2] M. Giulianini, E. R. Waclawik, J. M. Bell, M. Scarselli, P. Castrucci, M. D. Crescenzi, N. Motta, Polymers 2011, 3, 1433; M. Giulianini, E. R. Waclawik, J. M. Bell, M. De Crescenzi, P. Castrucci, M. Scarselli, N. Motta, Applied Physics Letters 2009, 95; M. Giulianini, E. R. Waclawik, J. M. Bell, N. Motta, Applied Physics Letters 2009, 94; R. G. S. Goh, N. Motta, J. M. Bell, E. R. Waclawik, Applied Physics Letters 2006, 88.

[3] W. Choi, S. Ohtani, K. Oyaizu, H. Nishide, K. E. Geckeler, Advanced Materials 2011, 23, 4440.

[4] J. F. Campbell, I. Tessmer, H. H. Thorp, D. A. Erie, J. Am. Chem. Soc. 2008, 130, 10648.

[5] F. A. Lemasson, T. Strunk, P. Gerstel, F. Hennrich, S. Lebedkin, C. Barner-Kowollik, W. Wenzel, M. M. Kappes, M. Mayor, J. Am. Chem. Soc. 2011, 133, 652.

[6] F. M. Chen, B. Wang, Y. Chen, L. J. Li, Nano Letters 2007, 7, 3013.

[7] Q. Liu, J. Mao, Z. F. Liu, N. Zhang, Y. Wang, L. Y. Yang, S. G. Yin, Y. S. Chen, Nanotechnology 2008, 19.

[8] M. Trznadel, A. Pron, M. Zagorska, Macromolecules 1998, 31, 5051.

[9] E. P. Randviir, C. E. Banks, Rsc Advances 2012, 2, 5800; A. M. O. Brett, S. H. P. Serrano, Journal of the Brazilian Chemical Society 1995, 6, 97.

[10] M. Ates, A. S. Sarac, C. M. Turhan, N. E. Ayaz, Fibers and Polymers 2009, 10, 46.

[11] X. Xu, H. Chen, E. F. Huo, X. R. Cai, Y. Li, Q. Jiang, Polymer Bulletin 2008, 60, 7.

[12] M. Numata, M. Asai, K. Kaneko, A. H. Bae, T. Hasegawa, K. Sakurai, S. Shinkai, J Am Chem Soc 2005, 127, 5875; Y. Liu, P. Liang, H. Y. Zhang, D. S. Guo, Small 2006, 2, 874.

[13] A. Kongkanand, P. V. Kamat, Journal of Physical Chemistry C 2007, 111, 9012.

[14] S. M. Kim, J. H. Jang, K. K. Kim, H. K. Park, J. J. Bae, W. J. Yu, I. H. Lee, G. Kim, D. D. Loc, U. J. Kim, E. H. Lee, H. J. Shin, J. Y. Choi, Y. H. Lee, J. Am. Chem. Soc. 2009, 131, 5010.

[15] V. A. Constantin, L. C. Cao, S. Sadaf, L. Walder, Physica Status Solidi B-Basic Solid State Physics 2012, 249, 2395; V.-A. Constantin, D. Bongard, L. Walder, European Journal of Organic Chemistry 2012, 2012, 913.

[16] W. Guo, Y. X. Yin, S. Xin, Y. G. Guo, L. J. Wan, Energy & Environmental Science 2012, 5, 5221; N. Chikushi, H. Yamada, K. Oyaizu, H. Nishide, Science China Chemistry 2012, 55, 822.

[17] V. A. Constantin, L. Cao, S. Sadaf, L. Walder, Phys. Status Solidi B 2012.

[18] H. P. Chang, A. J. Bard, Langmuir 1991, 7, 1143.

[19] J. Kim, Pure Appl. Chem. 2002, 74, 2031.

[20] I. Swart, L. Gross, P. Liljeroth, Chemical Communications 2011, 47, 9011.

[21] J. I. Paredes, A. Martinez-Alonso, J. M. D. Tascon, Carbon 2001, 39, 1575.

Chapter 5

STM and EC-AFM of Graphene oxide and Redox Polymers for Organic Batteries Application

Introduction

In this chapter I present published results which I co-authored. It is restricted to my specific contribution, i.e. the morphology of cathodic poly-ferrocene and anodic poly-viologens. Interesting questions were: Can the energy materials be imaged on the molecular or submolecular level? How does the energy material change their structure upon reduction/oxidation or upon electrochemical transformation of graphene oxide to reduced graphene oxide? Can the flow of ions and solvent into the battery material be imaged?
These questions can partially be solved by STM; others need a combination of AFM and electrochemistry.

To understand, develop, and optimize battery materials is the capability to decode individual mechanisms responsible for battery functionality including ion movement, electron transport and electrochemical kinetics locally, at the level of particle assemblies, sub-micrometer particles and ultimately, at the nanometer scale of individual structural and morphological defects. Significant progress in this direction has been achieved with optical and micro-Raman imaging of battery materials that provide information on local chemical composition and lithiation state in lithium batteries.[74] However, the spatial resolution of optical methods is generally limited to

0.3–1 μm level precluding the studies of energy materials below single-grain level. Furthermore, the information on, e.g., electrostatic potential distributions and local current densities is generally not accessible, thus, yielding only one of many aspects of battery functionality and operations. Combined AFM techniques as well as STM have recently been applied to tackle these questions.[6] The SPM methods provide detailed information on the atomic and mesoscopic structure and morphology of solid-liquid interfaces, kinetics and thermodynamics of interfacial processes. At the same time, particularly of interest for battery applications are phenomena within the solid materials including local electronic, ionic transport and electrochemical reactivity. The development of surface-structure-sensitive techniques in recent years has led to in situ electrochemical atomic force microscopy (EC-AFM), which has made possible the detailed studies of the surface chemistry, morphology, 3D structure, electrochemical response, and performance of battery electrodes.

So far, In situ AFM has been used to study mostly the surface morphology of Li ion electrodes [29,75] and co-intercalation of solvent for lithium batteries.[76]

This chapter deals with the content of two publications which I am going to describe here.

Poly(vinylferrocene) - Reduced Graphene Oxide as a High Power / High Capacity Cathodic Battery Material

Seyyed Mohsen Beladi-Mousavi, Shamaila Sadaf, Lorenz Walder [*], Markus Gallei, Christian Rüttiger, Siegfried Eigler, Christian E. Halbig,

Advanced Energy Materials, 6, 2016, 1600108

The structure of poly(vinyl ferrocene) was studied as thin polymer layer on GC (Fig. 1, b,b',c,c') it is compared to the structure of GO@GC(Fig. 1, a, a'). Pure GO@GC (a and a') shows long range architectures of folded/wrinkled GO platelets/GO sheets with distinct folds over several µm (broken curve), extended surfaces (broken line square) and >50 nm deep holes/tunnels (broken circle). Pure ($PVFc^{x+} \cdot xNO_3^-$)@GC (b and b') consisting of average 57 PVFc subunits shows overlaid oval shapes with smallest resolvable lengths of ca. 60*40 nm (limit of lateral resolution of the AFM tip, broken square) and smallest heights of 2-3 nm.

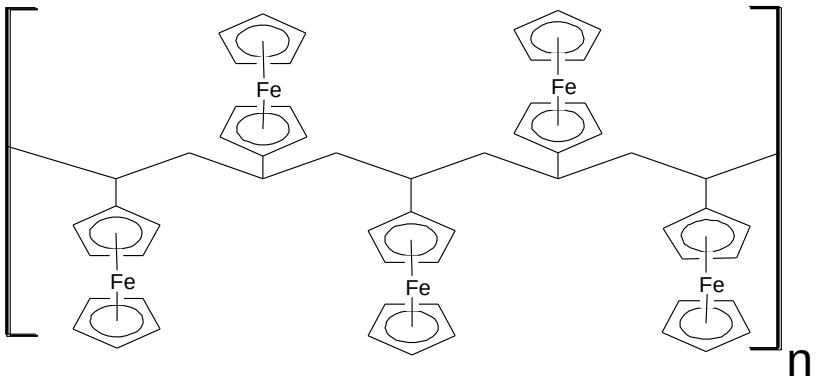

Semiempirical PM7 geometry optimization predicts a curved cylindrical shape for a hexadecameric PVFc with 1.6 nm diameter and 3.4 nm length, i.e. a length of 12 nm for the

polymer in use with 57 average subunits (see d in Fig. 1). We observe some tendency for chain formation of the globuli by lateral stacking (broken curves without principal direction).

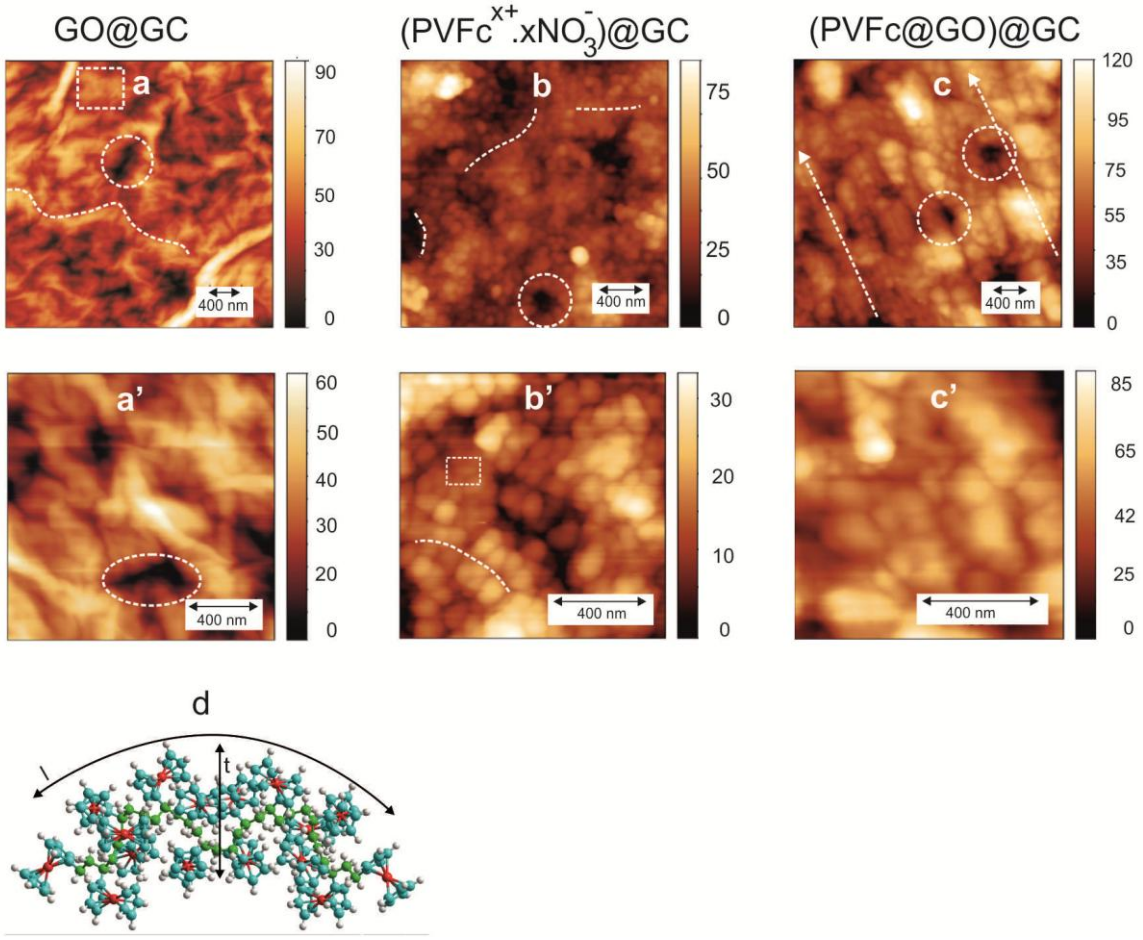

Figure 1: *AFM images of ca. 500nm thick layers of ca. 20 µg cm^{-2} GO@GC (a, a'), of > 12 µg cm^{-2} (PVFc^{x+}· xNO$_3^-$)@GC (b, b') and of ca. 14.7 µg cm^{-2} (PVFc@GO)@GC (mass ratio PVFc^{x+} / GO^{m-}= 1) (c, c'), scan lengths: ca. 3µm (a-c) and ca. 1 µm (a'-c'); pure GO@GC (a and a'): long range architectures of folded/wrinkled GO platelets/GO sheets with distinct folds over several µm (broken curve), extended surfaces (broken line square) and >50 nm deep holes/tunnels (broken circle); pure (PVFc^{x+}· xNO$_3$)@GC (b and b', average PVFc subunits: 57): smallest resolvable lengths of ca. 60*40 nm (broken square, limit of lateral resolution of the AFM tip, broken square) and smallest heights of 2-3 nm; chain formation of the globuli by (broken curves) and tunnels from circular/cylindrical aggregation of the globuli (broken circles); (PVFc@GO)@GC (c,c') with principal direction of the PVFc globuli (c), (broken arrows) and cylindrical mesopores (broken circles); d) PM7-optimized structure of an uncharged 16mer PVFc oligomer (green atoms: backbone carbons) showing a thickness (t) of ca. 1.6 nm and a length (l) of ca. 3.4 nm.*

Furthermore, the formation of tunnels by circular/cylindrical aggregation of the globuli (broken circles) is observed. Most interesting is the AFM of (PVFc@GO)@GC (c,c' in Fig. 1). The low weight ratio of PVfc / GO=1 used for the composite preparation allows to see some features of the specific interaction. Most obvious is a principal direction of the PVFc globuli over several µm (c, broken arrows). Such parallel long range arrangement is not observed in the AFM image of the pure polymer without GO, nor with GO without PVFc. We interpret these lines as a result of PVFc decorated GO sheets which have been flattened and parallel stacked during the process of complex formation and drying, respectively. In addition, we observe again cylindrical mesopores (broken circles). In conclusion, the AFM images indicate an ion percolating structure, which may also become electron percolating after GO/rGO transformation.

We have observed ion breathing of PVFc@GO as a reversible oscillation of the polymer height using electrochemical atomic force microscopy (**Fig. 2**). Instead of a linear potential scan as in the EQCM experiment, a square wave potential (0→+0.8→0→ ....) with 30 s step time was applied to the working electrode (PVFc@rGO)@$_n$GC. Thus, during complete picture acquisition which takes 400 s, 13 potential switches (30 s) of the redox state of the whole PVFc composite have occurred, and the 13 stripes in the final AFM image reflect the two states (dark: down, light: up). As seen from the amperometric current spikes, and from the sharp height transitions in the AFM image, the response is in the range of a second. The average height of the reduced $PVFc^0$ composite above the scratched GC area (left) is 223 nm, and 256 nm for the oxidized $PVFc^+$ composite yielding 33 nm average height breathing, i.e. 13 % of the (PVFc@rGO)@$_n$GC height.

The prior GO/rGO electrocatalytic transformation was also studied by electrochemical AFM (Fig. 3). A decrease of the composite height from 560 to 517 nm, i.e. 7.7 % was observed.

It is interesting to compare mass changes from EQCM with the corresponding height changes obtained from EC-AFM. Thus, for the irreversible GO/rGO transition we observed 7.6 % total mass reduction and 7.7% total height decrease, whereas for the reversible ClO_4 ion breathing we observed 42% mass increase upon oxidation accompanied by only 13 % total height increase. From the AFM analyses in the x-y plane we see in both cases that typical topographic features do not leave the observed sector, but pores undergo changes in diameter and connectivity.

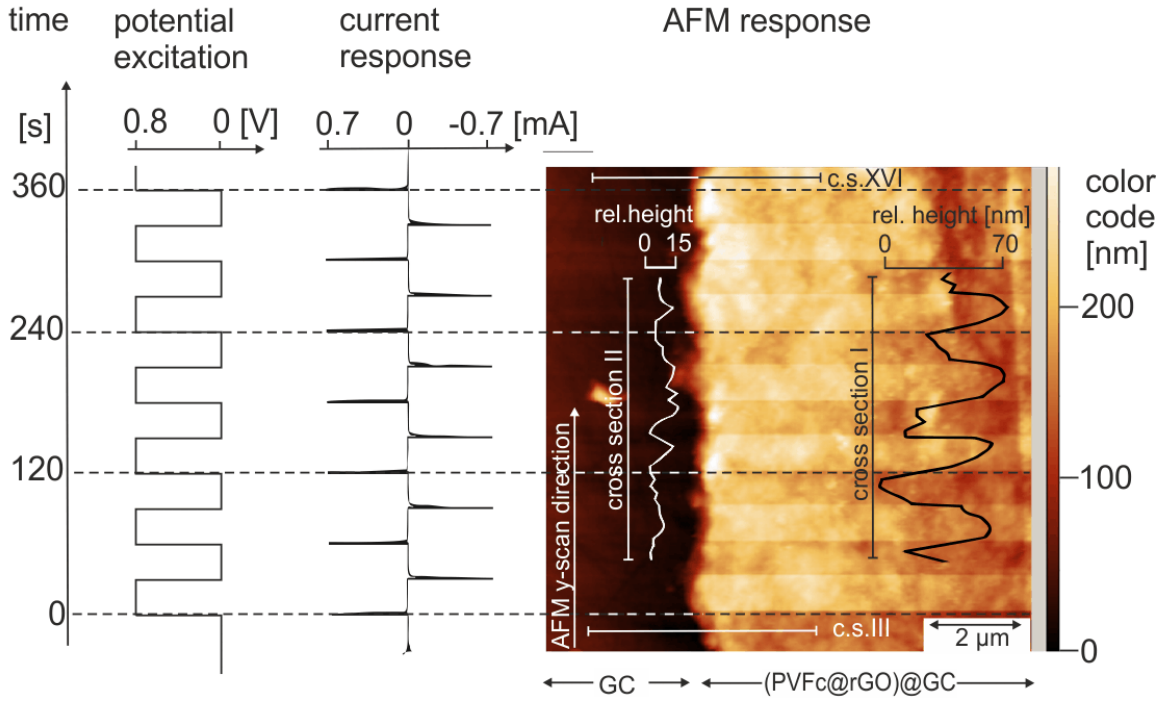

Figure 2: *Electrochemical redox switching of (PVFc@rGO)@GC during AFM image acquisition. Electrochemistry: electrolyte: 0.1 M $LiClO_4/H_2O$, excitation: square wave potential: 0→+0.8→0→ .... (13 steps with 30 s step time), current response (chronoamperometric): anodic (positive current (left)) and cathodic spikes.AFM image: (PVFc@rGO)@GC (0.95µg PVFc@rGO with weight ratio PVFcx+ / GOm-=4.4) on 0.07 cm2 GC corresponding to $\Gamma_{PVFc} = 5.7*10^{-8}$ mol cm^{-2}; left part of image: GC (PVFc@rGO scratched away), AFM scan direction upwards, total AFM acquisition time: 400s, 13 potential steps during AFM acquisition correlate with 13 stripes (dark/light) in the composite covered region but not in the scratched region (vertical cross section I and II in y-direction): typical height increase upon oxidation: 20 to 60 nm; averaged height change: 14 % (see Fig 3).*

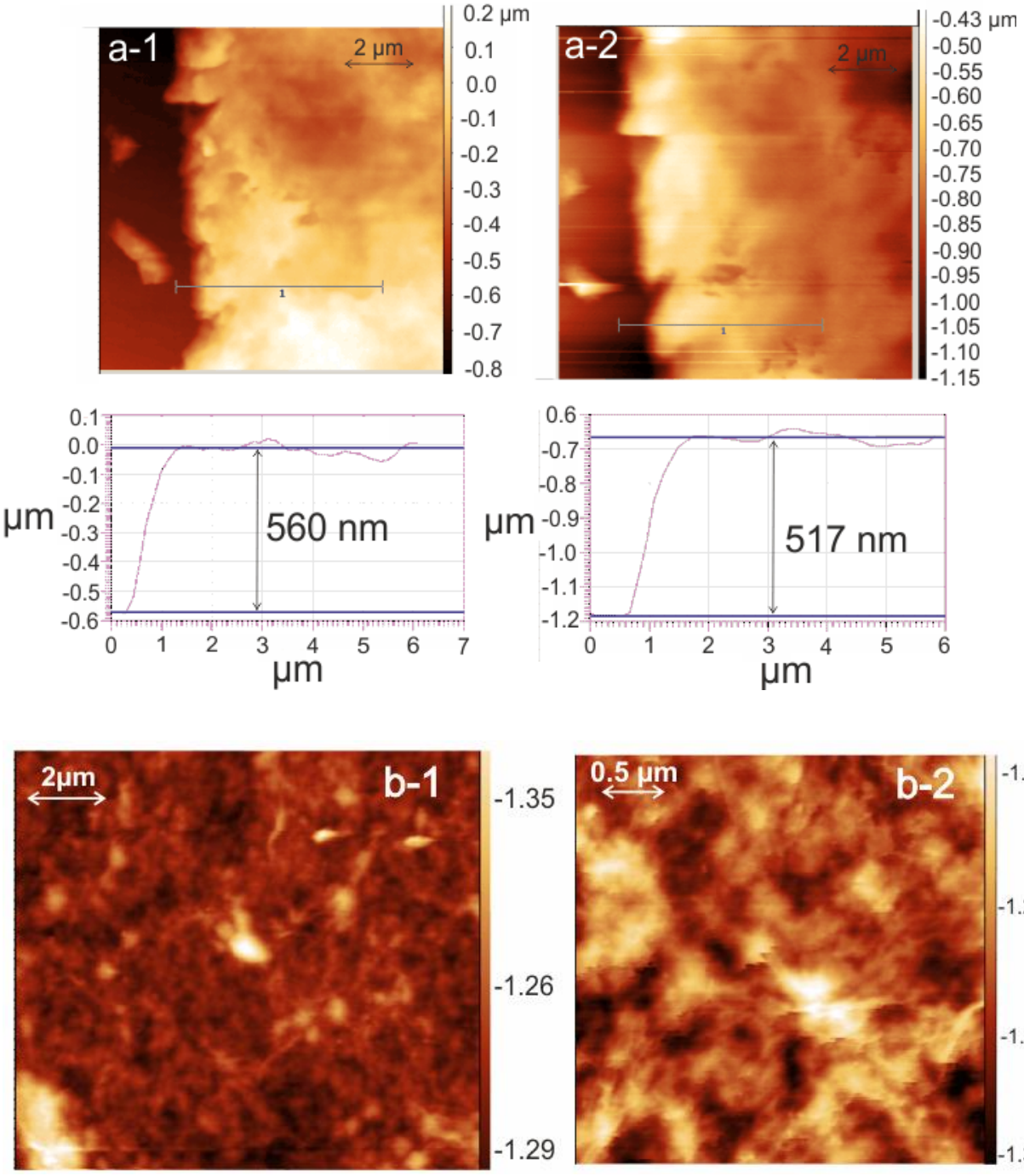

Figure 3: **GO/rGO transformation** *a) Electrochemical AFM analyses of the same region before (a-1) (PVFc@GO)@GC and after (a-2) (PVFc@rGO)@GC) GO/rGO transition, both measured under potential = 0 V in aqueous 0.1M LiClO4/4mM MV; arbitrarily selected cross sections at the same place indicate a decrease of height between the GC plane (left) and the composite top from 560 to 517 nm due to the GO/rGO transition. b) AFM images of (PVFc@rGO)@GC in the dry state with scan length of ca. 10.5 µm (b-1) and scan length of 3.3 µm (b-2). Mesoporous morphology throughout the composite film is observed.*

High Performance – Poly(viologen)–Graphene Nanocomposite Battery Materials with Puff Paste Architecture

S. Mohsen Beladi-Mousavi, Shamaila Sadaf, Arsalan Mado Mahmood, Lorenz Walder[*],

ACS Nano, doi:10.1021/acsnano.7b02310 (2017)

Structural characterization

This publication concerns the following poly-viologen, abbreviated as PV1.

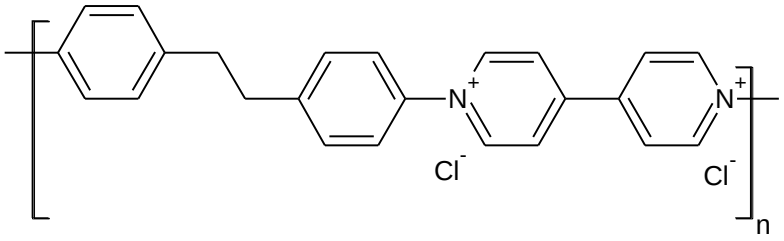

The colloidal solution of PV1@GO with a PV1/GO ratio = 3 (zeta potential = 38 mV) was drop casted and dried on a CC (current collector). Depending on the desired thickness, this step was repeated several times, yielding surface-modified electrodes (PV1@GO)@CC. The AFM images of GO@GC (Fig. 4a) show long range architectures of folded/wrinkled GO platelets/GO sheets with distinct folds over several μm (broken curve), extended surfaces (broken line square) and > 50 nm deep holes/tunnels (broken circle).[5] PV1@GC (Fig. 4b) shows several overlaid racetracks of ca. 7×120 nm (limit of lateral resolution of the AFM tip), and parallel lines.

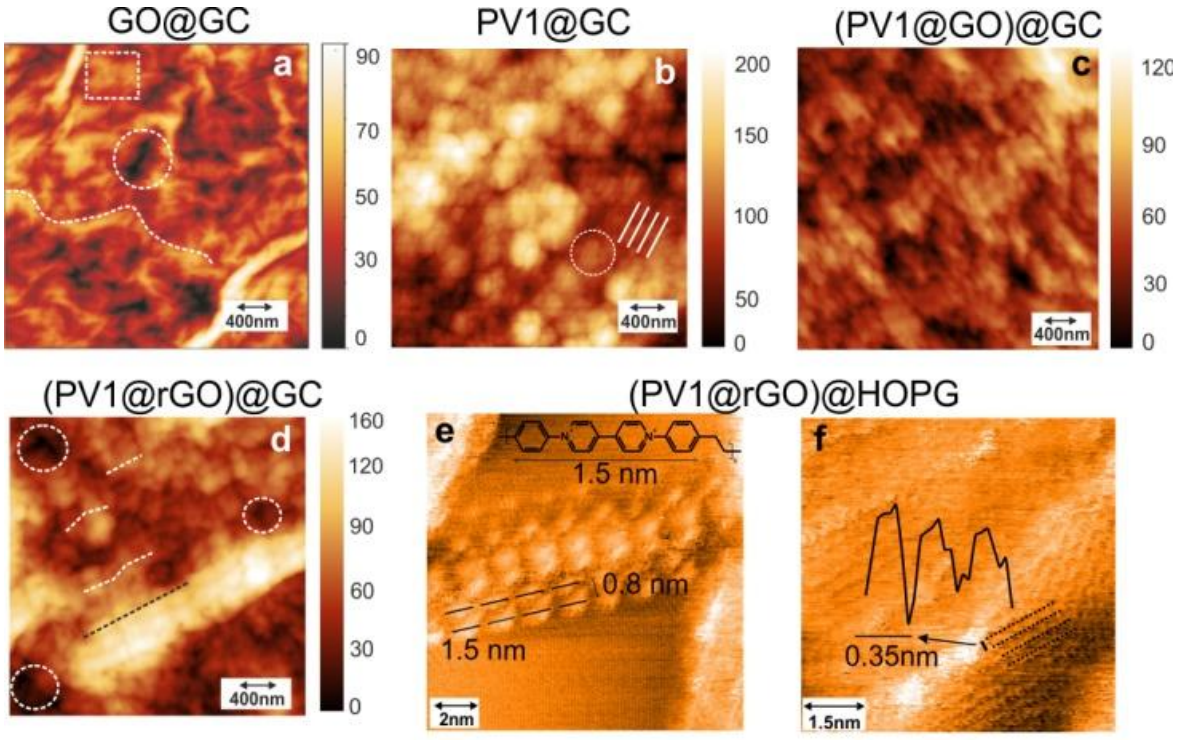

Figure 4: Structural characterization. *(a) GO@GC, 20 µg cm^{-2}: long range architectures of folded/wrinkled GO platelets/GO sheets with distinct folds over several µm (broken curve), extended surfaces (broken line square) and > 50 nm deep holes/tunnels (broken circle).*[5] *(b) PV1@GC, ~5 µg cm^{-2}: average PV1 subunits (n): 4 < n < 10 ca. 70%, n >> 10 ca. 30%.): racetrack oval shapes (white lines) with length of ~300 ± 50 nm and with thinnest width of ~7 nm; aggregated cylinder chains forms tunnels with length of 50-200 nm. (c) (PV1@GO)@GC, PV1/GO = 3, 5 µg cm^{-2}: overlaid racetrack oval shapes patterned by the GO sheets. (d) (PV1@rGO)@GC, PV1/rGO = 5.7, 10 µg cm^{-2}: polymers are patterned by rGO sheets. AFM images are from ca. 500 nm thick layers. Zoomed in AFM images of "a-d" in Fig. 5. (e) Scanning tunneling microscopy (STM) of (PV1@rGO)@HOPG, 2.8×10^{-10} mol polymer subunit cm^{-2}: polymer chains are lying on a rGO sheet, black lines are representing each subunit of PV1 (inset, length: 1.5 nm). (f) STM images of stacks of rGO sheets with measured distance of 0.35 nm; the profile of 3 stacks is shown.*

High resolution STM, albeit after the GO/rGO transformation (see later), exhibits 2d crystallinity of laterally stacked PV1 on rGO with inter chain distance of ~0.8 nm (Fig. 4e), but partially clustered strands with ~5 nm diameter are also observed, similar to the racetrack structures in AFM. The 2d crystalline region of PV1 on rGO reveals single pyridinium resolution and a high degree of parallel arrangement (Fig. 4e-f).

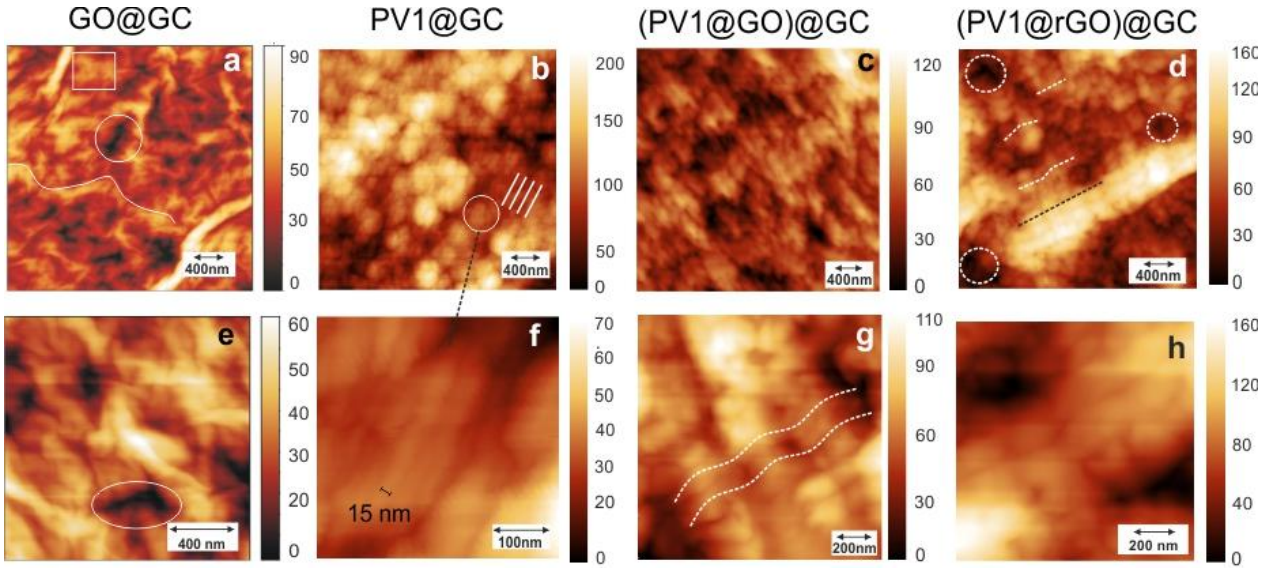

Figure 5: Zoomed in AFM images of GO, PV1 and composites. *AFM images of ca. 500 nm thick layers of ca. 20 µg cm^{-2} GO@GC (**a, e**), of ~5 µg cm^{-2} PV1@GC (**b, f**), of 5 µg (PV1@GO)@GC (mass ratio PV1@GO = 3) (**c, g**) and of ca. 10 µg cm^{-2} (PV1@rGO)@GC (mass ratio PV1 /rGO = 5.7) (**d, h**), scan lengths: ca. 3µm (a-d, form Fig. 4 in the main text) and ca. 1 µm (e-h).*

The AFM of (PV1@GO)@GC (c in Fig. 4) shows deposition of polymers on the surface of GO with the same lateral stacking; however a patterning from folded/wrinkled GO sheets over several µm are clearly observed. The AFM images of (PV1@GO)@GC (Fig. 4c) shows > 50 nm holes, indicating an ion percolating structure, which may also become electron percolating after GO/rGO transformation. Zoomed in images of Fig. 4 a-d are shown in Fig. 5.

An electrochemical AFM (EC-AFM) study showed that the irreversible mass loss is accompanied by ~13% height decrease of the composite (533 to 466 nm) Fig. 6, arbitrarily selected cross sections at the same place indicate a decrease of height between the GC plane (right) and the composite top (left) from 588, 450 and 563 (a´ – c´) to 517, 379 and 504 nm (a´ – c´), due to the GO / rGO transition. The reduction results to average height change from 533 to 466 nm, which attribute to 12.6% decrease in initial height.

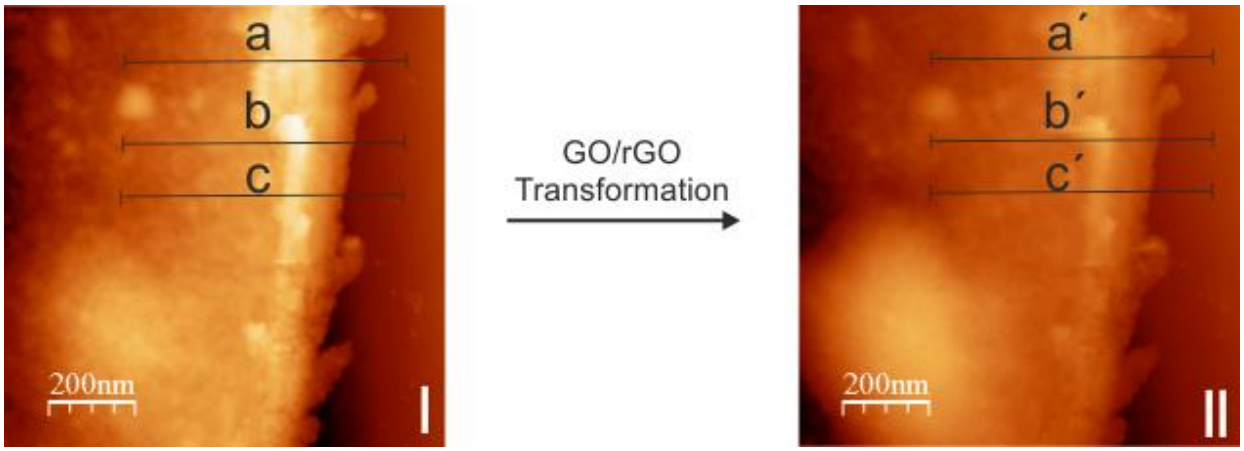

***Figure 6: GO/rGO transformation**, Electrochemical AFM images of (PV1@GO)@GC (I) and (PV1@rGO)@GC (II) captured from a same region before (I) and after (II) GO / rGO transformation. Both analysis measured under a constant potential = 0 V in 0.1 M KCl/H_2O.*

This is in good agreement with STM images which reveal stacks of rGO with sheet distances of ~0.35 nm (Fig. 4f and Fig. 7e). A detailed STM study showed crystallinity of the polymer chains, which tightly wrap single or platelet of rGO sheets (Fig. 7).

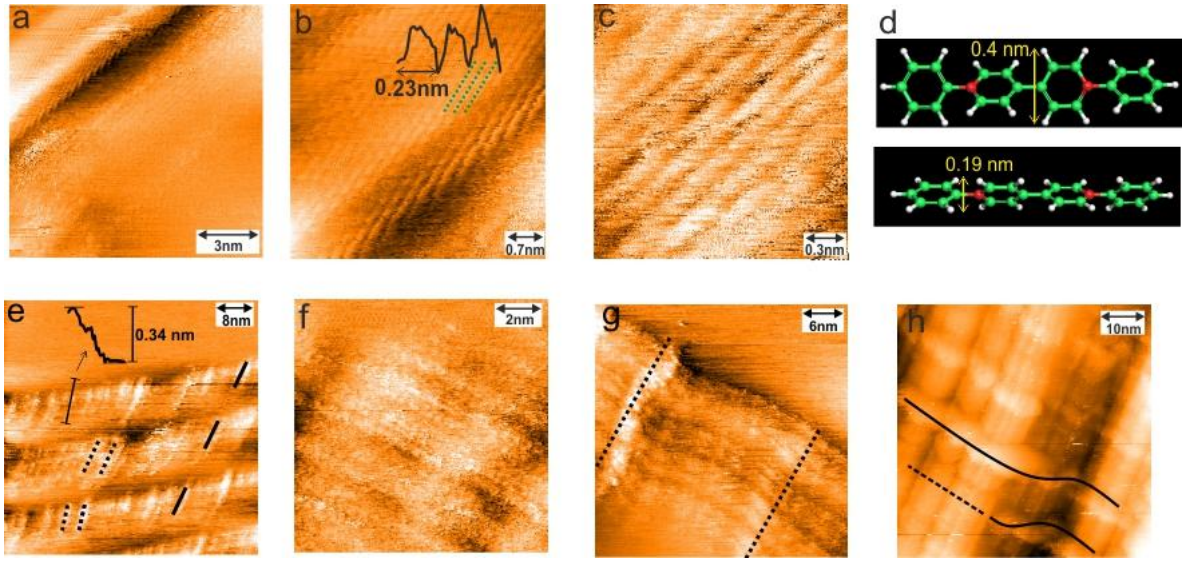

***Figure 7: STM images of (PV1@rGO)@HOPG.** Scanning tunneling microscopy (STM) images of (PV1@rGO)@HOPG (2.8×10^{-10} mol polymer subunit cm^{-2}) at different scan length (**a-c, e-h**); **d**) geometry of a PV1 subunit, optimized by semi-empirical method (PM3) using the ArgusLab software. Preparation in main text, Experimental Section IV-c.*

The high resolution STM images exhibit polymer strands decorating the edge of an rGO substrate (probably an rGO platelet) (Fig. 7 **a-c**). The distance between polymer chains are ~0.23 (the profile is shown in "b"). Considering the width of polymer subunit 0.19 – 0.4 nm (Fig. 7 d) and the observed distance (0.23 nm), the polymers strands are tightly packed. The rGO sheets were wrapped by polymer chains by two main manners: polymers wrap single sheets ((Fig. 7 **e-f**) or platelets ((Fig. 7 **g-h**) of rGO. (Fig. 7 **e**) As it is shown by dotted lines in different directions, polymer strands do not cover the entire rGO platelet (4 sheets are shown), and after each single sheet a new polymer sheet is observed. However, in few cases (solid lines) a polymer chain wrapped more than a single sheet; the profile of an rGO sheet was also shown, which confirm presence of single rGO sheets covered by polymers (in agreement with STM in Fig. 4f,). Many polymer chains packed on the surface of rGO are shown in (Fig. 7 **f**).

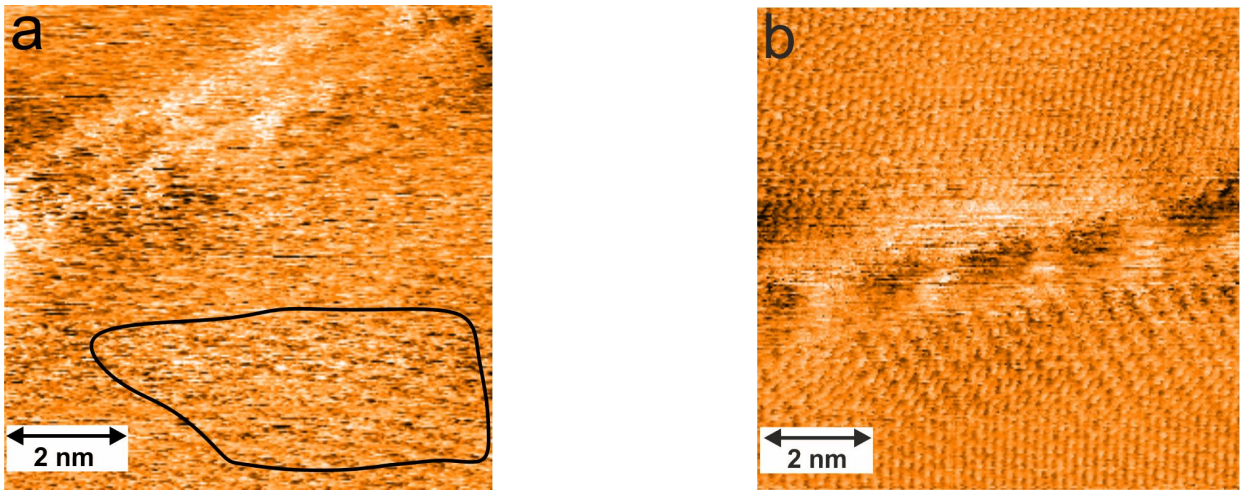

Figure 8: GO/rGO transformation, STM. *Scanning tunneling microscope (STM) images of (PV1@GO)@HOPG* ***(a)*** *(2.8×10^{-10} mol polymer subunit cm^{-2}) and (PV1@rGO)@HOPG* ***(b)*** *(Preparation in main text, Experimental Section IV-c.) taken under ambition condition. Polymer chains are observed in both images*.

The hexagonal graphene lattices of rGO are observed in a region on top of the images. Polymers wrap a platelet of rGO (Fig. 7 **fg**). Dotted black lines are showing chains of polymer around

several rGO sheets. Polymer chains (black lines) which wrap a platelet of rGO (Fig. 7 **f h**). The dotted line shows the continuation of a polymer chain, which is hidden under rGO sheets.

STM measurements point to the recovery of the hexagonal network of carbon atoms, its hydrophobicity and its planarity (Fig. 8). An example of a GO sheet decorated by polymer chains is shown in (Fig. 8a). As it is shown by a black contour, the hexagonal lattices of GO sheet are still partially preserved, which is distinguishable from the oxidized sites, lacking ordered lattice features. On the other hand, in (Fig. 8b) polymer chains are observed on the surface of an rGO sheets, in which oxygenated domains of GO are fully transformed to hexagonal graphene lattices.

Finally, the composite material after transformation still exhibits a mesoporous structure with the charge storing polymer still in place was visualized with AFM (Fig. 4d and Fig. 9).

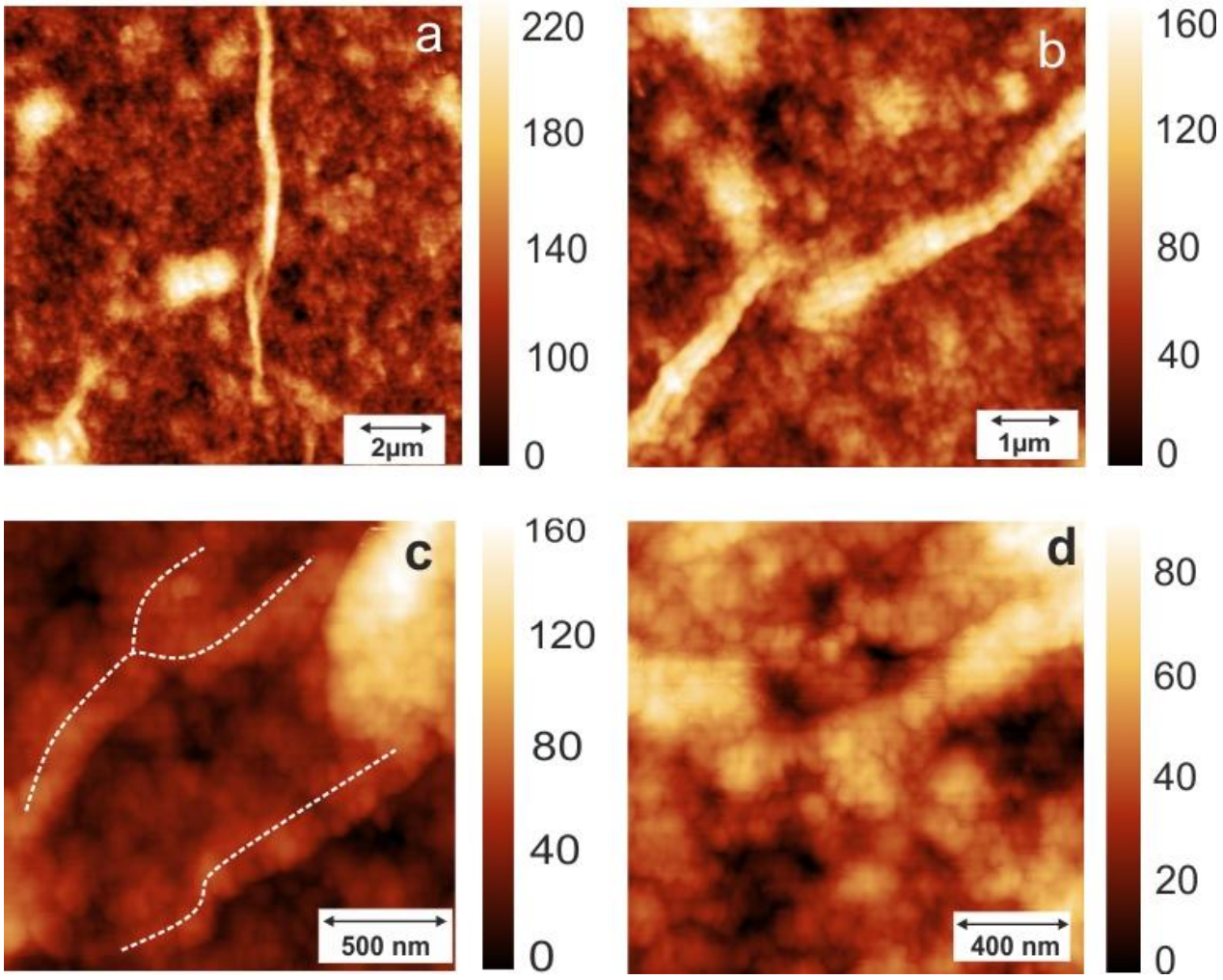

Figure 9: Porous structure of PV1@rGO, AFM. *AFM images of ca. 500 nm thick layer of ca. 10 µg cm^{-2} (PV1@GO)@GC (mass ratio PV1 /rGO = 5.7), scan lengths: ca. 12µm* ***(a)****, ca. 7 µm* ***(b)*** *and ca. 1.6 µm* ***(c-d)****.*

The mesoporous structures with holes in the nanometer range were observed all over the electrode. As shown in (Fig. 9c), polymers decorated GO sheets (dotted curves).

Height and mass ion breathing

Ion breathing is a typical property of organic polymeric battery materials. It shows up in EQCM mass changes and in AFM height changes. The mass decrease/increase is accompanied by a

height decrease/increase as documented by ecAFM in Fig. 10a and 10b. This experiment was restricted to a small area (< 100 nm) of composite during 3 consecutive CV cycles. The composite is 21% less thick in the reduced state (~ 47 nm height decreases in a 230 nm thick PV1@rGO). Height and mass changes are perfectly correlated (Fig. 10b). The height breathing averaged over a larger area (~10µm) showed 14% thickness oscillation Fig. 11-12, whereas the mass change in ion breathing is 70 % (see later).

At this point the question arises if the observed height breathing of ca. 21 % is accompanied by a similar lateral structural compression/dilatation of the composite. Fig. 10c-d shows the ecAFM topology of PV1@rGO in the completely oxidized an reduced state including three cross-section analyses. Notably, these measurements do not show the 21% height difference because a thick composite layer was used, and the color is coded for relative heights. Obviously, the two topologies do not show any systematic lateral structural differences in the 20% range. Thus, the composite material shows anisotropic behavior i.e., significant height distance changes but no obvious lateral distance changes. This is probably related to the rGO adopting an extended puff-paste structure with the rGO planes extended parallel to the current collector underneath. As poly(viologen) is multilayer tightly stacked between the rGO planes. Upon oxidation, the counter ions move between the stacked PV@rGO sheets to the individual pyridinium subunits in order to achieve local charge compensation. The space required by the hydrated chloride anions can only be compensated by an increase of the rGO stacking distance (see PV@rGO stacking distance in Fig. 4f). The anisotropic thickness breathing in z-direction is therefore a consequence of the observed puff paste structure with rGO sheets extending preferentially in the x-y plane parallel to the current collector.

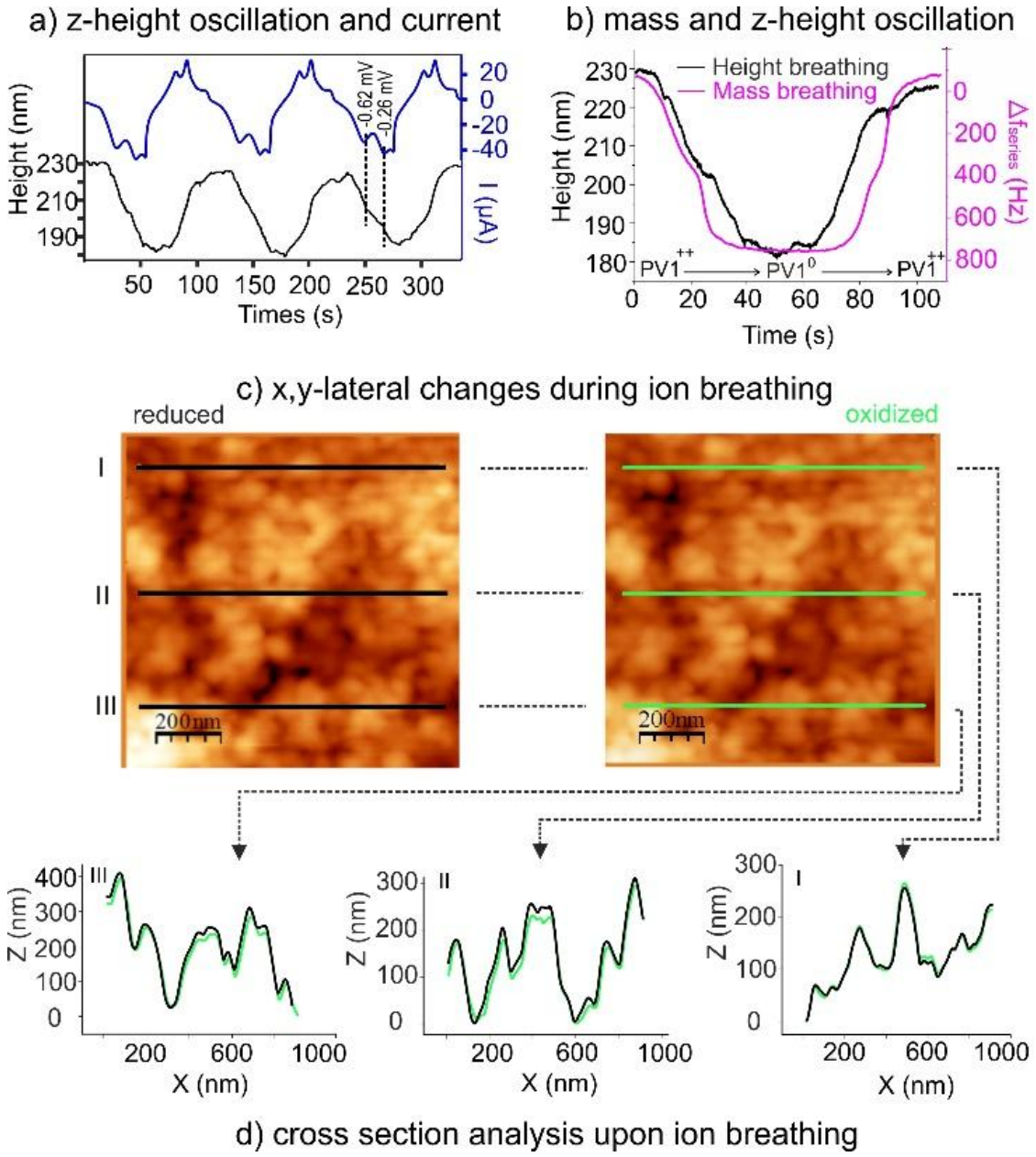

Figure 10: *Height and mass ion breathing. (a) Electrochemical AFM of (PV1@rGO)@GC composite (8.8 µg from PV1/GO = 5.7, Γ_{PV1} = 2.2×10^{-8} mol cm^{-2}); time vs. height (AFM) and vs. current represented with common time axis; CV (blue, top): 0.1 M KCl/H_2O, potential scanning for 3 cycles (0.3 ↔ -0.8) at v = 20 mV s^{-1}; AFM (black, bottom), AFM tip hold at fixed position; typical height decrease upon reduction: 44 to 51 nm; averaged height change: 21 %, both related to counter ion loss. (b) Simultaneous height (black, ecAFM, conditions as in "a") and mass (magenta, from eQCM, Fig. 3b) from two experiments. (c) x-y lateral distance change upon oxidation/reduction; op: ecAFM (1*1 µm) of (PV1@rGO)@GC in the reduced (left, E = -0.8V) and oxidized (right, E = 0.3V) state of the same region, solvent/electrolyte as in "a"; Green/black lines: location of the horizontal height profiles I, II and III. (d) height profiles I, II and III (green: oxidized, black: reduced). Z: relative height. Potentials are vs Ag/AgCl.*

We have observed "ion breathing" of PV1@rGO as a reversible mass change by eQCM during potential cycling. In Fig. 11, we show that the oscillation of mass is connected to an oscillation of the polymer height using electrochemical atomic force microscopy. Instead of a linear potential scan as in the eQCM experiment, a square wave potential (0 → - 1.3 → 0 → ….) with 30 s step time was applied to the working electrode (PV1@rGO)@GC. Thus, during complete picture acquisition which takes 300 sec, 10 potential switches (30 sec) of the redox state of the whole PV1 composite have occurred, and the 10 stripes in the final AFM image reflect the two states (dark: down, light: up).

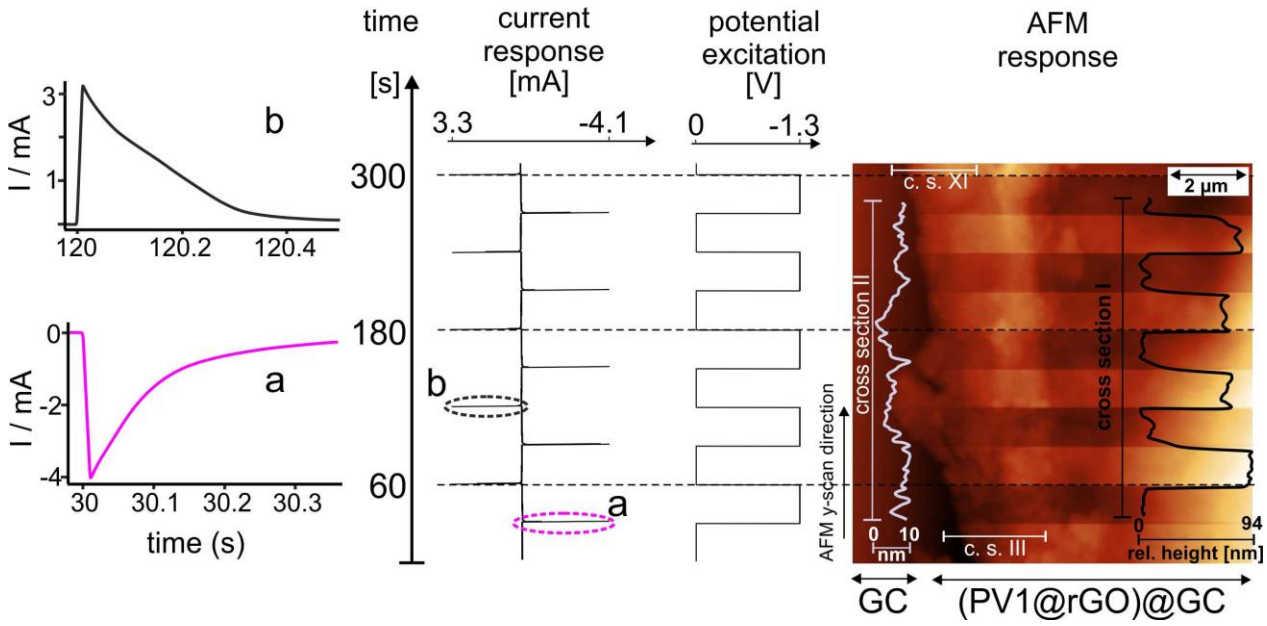

Figure 11: Vertical distance changes, "Height breathing". *Electrochemical redox switching of (PV1@rGO)@GC during AFM image acquisition. Electrochemistry: electrolyte: 0.1 M KCl / H_2O, excitation: square wave potential: 0→-1.3→0→ .... (10 steps with 30 s step time), current response (chronoamperometric): anodic (positive current (left)) and cathodic spikes;* ***(a)*** *the first cathodic current applied after 30 sec and* ***(b)*** *second anodic current applied after 120 sec (reversible coloumbic charge observed: 8.57 mC cm^{-2}). AFM response of vertical distance change: (PV1@rGO)@GC (2.5 µg PV1@rGO with weight ratio PV1 / rGO = 5.7) on 0.07 cm^2 GC corresponding to Γ_{PV1} = 8.6*10^{-8} mol cm^{-2}; left part of image: GC (PV1@rGO scratched away), AFM scan direction upwards, total AFM acquisition time: 310 s, 10 potential steps during AFM acquisition correlate with 10 stripes (dark/light) in the composite covered region but not in the scratched region (vertical cross section I and II in y-direction): typical height increase upon oxidation: 562 to 656 nm; averaged height change: ~14 % (see Fig. 12).*

As seen from the amperometric current spikes, and from the sharp height transitions in the AFM image, the response is in < 0.4 sec. The average height of the reduced PV1 composite above the scratched GC area (left) is 656 nm, and 562 nm for the oxidized and reduced PV1 composite, respectively and composite yielding 94 nm average height breathing, i.e., 14% of the (PV1@rGO)@GC height (see Fig. 12).

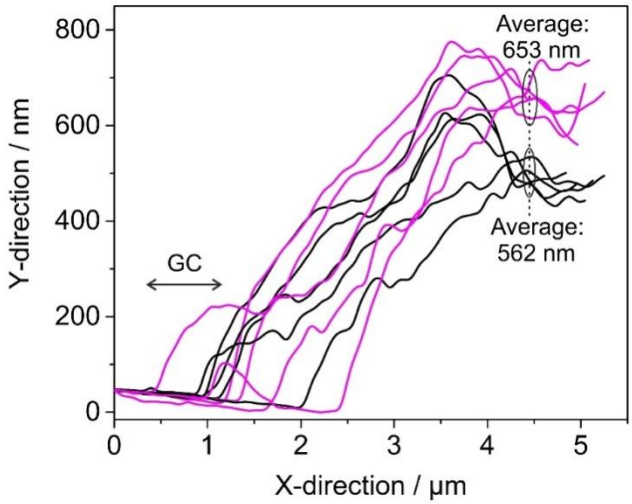

Figure 12: Average height change. *Height analysis of the multiple redox switched composite including 8 stripes for horizontal cross sections III to X Fig. 11.*

Conclusion

1. Cathodic and anodic energy storing materials consisting of organic polymeric redox compounds on graphene oxide or on reduced graphene oxide were imaged by AFM and STM. Image analysis allows to identify the close interaction of nanoscopic current collectors and the energy storage material.
2. Using electrochemical AFM it was possible to follow the electroreductively induced water elimination in the GO / rGO transition.
3. Using electrochemical AFM, it was possible to show that mass breathing (from EQCM) is related to composite height breathing. The control of such properties is important for the future design of full battery construction because height breathing can lead to pressure build-up within the battery.
4. From STM measurements it was possible to identify 2d crystalline viologen@rGO structures. These may be the underlying reason for the high current densities observed for this material.

Experimental

AFM and electrochemical AFM

AFM images were captured with Flex-Axiom "Nanosurf" using Supersharp silicon probe (SSS-NCLR, NANOSENSORSTM) in dry state, or PointProbe Plus Contact Mode Short Cantilever – Au Coating probe (PPP-NCSTAuD NANOSENSORSTM) for ecAFM on the Electrochemistry Stage ECS 204 in 0.1 M KCl/H_2O. The potential of the modified GC electrode was scanned (Fig. 10a, b) or stepped Fig. 11 versus an Ag/AgCl reference using a Pt wire counter electrode and a potentiostat (Gamry, Interface 1000).

STM

STM imaging was carried out with an EasyScan Nanosurf instrument at room temperature using typically 0.050 V bias voltages and 1.000 nA tunneling current (All images were taken in a constant current mode). The images are raw data without filtering. The STM tips were cut from Pt/Ir wire (0.25 mm, Schaefer Technologie GmbH, Langen, Germany). The reduced composite-covered HOPG electrode (5*5 mm piece) was glued onto the magnetic support and the surface was electrically connected to the support with silver lacquer painted over the glass edge.

References

[1] K. Ozawa, *Lithium ion rechargeable batteries*, Wiley-VCH, Weinheim 2009.

[2] C. Gerber, H. P. Lang, Nat Nanotechnol 2006, 1, 3.

[3] Y. S. Cohen, Y. Cohen, D. Aurbach, J Phys Chem B 2000, 104, 12282; C. R. Becker, K. E. Strawhecker, Q. P. McAllister, C. A. Lundgren, Acs Nano 2013, 7, 9173.

[4] Y. S. Kim, S. K. Jeong, J Spectrosc 2015, 1.

Chapter 6

Doxorubicin adsorbed on Carbon Nanotubes: Helical Structure and New Release Trigger

Shamaila Sadaf, Lorenz Walder,*

Advanced Materials Interfaces, 4, 2017, https://doi.org/10.1002/admi.201700649

In this chapter I present the above mentioned publication. The supporting information mentioned in the text is given in the appendix of this chapter

ABSTRACT

The well known drug delivery system "Doxorubicin physically loaded on carbon nanotubes" (Dox@CNT) is visualized by scanning tunneling microscopy at the molecular level, revealing rich architectural variability of Dox@CNT, and allowing to measure and rationalize reported loading efficiencies (80 to 200 %) for the first time from image analysis. Reduction of Dox@CNT is identified as a so far unknown intrinsic release mechanism of biochemically relevance for Dox from Dox@CNT requiring no further CNT surface modification beside Dox loading. Electron injection into Dox@CNT from an electrode or from the biological reducing agent glutathione (GSH) leads to irreversible release of Dox. Its rate follows a linear free energy relationship (reduction potential *vs* log (Dox release rate)) with half life times from below a seconds to hours. With extracellular GSH levels in the µM range and intracellular GSH concentrations of 10mM or even higher, our findings can explain the preferential intracellular

release of Dox from its physically adsorbed state on CNTs. The influence of acidity on the release rate of Dox on pristine 6,5-CNTs in the absence of GSH was found to be negligible. The experimental findings are strongly supported by semi-empirical calculations.

6.1. Introduction

Nanoparticles have developed as an important drug delivery system in recent years[1-4, 5-9]. A well constructed drug carrier finds its way through the body fluid without losing the drug load. It anchor then with its tailored sites to specific receptors at the targeted cell, enters the cell and releases the drug upon the action of a cell specific chemical trigger. Nanoparticles offer a large area/volume ratio with much place for concurrent (i) drug loading, (ii) solubilizing agents, (iii) recognition sites and (iv) even luminiscence labeling (Supporting Information Fig. S1). Carbon nanotubes [5, 6, 8, 9] and nano graphene oxide [4] have extremely high surface/volume ratios and are therefore interesting drug carrier candidates. Furthermore, their chemical modification is simple and well described.

Loading efficiencies of drugs on carriers (drug@carrier) are defined by eq. 1

Loading efficiency = 100*(weight drug) / (weight carrier) in % eq. 1

and can reach values > 100% in case of carrier=CNT and drug=doxorubicin.[3, 5, 7, 9]

Immobilization of drugs at carbon nanotubes is carried out by encapsulation within a large diameter CNT [10], by covalent binding [2, 6] to modified CNT, or by physical adsorption to the outer surface of pristine CNT. [5, 6, 8, 9] Physical adsorption relies on a mix of (i) electrostatic, (ii) hydrophobic, (iii) $\pi-\pi$ interactions and hydrogen bonding between the drug and CNT or

graphene oxide.[11] Because it is reversible, physical adsorption is the smoothest way for drug transport.[5, 6, 8, 9, 11]

Doxorubicin (Dox) - a dihydroxy anthraquinone derivative - is the most widely used anti cancer drug, today. Many papers report on Dox carriers based on graphene oxide [4] and carbon nanotubes [2, 3, 5, 6, 9, 12, 13]. Dox can be reversibly adsorbed on the outer CNT surface and/or encapsulated in the inner space (CNT diameter > 1.3 nm)[10] by a self-assembling process, and Dox@CNT can easily penetrate the cell membrane.[3, 14] The supramolecular Dox@CNT complex is reasonable stable, has been characterized by many methods, e.g. UV-Vis [3, 5, 9], Raman[1], FTIR.[12], and zeta potential[7, 9], and exhibits a large drug loading efficiency, of 70 to 130 %, as measured by UV/Vis [7, 9, 15]. For additional PEG functionalized single wall carbon nanotubes loading efficiencies from 50 up to 400 % have even been claimed [5]. TEM measurements on the self-assembled systems [7, 9, 14] show Dox as clusters on CNT,[14] and adsorbed at the interstitial space of helically wrapping polymers, [7, 9] as further supported by AFM[1, 3] and SEM studies.[1] Recently scanning tunneling microscopy (STM) results with molecularly resolved Dox physically adsorbed on CNT have been reported,[16] showing Dox on the cylindrical CNT surface in a helical arrangement with a 50° inclination of Dox with respect to the CNT axis. However, the reported STM image does not reveal structural variability and it cannot explain loading efficiencies in the 100 to 200 % range.

Several MD, semi-empirical and DFT type calculations and modeling approaches have been applied to Dox [10, 16] (or other drugs [17]) on CNT. A. R. Galvan used DFT on a fulleroid/Dox complex and found strong attractive interaction. Wang used semi-empirical PM6-DH2 and found that protonation and diameter of tube influences drug loading and release.[10]

Many reports claim to use the slightly more acidic pH in cancerous cells for fast Dox release. [1] However, the trigger effect is not very strong and reported half lives scatter. Half life's of ca. 30 h were reported for Dox release from pure or chitosan modified CNTs and ca 20 h from chitosan/hyaluronic acid modified CNTs at pH 5.5, but no release at pH 7.4, [7] or a half life of ca. 2 days at pH 5.5 and almost no release at pH 7.4 and 9 for Dox on CNT modified with PEG, [5] or a half life of ca. 60h in case of Dox loaded on (partially) chitosan modified CNTs and even more than 60h in case of pure CNT at pH 5.5. [9] Notably, Dox is in the ammonium state at a pH below 9 and the acid triggered release mechanism is probably due to an increase of positive repulsive charge in the Dox@CNT environment, i.e. chitosan ($-NH_2/-NH_3^+$, broad titration pKa 6.5) modified CNT is more pH responsive than a chitosan with fewer amin groups.[18] Theoretical studies claim that small molecules with sharp and tailored pKa (6.5-5.5) are ideal for more specific release in cancerous cells, especially if the drug is loaded inside a thick MW CNT.[19] A Ca phosphate crowned thick MW-CNT is another example, it opens and releases the drug content from the inner void at pH 5.5 as Ca phosphate is dissolved under acidic conditions.[20] In case of Dox release from physically adsorbed Dox@CNT without any on-purpose introduced basic sites (such as chitosan) or without introduction of a Ca-phosphate molecular gate, the "natural loss" of Dox at high dilution and elevated temperature has to be taken into account.[12, 21]

Another unique feature of intracellular vs extracellular media and cancerous cells specifically is an increased level of intracellular glutathione (GSH).[22] GSH as a potential release trigger has lead to the synthesis of Dox anchored to CNT via a reductively cleavable disulfide linker. [23] We could not find any report on the release of Dox physically π-stacked as Dox@CNT as triggered by a reducing agent.

In conclusion, (i) the smoothest and most simple method of holding Dox on the outer walls of a CNT drug carrier is by physical adsorption, (ii) it is not clear, why reported Dox loading efficiencies vary by a factor of at least 2, (iii) the claimed acid triggered release is effective only upon introduction of a pH gated molecular switch on the CNT surface, (iv) it has not been checked if a reducing environment can trigger the release of Dox physically adsorbed on pristine CNT, so far.

Here we present clear structural evidence for the reported loading efficiency of Dox on CNT in the range 70 to 150 %. Using STM we observed countable Dox molecules with a rich structural diversity for Dox@CNT, displaying single- or multi-strand helical wrapping of Dox monomers or dimers on the CNT cylinder. We demonstrate that loading efficiencies can be deduced from microscopic image analysis. We tackled then the question, if electron transfer can stimulate the release of physically absorbed Dox from Dox@CNT and if protons play a role alone and under reducing conditions. We found that electron injection into Dox@CNT leads to expulsion of Dox from Dox@CNT, that the influence of pH (range 4-7) is negligible under non-reducing conditions, and that the release of Dox under reducing conditions is not affected by pH in the pH range 4-7. The mechanism is further rationalized by molecular modeling using semi-empirical methods. These clearly show that Dox is efficiently released from the Dox@CNT upon reduction (electron injection), and that Dox is not released from Dox@CNT upon oxidation (electron extraction).

6.2. Result and Discussion

6.2.1. Formation of Dox@CNT

The Zeta potential of dispersions of pristine 6,5 single wall carbon nanotubes (6,5-SWCNT, ca. 1nm diameter, abbreviated here as CNT) in the presence of different amounts of doxorubicin (Dox) is shown in Fig.1. The pure CNT solution exhibits a negative zeta potential of -20 mV at pH 7.3 as reported earlier (-13 and -2 mV at pH 7.4 and 5.5, respectively, and -63 mV at pH 7.4 for on-purpose carboxylated CNTs)[7, 9]. Upon Dox addition the Zeta potential moves from -20 mV to +30mV following a sigmoidal dependence on the Dox/CNT weight ratio, reflecting positively charged Dox adsorbing onto the CNT (Supporting Information Table S1.1). A change of slope at ca. 0.8:1 Dox/CNT is observed. According to our STM studies, this weight ratio is compatible with a closely packed helical strand of monomeric Dox on CNT (Fig. 2a, Table 1).

Table 1: Loading Efficiency and structure of Dox@CNT from pick-up, from EA and from STM analysis

UV-vis and Elemental Analysis (E.A.)		**STM structural analysis (Fig. 2, S2.2)**	
Calc. from	Wt. Ratio Dox/CNT mg/mg	Calc. from structure type	Wt. Ratio Dox/CNT mg/mg
conc. drop of free Dox during formation / Uv-vis (S1.2)	1.7/1	**monomer loading** single stranded pitch: 2.6 nm Dox per turn: 4	**0.81/1**
E.A of product Dox@CNT / E. A. (S2.1)	1.6/1	**dimer loading** double stranded pitch: 3 nm Dox per turn: 10	**1.8/1**

For higher Dox/CNT weight ratios, the zeta potential is steadily increasing, indicating further loading but with lower driving force. According to the STM and modeling studies (see later) the 1.7/1 ratio is typical for a closely packed helical structure of dimeric Dox on CNT (Table 1).

The process of Dox loading on CNT was further investigated from the Dox pick-up in solution by pristine CNTs (UV-vis absorbance drop of a Dox solution, Table 1, Supporting Information S1.2 and Fig. S2). The Dox/CNT ratio in the isolated, solid state Dox@CNT was checked by elemental analysis (EA) yielding a weight ratio Dox/CNT of 1.6/1 (applying the procedure of N. Hadidi et al.[24]) and based on the experimental EA of Dox@CNT, pure Dox and pure CNT (Table 1, Supporting Information S2.1).

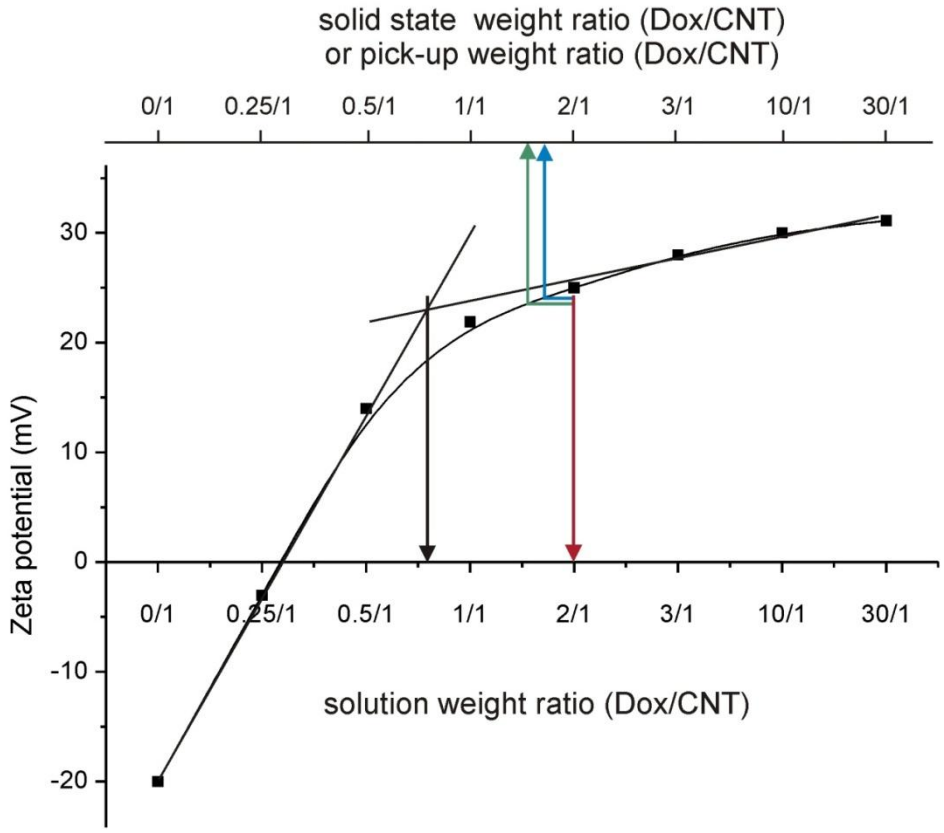

Figure 1: *Zeta potential vs. weight ratio Dox/CNT. Weight (CNT) 25 µg, weight (Dox) 0 to 750 µg (weight ratio Dox/CNT in solution from 0/1 to 30/1, lower scale), and observed weight ratios in solid Dox@CNT (upper scale); Zeta values are averaged from three measurements; black arrow: slope change (monomer strand formed); red arrow: ratio used for the preparation of Dox@CNT for most experiments, green and blue arrows: ratio observed in elemental analysis and calculated from the pick-up experiment, respectively (Table 1).*

6.2.2. Structure of Dox@CNT

STM measurements of Dox@CNT show ellipsoidal shiny structures in a helical arrangement (main axis length: 1.2 nm, Fig. 2a), typical for amplified tunneling currents reported for aromatic redox systems on CNT)).[25] We interpret them as the conductive tricyclic dihydroxy anthraquinone subunit in Dox, which is hold by π– π interactions on the benzene rings of the CNT. In contrast to Rodriguez-Galvan,[16] we interpret the arrangement of the tricyclic aromatic system as parallel to the CNT axis. Probably the less crowded side of Dox is interacting with the CNT and the sugar moiety is pointing away from the CNT (Fig. 2a', 2f). The shiny ellipsoidal disk interpreted as the quinizarin subunit in Dox@CNT is confirmed by STM analysis of quinizarin@CNT (Supporting Information Fig. S4). In most cases we observe more tightly packed Dox with enlarged shiny regions. These are probably face-to-face π-stacked dimeric Dox molecules with one Dox sandwiched between the upper Dox and the CNT surface (Fig. 2b, b', g, h, i). Notably, the formation of Dox dimmers in solution phase is well documented, [26] and such dimers seem to adsorb as an entity or build up on CNT. Analysis of pitch and angles of the helical Dox chains reveals the existence of single-stranded (Fig. 2 a",b") or double stranded (Fig. 2 c") helical arrangements of Dox on CNT.

In (Fig. 2g,h,i) we show the model used for the calculation of Dox loading from structure, here exemplified for the dimeric, single stranded case. As Dox is sitting ca 0.3 nm above CNT (typical π-stacking distance) the circumvent was corrected according to: circumvent = π*(0.8 +(2*0.3)) = 4.4 nm. The cylinder was then cut and unfolded to a plane (light green plane in Fig. 2g) with 4.4 nm sheet width and 3nm height (pitch, Table 1). The Dox structure was geometry optimized and placed onto the green sheet respecting reasonable intermolecular distances. The

modeled situation includes 4 Dox molecules per helical turn as observed by STM. (ca. 5 dimeric Dox, Fig. 2b, 2b"). From the observed ratio of Dox molecules per helical turn, the corresponding weight ratio Dox/CNT was calculated.

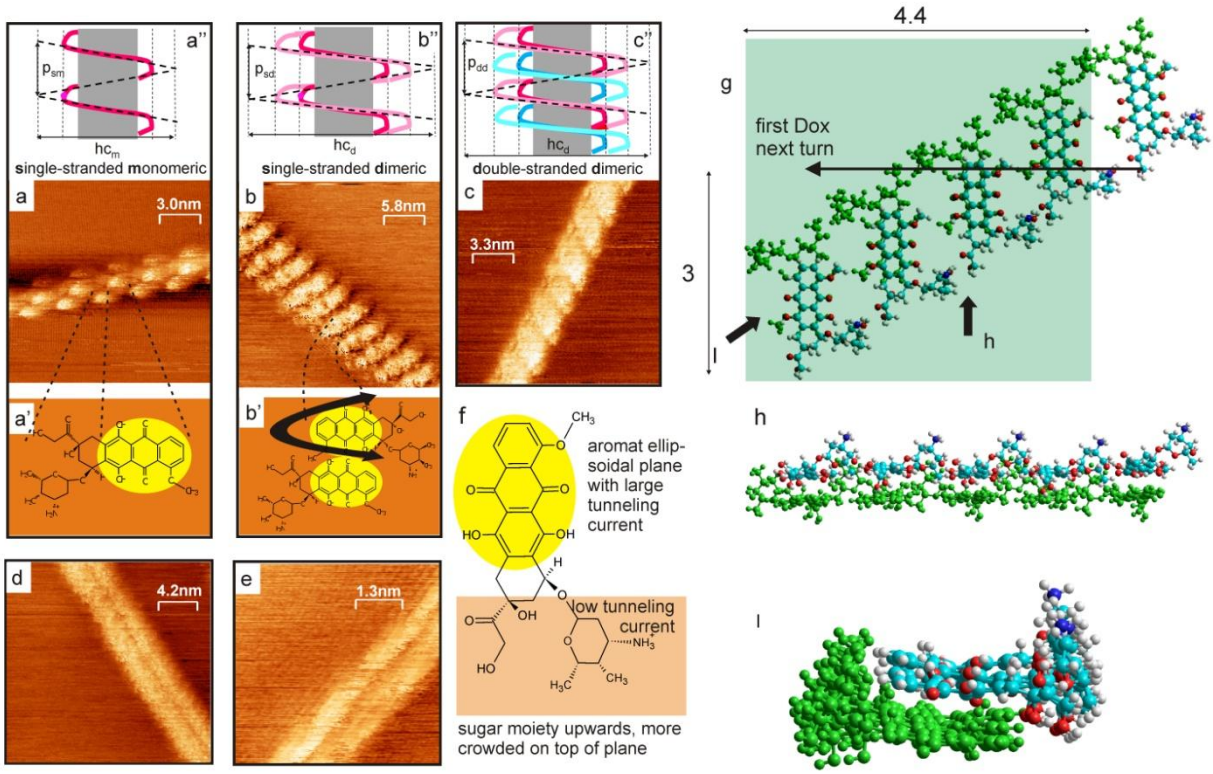

Figure 2: *Structure of the Dox@CNT complex a-d: STM images of helical self-assembled Dox@CNT structures (a: **s**ingle-stranded **m**onomeric Dox (**sm**, few); b: **s**ingle-stranded **d**imeric Dox (**sd**, most); c: **d**ouble-**s**tranded dimeric Dox (**dd**, few); d: bundle of two individually Dox-wrapped CNTs; e: pure CNT (bundle of two); f: structure of Dox with STM-conductive ellipsoidal subunit (yellow, aromatic) and non-conductive subunit (brown, sugar); a': main axis of conductive ellipsoid parallel to CNT main axis with monomeric Dox@CNT; b': STM current tunneling through dimeric Dox (ellipsoidal main axis less clear) upper Dox has rotational freedom[26]); a''- c'': analysis of helical pitch (p_{sm}, p_{sd} and p_{dd}) and analysis of single and double stranded by projection of loaded CNT cylinder on flat sheet with width = half circumvent (h_{cm}, h_{cd} and h_{cd}, respectively);[27] (g-i) arrangement of dimeric Dox on CNT projected on a flat green surface with width = 4.4 (all numbers in nm) and height = 3 (corresponding to the helical pitch, Table 1) green: inner Dox strand, carbon-blue: outer Dox strand; dimeric Dox are π-stacked (blue on green quinizarin subunit) g) from top, h) along the CNT cylinder axis and i) along the strand (for an alternative arrangement of Dox dimers see (Supporting Information Fig. S2.3).*

The occupied surface area for the monomeric and the dimeric case are similar, but the helical pitch and the compactness are increased (Fig. 2.g-i). Most important, the loading efficiency is doubled due to the dimeric stacking, allowing us to explain the results from the pick-up experiment, those from elemental analysis, as well as those reported in literature[26], for the first time from structural analysis of a Dox@CNT STM image.

It is interesting that in literature most authors reported loading efficiencies of ca. 80 % to ca. 160.[15] [7, 9, 13] This may be related to our new findings, i.e. that either mono or dimeric structures of Dox on CNT can form by self-assembly. A helical Dox@CNT arrangement shown earlier by Rodriguez-Galvan for a low Dox density.[16] Here, we show that the helical Dox arrangements persist in the high loading rang, and that rich architectural variations are possible, i.e. mono- and dimeric Dox structures, as well as single and double stranded helical arrangements. Most importantly, image analysis of the STM pictures is used for the first time to calculate the loading efficiency, yielding values in the range 80 – 160 %.

6.2.3. Reductive release of Dox from Dox@CNT

Dox@CNT was prepared according to the Methods section in the Supporting Information, p3. The washing process insures that all Dox is present as π-stacked Dox@CNT. Doxorubicin contains the 1,4-dihydroxyanthraquinone (quinizarin) subunit which is principally reducible by $2e^-/2H^+$ to leucoquinizarin and oxidizable to anthracenetetrone again involving $2e^-/2H^+$ according to the top line in Fig. 3. The reduction can show up electrochemically reversibly,[28-30] and molecular oxygen can oxidize leucoquinizarin back to the quinizarin subunit.[28] Upon electrochemical oxidation Dox undergoes irreversible chemical follow-up reactions.[28, 30] The

cyclic voltamogramm (CV) of Dox in aqueous KCl (Fig. 3, black trace) is in agreement (for its pH dependence, see Supporting Information S3.1. and S3.2 and Fig. S6). The CV of Dox@CNT painted onto a glassy carbon electrode (Dox@CNT@GC (see Experimental section) shows a dominant first reduction peak at ca. -0.6 V followed by rather small diffusion-type waves (Fig. 3a). It is accompanied by the formation of a dark red cloud dropping downwards from the Dox@CNT@GC modified electrode to the bottom of the cell (Fig. 3 e) →f), b) →c)). This is free Dox released from Dox@CNT@GC and dropping because of its high concentration and local density. Notably, Dox@CNT in suspension appears grey and not reddish! Inspection of the electrode surface after a full CV scan reveals naked CNT on the electrode surface, as visualized by stamping the electrode onto a tissue (d) in Fig. 3). Further analysis of the electrochemical Dox release from Dox@CNT@GC stems from rotating disk experiments (Supporting Information S4.1. and Fig. S7). It shows that (i) at rotating rates up to 1000 rpm neither Dox nor Dox@CNT is lost from the electrode (electrode potential 0 V), (ii) that ca. 80 % of electrochemically accessible Dox is lost at the stationary electrode if a complete CV cycle is executed, and (iii) that almost all Dox is lost upon reduction at the rotating disc in one CV cycle. Obviously, some part of the freed Dox is entrapped in the naked CNT network, but complete release is observed in case of convection and application of the reducing potential during CV.

In Fig. 3g-j an AFM analysis of the Dox@CNT@GC electrode before and after the reductive scan is presented. The sample consists of a much thicker Dox@CNT layer than used for the STM measurements and many CNTs stick together. Furthermore, the lateral AFM resolution is limited to ca 50 nm. The horizontal structures observed are individually and/or collectively Dox wrapped CNT bundles (vertical structures). After reduction the horizontal Dox structures have

disappeared and only the vertical naked CNT bundles persist, as quantified in the histograms maxima shifting from >100 nm to < 100 nm (Fig. 3 j → i).

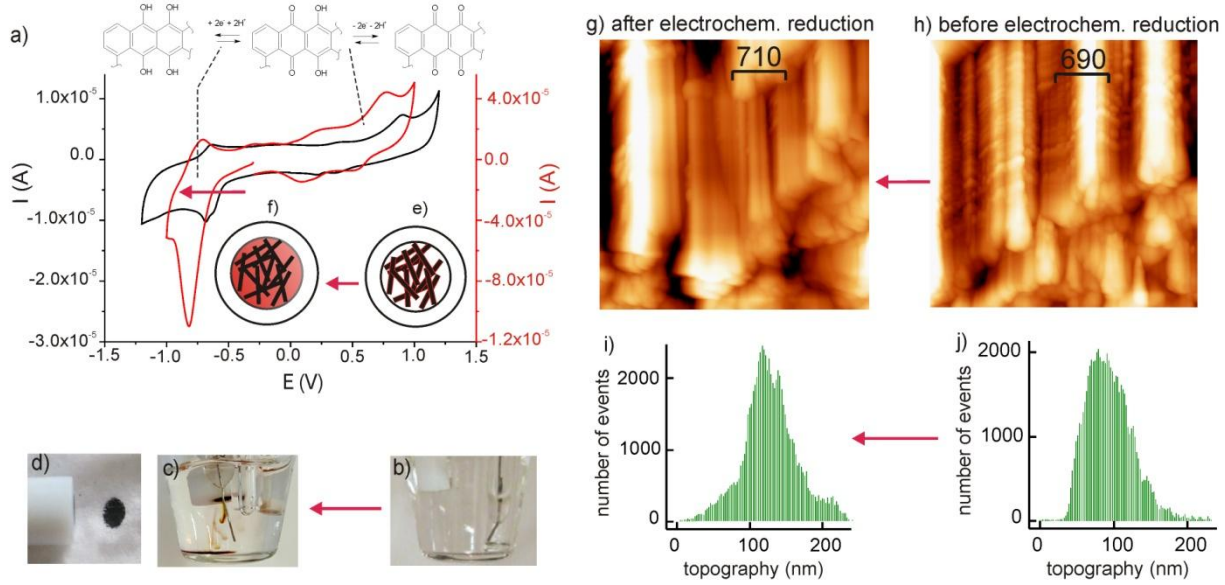

Figure 3: *Electrochemical reductive release of Doxorubicin: a) Electroreductive release of Dox from Dox@CNT@GC scan: -0.2 → -1.0 → +1.0 → -0.2 (red) and CV of free Dox (140 µM) in 0.1 M KCl, scan: 0 → -1.2 → +0 (black trace, for comparison) with annotation of redox reactions; b)exp. set-up Dox@CNT@GC prior to reduction and corresponding model (e), with Dox at the surface of CNT), and after reduction showing Dox clouds dropping to the bottom of the cell (c), d): visual analysis of the blank CNTs transferred from the electrode to a tissue after Dox release, f) model showing released Dox partially entrapped in the CNT network; (g-j)AFM images of Dox@CNT (40-50 µg) on a GC electrode in dry state, measured before (g) and after (h) electrochem. reduction, position and zoom slightly different; many Dox strands (ca. horizontal structures) in a), only a few in (h) on bundles of CNT (vertical structures); (i-j): frequency distribution of particle size vs. particle size with main peak < 100nm before and >100 nm after reduction; red arrow in release direction.*

A more quantitative analysis of the reduction triggered Dox release is based on a gravimetrical method, i.e. an electrochemical quartz crystal microbalance (eQCM). This technique allows to determine the mass of an adsorbed layer on the gold electrode of an oscillating quartz as a function of the applied potential via the resonance frequency change of the quartz according to

the Sauerbrey equation. [31] Only tightly hold components at the gold electrode but no particles or molecules trapped in the solution phase between the CNTs are expected to contribute to the observed mass change. A series of representative experiments with potential steps 0 to -0.6, -0.7, -0.75, -0.8, and -1.0 V is shown in Fig. 4 (further details in: Supporting Information S4.2.) As long as the Dox@CNT@Au electrode is hold at 0 V no frequency change (no mass loss) is observed over 1 h. Upon application of the potential step 0 → -1V (experiment Q1, Supporting Information Table S1) an immediate frequency increase of 18.2 kHz corresponding to a Dox-mass loss of 90 µg is observed. The weight change is faster than 1s, i.e. faster than the response time of the used frequency analyzer. The solution in the cell was carefully collected (including inter-CNT-trapped Dox) and analyzed by vis spectroscopy (spectra compatible with Dox and amount from absorbance: 85µg, close to the value determined by eQCM). The release efficiency (100 * $W_{Dox\ released}$ / W_{CNT}) can be grossly judged in the range of 130 to 140 %, close to the loading efficiency. The solution pH was restricted to 7 (unbuffered) in the eQCM measurements, because a positive shift of the reduction wave is observed only outside of the biologically relevant pH range (Supporting Information SchemeS1, Fig. S6c).

In Fig. 4 b) the experimental frequency vs time data are plotted as %Dox released vs time for different electrode potentials (for raw data see Supporting Information Table S6) . The importance of the applied potential step is obvious. Linear $\%Dox_{released}$ vs time traces are observed at short times indicating zero order kinetics, but the slower traces tend towards an equilibrium situation at longer times. Notably, zero order release kinetics have been claimed earlier for the release of 6-mercaptopurine from CNTs.[32]The inflection point between the two kinetic regions is not sharp and shifts from a few percent of total release at -0.6 V to > 80% for -0.8 V. The drug release rate for the -1V reduction step is too fast for the frequency analyzer.

The slopes of the 0-order straight lines, i.e. $\%Dox_{released}/s$ were determined and plotted as $\log(\%Dox_{released}/s)$ vs. the reduction potential (Fig. 4c). In electrochemistry plots of log(current ratio) *vs.* electrode potential are known as Tafel plots. Here, the current ratio is replaced by $\%Dox_{released}/s$ presenting a dimensionless rate according to eq 2,

$$E\ (V) = A * \log(\%Dox_{released}/s) \qquad \text{(eq. 2)}$$

which represents a linear free energy relationship. Using the four reliable points we A = 60 mV/decade.

Having shown that Dox can be released effectively from Dox@CNT by an electrochemical reduction process, we studied the Dox release from suspended Dox@CNT triggered by the biological reducing agent glutathione (GSH) (Supporting Information S4.3). Notably, GSH is present in the 5 to 20 mM range in cells. The reduction potential (E) of a GSH solution containing 1 % of GSSG *vs* the Ag/AgCl reference is -0.485 V at pH 7 according to eq. 3 (details in Supporting Information S4.4).

$$E = E^{0,} - 0.058\ V * \log([GSH]) + 0.029\ V * \log[GSSG] - 0.058\ V * (pH_{exp}-7) \quad \text{eq. 3}$$

Observed Dox release vs. time traces using homogenously suspended Dox@CNT and GSH (containing ca. 2 % GSSG) under pseudo-first order conditions ([GSSH] ca 100*[Dox]) are shown in Fig. 5a. The release traces are linear in the pseudo-first order presentation (Fig. 5a,5b). Further measurements under different conditions (pH, GSH concentration) are presented in the Supporting Information (S.4.3, Fig. S9 and S10).

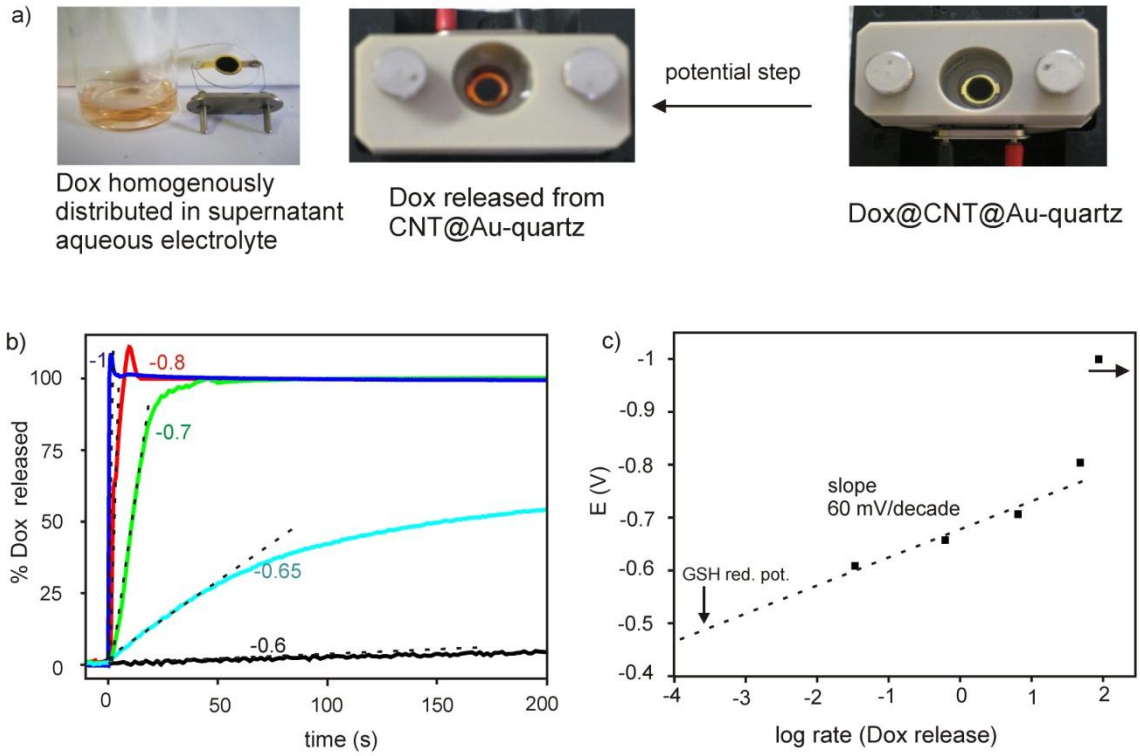

Figure 4: *Reductive Dox release observed by eQCM : a) eQCM cell and quartz; left: before potential step, Dox@CNT@Au-quartz viewed from top through 0.1 M KCl solution; right: after potential step (0 to -1 V), Dox released from CNT@Au-quartz viewed from top (red dox in the vicinity of the electrode), far right: quartz and collected electrolyte solution after cell disassembly: CNT still present at gold of quartz, Dox homogeneously distributed in electrolyte solution; b) voltage dependent Dox release from Dox@CNT@QCM in percent as a function of time (for data treatment and additional reduction steps, see Supporting Information S4.2) . c) Tafel plot (free energy relationship) of applied potential vs. log(rate of Dox release) from the linear slope at early times after the potential step yielding a Tafel slope of 65 +/- 10 mV / decade. The rate for the -1V step is too fast for frequency analyzer). E^0 of the GSSG/2GSH couple is indicated, it corresponds to a release rate with $\tau_{1/2} = 58*10^3$.*

In conclusion, we find (i) in the absence of GSH, a natural release of Dox from Dox@CNT suspended in water with a half life of ca. 4 days independent of the pH in the range 7 to 4 is observed, (ii) in presence of 10-20 mM GSH the release rate is 10-20 times faster, (iii) GSH

enters with molecularity 1 in the rate law (doubling of pseudo-first order rate constant upon doubling of GSH concentration) and its 2^{nd} order rate constant is $1.8 * 10^{-3}\ s^{-1}M^{-1}$.

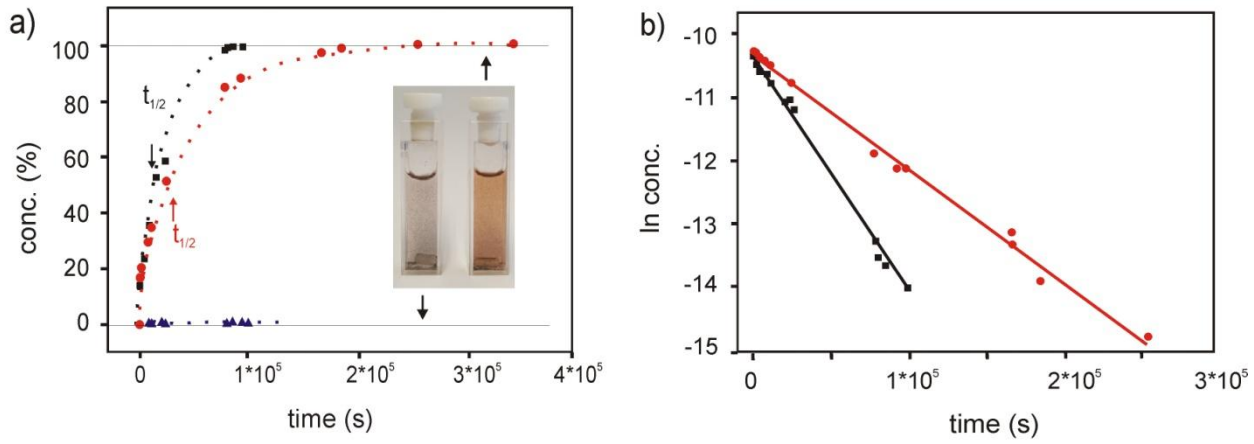

Figure 5: *Reductively triggered release of Dox from water suspended Dox@CNT by GSH. a) percentage of Dox observed vs. time for conc. GSH=0 (blue triangles), conc. GSH=10 mM (red circles, pH=3.5) and conc. GSH= 22 mM (black squares, pH=2.8); inset visual impression of the cuvettes with no GSH present (left) and with GSH after complete Dox release; b) pseudo-first order analysis of the disappearance of Dox@CNT (calculated from the Dox appearance), i.e. ln($[Dox_{t=\infty}]$ - ($[Dox_t]$) vs time, for b) cGSH = 10mM (pH 3.5) and c) cGSH = 22 mM (pH 2.8) , analysis see (Supporting Information Table S7)*

From eq. 3 it is evident that lower pH shifts $E^{0'}$ to more positive potential, i.e. a slower release may be expected for thermodynamically equilibrated situation. Obviously, we do not observe a pH dependence in the 4-7 pH range indicating a mechanism involving only the GSH concentration.

6.2.4. Semi-empirical modeling of the reductive release of Dox from Dox@CNT

Gas phase, semi-empirical calculations were done on a short 3.8 nm 6,5-CNT and one Dox coordinated to CNT (denoted as cal-Dox-CNT) using the PM7 QM program of Stewart (see Experimental section)[33] Guided by the STM results, the dihydroxy anthraquinone subunit was placed with its long axis parallel to the CNT cylinder at ca. 1-2 nm from the CNT cylinder. The following questions were tackeled: (i) interactions of Dox- and CNT-localized orbitals in the frontier orbital region, (ii) orientation of cal-Dox-onCNT, (iii) change of attractive interaction between CNT and Dox with different charge on the system (iv) reductive Dox release and (iv) fate of Dox upon oxidation. Isolated cal-Dox^{+} and isolated neutral cal-CNT have a HOMO-LUMO gap of 0.275 hartree (7.48 eV) and 0.143 hartree (3.89 eV), respectively, with the LUMO of Dox within the HOMO/LUMO gap of the semi-conducting CNT (Supporting Information, Fig. S14).

With Dox placed on CNT using -3, +1 or +3 total charge on the system stable situations result, i.e. no release of Dox from CNT upon geometry optimization is observed. The total charge -3 partitions with +0.98 on Dox and -3.98 on CNT, i.e. Dox is in its protonated state and CNT with 4 extra electrons (Fig. 6 I)). The same Fig. 6I reveals that the LUMO of cal-Dox-CNT^{-3} is purely Dox-localized (red energy levels), and that empty orbitals just above LUMO are either Dox or mixed Dox-CNT localized. The reduction by 8 electrons (Fig. 6I→II, a) b)) consists therefore of filling-up these Dox localized orbitals.

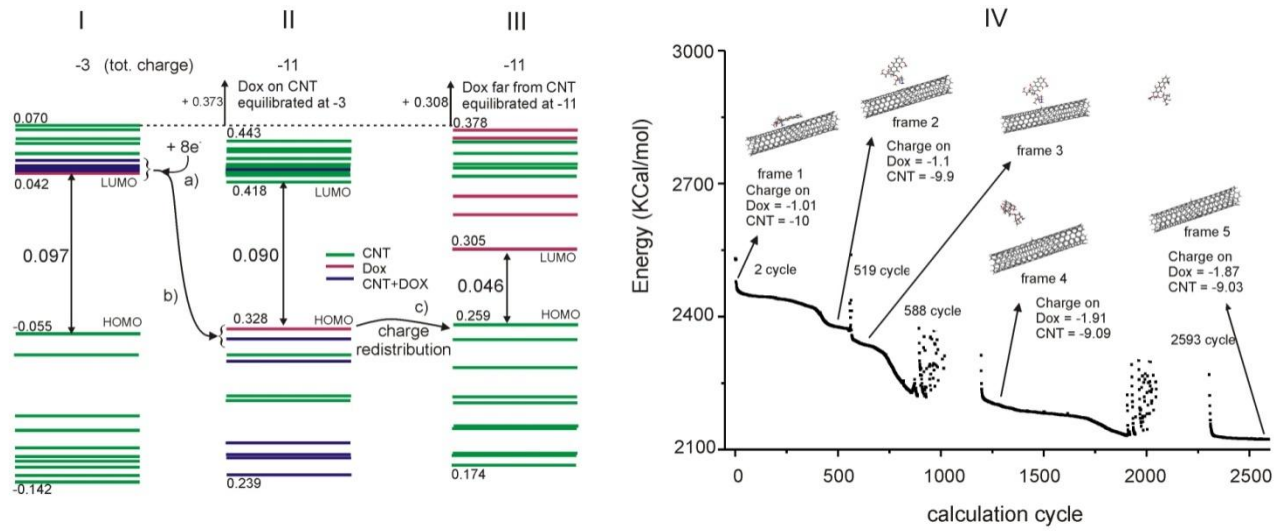

Figure 6: *Semi-empirical PM7 simulation of the reductive release of Dox from CNT: I-III: Frontier orbital region of cal-Dox-CNT at dfferent charge (red: Dox-localized, green: CNT-localized, violet: CNT-Dox mixed orbital localized) of I: (cal-Dox-CNT)$^{-3}$ after geometry opt. at total charge -3, II: (cal-Dox-CNT)$^{-11}$ as in I) after 8 e$^-$ injection (tot. charge -11) without geometry optimization; III: (cal-Dox-CNT)$^{-11}$ after geometry opt. including reduction induced separation (frame 5 in IV); a) →b): 8 electron charge injection into Dox-(and mixed Dox-CNT) localized LUMOs in I, new CNT-localized LUMO in II; II →III (c)) electron repartitioning upon geometry opt. (Dox-release); IV: Geometry optimization (total energy vs. cal cycle) of (cal-Dox-onCNT)$^{-11}$; first situation is geometry opt. optimized cal-Dox@CNT^{-3}; at cycle 0: 8 electron charge injection yielding cal-Dox@CNT^{-11} followed by geometry optimization (2593 cal. cycles, PM7, keyword mozyme); during optimization: total energy 2531 → 2123 kcal/mol; selected geometries are shown including charge on Dox and on CNT (frame 1-5) (charge calculated from single point energy on the geometry from the mozyme calc.) frame 1 → frame 2: Dox originally in a stable π–π stacked conformation on CNT, but π-stacking is disrupted upon charge injection, the dihydroxyanthraquinone moves away from CNT and Dox is hold at CNT only by electrostatic interaction between positively charged ammonium and the neg. charged CNT; frame 2 → frame 3: proton transfer from H_4N^+-Dox to CNT; charge on Dox prior to H^+-transfer: -1.01, after H^+-transfer: -1.9; frame 3 – frame 5: repulsive coulombic interaction leads to separation; discontinuities of the energy trace due to high activation barriers.*

After 8 electron charge injection, two additional electrons are found on Dox, i.e. Dox-charge: -1.01 and and ten electrons on CNT, CNT-charge: -10 (Fig. 6, II and frame 1). The HOMO in Fig. 6, II is now Dox-localized, and the LUMO as well as the other empty frontier orbitals are mainly CNT localized. According to frame 2 in Fig. 6, the attractive π-stacking interaction

breaks down, the aromatic system turns away from CNT and the ammonium group approaches CNT. The $–NH_4^+$ - CNT^- interaction holds Dox still in the vicinity of CNT (albeit total charge on Dox and CNT are both negative, but charge on $–NH_4^+$ of Dox acts as the positive pole of a dipole closely positioned at CNT). Then (Fig. 6, frame 3) proton transfer from $–NH_4^+$ on Dox to CNT destroys this attractive interaction, Dox is freed and moves away from CNT (Fig. 6, frames 3-5). The reductive cleavage of cal-Dox-on-CNT follows nicely the observed experimental results (see movie 1 reduction). However, some details which have to be taken into account when comparing modeling and experimental results. (i) The calculation was performed in gas phase and that's why proton and electron transfer are energetically over-estimated in the calculation; (ii) in the calculation Dox is leaving CNT in a 2-electron reduced state, i.e. with a two-electrons reduced quinone subunit, whereas in the experiment we observed Dox in its original oxidation state leaving the Dox@CNT assembly. Anyhow, the active frontier orbital levels are closely spaced and a back-electron reaction cannot be excluded, or traces of oxygen may have oxidized a reduced intermediate back to Dox.[28]

Electrochemical oxidation of Dox@CNT delivered a more complicated CV than its reduction, anyhow, no indication for Dox release upon oxidation was experimentally observed. We have modeled the oxidation by a charge extraction using the same pm3/mozyme method as described for the reduction. Detailed results are shown in the Supporting Information Fig. S13 and Scheme S2. The cal-Dox-on-CNT^{+3} was found stable towards dissociation, again with many interdigitated frontier orbitals of Dox-, CNT- and mixed character. Notably, both subunits carry a positive charge (Dox: +0.71, CNT: +2.29) but they do not separate, indicating that charge repulsion cannot counterbalance the attractive π–π stacking energy. Upon further 8 electron charge extraction corresponding to the transition cal-Dox-on-CNT^{+3} → cal-Dox-on-CNT^{+11}, the

originally flat aromatic dihydroxy anthraquinone system adopts a bent ribbon shape (Supporting information Fig. S13, frame 2,3), but attractive interaction persists even for the partial charge partitioning Dox+1.17 p-stacking on CNT+9.83 in cal-Dox-on-CNT^{+11}. Further geometry optimization leads finally to covalent ether formation between Dox and CNT, i.e. the carbonyl function in the side chain of the cyclohexane subunit of Dox attacking the CNT (Supporting Information Fig. S13, frame 3,4 and movie 2).

In conclusion, the QM simulation can be summarized as: (i) the LUMO of cal-Dox-on-CNT^{-3} is Dox-localized. It reflects the experimental CVs, i.e. reduction of Dox@CNT occurs at a potential similar to the one observed for free Dox in solution, (ii) the calculation is in agreement with the experimental fact that Dox@CNT can easily be cleaved reductively, (iii) oxidatively triggered release of Dox from cal-Dox-on-CNT^{+11} is not possible. In contrast to charge injection, charge extraction tends to stabilize the $\pi-\pi$ interaction, and ultimately triggers an irreversible bond formation between Dox and CNT.

6.3. Conclusion

Carbon 150lutathio (CNT) based drug delivery of doxorubicin (Dox) is recognized as a promising technique in the fight against cancer. In many cases, Dox is just physically adsorbed on pristine CNT. Our STM analysis shows Dox as mono- or dimeric π-stacking molecules in single or double stranded helical conformation on the outer surface of the CNT. The molecular resolution of Dox@CNT achieved with STM allows for the first time to measure loading efficiencies of Dox on CNT from image analysis. Furthermore, the broad range of reported loading efficiencies spanning a factor of two can be rationalized by the observed presence of mono- or dimeric Dox π-stacked on CNT. Helical π-stacking of mono and dimeric Dox on the

CNT cylinder is also expected in case of CNTs with less accessible tube surface after modification with solubilizing agents or recognition sites.

Two “small molecule triggers” typical for the intracellular state of cancerous cells, i.e. protons (increased acidity) and GSH level (a more negative cellular reduction potential as compared to the extracellular conditions) have been used in recent years as functional conditions for the expulsion of Dox from physically adsorbed Dox@CNT. The increased acidity can act as an efficient release trigger only if additional basic sites have been introduced on the CNT such as chitosan. The pH triggered release of Dox is in this case explained by the repulsive electrostatic interaction between protonated chitosan and protonated Dox on CNT. Use of GSH as a reductive release trigger has been realized by Hou et al. and relies on the reductive cleavage of a disulfide linkage of a Dox prodrug covalently linked to CNT. [23]

In this study we have focused on the intrinsic reactivity of physically adsorbed Dox@CNT towards protons and towards electrons in the absence of any other complicating ingredients on the CNT surface. We found, that the “low-pH release-trigger” cannot be used for Dox release from simple physically adsorbed Dox@pristine-CNT, i.e. without an additional basic polymer on the CNT surface. On the other hand we found that an increased GSH level can lead to efficient expulsion of Dox from Dox@pristine-CNT. Thus, a 10-20 mM solution of glutathione (a typical intracellular concentration) is one to two orders of magnitude more efficient than the natural release of Dox in pure water in the 4-7 pH range in the absence of GSH. If the reduction potential is more negative, e.g. -0.8 V, Dox release is even instantaneous. In absence of reducing agents, Dox and CNT seem to be in equilibrium with Dox@CNT. Thus, after preparation, a high Dox@CNT content is established in the colloidal stock solution with free Dox in solution and this situation holds over months. However, natural (un-triggered) Dox release with a half life of

some days is observed if the highly concentrated stock solution is diluted with pure water. This "natural release in pure water" is much slower than if 152lutathione is present. The discovery of the reductive release trigger is of importance for the understanding and further development of CNT based drug delivery systems.

We have modeled the stability of physically adsorbed Dox@CNT before and after electron injection on a semi-empirical QM level. Stability prior to reduction is in agreement with charge transfer interactions as indicated by the interdigitated and mixed HOMO/LUMO orbitals of CNT and Dox. Release of Dox from the CNT bound state upon reduction was also modeled and is related to electron filling of the LUMO's. The correct modeling results for Dox@CNT offer the opportunity to screen possible other drug candidates by that could be carried as drugs@pristine-CNT and released upon electron transfer by semiempirical methods. Furthermore, the STM method shown here and giving access to the Dox arrangement and to the loading efficiency of Dox@CNT can probably be generalized and used as an experimental method to find new drug candidates that may be transported by the CNT carrier.

6.4. Experimental

Materials

6,5-SWCNTs were from *Sigma Aldrich*, Doxorubicin hydrochloride from *Sigma Aldrich*, 1,4-Dihydroxyanthraquinone from *Fluka*, 3,6-Diaminoacrdine hydrochloride from *Sigma Aldrich*, L-Glutathione (GSH) reduced from *Sigma Aldrich*.

Zeta potentials

Colloidal Solution of Dox and CNT: Zeta potentials were determined with a Zetasizer nano ZS (Malvern Instruments, Model ZEN3600) at 25°C with a 633nm laser in a DTS1070 cell. A clear stock solution of 1 mg CNT in 20 ml H_2O was prepared by ultrasonic treatment. To aliquots of 0.5 ml CNT solution, varying volumes of Dox (2 mg in 1 ml H_2O) were added. To these mixtures H_2O was added to reach a total volume of 5 ml.

Vis-spectroscopy, loading efficiency of Dox on CNT

UV-vis spectroscopy was performed on a *Hewlett-Packard* 8453 spectrophotometer or an AvaSpec 3648 spectrometer and AvaLight- DHC in connection with two optical fibers (all from *Avantes*).

2.5 mg doxorubicin were dissolved in 25ml water (pH = 8.53, adjusted by KOH addition). 5 ml of this stock solution was stepwise diluted and used for the calibration curve. To the remaining 20 ml 1.2 mg 6,5-CNT was added and ultrasonicated for 30 min followed by stirring for 48 hrs, then filtered through a 0.2µm pore sized polyamide membrane (*Sartolon* polyamide, pore size 0.2 µm). The amount of free Dox in the filtrate was determined using the UV-vis calibration *curve.*

STM of Dox@CNT

Scanning tunneling microscopy (STM) was performed with an EasyScan II from *NanoSurf* at RT. The measurements were made mostly at a bias of 0.050 V and 1 nA tunneling current. The STM tips were prepared from a Pt/Ir (80/20) wire of 0.25 mm diameter from *PHYWE*. Highly ordered pyrolytic graphite (HOPG) from *Mikromesh* was used as a substrate. Dispersions of Dox@CNT were prepared by dissolving 2 mg doxorubicin hydrochloride in 2 ml of water, then 1mg of chiral 6,5-CNT was added and ultrasonicated in an ice bath for 20 min. 2-5 µl of this dispersion was spread on the HOPG substrate and dried overnight. The amount applied results in a thin layer of single CNTs on HOPG. Then the measurements were made at different positions. STM images were analyzed by using the WSxM software.[34]

Prepartion of Dox@CNT

Doxorubicin hydrochloride (12mg) was dissolved in 25 ml of water (slightly basic 7.8 pH adjusted with KOH) and 5mg of 6,5-CNT was added. The resulting suspension was sonicated for 30 min in ice cold water. A homogenous dispersion of Dox@CNT with still free Dox in solution resulted. The solution was further stirred overnight in dark at room temperature. The resulting dispersion was filtered through a polyamide membrane (*Sartolon* polyamide, pore size 0.2 µm). The filtrand was washed extensively with water until the filtrate was completely colorless. The Dox@CNT complex was collected from the polyamide membrane and re-dispersed in ca. 5 ml water under ultrasonification, then filtered and washed again, and finally dried under high vacuum and preserved.

Elemental analysis

Elemental analyses were done on a “Elementar” instrument from *Vario* Micro Cube. The above washed and dried Dox@CNT was used for elemental analysis.

Stock Solution of Dox@CNT for further analysis: The 3mg of above prepared Dox@CNT was redispersed in 2 ml of water by ultrasonification for some minutes and then used as a stock solution for further experiments. The colloidal stock solution was stable for almost 2 months and developed a slightly pink color due to naturally released Dox ($A_{Dox,480,t0}$ = 0.075, $c_{Dox,\ t0}$ = $6.5*10^{-6}$ mol/l).

Electrochemical measurements of Dox@CNT@GCE

All electrochemical experiments were performed under three-electrode conditions using an Autolab potentiostat (PGSTAT 20, *Autolab*) interfaced with a PC running the GPES software. For the preparation of Dox@CNT - modified electrodes, ca. 15-20µl of stock soln. was casted on a freshly polished glassy carbon electrode (GCE, 0.07 cm^2). After drying at 30^{o}C, CVs were initiated in 0.1 M KCl (neutral conditions) or upon addition of KOH or HCl for varying (un-buffered) pH ranges.

AFM of Dox@CNT@GCE

Atomic force microscopy (AFM) was performed on a Flex-Axiom from *NanoSurf* at RT using PointProbe Plus nonContact Mode Short Cantilevers – Au Coating probe (PPP-NCSTAuD, *Nanosensors*). Ca. 15-20µl of stock soln. was casted on a freshly polished glassy carbon electrode and fixed in EC-AFM electrochemical cell. "Dry measurements" with intermediate electrochemistry were made with Dox@CNT on glassy carbon in the dry state, then 0.1 M KCl was added and the CV was performed at a scan rate of 100mV/s to release the Dox, then the

solvent/electrolyte was carefully removed, in order to hold the x-y position, then the electrode was measured again.

eQCM of Dox@CNT@Au-Quartz

The Electrochemical quartz crystal microbalance eQCM experiments were conducted in a three-electrode cell from *ALS* Co., Ltd, Japan (eQCM Flow cell kit) under stationary conditions. A 5 MHz quartz crystal resonator metalized with a gold key-hole type electrode (0.28 cm^2) was used. The potential was controlled by a potentiostat from *Gamry* (Interface 1000) and a frequency analyzer from *Gamry* (eQCM 10 m). The electrolyte was a 0.1 M KCl solution. Ca. 50-70 µl of stock soln. was casted on gold-on-quartz electrode, after drying at 30^oC, eQCM measurements were initiated in 0.1 M KCl. After a measurement, the electrolyte solution was carefully collected and the Dox content was determined by Vis spectroscopy.

GSH-induced Dox release from Dox@CNT

Two cuvettes (l = 1 cm) containing each 10µl of the stock solution and 3 ml water under argon were prepared (m_{CNT} ~ 30µg). At time 0, to one of the cuvettes, 20 mg (22 mM) GSH was added (sample). A third cuvette containing m_{CNT} (~ 40µg) and GSH (10 mM) at t = 0 was prepared. Notably, it was not possible to control the amount of modified CNT in the addition process accurately, because of partial coagulation. All cuvettes contained a magnetic bar at the bottom and stirring was maintained between the measurements. UV vis spectra of the sample and the blank were taken at reasonable intervals. Scattering of light due to partial clustering of tubes was corrected by subtracting the absorbance at A_{750} nm from A_{480} to yield A_{480c}. A further correction was done for the natural release of Dox during the stocking period (ca 15 %) present at t=0. All measured absorbances, $A_{480,t}$ were corrected for this natural release present at t=0.

From this corrected absorbance (A_{480c}) measured at long times ($A_{t=\infty}$), the absorbances for intermediate and totally released Dox was calculated in molarity and percentage using $\varepsilon_{Dox,\,480}$ = 11450 $M^{-1}cm^{-1}$. The sample without GSH did not show any measurable release over 28 h.

PM7 modeling calculations

Dox@CNT was modeled in the gas phase using the semi-empirical method PM7 from the MOPAC package of Stewart [33] using GABEDIT [35] as graphical interface The heavily Dox loaded CNTs was modeled by a short 3.8 nm 6,5-CNT with hydrogens saturating the open peripheral tube valences, and with a single protonated Dox on top (total number of atoms: 455 atoms designated as cal-Dox-CNT in contrast to the experimental Dox@CNT consisting of many Dox on longer 6,5-CNTs). Calculations were accelerated using the keyword MOZYME. In some calculation the SETPI command was further used. All calculated total energies stem from the mozyme calculations; orbital energies (in hartree) were calculated from single point calculations using the appropriate geometry from the mozyme file as a starting point. Charges on Dox and CNT in the cal-Dox-CNT complex were calculated from atomic charges.

References

[1] E. Heister, V. Neves, C. Tilmaciu, K. Lipert, V. S. Beltran, H. M. Coley, S. R. P. Silva, J. McFadden, Carbon 2009, 47, 2152.

[2] J. Y. Chen, S. Y. Chen, X. R. Zhao, L. V. Kuznetsova, S. S. Wong, I. Ojima, J Am Chem Soc 2008, 130, 16778.

[3] Z. Liu, A. C. Fan, K. Rakhra, S. Sherlock, A. Goodwin, X. Y. Chen, Q. W. Yang, D. W. Felsher, H. J. Dai, Angew Chem Int Edit 2009, 48, 7668.

[4] a) X. Y. Yang, X. Y. Zhang, Z. F. Liu, Y. F. Ma, Y. Huang, Y. Chen, J Phys Chem C 2008, 112, 17554; b) X. M. Sun, Z. Liu, K. Welsher, J. T. Robinson, A. Goodwin, S. Zaric, H. J. Dai, Nano Res 2008, 1, 203; c) H. Y. Wen, C. Y. Dong, H. Q. Dong, A. J. Shen, W. J. Xia, X. J. Cai, Y. Y. Song, X. Q. Li, Y. Y. Li, D. L. Shi, Small 2012, 8, 760; Q. Zhang, W. W. Li, T. Kong, R. G. Su, N. Li, Q. Song, M. L. Tang, L. W. Liu, G. S. Cheng, Carbon 2013, 51, 164; d) T. Zhou, X. M. Zhou, D. Xing, Biomaterials 2014, 35, 4185.

[5] Z. Liu, X. M. Sun, N. Nakayama-Ratchford, H. J. Dai, Acs Nano 2007, 1, 50.

[6] L. J. Meng, X. K. Zhang, Q. H. Lu, Z. F. Fei, P. J. Dyson, Biomaterials 2012, 33, 1689.

[7] Y. Mo, H. Wang, J. Liu, Y. Lan, R. Guo, Y. Zhang, W. Xue, Y. Zhang, Journal of Materials Chemistry B 2015, 3, 1846.

[8] Y. J. Wang, H. Xu, H. Z. Liu, Y. Wang, J. Sun, Z. G. He, J Biomed Nanotechnol 2012, 8, 450.

[9] X. K. Zhang, L. J. Meng, Q. H. Lu, Z. F. Fei, P. J. Dyson, Biomaterials 2009, 30, 6041.

[10] Y. X. Wang, Z. F. Xu, Rsc Adv 2016, 6, 314.

[11] a) Y. Yang, Y. M. Zhang, Y. Chen, D. Zhao, J. T. Chen, Y. Liu, Chem-Eur J 2012, 18, 4208; b) S. L. Wu, X. D. Zhao, Y. H. Li, Q. J. Du, J. K. Sun, Y. H. Wang, X. Wang, Y. Z. Xia, Z. H. Wang, L. H. Xia, Materials 2013, 6, 2026; c) M. Balcioglu, M. Rana, M. V. Yigit, J Mater Chem B 2013, 1, 6187; H. Wang, W. Gu, N. Xiao, L. Ye, Q. Y. Xu, Int J Nanomed 2014, 9, 1433.

[12] S. H. Liu, A. C. T. Ko, W. Y. Li, W. Zhong, M. Xing, Journal of Materials Chemistry B 2014, 2, 1125.

[13] P. Jeyamohan, T. Hasumura, Y. Nagaoka, Y. Yoshida, T. Maekawa, D. S. Kumar, Int J Nanomed 2013, 8, 2653.

[14] H. Ali-Boucetta, K. T. Al-Jamal, D. McCarthy, M. Prato, A. Bianco, K. Kostarelos, Chemical Communications 2008, 459.

[15] Z. F. Ji, G. F. Lin, Q. H. Lu, L. J. Meng, X. Z. Shen, L. Dong, C. L. Fu, X. K. Zhang, J Colloid Interf Sci 2012, 365, 143.

[16] A. Rodriguez-Galvan, O. Amelines-Sarria, M. Rivera, M. D. Carreon-Castro, V. A. Basiuk, Nano 2016, 11.

[17] Z. X. Li, T. Tozer, L. Alisaraie, J Phys Chem C 2016, 120, 4061; M. El Khalifi, E. Duverger, H. Boulahdour, F. Picaud, Anal Methods-Uk 2015, 7, 10145.

[18] Z. A. Mohammadi, S. F. Aghamiri, A. Zarrabi, M. R. Talaie, Chem Phys Lett 2015, 642, 22.

[19] T. Panczyk, P. Wolski, L. Lajtar, Langmuir 2016, 32, 4719.

[20] S. S. Banerjee, K. J. Todkar, G. V. Khutale, G. P. Chate, A. V. Biradar, M. B. Gawande, R. Zboril, J. J. Khandare, Journal of Materials Chemistry B 2015, 3, 3931.

[21] J. J. Liu, C. Wang, X. J. Wang, X. Wang, L. Cheng, Y. G. Li, Z. Liu, Adv Funct Mater 2015, 25, 384.

[22] S. He, Y. Cong, D. Zhou, J. Li, Z. Xie, X. Chen, X. Jing, Y. Huang, Journal of Materials Chemistry B 2015, 3, 8203.

[23] L. Hou, X. M. Yang, J. X. Ren, Y. C. Wang, H. J. Zhang, Q. H. Feng, Y. Y. Shi, X. N. Shan, Y. J. Yuan, Z. Z. Zhang, Int J Nanomed 2016, 11, 607.

[24] N. Hadidi, F. Kobarfard, N. Nafissi-Varcheh, R. Aboofazeli, Aaps Pharmscitech 2013, 14, 593.

[25] L. C. Cao, S. Sadaf, S. M. Beladi-Mousavi, L. Walder, Eur Polym J 2013, 49, 1923.

[26] P. Agrawal, S. K. Barthwal, R. Barthwal, Eur J Med Chem 2009, 44, 1437.

[27] J. N. Coleman, M. S. Ferreira, Appl Phys Lett 2004, 84, 798.
[28] I. Serbanescu, M. Enache, E. Volanschi, Analele Universitatii Bucuresti : Chimie 2003.
[29] K. Y. Zhang, Y. Z. Zhang, Microchim Acta 2010, 169, 161.
[30] A. Latus, E. Volanschi, Rev Roum Chim 2008, 53, 1131.
[31] G. Sauerbrey, Z Phys 1959, 155, 206.
[32] S. Ghoshal, S. K. S. K. , M. S. a. P. , Tiwari, American Journal of Advanced Drug Delivery 2014, 2, 213.
[33] James J. P. Stewart, Colorado Springs, CO, USA, MOPAC2016.
[34] I. Horcas, R. Fernandez, J. M. Gomez-Rodriguez, J. Colchero, J. Gomez-Herrero, A. M. Baro, Rev Sci Instrum 2007, 78.
[35] A. R. Allouche, J Comput Chem 2011, 32, 174.

Appendix

S1. Formation of Dox@CNT

S1.1 Zeta potential measurements

S1.2 Dox pick-up by UV-Vis absorption

S2. Elemental and Structural Analysis

S2.1 Elemental analysis of Dox@CNT

S2.2 Additional STM images of Dox@CNT and Alternative arrangement of dimeric Dox on CNT

S2.3 STM images of Quinizarin@CNT (a model compound)

S2.4 XRD spectra of Dox, Dox@CNT and CNT on different substrates and SEM images

S3. UV-vis and Electrochemical pH –titration

S3.1 UV-vis- pH –titration of Dox in water

S3.2 Electrochemical pH –titration of Dox in 0.1 M KCl and Dox@CNT@GC

S4. Reductive release

S4.1 Electrochemical reductive Dox release

S4.2 eQCM Study of reductive Dox release by

S4.3 GSH triggered Dox release from Dox@CNT

S4.4 Nernst potentials of the GSSG / 2 GSH redox couple at different pH

S5. Molecular modeling

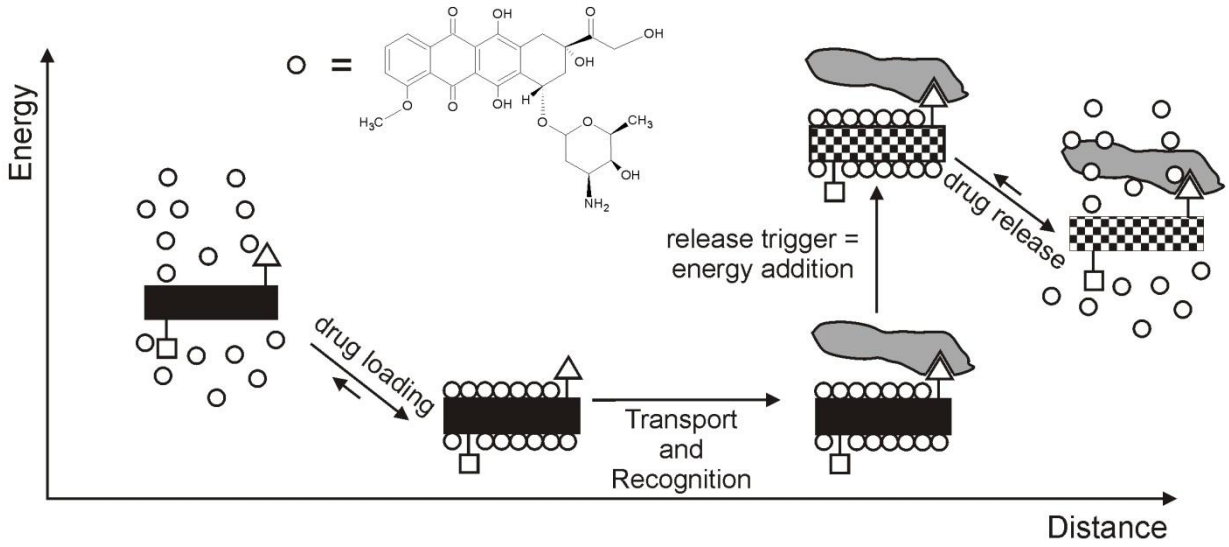

Figure S1: Loading, transport and release of a drug on/from a nanoparticl in an energy vs. distance scheme*. Circle: drug, black bar: nano particle (ground state), chessboard bar: nano particle (NIR-excited, reduced, oxidized, ...) state, triangle: recognition site for biological host, gray: biological host, square: solubilizing agent, fluorescent tag and other functions.*

The simplified Fig. S1 relies on drug loading after prior addition of the recognition centers. The trigger is interpreted as a change of the physical chemical situation at or in the targeted cell which shifts the relative energy of drug complexation to drug release. However, the variety of published systems is much wider. The drug can principally be encapsulated [1], covalently attached [2-4] to the nanocarrier or reversibly adsorbed [5] at the surface of the carrier. The controlled release [6] of drugs from the nanocarriers (either from a complexed state or by bond breaking) is achieved by the physicochemical conditions present within the cell (e.g. temperature, pH, [2, 7], enzymatic activity, [4]) or by an external focused energy source (e.g. NIR illumination [7]).

S1. Formation of Dox@CNT

S1.1 Zeta potential measurements

TableS1: Dox/CNT Weight ratios for Zeta potential measurements

Sample number	CNT amount µg in 5 ml	Dox amount (µg) in 5ml /concentration (µM]	Weight ratio CNT / Dox	Zeta potential mV
1	25	0 / 0	1/0	-20
2	25	6.3 / 2.2	1/0.25	-3
3	25	12.6 / 4.4	1/0.5	14
4	25	25 / 8.7	1/1	21.9

5	25	50 / 17.3	½	25
6	25	75 / 25.9	1/3	28
7	25	250 / 86.4	1/10	30
8	25	750 / 259.1	1/30	31.1

S1.2 Dox pick-up by UV-Vis absorption and calibration Curve

The absorption of the modifying Dox solution before and after interaction with CNTs is shown in Fig. S2. The amount of Dox picked up by CNTs is calculated from the absorbance difference.

For this purpose the UV-vis of a Dox solution (water pH 7.8, KOH adjusted, un-buffered) was measured before addition of CNTs. Then CNTs were added (weight ratio Dox/CNT = 2/1) and stirred for 48 hours. The solution was then filtered and the remaining amount of Dox was determined from the drop of absorbance yielding a 1.7/1 weight ratio for the Dox@CNT complex (see blue arrow in Fig. 1(main text) and Table S1.2). Notably, the ´Dox/CNT ratio is easily transformed into the loading efficiency according to eq. S1

Loading efficiency = 100 % (wt. of Dox in Dox@CNT / wt. of CNT in Dox@CNT) eq. S1

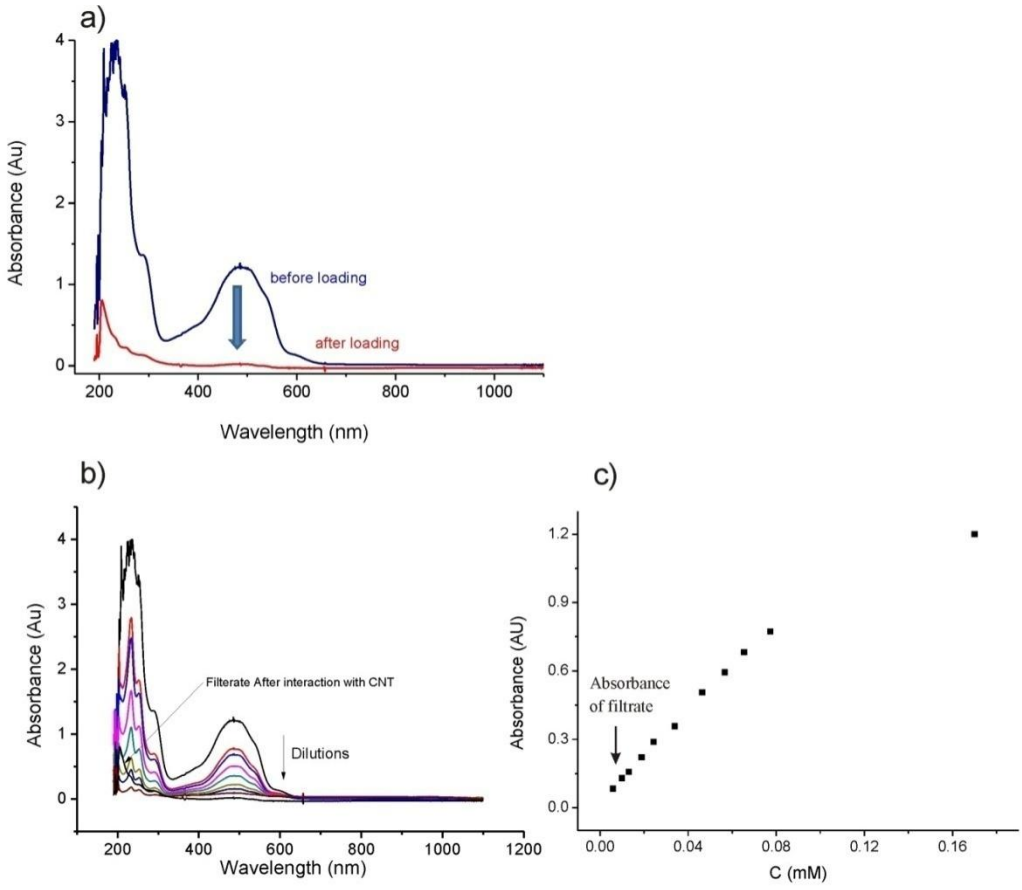

Figure S2: UV-vis spectroscopy of Dox solution *(a) before and after interaction with CNT (b) absorption spectra of Dox dilutions at different concentrations used as calibration curve (c) calibration curve yielding 1.7 mg Dox / mg of CNT.*

Table S1.2: Dox -pick up from solution

Technique	Wt. Ratio Dox/CNT mg	Loading efficiency of Dox
Uv-vis	1.7/1	170%

S2. Elemental and Structural Analysis

S2.1 Elemental analysis of Dox@CNT

From eq. S2 and S3 the contribution of Dox and CNT in from the carbon content of exp. Carbon content in pure Dox, pure CNT and Dox@CNT were calculated according to the adjusted formula of N. Hadidi et al. [8]

$0.68 = (0.87xA) + (0.56xB)$ (eq. S2)

$A + B = 1$ (eq. S3)

with
0.68: exp. Carbon content in Dox@CNT)
0.87: exp. Carbon content in pure CNT
0.56: exp. Carbon content in pure Dox
A: contribution of CNT in Dox@CNT
B: contribution of Dox in Dox@CNT

Table S3: Elemental analysis the pure SWCNT, Dox and Dox@CNT

Technique		Carbon	Hydrogen	Nitrogen	Wt. Ratio Dox/CNT mg	Loading efficiency of Dox
Elemental Analysis	pure SWCNT[a)]	87.45	1.296	0.08		
	Doxorubicin [a)]	56.04	5.23	2.39		
	Dox-SWCNT [b)]	68.08	3.166	1.17	1.61/1	161%

a) As received
b) Dox@CNT after washing

S2.2 Additional STM images of Dox@CNT and alternative arrangement of dimeric Dox on CNT

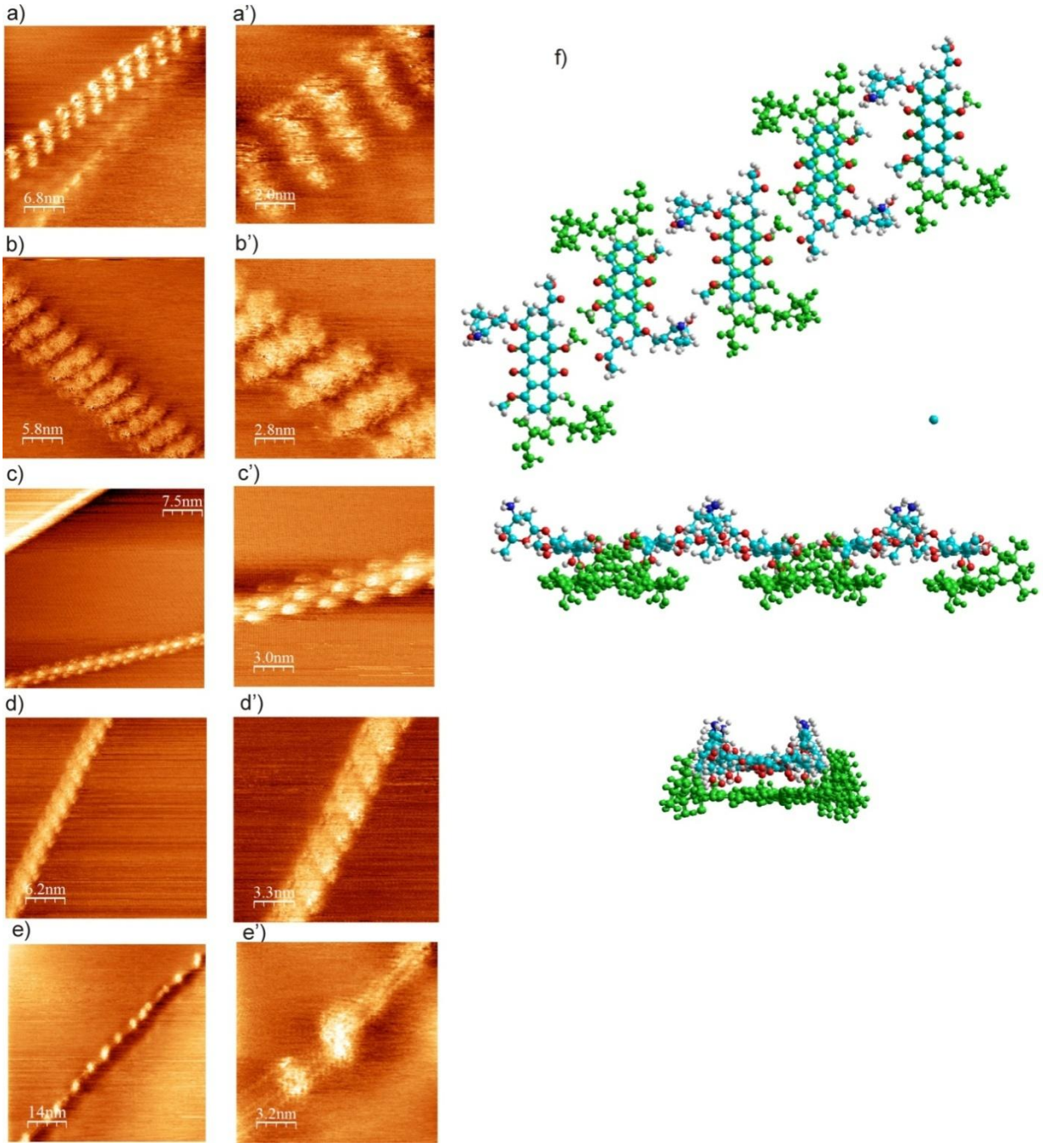

Figure S3: Additional STM images and alternative arrangement of dimeric Dox on CNT. *a) example of a double stranded Dox@CNT probably consisting of dimeric Dox with (a') the corresponding zoom-in; b) monostranded Dox@CNT with dimeric Dox molecules and (b') zoom-in; c) monostranded Dox@CNT with monomeric Dox molecules and zoom-in (c'); d) double stranded Dox@CNT consisting of dimeric Dox with (d') the corresponding zoom-in; e) is an example of low coverage of Dox@CNT consisting of mono or dimeric Dox clusters occupy collectively 2-3 CNTs (e') the corresponding zoom-in with the resolution of benzene rings of naked CNT in between successive Dox molecules; (f) Alternative arrangement of dimeric Dox on CNT, with anti-parallel arrangement of aside Dox molecules, from top to bottom: top-view, side view side view (viewing angle as in Fig 2g-i(main text)).*

Table S4: STM analysis of Dox@CNT

image	Dox type	Helical turns / distance on CNT	Helical pitch / Dox per turn	Dox per 10 nm	Dox weight per 10 nm CNT.HCl	CNT weight per 10 nm	Struct. Loading efficiency
a	bare						
b	Monomer loading	5 / 13nm	2.6 nm / 4	15.4	8874	10920	81.3%
c	dimeric	3 / 9 nm	3 nm / 10	33.3	19314	10920	177 %
d	Double stranded dimeric	Not analyzed					
e	Bundle of 2 CNTs	Each CNT shows individual helical wrapping					

S2.3 STM images of Quinizarin@CNT (a model compound)

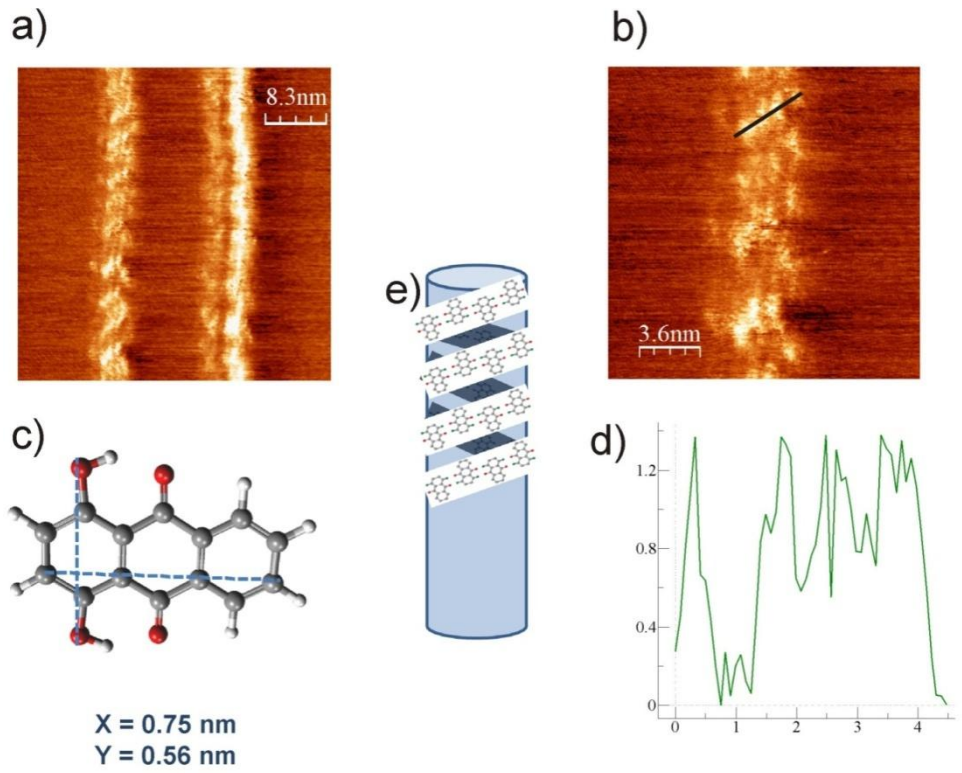

Figure S4: STM images of Quinizarin@CNT (a model compound) *a,b) topography; c)structure of quinizarin; e) proposed model of quinizarine@ CNT considering STM images; d) profile from STM image b.*

Quinizarin contains the same aromatic system as Dox. It is neutral and only slightly soluble in water (missing positive charge of Dox). In order to overcome solubility problems ca. 25 % DMF was added. The colloidal solution of quinizarin and CNT was not established quickly and all through. Only the diluted upper part of the solution was used for casting on the HOPG electrode.

The STM image shows principally a similar arrangement as for Dox@CNT, i.e. the ellipsoidal main axis parallel to the CNT axis. The lateral distance between the quinizarin molecules is ca. 0.9 nm (slightly smaller than in case of Dox@CNT). In other images clustering of quinizarin in packages was observed.

S3. UV-vis and electrochemical pH –titration

S3.1 UV-vis- pH –titration of Dox in water

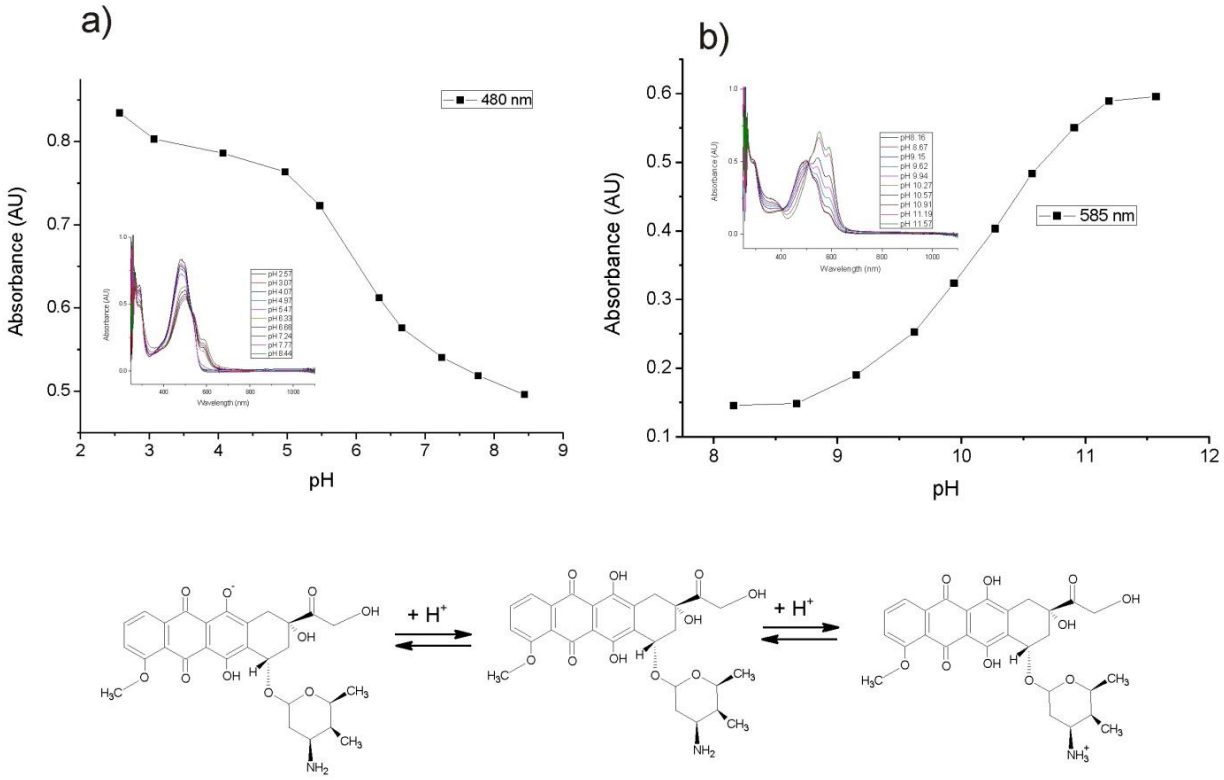

Figure S5: Dox (140µM) was pH titrated using KOH and HCl yielding two pKa values*, i.e. 10.1 and 6.1. The 10.1 value is related to the deprotonation of –NH_4^+, and according to Munnier [12] also to the phenol deproptonation. The 6.1 value is less clear (no indication in literature), but could be related to coupled Dox dimerisation processes.*

S3.2 Electrochemical pH –titration of Dox in 0.1 M KCl and of Dox@CNT@GC

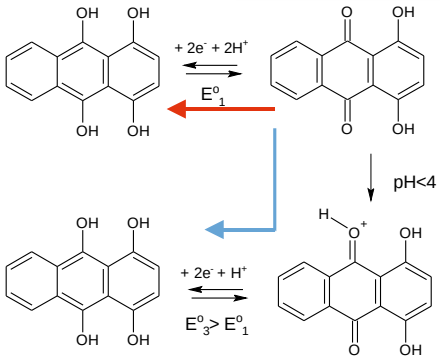

Scheme S1: *Scheme of square for the dihydroxy anthraquinone subunit. The red arrow is active in the higher pH range (concomittant electron and proton transfer), the blue arrow (protonation prior to electron tranfer) is active in the lower pH range (see a) and c) in Fig. S6.*

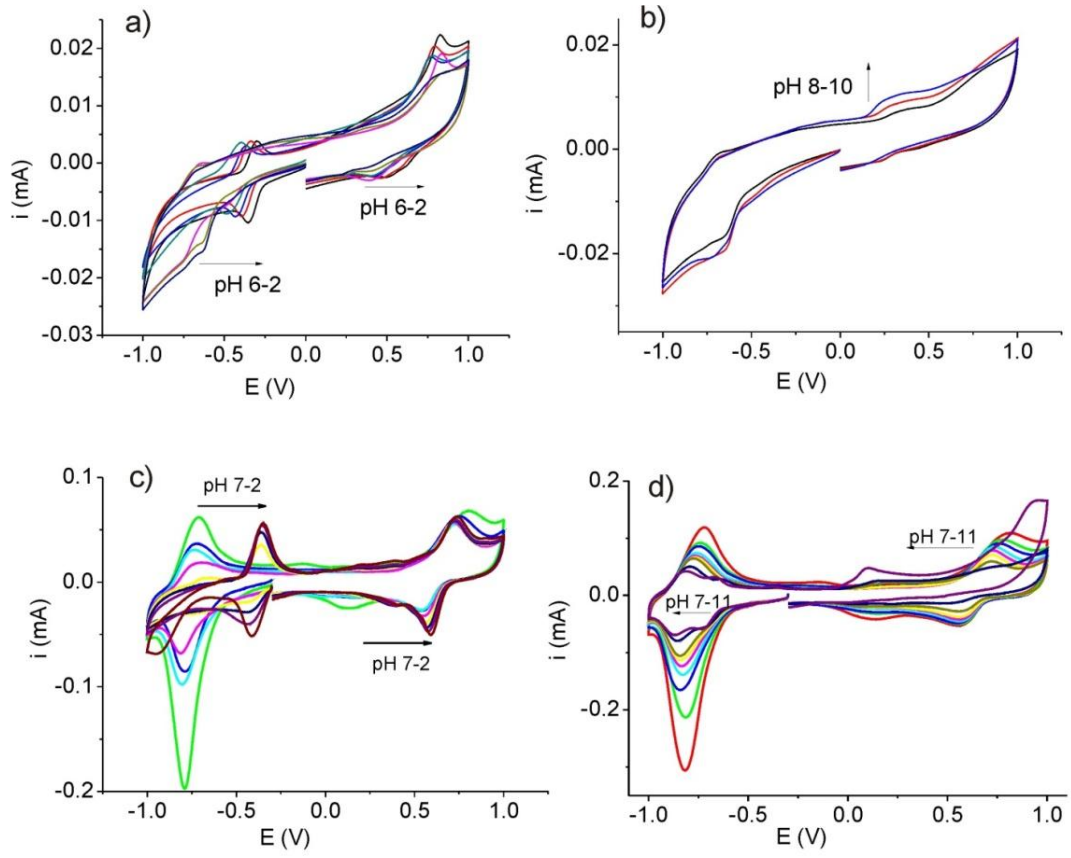

Figure S6: CV of Dox in 0.1 M KCl and of Dox@CNT@GC at different pH. *CV of 140µM Dox at GC electrode in 0.1M KCl v = 100 mV/s scan 0 → -1 → +1 → 0 V, (a) acidic conditions (b) basic conditions , E vs. Ag/AgCl c,d): CV of a Dox@CNT@GC electrode in 0.1 M KCl v = 100 mV/s, GC surface = 0.07cm², E vs. Ag/AgCl. (c) under acidic conditions (transition for the reduction observed at pH ca. 3.5 with reversible wave -0.7 V at pH 7-4 and a new wave at -0.4 for pH 4-2) and continuous shift of peak potentials for the oxidation to more positive values with decreasing pH for the oxidation); (d) under basic conditions*

S4. Reductive release

S4.1 Electrochemical reductive Dox release at stationary and rotating disk

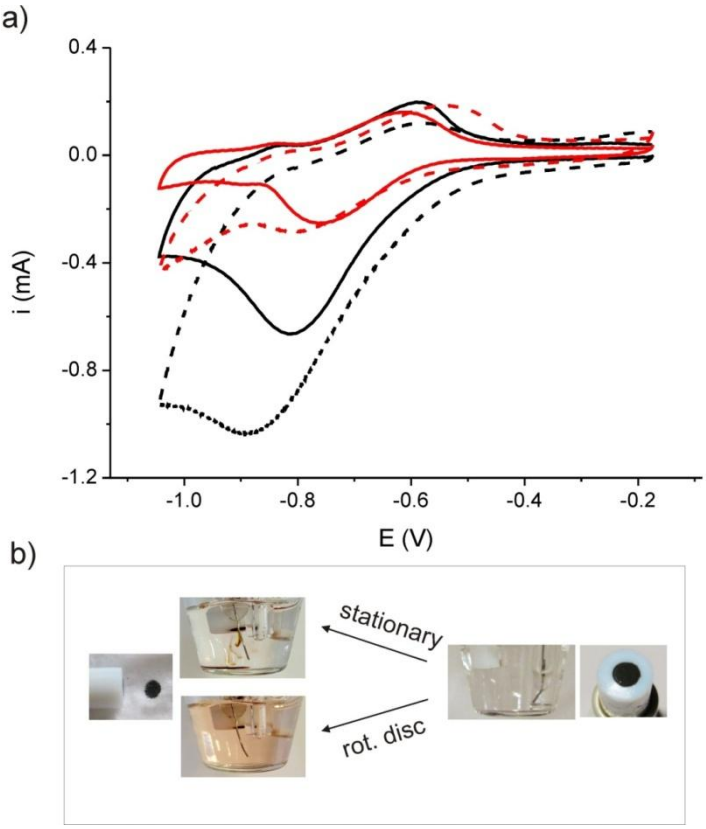

Figure S7: Electrochemical reductive Dox release at stationary and rotating disk. *a) Cyclic voltammogram (black: 1st cycle, red: 2nd cycle) of a Dox@CNT@GC electrode in 0.1 M KCl (solid: stationary, broken line: rotating disk (1000 rpm); v = 100 mV/s, GC surface = 0.07cm², E vs. Ag/AgCl. b) on right side; glassy carbon electrode (CG) with a Dox@CNT layer (ca. 35 µg) and side view of the 3-electrode cell with inserted GC – no Dox release observed); on the left side: (upper) 3-electrode cell (side view) after first reduction cycle at the stationary electrode, (lower): 3-electrode cell (side view) after first reduction cycle at the at rotating disc electrode; far left: removal of naked CNT from GC with a filter paper after 2nd scan.*

S4.2 Study of reductive Dox release by eQCM

Table S5: Frequency and mass change in solution of DOX@CNT@eQCM upon electrochemical reduction

Exp. No	Potential step Start / 1st / (2nd) in (V) with step times 1000 s start pot. = 0 V		Frequency change (Δf (kHz)) upon pot. step for 1st (2nd) and sum (total)			mass change (Δm (µg)) upon pot. Step 1) for 1st (2nd) and sum (total) interpreted as Dox released			$Abs_{(480)}$ of supernatant Solution / amount Dox released (µg)	
	1st step (V)	2nd step (V)	Δf 1st	2nd step	total	1st step	2nd step	Total µg	Abs	amount (µg) / used volume
Q1	-1		18.19	-	18.19	89.99		89.99	0.21	85.30 / 0.9ml
Q2	-0.8	-1	12.66	-	12.66	62.62		62.62	0.15	60.92 / 0.8ml
Q3	-0.7	-1	14.16	-0.21	13.95	69.01		69.01	0.13	66.01 / 1ml
Q4	-0.65	-1	11.15	4.46	15.61	55.16	22.06	77.22	0.15	68.54 / 0.9ml
Q5	-0.6	-1	2.174	13.65	15.82	10.75	67.53	78.28	0.18	62.03 / 0.8ml

1) corrected for electr. Area

Quartz crystals were modified with Dox as described in the experimental section. The solution electrolyte was aqueous KCl (0.1 M). In table S6 the applied potential steps are given as start / 1st / 2nd .

All electrodes were equilibrated at 0 V (Start) for 200 s. When the 1st (1000 sec) was not sufficient for complete release of Dox from the Dox@CNT@gold layers (cases-0.7 to -0.6 V) , a second step of -1V was applied. The corresponding column 3 with masses was obtained from the Sauerbrey equation taking the area (0.28 cm^2) and the sensitivity factor 56.6 Hz / µg cm^{-2} for the 5 MHz quarz into account. In column 4 the spectroscopic absorbance at 480 nm of the supernatant solution (abs) after the 2nd pot. step is reported. The amount of released Dox was calculated from Beer-Lambert using (ε = 9848 in 0.1 M KCl), and a varying cell volume, however, it was difficult to ensure that all released Dox is present in the supernatant volume which was spectroscopically analyzed. This is due to the thickness of the Dox@CNT film, to the geometry of the cell and to the difficulty to collect all CNT entrapped Dox.

The amount of released Dox from Dox@CNT calculated from the eQCM mass change is in crude agreement with the one observed from the absorption spectra of the supernatant solution with an error of $\pm$ 10 µg.

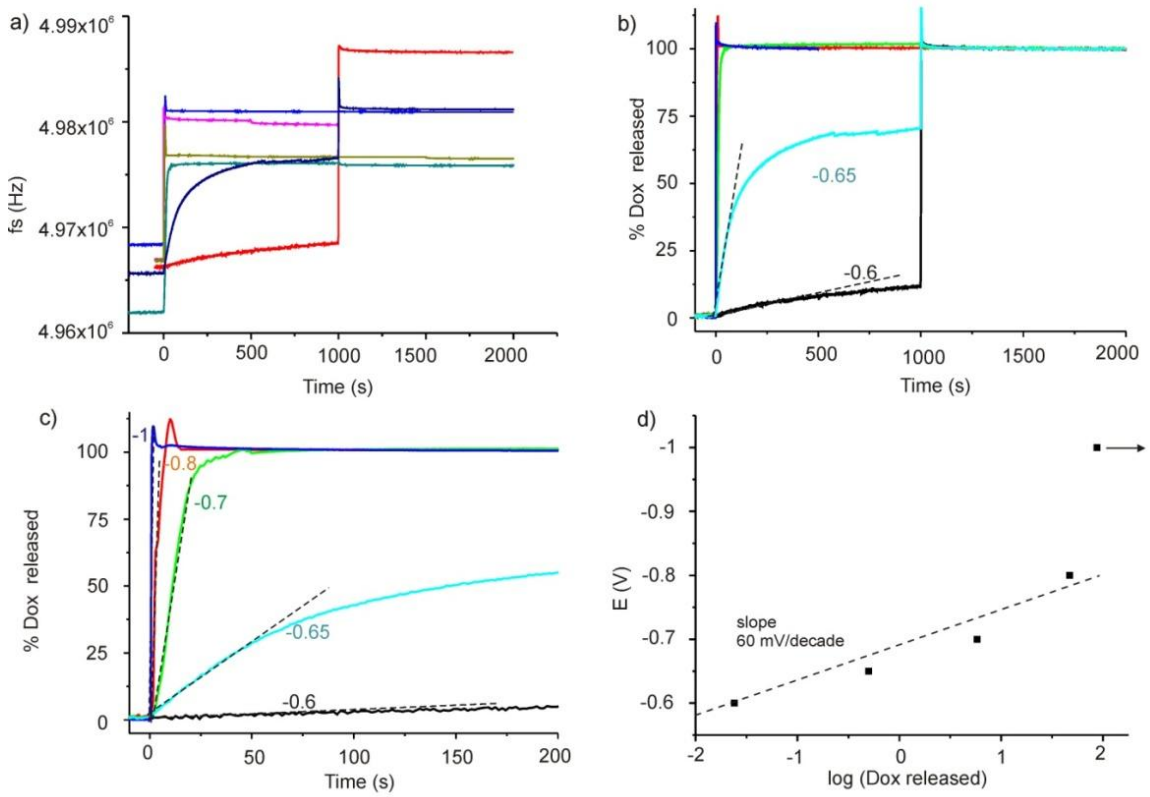

Figure S8: Voltage dependent rate of Dox release from Dox@CNT@QCM*. a) Experimental eQCM traces used for table S6 and for Fig 4(maintext);(b-c) all starting frequencies were set to zero and a percentage y-scale was used with 100% = totally observed release at -1 V; b) ,c)percent release of Dox after application of a potential of -0.6 and -0.65 V (b) long times), or -0.6, -0.65, -0.7, – 0.8 and -1.0 V (c), short times) as a function of time. The percent of Dox released as a function of time was calculated from the frequency prior to reduction and after complete reduction (-1V, long time, difference = 100 %) and converting all data to percent release. Linear regression was applied all traces directly after the potential step. Slopes are reported in Table S7 d) Tafel type correlation of the rates (=slopes from a) and c)) versus applied potential yielding a linear free energy relationship for four data points, the point at -*

1 V is not on the regression line as its rate is too fast to be resolved by the eQCM response. The slope is 60 mV/decade indicating a one electron transfer with asymmetric transition state (0.5 < α < 1)

Table S6: Slopes for Tafel plot

No.	Potential step	slope	log(slope)
1	-0.6	0.024	-1.61979
2	-0.65	0.5	-0.30103
3	-0.7	5.8	0.76343
4	-0.8	47	1.6721
5	-1	87	1.93952

S4.3 GSH-induced Dox release from Dox@CNT:

Two cuvettes (l = 1 cm) containing each 10µl of the stock solution and 3 ml water under argon were prepared (m_{CNT} ~ 30µg). At time 0, to one of the cuvettes 20 mg (22 mM) GSH was added (resulting pH=2.8, sample). A third cuvette containing m_{CNT} (~ 40µg) and GSH (10 mM, pH=3.5) at t = 0 was prepared. All cuvettes contained a magnetic stirring bar at the bottom and stirring was continuously maintained between the measurements. UV-vis spectra of the sample and the blank were taken at reasonable intervals.

Scattering of light due to partial clustering of tubes was corrected by subtracting the absorbance at A_{750} nm from A_{480} to yield A_{480c}. A further correction was done for the Dox amount present at t=0, which has build up during the stocking period (several weeks, ca 15 %). All measured absorbances, $A_{480,t}$ were correspondingly corrected. From this corrected absorbance (A_{480c}) measured at long times ($A_{t=\infty}$), the absorbance for totally released Dox was calculated in molarity and percentage using $\varepsilon_{Dox,\,480}$ = 11450 $M^{-1}cm^{-1}$. In Fig. 5(main text), plot the percentual release is plotted vs. time for the 22 mM GSH (black squares), 10 mM GSH (red circles) and for no GSH (blue triangles). An exponential behavior of the plots ($A_{480,t}$) is observed for 10 and 22 mM GSH showing half lives at $38*10^3$ s and $18*10^3$ s, respectively. The sample without GSH does not show any measurable release over 28 h, as expected from its 15 % release over 2 months. A plot of ln(Dox@CNT) vs time for 22 (b)) and 10 (c)) mM GSH yields a linear behavior with slopes given in table S7.

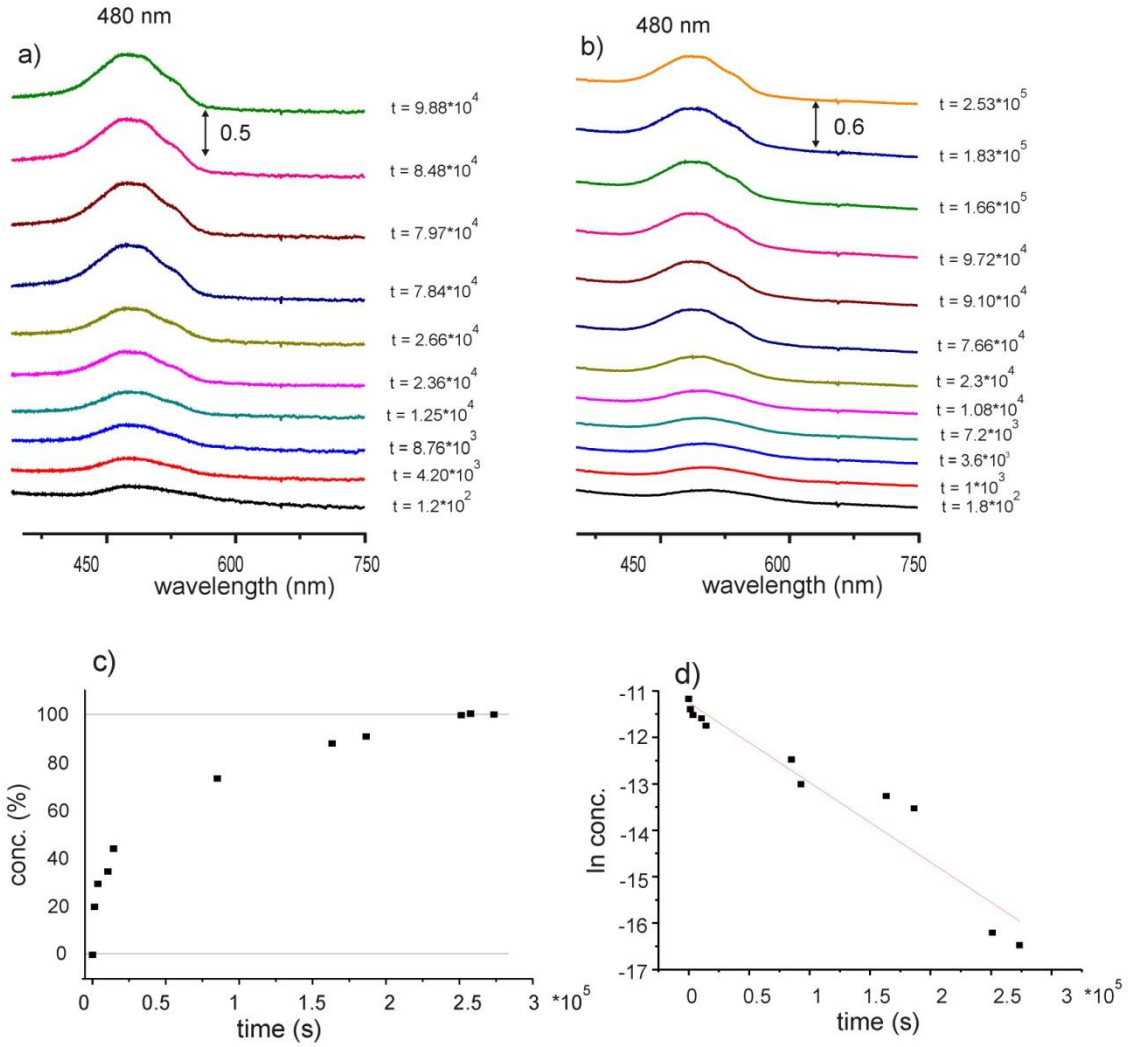

Figure S9: GSH-induced Dox release from Dox@CNT. *UV/Vis spectra taken at different time intervals of Dox@CNT (ca. 30µg) in 3ml H_2O with addition of (a) 22 mM (b) 10 mM, GSH at t=0; stacked absorbance spectra with shifted y axis for clear presentation of the single spectra. Final absorbance due to Dox is 0.44 corresponding to c(Dox) = 3.8*10^{-5} mol/l using ε(Dox, 480) = 11450. The final absorbance value was corrected for scattering and for the concentration of free Dox just prior to t=0 in Fig.5 in the main text.*

(c-d) Reductively triggered release of Dox from water suspended Dox@CNT by GSH; c) percentage of Dox observed vs. time 9.3 mM GSH (pH adjusted to 6.9; d) pseudo-first order analysis of c)

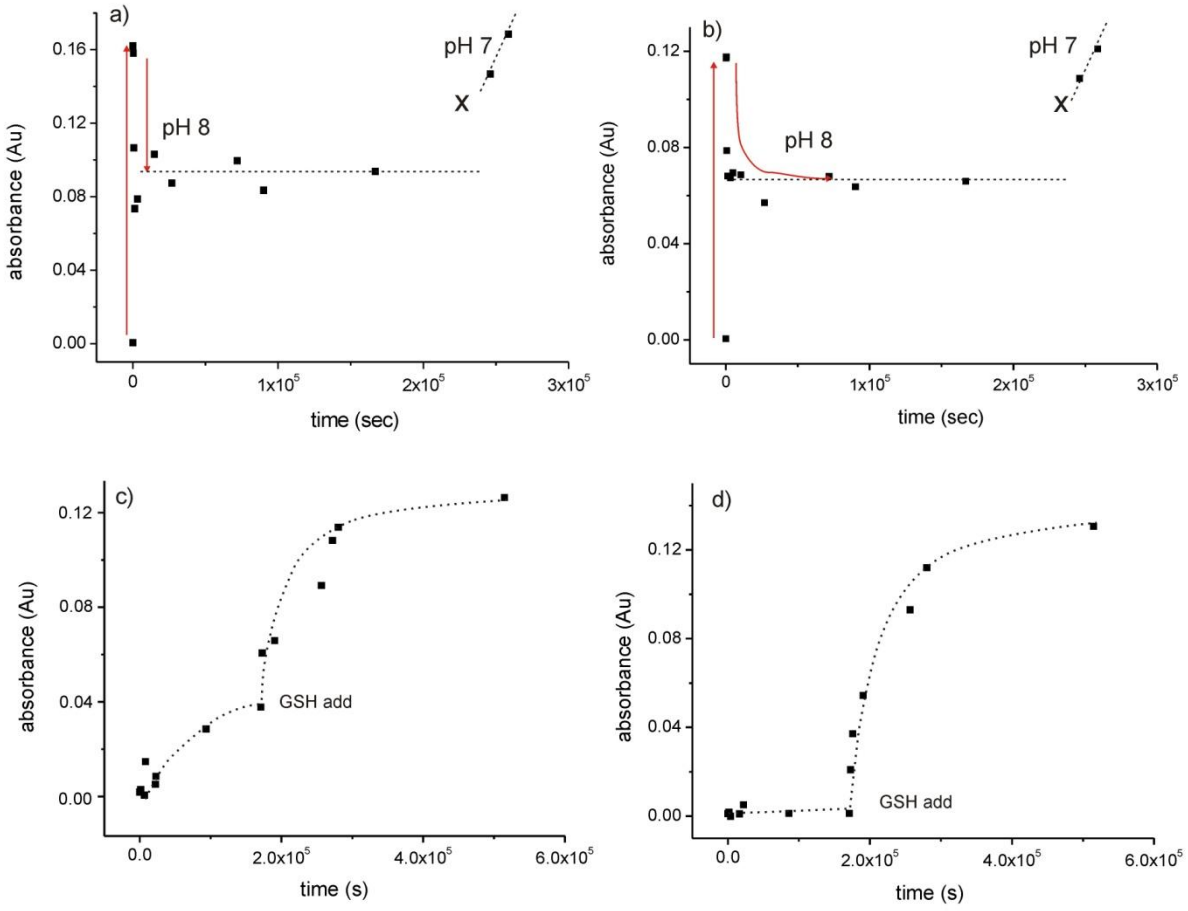

Figure S10: GSH-induced Dox release from Dox@CNT. *Dox@ CNT reductively triggered release of Dox from water suspended Dox@CNT by GSH under basic conditions; released Dox observed vs. time (a) in presence of 20 mM GSH and (b) 10 mM GSH (pH adjusted to 8 with KOH); initially fast release was observed, later an equilibrated situation is observed (note pH 8 is favorable for Dox@CNT complex formation).*

Notably, at the end of the measurements at pH8 the pH was adjusted to 7 (x) and fast Dox release with half lives as reported in table S6 was observed.

(c-d) Dox release from Dox@ CNT under acidic conditions (HCl), then complete release triggered by GSH addition; released Dox observed vs. time (c) initial pH was set to 3.8 with HCl (final pH: 4.7, $\tau^{1/2}$ ca. 4.5 days) (measurements taken until 48 hr); (d) initial pH was set to 4.9 with HCL (final pH: 5.8, $\tau^{1/2}$ > 7 days) (measurements taken until 48 hr), then added 10mM GSH.

Table S7: Chemical release of Dox from CNT under different conditions

Sr. No.	pH	Conc. GSH	$E^{0'}$	τ1/2 (s)	$k_{(pseudo\ first\ order)}$	$k_{2nd\ order}$
1.	3.5	$10 * 10^{-3}$ M	-0.282 V	$38*10^3$	$1.81*10^{-5}$ s^{-1}	$1.81*10^{-3}$ $s^{-1}M^{-1}$
2.	2.8	$22 * 10^{-3}$ M	-0.241 V	$18*10^3$	$3.89*10^{-5}$ s^{-1}	$1.77*10^{-3}$ $s^{-1}M^{-1}$
3.	6.9	$9.3* 10^{-3}$ M	-0.485 V	$40*10^3$	$1.72* 10^{-5}$ s^{-1}	$1.84*10^{-3}$ $s^{-1}M^{-1}$
4.	7	0		$>5.2*10^6$ a)	-	-
5.	8	$10 * 10^{-3}$ M	-0.545 V	ca. 50		
6.	8	$20 * 10^{-3}$ M	-0.545 V	< 50		
7.	3.8-4.7	0		$>6*10^5$		
8.	4.9-5.8	0		$>4*10^5$		

a) Low volume stock solution with corresponding high conc. of free Dox, CNT and Dox@CNT leading to equilibrated situation.

Interpretation:

(i) in the absence of GSH, the acidity does not influence the natural release of Dox from Dox@CNT (pH 7: $t_{1/2}$ > 60 days [a)], pH. 5.4: 4.6 days, pH 3.8-4.7: 7 days, pH 4.9-5.8: 4.6 days. The increased stability at pH 7 is related to the equilibrated situation a) in Table S7

(ii) GSH enters with molecularity 1 (doubling of pseudo-first order rate upon doubling of GSH concentration (Sr. No. 1 and 2), allowing us to calculate the 2nd order rate constant = $1.8 * 10^{-3}$ $s^{-1}M^{-1}$.)

(iii) GSH triggered release at pH 8 is very fast, but equilibrates with the complex formation back reaction (Sr. No. 5 and 6); initial release rate shows $t_{1/2}$ ca 50 s.

S4.4 Formal potentials of the GSSG / 2 GSH redox couple at different pH vs. Ag/AgCl reference:

The half cell reduction potential of GSH is defined by eq. S4 and the observed electrode potential by the resulting concentration dependencies eq. S4-6.

$$GSSG + 2e^- + 2H^+ \rightarrow 2\ GSH \quad \text{(eq. S4)}$$

$$E = E^{o'} - 0.058/2\ V * \log([GSH]^2) / ([GSSG]\,[H^+]^2)) \quad \text{(eq. S5)}$$

$$E = E^{o'} - 0.058\ V * \log([GSH]) + 0.029\ V * \log[GSSG] - 0.058\ V * (pH_{exp}-7) \quad \text{(eq. S6)}$$

Using $E^{0'}{}_{(GSSG/2GSH)}$ at pH 7 = -0.263 (vs SHE)[9] , $E^{0'}{}_{(GSSG/2GSH)}$ = -0.485 V (vs Ag/AgCl/KCl) (Cl^- = 3 M) under our conditions (see $E^{0'}$ in Fig. 4c(main text)) can be calculated.

With 10 mM GSH, 0.1 mM GSSG, pH=7 (corresponding to a typical contamination of GSH by GSSG in the 1 % range) we get with $E^{o'}$ = -0.485 V

$E = E^{o'} - 0.058\ V * \log 10*10^{-3} + 0.029\ V * \log 0.1*10^{-3} - 0.058\ V * pH_{exp}-7$

E(pH 9): $E^{o'}$ – 0.116 V = -0.601

E(pH8): $E^{o'}$ – 0.058 V = -0.543

E(pH7): $E^{o'}$ = -0.485

E(pH6): $E^{o'}$ + 0.058 V = -0.427

E(pH5): $E^{o'}$ + 0.116 V = -0.369

E(pH4): $E^{o'}$ + 0.174 V = -0.311

S5. Molecular Modeling

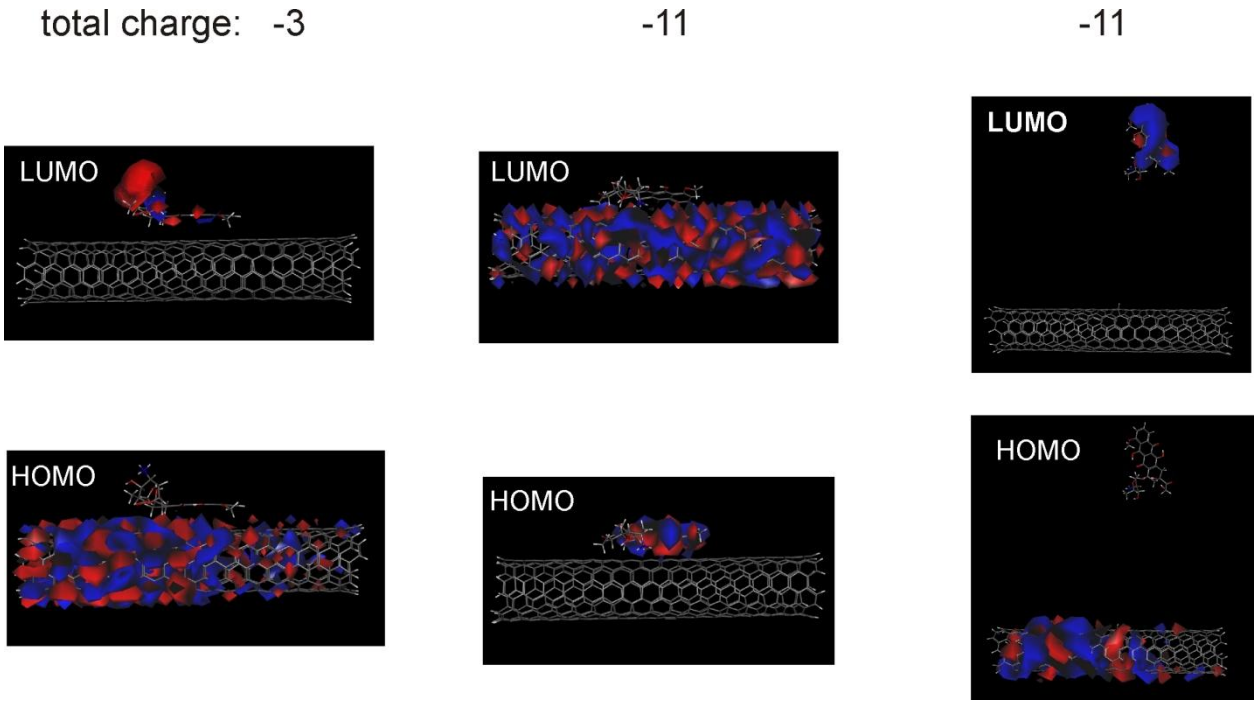

Figure S11: HOMO and LOMU of Dox@CNT at different total charge. *The presentations correspond to the HOMO and LUMOs shown in Fig. 6, I, II, and III (main text). Such presentations have been used to judge the MO localization in the frontier orbitals range -10 to +10 and have been coded in Fig. 6(main text) accordingly.*

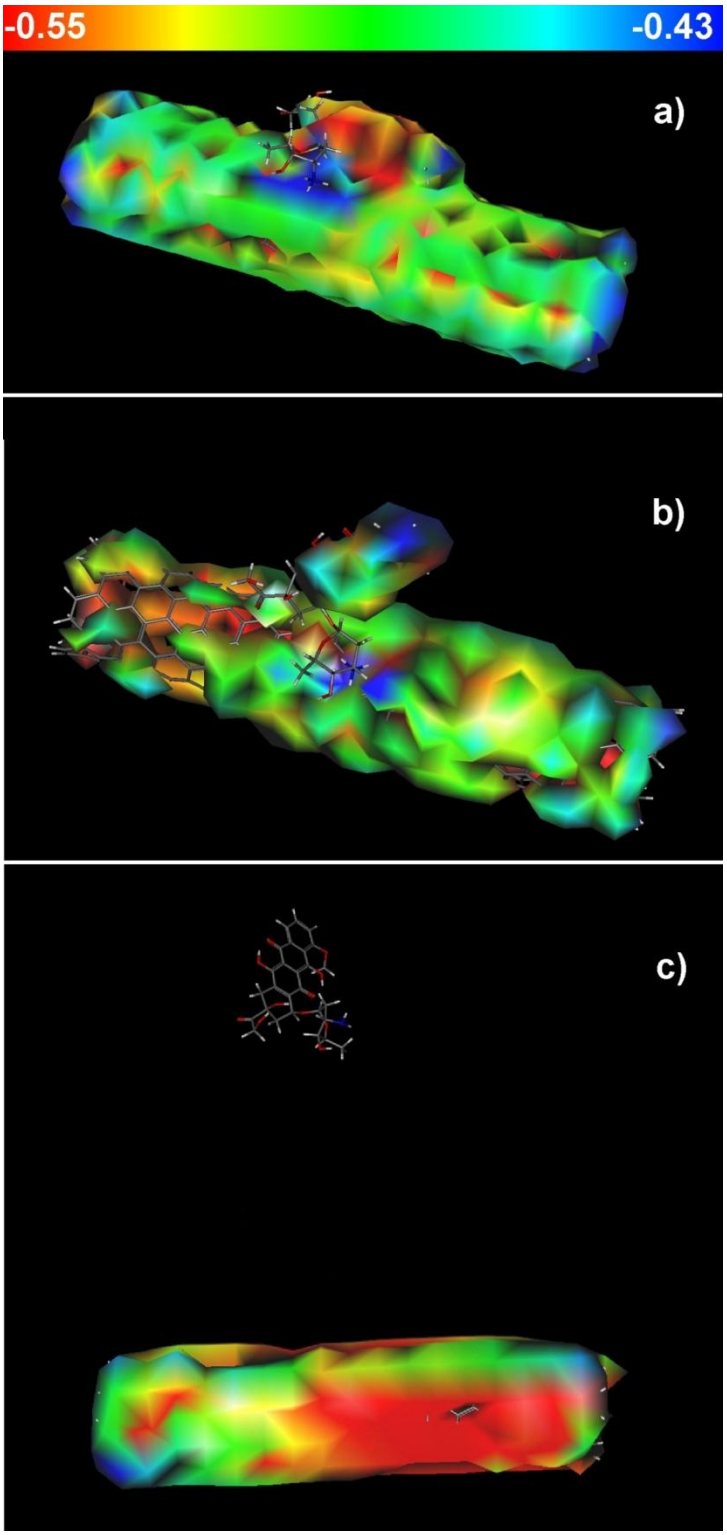

Figure S12: Molecular electrostatic potential. *Molecular electrostatic potential mapped on electron density (using partial charges) at different geometries using single point energies of the -11 case shown in Fig. 6 IV(main text). Charges on CNT and Dox are from the sum of NET ATOMIC CHARGES on CNT and Dox atoms, respectively. The geometries are from intermediate results (calc. cycle) of a pm7 mozyme geometry optimization.*

Color code indicates MEP value. a) calc. cycles 2: geometry optimization (MOZYME): Dox-CNT π-complex present, amine protonated, excess negative MEP (red) is observed on Dox with a mirror image (blue, lack of neg. charge) on CNT underneath. Charge on CNT is -10 and -1.1 on Dox (including the +1 charge on –NH3+). b) calc. cycles 519: geometry optimization (MOZYME), Dox-CNT π-complex disrupted, amine protonated, no MEP mirror image present. Charge on CNT is -9.9 and -1.1 on Dox. c) after calc. cycles 1231 geometry optimization (MOZYME), as all filled frontier orbitals are CNT localized, no electron density on Dox is present. Charge on CNT is -9.09 and -1.91 on Dox (after proton transfer, Dox with deprotonated –NH_3^+, CNT protonated).

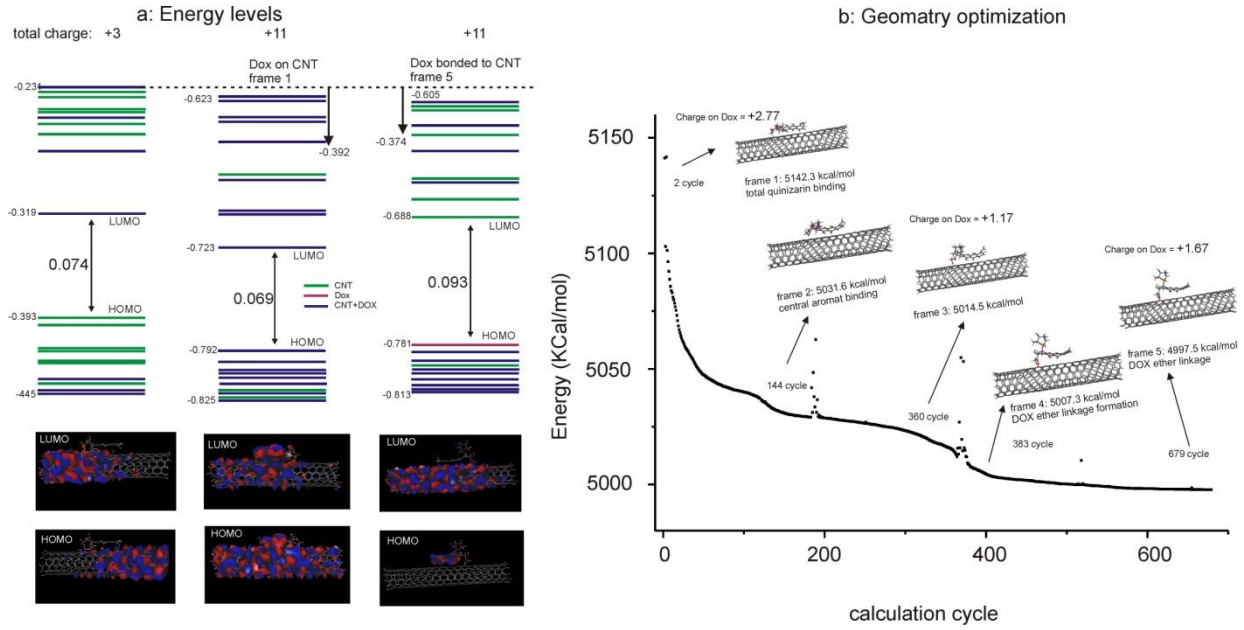

Figure S13: Semiempirical pm7 simulation of Dox@CNT upon oxidation. *(a) Energy level diagram of Dox on CNT with total charge +3 and +11. All values in hartree; energy levels shown are LUMO +9 to HOMO-9; the absolute energy scale is adapted for the graphical representation (see arrows from dotted line for applied shifts);green: orbitals localized on CNT; red: orbitals localized on Dox, violet: orbitals with composite Dox and CNT localisation;*

first column: +3 total charge: occupied levels in the frontier orbital region are CNT localized, LUMO and close to LUMO unoccupied levels are mixed Dox-CNT or CNT localized.

Second column: +11 total charge (Dox-on-CNT): (geometry equilibrated with tot. charge +3, than charged to +11), HOMO and LUMO are mixed Dox/CNT localized.

Third column: +11 total charge (Dox covalently linked to CNT)

Interpretation: Electron transfer originally from CNT (green HOMO in +3 state), followed by charge redistribution, bond formation yields Dox localized HOMO.

(b) Geometry optimization of one Dox on CNT; original situation is geometry optimized for a total charge of +3 (Dox@CNT^{+3}); at cycle 0 the positive total charge was set to +11 and the system was geometry optimized over 679 cycles using the mozyme keyword in pm7; during optimization the energy drops from 5143 to 4998 kcal; for selected calc. cycles (frame 1-5) the geometry, energy, and charge partitioning between Dox and CNT are shown (charge calculated from single point energy on the geometry from the mozyme calc.).

Frame 1 – frame 3: partial charge on Dox was originally +2.77 and on CNT +8.23; this changes to +1.17 and +9.83 for Dox and CNT, respectively in frame 3. At the same time the ammonium moves away from CNT but the π–π interaction persists, but the dihydroxyanthraquinone becomes more and more distorted.

Frame 3 – frame 4: the carbonyl function attacks the CNT as a nucleophile – yielding ether – carbenium covalently linked Dox on CNT (Scheme S2). After the C,O bond formation the distortion of the dihydroxy anthraquinone is less pronounced, but still present.

Frame 3 – frame 5: upon C,O bond formation the charge partioning changes from +1.17 and +9.83 to +1.67 and 9.33 on Dox and CNT moiety, respectively.

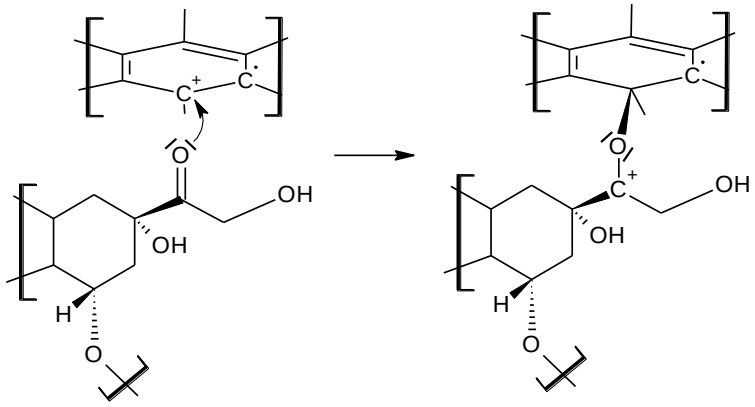

Scheme S2: *Chemical description of the observed bond formation between Dox and CNT. The partial charge transport from CNT to Dox in the calculation is rationalized by the reaction.*

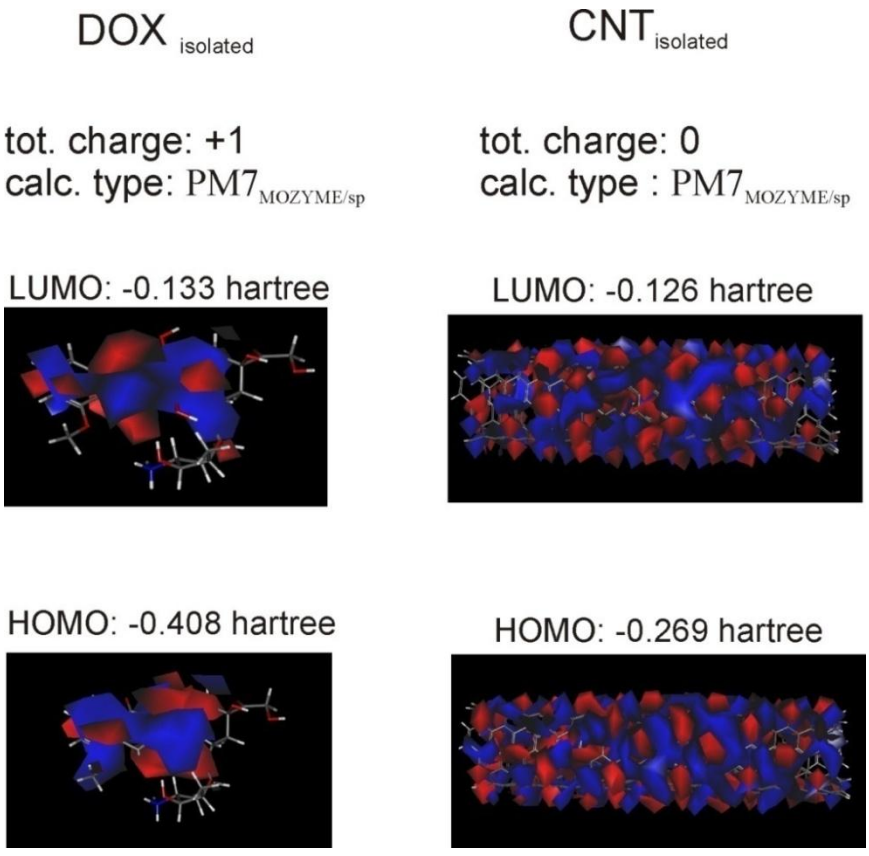

Figure S14: HOMO and LUMO of isolated Dox and CNT. *LUMO (up) and HOMO (down) of isolated Dox (+1) and CNT (0) and the corresponding orbitals as a reference.*

References

[1] O. Vostrowsky, A. Hirsch, Angewandte Chemie-International Edition 2004, 43, 2326.

[2] X. K. Zhang, L. J. Meng, Q. H. Lu, Z. F. Fei, P. J. Dyson, Biomaterials 2009, 30, 6041.

[3] L. J. Meng, X. K. Zhang, Q. H. Lu, Z. F. Fei, P. J. Dyson, Biomaterials 2012, 33, 1689.

[4] J. Y. Chen, S. Y. Chen, X. R. Zhao, L. V. Kuznetsova, S. S. Wong, I. Ojima, Journal of the American Chemical Society 2008, 130, 16778.

[5] a)H. Ali-Boucetta, K. T. Al-Jamal, D. McCarthy, M. Prato, A. Bianco, K. Kostarelos, Chemical Communications 2008, 459; b) Z. Liu, A. C. Fan, K. Rakhra, S. Sherlock, A. Goodwin, X. Y. Chen, Q. W. Yang, D. W. Felsher, H. J. Dai, Angewandte Chemie-International Edition 2009, 48, 7668; c) Z. Liu, X. M. Sun, N. Nakayama-Ratchford, H. J. Dai, Acs Nano 2007, 1, 50.

[6] T. M. Sun, Y. S. Zhang, B. Pang, D. C. Hyun, M. X. Yang, Y. N. Xia, Angewandte Chemie-International Edition 2014, 53, 12320.

[7] S. H. Liu, A. C. T. Ko, W. Y. Li, W. Zhong, M. Xing, Journal of Materials Chemistry B 2014, 2, 1125.

[8] N. Hadidi, F. Kobarfard, N. Nafissi-Varcheh, R. Aboofazeli, Aaps Pharmscitech 2013, 14, 593.

[9] K. K. Millis, K. H. Weaver, D. L. Rabenstein, J Org Chem 1993, 58, 4144.

Abbreviations

µm	micrometer
µM	microMolar
A	acceptor
A_{Dox}	Absorption of Dox
AFM	Atomic Force Microscopy
BA-V-cc	Butoxy Anisidine -Viologene-current collector
c_{Dox}	concentration of Dox
cfm	confirmed
CNTs	Carbon Nanotubes
CV	cyclic voltammetry
D	donor
DMA	dimethyl amine
DMF	dimethyl formamide
Dox	Doxorubicin
ε	molar absorptivity constant
EA	elemental analysis
EC-AFM	Electrochemical Atomic Force Microscopy
EC-STM	Electrochemical Scanning Tunneling Microscopy
eQCM	electrochemical Quartz Crystal Microbalance
FET	Field Effect Transistors
GC	Glassy carbon
GCE	glassy carbon electrode
GO	Graphene oxide
GSH	Glutathione (reduced)
GSSG	Glutathion disulfide (oxidized)
H_f	heat of formation
HOMO	Highest Occupied Molecular Orbital
HOPG	Highly Oriented Pyrolytic Graphite
LUMO	Lowest Unoccupied Molecular Orbital
MA-V-m-CNT	Methoxy Anisidine- Viologen-metallic Carbon Nanotubes
MeCN	acetonitril
MeOH	methanol
MM+	Molecular modeling
mV	millivolt
MWNTs	Multi Wall Carbon Nanotubes
nA	nanoAmpere
nm	nanometer
NMP	N-methyl-2-pyrrolidon
NTCDA	naphthalenetetracarboxylic dianhydride
P	presursor
pegA-V-PV	pegylated Anisidine-Viologen-Polyviologen
P-V	Phenyl-Viologen
PVDF	poly-vinylidene fluoride
PVFc	Poly(vinylferrocene)
r.t.	room temprature
rGO	Reduced graphene oxide
sc-CNT	Semiconducting Carbon Nanotube
STM	Scanning Tunneling Microscopy
SWNTs	Single Wall Carbon Nanotubes
TEMPO	2,2,6,6-tetramethylpiperidin-1-oxyl
tetraM-P-V	tetraMethyl-Phenyl-Viologen
VGCF	Vapour Grown Carbon Fibers
HOPG	Highly Oriented Pyrolytic Graphite

Publications related to my thesis

1. **S.Sadaf** and L. Walder. Doxorubicin adsorbed on Carbon Nanotubes: Helical Structure and New Release Trigger. ,Adv. Mater. Interfaces 2017, https://doi.org/10.1002/admi.201700649
2. Beladi-Mousavi, S. M., **Sadaf, S**., Mahmood, A. M. & Walder, L. High Performance Poly(viologen)–Graphene Nanocomposite Battery Materials with Puff Paste Architecture. *ACS Nano*, doi:10.1021/acsnano.7b02310 (2017).
3. S.M. Beladi-Mousavi, **S. Sadaf**, L. Walder, M. Gallei, C. Ruttiger, S. Eigler, C.E. Halbig Poly(vinylferrocene)-Reduced Graphene Oxide as a High Power/High Capacity Cathodic Battery Material. Adv. Energy Mater. *12*, 2016
4. L. Cao, **S. Sadaf**, S. M. Beladi Mousavi, L. Walder, Poly-TEMPO and Poly-Viologen on Carbon Nanotubes Synthesis, Structures and Organic Battery Application, European Polymer Journal, 49 (8) 1923-1934 (2013)
5. V.-A. Constantin, L. Cao, **S. Sadaf**, L. Walder, Oligo-viologen / SWCNT nano-composites: preparation and characterizationm, Physica status solidi (b)" 249(12) 2395–2398 (2012)

Publications from collaborations during my thesis:

6. H. Schäfer, D. M. Chevrier, P. Zhang, J. Stangl, K. M. Müller-Buschbaum, J. D. Hardege, K. Küpper, J. Wollschlaeger, U. Krupp, S. Duehnen, M. Steinhart, L. Walder, **S. Sadaf**, M. Schmidt, Electro-Oxidation of Ni42 Steel: A Highly Active Bifunctional Electrocatalyst. Adv. Funct. Mater., 2016, *26*, 6402
7. H. Schäfer, **S. Sadaf**, L. Walder, K. Küpper, S. Dinklage, J. Wollschlaeger, L. Schneider, M. Steinhart, J. Hardege,D.Daum. Stainless steel made to rust: A robust water-splitting Catalyst with Benchmark Characteristics. Energy Environ. Sci., 2015, *8*, 2685.
8. H. Schäfer, K. Küpper, J. Wollschläger, N. Kashaev , J. Hardege, L. Walder, S. M. Beladi-Mousavi, B. Hartmann-Azanza, M. Steinhart, **S. Sadaf**, F. Dorn Oxidized Mild Steel S235: An efficient Anode for Electrocatalytically Initiated Water-Splitting ChemSusChem, 2015, *21*, 8, 3099.
9. H. Schäfer, S. M. Beladi-Mousavi, L. Walder, J. Wollschläger, O. Kuschel, S. Ichilmann, **S. Sadaf**, M. Steinhart, K. Küpper, L. Schneider,Surface Oxidation of Stainless Steel: Oxygen Evolution Electrocatalysts with High Catalytic Activity ACS Catal., 2015, *5*, 2671.
10. S. Ok, **S. Sadaf**, L. Walder, Basic characterization and investigation of a fluorinated terpolymer in pure state and in mixtures with kaolinite at solid interphases of thin films prepared by facile solution cast and nonsolvent methods, High Performance Polymers. High Performance Polymers, **2014**, Vol. *26* (7), 779-789

Curriculum Vitae

Name	Shamaila Sadaf
Father's Name	Muhammad Amin Bhatti
Postal Address	i605, Jahnplatz 6, 49080 Osnabrück, Germany
Permanent Address	Chak No 7 N/B Tehsil Bhalwal- 40410 District Sargodha Pakistan
Civil Status	Female, Married. Born November 20th, 1979. Citizen of Pakistan
Birth of my Son	27 September 2013

Education	**Year / Institution**
PhD	2017 / University of Osnabrück, Germany
M Phil (Chemistry)	2007 / University of Engineering and Technology Lahore
M Sc (Chemistry)	2001 / University of Engineering and Technology Lahore
B Sc (Chemistry, Botany, Zoology)	1999 / University of Punjab Lahore
B Ed (Chemistry, Biology)	2005 / Allama Iqbal Open University Islamabad

Awards

2010-2012	DAAD stipendium for part of PhD study
May 2007	HEC of Pakistan travel grant to make oral presentation at 211th meeting of the Electrochemical Society Chicago-Illinois USA
2005-2010	HEC of Pakistan Indigenous Fellowship
2007-2009	Awarded student membership of The Electrochemical Society, 65 South Main Street, Building D Pennington, New Jersey 08534-2839 USA (Thrice)

Experience	**From / To**	**Institution**
Research Assistant	2011/date	Institute of Chemistry University of Osnabrueck, Germany

Research Fellow	2007 / 2010	University of Engineering and Technology Lahore-Pakistan
Teacher	2004 / 2005	Fauji Foundation Model School Sheikhupura-Pakistan
Teacher	2002 / 2004	Merry Dall High School Bhalwal-Pakistan

Internship 2000 Internship at quality control division, and distillery plant of Noon Sugar Distillery, Noon Sugar Mills Bhalwal-Sargodha-Pakistan

Short Courses

2013 Electro Chemistry School, Electrochemistry at the Nanoscale, Department of Chemistry and Biochemistry, University of Bern, Switzerland

2012 Scanning Probe microscopy on soft matter and polymeric materials, Kerkrade, the Netherlands

2009 Modern Mass Spectrometry, Conducted by Prof Dr. David L. Smith Former Director of the Nebraska Lincoln, NE 68006 USA at University of Karachi-Pakistan

Publications

1. **S.Sadaf** and L. Walder. Doxorubicin adsorbed on Carbon Nanotubes: Helical Structure and New Release Trigger. , Adv. Mater. Interfaces 2017, https://doi.org/10.1002/admi.201700649
2. Beladi-Mousavi, S. M., **Sadaf, S**., Mahmood, A. M. & Walder, L. High Performance Poly(viologen)–Graphene Nanocomposite Battery Materials with Puff Paste Architecture. *ACS Nano*, doi:10.1021/acsnano.7b02310 (2017).
3. S.M. Beladi-Mousavi, **S. Sadaf**, L. Walder, M. Gallei, C. Ruttiger, S. Eigler, C.E. Halbig Poly(vinylferrocene)-Reduced Graphene Oxide as a High Power/High Capacity Cathodic Battery Material. Adv. Energy Mater. *12*, 2016
4. H. Schäfer, D. M. Chevrier, P. Zhang, J. Stangl, K. M. Müller-Buschbaum, J. D. Hardege, K. Küpper, J. Wollschlaeger, U. Krupp, S. Duehnen, M. Steinhart, L. Walder, **S. Sadaf**, M. Schmidt, Electro-Oxidation of Ni42 Steel: A Highly Active Bifunctional Electrocatalyst. Adv. Funct. Mater., 2016, *26*, 6402
5. H. Schäfer, **S. Sadaf**, L. Walder, K. Küpper, S. Dinklage, J. Wollschlaeger, L. Schneider, M. Steinhart, J. Hardege,D.Daum. Stainless steel made to rust: A robust water-splitting Catalyst with Benchmark Characteristics. Energy Environ. Sci., 2015, *8*, 2685.
6. H. Schäfer, K. Küpper, J. Wollschläger, N. Kashaev , J. Hardege, L. Walder, S. M. Beladi-Mousavi, B. Hartmann-Azanza, M. Steinhart, **S. Sadaf**, F. Dorn Oxidized Mild Steel S235: An efficient Anode for Electrocatalytically Initiated Water-Splitting ChemSusChem, 2015, *21*, 8, 3099.
7. H. Schäfer, S. M. Beladi-Mousavi, L. Walder, J. Wollschläger, O. Kuschel, S. Ichilmann, **S. Sadaf**, M. Steinhart, K. Küpper, L. Schneider,Surface Oxidation of Stainless Steel: Oxygen Evolution Electrocatalysts with High Catalytic Activity ACS Catal., 2015, *5*, 2671.
8. S. Ok, **S. Sadaf**, L. Walder, Basic characterization and investigation of a fluorinated terpolymer in pure state and in mixtures with kaolinite at solid interphases of thin films prepared by facile solution cast and nonsolvent methods, High Performance Polymers. High Performance Polymers, **2014**, Vol. *26* (7), 779-789
9. L. Cao, **S. Sadaf**, S. M. Beladi Mousavi, L. Walder, Poly-TEMPO and Poly-Viologen

on Carbon Nanotubes Synthesis, Structures and Organic Battery Application, European Polymer Journal, 49 (8) 1923-1934 (2013)

10. V.-A. Constantin, L. Cao, **S. Sadaf**, L. Walder, Oligo-viologen / SWCNT nano-composites: preparation and characterizationm, Physica status solidi (b)" 249(12) 2395–2398 (2012)
11. I. U. Haque, **S. Sadaf**, Anodic Coupling of Aniline, J. Chem. Soc. Pak 4 (6) 1345-1351, 2012
12. I. U. Haque, A. Raza, **S. Sadaf**, Dispersed nickel oxide films for electro-oxidation of 1,4-butanediol. J. Chem. Soc. Pak., 33, 21-28(2011);
13. I. U. Haque, K.A. Asghar, **, S. Sadaf**, M. Tariq, A. Khan, A. Rashid, Voltammetry of aniline in 9:1 acetonitrile/water. ECS Trans., 35 ,27-35(2011)
14. I. U. Haque, J. Saleem, W. Akram, A. Raza, M. Tariq and **S. Sadaf**, Electron transfer at nickel electrode, Sci. Int.(Lahore), 21 (1), 33-36 (2009)
15. I. U. Haque, A. Khan and **S. Sadaf**, "Anion of quinocyanomethylene: simulation of dimerization", J. Chem. Soc. Pak., 30 (2) 165-169 (2008)
16. I. U. Haque, W. Akram, S. Iqbal and **S. Sadaf**. Linear sweep voltammetry of N-bromosuccinimide, ECS Trans., 13 (24) 71-76 (2008)
17. I. U. Haque, S. Sadaf, and M. Tariq. Ketamine-a short review, Sci. Intl., 20 (3) 197-203 (2008)
18. I. U. Haque, A. Khan and **S. Sadaf**, Anion radical of 3,5-bis(1,1-dimethylethyl)-4-oxo-2,5-cyclohexadienylideneacetonitrile: dimerization. Bull. Electrochem., 23, 61-65(2007);
19. I. U. Haque, **S. Sadaf**, and G. Fatima. Electrolytic behavior of ferrocene, ECS Trans., 6 (6) 79-86 (2007)
20. I.U. Haque, W. Akram, N. Aslam, **S. Sadaf** and K. Bano. Aqueous voltammetry of 1-bromopyrrolidin-2,5-dione, ECS Trans., 6 (6) 1-9 (2007)
21. Haque, I. U.; Khan, A.; **Sadaf, S**., Anion radical of 3,5-Bis(1,1-dimethylethyl)-4-oxo-2,5-cyclohexadienylideneacetonitrile: dimerization. ECS Trans., 6, 17-26 (2007)

Conference Presentations

1. **Talk title:** Oligo- and polymeric redox systems on carbon nanotubes S. Sadaf, S.M. Beladi-Musavi, V.-A. Constantin, L. Cao, L. Walder (June 2013)
2. **Talk title:** Self-assembling of Poly- and Oligo-Viologens on CNTs as Evidenced by STM given at the International Conference on Scanning Probe Microscopy on Soft and Polymeric Materials, Kerkrade, Netherlands (September 2012)
3. **Talk title:** Ketamine a short review given at International Chemistry Conference "Recent Advances in Chemistry" , organized by LCWU, Lahore (November 2007)
4. **Talk title:** Aqueous voltammetry of 1-bromopyrrolidin-2,5-dione , given at 211th Electrochemical society meeting, Chicago, Illinois, U.S.A (May 2007)
5. **Talk title:** Anion radical of 3, 5-bis (1,1-dimethylethyl)-4-oxo-2,5-cyclohexadienylideneacetonitrile: dimerization**,** given at 211th Electrochemical society meeting, Chicago, Illinois, U.S.A (May 2007)
6. **Talk title:** An overview of electrochemical techniques, , given at 1st International Chemistry Conference, organized by GC University, Faisalabad, Pakistan. (November 2006)
7. **Talk title:** Rejuvenation of a reference half cell. , given at 1st International Chemistry Conference, organized by GC University, Faisalabad, Pakistan. (November 2006)
8. **Talk title:** Voltammetry of quinocyanomethylene: simulation given at International Chemistry Conference " organized by BZU, Multan (April 2006)Voltammetry of

nitrate at solid cathodes.

Abstracts

1. Self-assembling of Poly-and Oligo-Viologens on CNTs as Evidenced by STM, Shamaila Sadaf, Veronica-Alina Constantin, Liancheng Cao, S. Mohsen Beladi Mousavi, Lorenz Walder, *Meet. Abstr SPM on SPM (the Netherlands 2012)*
2. Voltammetry of Nitrate at Solid Cathodes, Inam. U. Haque, Shamaila Sadaf and Muqaddas Tariq. *Meet. Abstr.-Electrochem. Soc*. **802**, 1531 (2008).
3. Electrochemical Determination of Lipoic Acid, Inam-Ul-Haque, Sana Amin, Shamaila Sadaf, Muhammad Sarwar, Imran Majeed and Abdul Rehman. *Abstract* **59th** *Pittsburgh Conference on Analytical Chemistry and Applied Spectroscopy* (Pittcon 2008)

Poster Presentations

1. STM investigations of Viologens, TEMPO-deivatives, and Anthracyclines self-assembled on CNTs, S. Sadaf, L. Walder, Electrochemistry at the Nanoscale, Department of Chemistry and Biochemistry, University of Bern, Switzerland (June 2013)
2. Self-assembling and Covalent Attachment of Oligo-Viologens on CNTs, Lorenz Walder, Shamaila Sadaf, Veronica-Alina Constantin, Liangcheng Cao, *XXVIth International Winterschool on Electronic Properties of Novel Materials*(Austria 2012)
3. Ketamine: Anodic Voltammetry, Inam. U. Haque, Shamaila Sadaf and Saima Idrees. The *Meet. Abstr.-Electrochem. Soc*. 801, 543 (2008).

M Phil Thesis (2007

Electrolytic vs. potentiostatic studies using ferrocene, Department of Chemistry, University of Engineering and Technology Lahore

Declaration

I hereby declare that this thesis is the summary of my Ph.D. work and has not been submitted to any other university. All the sources and materials used in this thesis are duly acknowledged and cited.

Osnabrück, October 2017

Shamaila Sadaf